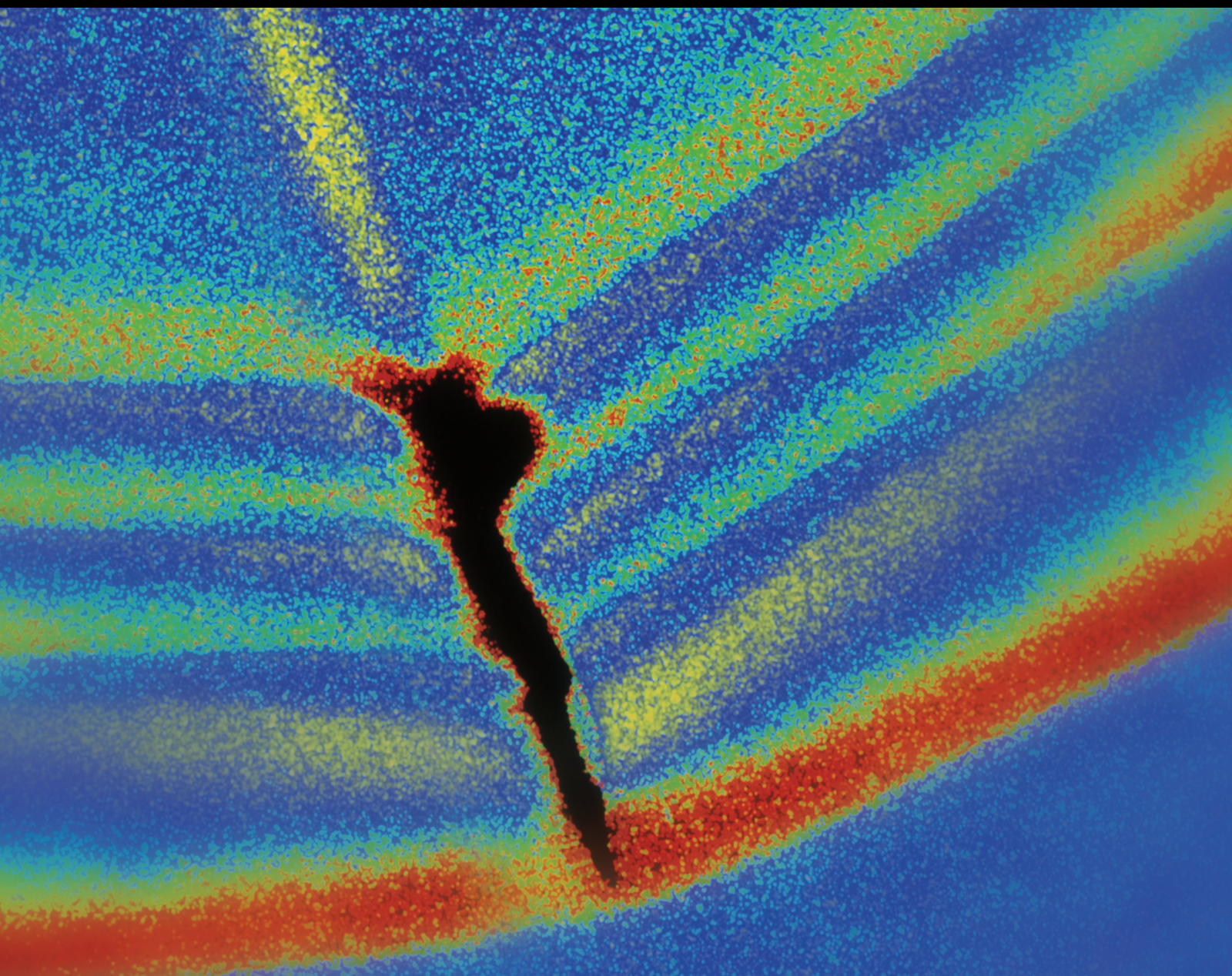


Vibration Analysis as a Diagnosis Tool for Health Monitoring of Industrial Machines

Guest Editors: Arturo Garcia-Perez, Juan Pablo Amezquita-Sanchez, Daniel Morinigo-Sotelo, and Konstantinos N. Gyftakis





Vibration Analysis as a Diagnosis Tool for Health Monitoring of Industrial Machines

Vibration Analysis as a Diagnosis Tool for Health Monitoring of Industrial Machines

Guest Editors: Arturo Garcia-Perez,
Juan Pablo Amezquita-Sanchez, Daniel Morinigo-Sotelo,
and Konstantinos N. Gyftakis



Copyright © 2016 Hindawi Publishing Corporation. All rights reserved.

This is a special issue published in "Shock and Vibration." All articles are open access articles distributed under the Creative Commons Attribution License, which permits unrestricted use, distribution, and reproduction in any medium, provided the original work is properly cited.

Editor-in-Chief

Mehdi Ahmadian, Virginia Polytechnic Institute and State University, USA

Editorial Board

Brij N. Agrawal, USA
Marco Alfano, Italy
Farbod Alijani, Canada
Sumeet S. Aphale, UK
Mariano Artés, Spain
Hassan Askari, Canada
Matteo Aureli, USA
Ranjan Banerjee, UK
Mahmoud Bayat, Iran
José A. Becerra Villanueva, Spain
Marco Belloli, Italy
Subhamoy Bhattacharya, UK
Ivo Caliò, Italy
Antonio Carcaterra, Italy
Dumitru I. Caruntu, USA
Noel Challamel, France
Athanasios Chasalevris, UK
Ashwin Chinnayya, France
Giorgio Dalpiaz, Italy
Farhang Daneshmand, Canada
Sergio De Rosa, Italy
Dario Di Maio, UK
Longjun Dong, China
Lorenzo Dozio, Italy
Mohamed El Badaoui, France
Mohammad Elahinia, USA
Fiorenzo A. Fazzolari, UK
Francesco Franco, Italy

Pedro Galvín, Spain
Alessandro Gasparetto, Italy
Gianluca Gatti, Italy
Anindya Ghoshal, USA
Nere Gil-Negrete, Spain
Hassan Haddadpour, Iran
M.I. Herreros, Spain
Hamid Hosseini, Japan
Reza Jazar, Australia
Sakdirat Kaewunruen, UK
Yuri S. Karinski, Israel
Jeong-Hoi Koo, USA
Georges Kouroussis, Belgium
Mickaël Lallart, France
Kenneth J. Loh, USA
Nuno M. Maia, Portugal
Giuseppe C. Marano, Italy
Laurent Mevel, France
Emiliano Mucchi, Italy
Tony Murmu, UK
Sundararajan Natarajan, India
Toshiaki Natsuki, Japan
Miguel Neves, Portugal
Coral Ortiz, Spain
Aleksandar Pavic, UK
Evgeny Petrov, UK
Antonina Pirrotta, Italy
Vitomir Racic, Italy

Carlo Rainieri, Italy
Didier Rémond, France
Francesco Ripamonti, Italy
Salvatore Russo, Italy
Edoardo Sabbioni, Italy
Jerzy T. Sawicki, USA
Onome E. Scott-Emuakpor, USA
Vadim V. Silberschmidt, UK
Kumar V. Singh, USA
Isabelle Sochet, France
Alba Sofi, Italy
Jussi Sopanen, Finland
Stefano Sorace, Italy
Narakorn Srinil, UK
Salvatore Strano, Italy
Chao Tao, China
Mario Terzo, Italy
Tai Thai, Australia
Carlo Trigona, Italy
Federica Tubino, Italy
Nerio Tullini, Italy
Marcello Vanali, Italy
Jörg Wallaschek, Germany
Zaili L. Yang, UK
Stana Živanović, UK
Lei Zuo, USA

Contents

Vibration Analysis as a Diagnosis Tool for Health Monitoring of Industrial Machines

Arturo Garcia-Perez, Juan Pablo Amezcuita-Sanchez, Daniel Morinigo-Sotelo, and Konstantinos N. Gyftakis
Volume 2016, Article ID 1235139, 2 pages

A Two-Stage Compression Method for the Fault Detection of Roller Bearings

Huaqing Wang, Yanliang Ke, Ganggang Luo, Lingyang Li, and Gang Tang
Volume 2016, Article ID 2971749, 11 pages

Feature Extraction and Selection Scheme for Intelligent Engine Fault Diagnosis Based on 2DNMF, Mutual Information, and NSGA-II

Peng-yuan Liu, Bing Li, Cui-e Han, and Feng Wang
Volume 2016, Article ID 3975285, 13 pages

Vibration Suppression for Improving the Estimation of Kinematic Parameters on Industrial Robots

David Alejandro Elvira-Ortiz, Rene de Jesus Romero-Troncoso, Arturo Yosimar Jaen-Cuellar, Luis Morales-Velazquez, and Roque Alfredo Osornio-Rios
Volume 2016, Article ID 6954012, 15 pages

A Fault Feature Extraction Method for Rolling Bearing Based on Pulse Adaptive Time-Frequency Transform

Jinbao Yao, Baoping Tang, and Jie Zhao
Volume 2016, Article ID 4135102, 12 pages

Multiple-Fault Detection Methodology Based on Vibration and Current Analysis Applied to Bearings in Induction Motors and Gearboxes on the Kinematic Chain

Juan Jose Saucedo-Dorantes, Miguel Delgado-Prieto, Juan Antonio Ortega-Redondo, Roque Alfredo Osornio-Rios, and Rene de Jesus Romero-Troncoso
Volume 2016, Article ID 5467643, 13 pages

Experimental Investigation into Vibration Characteristics for Damage Minimization in a Lapping Process

J. Suwatthikul, S. Sornmuang, T. Yaemglin, I. Cheowanish, and C. Supavasuthi
Volume 2016, Article ID 4836516, 13 pages

Bearing Fault Diagnosis Using a Novel Classifier Ensemble Based on Lifting Wavelet Packet Transforms and Sample Entropy

Lei Zhang, Long Zhang, Junfeng Hu, and Guoliang Xiong
Volume 2016, Article ID 4805383, 13 pages

A New Feature Extraction Technique Based on 1D Local Binary Pattern for Gear Fault Detection

Zrar Kh. Abdul, Abdulbasit Al-Talabani, and Ayub O. Abdulrahman
Volume 2016, Article ID 8538165, 6 pages

Fault Diagnosis of Rotating Machinery Based on Adaptive Stochastic Resonance and AMD-EEMD

Peiming Shi, Cuijiao Su, and Dongying Han
Volume 2016, Article ID 9278581, 11 pages

Vibration Analysis of Partially Damaged Rotor Bar in Induction Motor under Different Load Condition Using DWT

Jose Rangel-Magdaleno, Hayde Peregrina-Barreto, Juan Ramirez-Cortes, Roberto Morales-Caporal, and Israel Cruz-Vega

Volume 2016, Article ID 3530464, 11 pages

Nonlinear Vibroimpact Characteristics of a Planetary Gear Transmission System

Jianxing Zhou, Wenlei Sun, and Liang Yuan

Volume 2016, Article ID 4304525, 11 pages

Structural Damage Detection by Using Single Natural Frequency and the Corresponding Mode Shape

Bo Zhao, Zili Xu, Xuanen Kan, Jize Zhong, and Tian Guo

Volume 2016, Article ID 8194549, 8 pages

The Influence on Modal Parameters of Thin Cylindrical Shell under Bolt Looseness Boundary

Hui Li, Mingwei Zhu, Zhuo Xu, Zhuo Wang, and Bangchun Wen

Volume 2016, Article ID 4709257, 15 pages

Rolling Bearing Diagnosing Method Based on Time Domain Analysis and Adaptive Fuzzy C-Means Clustering

Sheng Fu, Kun Liu, Yonggang Xu, and Yi Liu

Volume 2016, Article ID 9412787, 8 pages

Editorial

Vibration Analysis as a Diagnosis Tool for Health Monitoring of Industrial Machines

**Arturo Garcia-Perez,¹ Juan Pablo Amezcua-Sanchez,²
Daniel Morinigo-Sotelo,³ and Konstantinos N. Gyftakis⁴**

¹HSPdigital, DICIS, Universidad de Guanajuato, 36885 Salamanca, GTO, Mexico

²Faculty of Engineering, Autonomous University of Queretaro, 76806 San Juan del Rio, QRO, Mexico

³Department of Electrical Engineering, University of Valladolid, 47011 Valladolid, Spain

⁴School of Computing, Electronics and Mathematics, Faculty of Engineering, Environment and Computing, Coventry University, Coventry CV1 5FB, UK

Correspondence should be addressed to Arturo Garcia-Perez; agarcia@hspdigital.org

Received 6 June 2016; Accepted 6 June 2016

Copyright © 2016 Arturo Garcia-Perez et al. This is an open access article distributed under the Creative Commons Attribution License, which permits unrestricted use, distribution, and reproduction in any medium, provided the original work is properly cited.

The need for health monitoring in industrial machines using vibration analysis for diagnosis is an ever growing requirement in all types of industries and equipment. Vibrations in machinery can take various forms, and most of the time these vibrations are unintended and undesirable. Therefore, monitoring the vibration characteristics of a machine can provide the information of its health condition, and this piece of information can be used to detect problems that might be incipient or developing.

The regular use of a machine condition monitoring system allows for observing the problems during their incipient stage or when they are developing. Sometimes a machine can be running into a major failure, even though it appears to be functioning normally. This could lead to a dangerous situation because if this faulty condition is not monitored and detected on time, the problem could lead to the manufacturing of poor quality products, large yield losses, rework costs, and so forth. The vibration signature of a specific machine can then be processed to extract the features related to the fault and give a diagnosis of the machine condition.

H. Li et al. propose a theory with experiment to investigate the influence on modal parameters of thin cylindrical shell (TCS) under bolt looseness boundary, where it can be found that bolt looseness boundary can significantly affect frequency and damping results which might be caused by

changes of nonlinear stiffness, damping, and position of connecting bolt looseness. S. Fu et al. present a new approach for mechanical fault diagnosis based on time-domain analysis and adaptive fuzzy C-means clustering. By analyzing vibration of the bearing, it could be detected fast and accurately, to estimate whether the rolling bearing is healthy or not, even single fault or multiple faults. J. Zhou et al. deal with a novel modeling method of planetary gear system, in which the Hertz contact theory is induced to describe impact of the gear pairs under the condition of the high speed and light load. The vibroimpact characteristics of the system are analyzed.

A damage detection method based on flexibility change by using single nonfirst mode is addressed by B. Zhao et al., and the results of the numerical examples (on a cantilever beam and a rod-fastened-rotor with different damage scenarios) indicate that the proposed method can effectively identify single, double, and multiple damage. L. Zhang et al. improve the fault detection accuracy for rolling bearings, an automated fault diagnosis system based on lifting wavelet packet transform (LWPT), sample entropy (SampEn), and classifier ensemble. Experiments were conducted on electric motor bearings considering various sets of bearing categories and fault severity levels. J. Rangel-Magdaleno et al. verify an experimental study of partially damaged rotor bar in induction motor under different load conditions based on discrete

wavelet transform analysis. The approach is based on the extraction of features from vibration signals at different levels of damage and three mechanical load conditions.

An adaptive stochastic resonance and analytical mode decomposition-ensemble empirical mode decomposition (AMD-EEMD) method is proposed for fault diagnosis of rotating machinery by P. Shi et al. Z. K. Abdul et al. have shown that 1D LBP (local binary pattern) is an effective technique to extract features for detecting fault in gear when data with the same speed and/or load are available in training and testing the model. Moreover, the 1D LBP is cheaper in terms of computation than the 2D LBP scheme. J. J. Saucedo-Dorantes et al. propose a methodology based on vibration analysis and current analysis for the diagnosis of different levels of uniform wear in a gearbox and the detection of bearing defects, both linked in the same kinematic chain. The methodology is based on the acquisition of vibration signals that are generated in the kinematic chain and induction motor current signals.

Besides those, there are several interesting works in the issue. D. A. Elvira-Ortiz et al. suggest a system capable of providing complete joint kinematics and position of an industrial robot and tested in a 6-degree-of-freedom robot. The system is based on KF technique for vibration suppression and for fusing the measurements of two primary sensors: gyroscopes and accelerometers. J. Yao et al. deal with a pulse adaptive time-frequency transform method to extract the fault features of the damaged rolling bearing. An experimental investigation into vibration characteristics of passed and failed lapping scenarios which discusses a potential solution to minimizing the serious damage so-called plate scratch which intermittently occurs in such process is presented by J. Suwatthikul et al. B. Li et al. propose a feature extraction and selection scheme for intelligent engine fault diagnosis by utilizing two-dimensional nonnegative matrix factorization, mutual information, and nondominated sorting genetic algorithms, and finally H. Wang perform a two-stage compression method to reduce the large amount of the faulty vibration signals induced by the condition monitoring bearings.

Acknowledgments

The guest editors would like to thank the authors for their contributions to the special issue and all the reviewers for their constructive reviews. We are also grateful to the Editor-in-Chief, Mehdi Ahmadian, for his support.

*Arturo Garcia-Perez
Juan Pablo Amezcua-Sanchez
Daniel Morinigo-Sotelo
Konstantinos N. Gyftakis*

Research Article

A Two-Stage Compression Method for the Fault Detection of Roller Bearings

Huaqing Wang, Yanliang Ke, Ganggang Luo, Lingyang Li, and Gang Tang

School of Mechanical and Electrical Engineering, Beijing University of Chemical Technology, Beijing 100029, China

Correspondence should be addressed to Gang Tang; tanggang@mail.buct.edu.cn

Received 22 January 2016; Revised 10 April 2016; Accepted 8 May 2016

Academic Editor: Daniel M. Sotelo

Copyright © 2016 Huaqing Wang et al. This is an open access article distributed under the Creative Commons Attribution License, which permits unrestricted use, distribution, and reproduction in any medium, provided the original work is properly cited.

Data measurement of roller bearings condition monitoring is carried out based on the Shannon sampling theorem, resulting in massive amounts of redundant information, which will lead to a big-data problem increasing the difficulty of roller bearing fault diagnosis. To overcome the aforementioned shortcoming, a two-stage compressed fault detection strategy is proposed in this study. First, a sliding window is utilized to divide the original signals into several segments and a selected symptom parameter is employed to represent each segment, through which a symptom parameter wave can be obtained and the raw vibration signals are compressed to a certain level with the faulty information remaining. Second, a fault detection scheme based on the compressed sensing is applied to extract the fault features, which can compress the symptom parameter wave thoroughly with a random matrix called the measurement matrix. The experimental results validate the effectiveness of the proposed method and the comparison of the three selected symptom parameters is also presented in this paper.

1. Introduction

Rotating machinery is widely applied in industrial fields, such as petrochemical industry, metallurgy industry, and power industry [1, 2]. Roller bearing, whose failure might result in the breakdown of the whole mechanical system, is considered as an integral component of rotating machinery [3, 4]. Therefore, it is essential to monitor the operating condition of the roller bearings, aiming at preventing the occurrence of the accidents.

Since much fault information is carried by the vibration signals, vibration-based diagnostic techniques have become the most commonly used and effective method for the fault diagnosis of roller bearings [5–7]. It is well known that the vibration-based fault diagnosis of roller bearings can be broadly classified into three categories, namely, time-domain analysis, frequency-domain analysis, and time-frequency analysis [8–10].

In the case of time-domain analysis, the characteristic statistical factors in time domain, including mean, peak, root mean square, skewness, can be viewed as descriptors to assess

the performance of roller bearings [11–13]. Wang et al. [14] proposed a comprehensive analysis based on time-domain and frequency-domain statistical factors in order to evaluate the performance degradation degree of roller bearings. Niu et al. [15] presented some new statistical moments for the early detection of bearing failure. Heng and Nor [16] investigated a statistical method to detect the presence of defects in a roller bearing. Although the symptom parameters are easily performed to evaluate the condition of roller bearings, the successful applications are limited owing to the weak anti-interference performance of these parameters.

Compared to time-domain analysis, frequency-domain analysis has an advantage in highlighting the certain frequency components of interest by transforming the time-domain wave into frequency spectrum. The traditional method in frequency-domain is fast Fourier transform (FFT). Due to the modulation phenomenon of faulty vibration signals, envelope demodulation should be carried out before performing FFT, which is called envelope analysis. Guo et al. [17] applied envelope analysis with independent component analysis, which can extract the impulse component

corresponding to the roller bearing faults and reduce the dimension of vibration sources. Wang et al. [18] developed a fault detection enhancement method based on the peak transform and envelope analysis. Cases proved that the envelope analysis can diagnose the faults of a roller bearing successfully when it is in combination with other approaches [17–19]. However, the frequency analysis will lose its effect when the vibration signals are embedded in strong noise. Thus, the time-frequency-domain analysis was developed. Many methods that belong to time-frequency analysis, such as empirical mode decomposition (EMD) [20] and wavelet transform [21], are employed to assess the performance of roller bearings. Ma et al. [22] combined local mean decomposition and time-frequency analysis, which can improve the reliability of the fault diagnosis. Li et al. [23] proposed a novel method for fault diagnosis of roller bearings based on CEEMD. Ahn et al. [24] applied wavelet analysis to eliminate noise. Though time-frequency analysis is effective in processing the nonstationary signals induced by faulty bearings, it is usually complicated and involves large computation, which is contrary to the real-time detection.

The cited literatures demonstrated that the fault diagnosis of roller bearings is developing increasingly. However, the aforementioned bearing fault diagnosis method is achieved by sampling the vibration signals under the Shannon sampling theorem. With the constraint of Shannon sampling theorem, a large amount of redundant vibration signals will be measured, increasing the burden of roller bearings' fault diagnosis. There is no doubt that the increasing amount of data will result in high accuracy of fault diagnosis with the efficiency decreasing. Thus, it is a really tough work to balance the accuracy and efficiency of fault diagnosis.

A newly developed theory named compressed sensing (CS) [25] brought a new insight to deal with the big-data problem, which puzzled the researchers in various fields. The core idea of the CS theory is to reconstruct the original signals from a small number of samples far below the Shannon sampling rate using sparse representation and a well-designed measurement matrix. The CS theory has been applied to numerous fields, such as image processing, medical field, and remote sensing. Khwaja and Ma [26] described two possible applications of the CS theory in synthetic aperture radar image compression. Zhu et al. [27] developed an adaptive sampling mechanism on the block-based CS, which focused on how to improve the sampling efficiency for CS-based image compression. Kim and Vu [28] applied the CS theory to magnetic resonance imaging, which can be viewed as a breakthrough technology in medical diagnosis. Ghahremani and Ghassemian [29] combined the ripple transform and the CS theory to remote sensing image fusion. All of the aforementioned studies demonstrated the possibility of applying the CS theory to the field of fault diagnosis. However, the applications of the CS theory in fault diagnosis are relatively limited. Although Zhu et al. [30] summarized the applications in the mechanical fields, no practical applications were reported. Chen et al. [31] presented a novel adaptive dictionary based on the CS theory to extract the impulse generated by the faulty bearings. Tang et al. [32] developed a representation classification strategy

for rotating machinery faults based on the CS theory. Wang et al. [33] proposed a novel decomposition for reconstruction from the limited observations polluted by noise based on the CS theory via the sparse time-frequency representation. However, the aforementioned studies were primarily focused on either the sparse representation of the vibration signals or the reconstruction of the original signals, and the amount of samples in these cases still needed to be compressed.

It is significant to ensure that the few observations contain adequate faulty information, which is an essential condition to guarantee the successful applications of the compressed sensing theory. Thus, a fault features' reservation method called the symptom parameter wave is developed to obtain sufficient faulty information. Combined with the compressed sensing theory, a two-stage compression method is described in this work to further decrease the amount of samples for fault diagnosis of roller bearings without losing significant information, through which the fault features of roller bearings can be detected timely. Compared to the work of sparse representation and reconstruction, the samples for the fault detection using the two-stage compression method are far less. First, the large amount of vibration signals is divided into several segments by a sliding window with a given size. Then, a time-domain symptom parameter is used to represent each data segment, through which a symptom parameter wave can be obtained and the original signals can be reduced to a certain level. With the symptom parameter wave, the dimension of the analyzed signals can be shrunk and it outperforms the traditional usage of these characteristic factors by representing the whole signals with single value in the presence of noise. Second, a well-designed measurement matrix is applied to compress the symptom parameter wave. Third, a fault detection method based on the CS theory is employed to extract the fault features with limited samples. Assisted by the matching pursuit, the fault features can be detected from a small number of samples, which are far below the Shannon sampling rate. Furthermore, the detection method in the current work does not need to reconstruct the original signals completely. When the components related to the fault features are detected, the reconstruction process can be finished, which means the fault diagnosis can be completed during the reconstruction procedure.

The rest of this paper is organized as follows. Section 2 introduces the basic concept of the two-stage compression strategy, followed by the compressed fault detection strategy in Section 3. The application cases are presented in Section 4. Section 5 describes the comparing results between the selected symptom parameters. Conclusions are drawn in Section 6.

2. Basic Concept of the Two-Stage Compression Strategy

2.1. First Stage of Compression by the Symptom Parameter Wave. As is known to all, the fault diagnosis of roller bearings based on the time-domain symptom parameters is the simplest method in time-domain analysis. The operating status of roller bearings can be identified according to the change of the time-domain symptom parameters. Generally

speaking, the symptom parameters can be classified into two categories: dimensional symptom parameters and nondimensional symptom parameters. The former, such as the peak value, the peak-to-peak value, and the root mean square value, reflect the magnitude change of a signal. The latter, such as kurtosis, crest factor, and shape factor, express the shape change of a signal.

Various symptom parameters have been utilized for fault diagnosis of roller bearings. Some of them can be calculated according to the following equations:

$$\begin{aligned}
 X_{\text{Peak}} &= \max \{x_1, x_2, \dots, x_N\}, \\
 \bar{X} &= \frac{1}{N} \sum_{i=1}^N |x_i|, \\
 X_{\text{RMS}} &= \sqrt{\frac{1}{N} \sum_{i=1}^N x_i^2}, \\
 X_{\text{ptp}} &= x_{\text{max}} - x_{\text{min}}, \\
 \text{SF} &= \frac{X_{\text{RMS}}}{\bar{X}}, \\
 K &= \frac{(1/N) \sum_{i=1}^N x_i^4}{X_{\text{RMS}}^4},
 \end{aligned} \tag{1}$$

where X_{Peak} is the peak value of a signal, \bar{X} represents the average of absolute value of a signal, X_{RMS} denotes the root mean square of a signal, X_{ptp} expresses the peak-to-peak value of a signal, x_{max} is the max value of a signal, x_{min} is the minimum value of a signal, SF describes the shape factor of a signal, and K indicates the kurtosis of a signal.

In the traditional sense, the operating status of roller bearing can be identified by representing the whole signals with a characteristic value. This fault diagnosis method mainly depends on the difference of the characteristic values between the normal state and faulty status. However, successful cases are limited due to the instability and insensitivity of these parameters when the target vibration signals are submerged by the noise, which means the traditional usage of these symptom parameters has a weak anti-interference ability. To strengthen the ability of antinoise, a concept of symptom parameter wave is proposed in the present study. Three time-domain symptom parameters are selected to represent the signals depending on the characteristics of the faulty vibration signals. The selected symptom parameters are X_{ptp} , SF, and K , which are more sensitive to the failures than other characteristic factors. A symptom parameter wave can be achieved through a sliding window in order to compress the raw signals and preserving the fault features of the faulty vibration signals. The flow diagram of symptom parameter wave is shown in Figure 1. The raw vibration signals are divided into several segments by a sliding window and a selected characteristic parameter is used to represent each segment, through which a symptom parameter wave can be obtained. The acquisition of the symptom parameter wave can reduce the original signals to a certain level with the fault

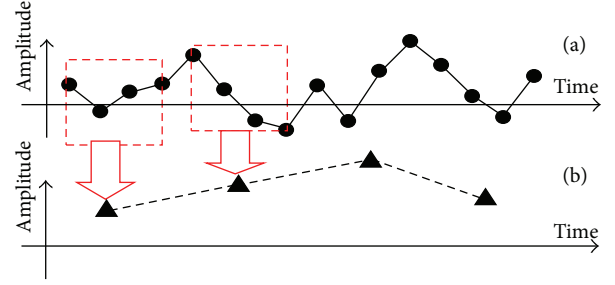


FIGURE 1: Flow diagram of obtaining the symptom parameter wave. (a) The original signals and (b) the symptom parameter wave.

features remaining, which is the first stage of compression in this work.

2.2. Second Stage of Compression by the Compressed Sensing Theory [34–36]. The traditional sampling scheme based on the Shannon sampling theorem results in the big data, which contains much redundant information. It is no doubt that large amount of signals increases the cost of data storage and makes signal processing more difficult. The proposal of the CS theory brings a new insight for data acquisition and signal processing by reconstructing the original signal from downsampled signals.

Provided $\text{SP}(t)$ is a $N \times 1$ symptom parameter wave, which can be further compressed by a measurement matrix:

$$y = \Phi \text{SP}(t), \tag{2}$$

where Φ is a $M \times N$ ($M \ll N$) measurement matrix.

The $N \times 1$ time-domain signal can be compressed to a $M \times 1$ signal using a measurement matrix according to (2).

The $\text{SP}(t)$ can be represented by a group of $N \times 1$ basis:

$$\text{SP}(t) = \psi \theta. \tag{3}$$

So

$$y = \Phi \psi \theta = A \theta, \tag{4}$$

where $\psi = \{\varphi_1, \varphi_2, \dots, \varphi_N\} \in N \times N$ is the basis vector, through which the original signals can be represented sparsely. θ denotes the representation coefficients. The signals can be said to be K -sparse, when θ contains only K nonzero coefficients ($K \ll N$). $A = \Phi \psi$ is called the sensing matrix.

It is impossible to solve the model in (3), which is an ill-posed equation. The solution of the CS model can be expressed as

$$\begin{aligned}
 \min \quad & \|\theta\|_0 \\
 \text{s.t.} \quad & y = A \theta.
 \end{aligned} \tag{5}$$

The solution becomes possible owing to the sparsity of θ , which can reduce the unknowns. It is more likely to reconstruct the signals from the limited samples without meeting the requirement of Shannon sampling theorem, when A satisfies the restricted isometry property (RIP).

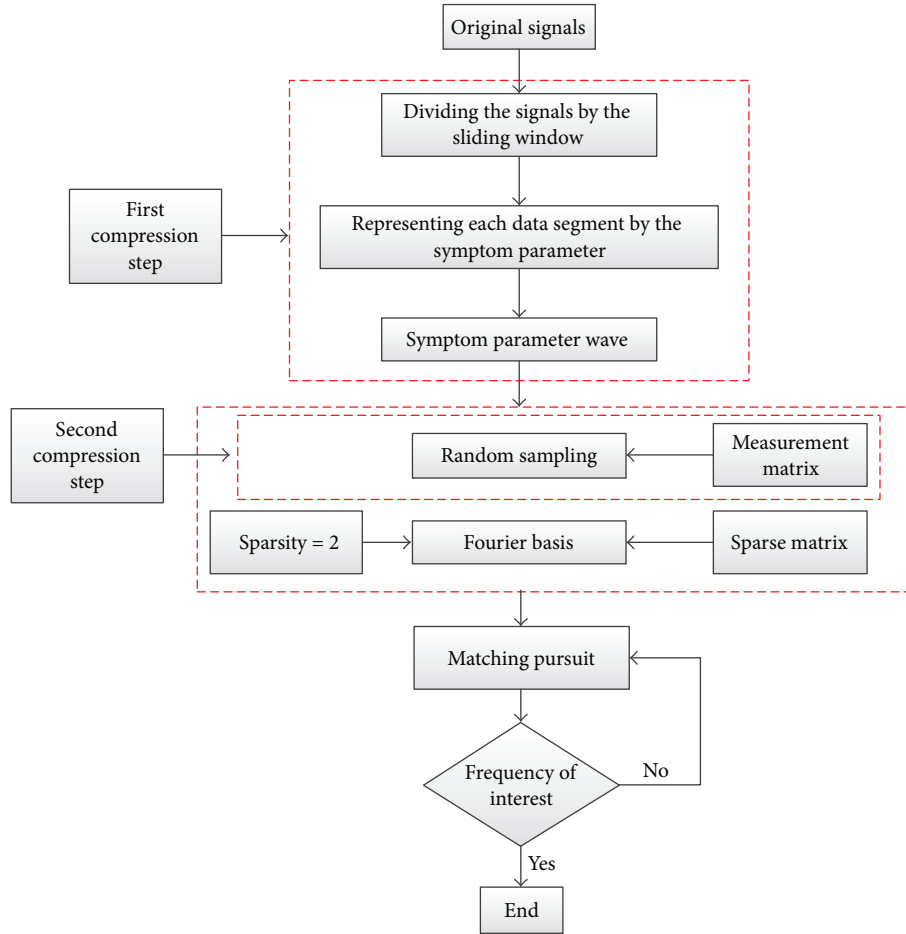


FIGURE 2: Flow diagram of the compressed fault detection strategy.

3. The Compressed Fault Detection Strategy

A force impulse is generated when operating a roller bearing with a local defect and the resonance of the bearing system occurs. In addition, each time the ball passes through the location with a fault, a periodic impulse will be produced, namely, the fault characteristic frequency, which is an indicator of the existence of a fault. Due to the phenomenon of resonance, the fault characteristic frequency will be modulated. Thus, the faulty vibration signals need to be demodulated in order to obtain the fault characteristic frequency.

An obstacle should be overcome in case of the application of the CS theory to fault diagnosis of roller bearings. In fact, the faulty vibration signals, which contain many periodic impulses, are not significantly sparse neither in time domain nor in Fourier domain. In this case, the reconstruction error will be high, which means that it makes no sense to reconstruct the signals. Thus, we choose to detect the harmonic signals induced by the faulty roller bearings. In addition, it is well known that the sparsity of the harmonic signal in Fourier domain is two. Furthermore, the advantage of the fault detection over the reconstruction is that if the frequency of the detected signal is of interest, the process can be completed, which can also be called the incomplete reconstruction.

The flowchart of the compressed fault detection approach in this work is presented in Figure 2. The amount of the original signals can be reduced by the time-domain symptom parameter wave through a size-fixed sliding window. As mentioned above, a variety of impulses exist in the faulty vibration signals and the peak-to-peak value, kurtosis, and shape factor are more suitable to represent the fault characteristics. Thus, the peak-to-peak value, kurtosis, and shape factor are chosen to obtain the symptom parameter wave. Then, the symptom parameter wave can be acquired and the dimension of the original signals is reduced to a certain level with the faulty information remaining. Additionally, the vibration signals of faulty bearing can be demodulated by the symptom parameter wave. Thus, it is unnecessary to adopt the envelope demodulation to process the analyzed signals. The measurement matrix is utilized as a compressor to further shrink the amount of samples. At last, fault detection based on the CS theory is employed to extract the fault features with the help of matching pursuit. If the detected harmonic signal is almost equal to the theoretical fault characteristic frequency, the conclusion that there is a fault in this roller bearing can be made. Otherwise, the detection process should be continued until the frequencies of interest are extracted. Here, the basis group is the Fourier basis for the sparsity of harmonic signal

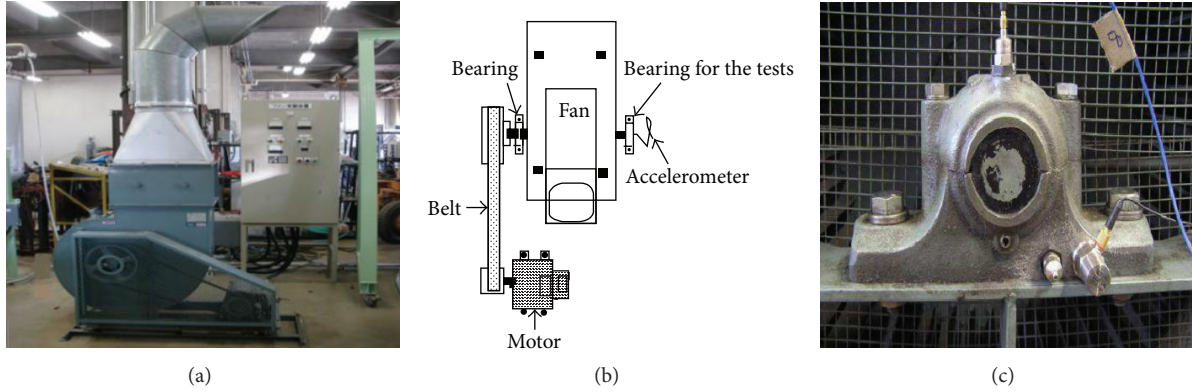


FIGURE 3: (a) Fault test rig, (b) flow diagram of the fault test rig, and (c) location of the sensors.

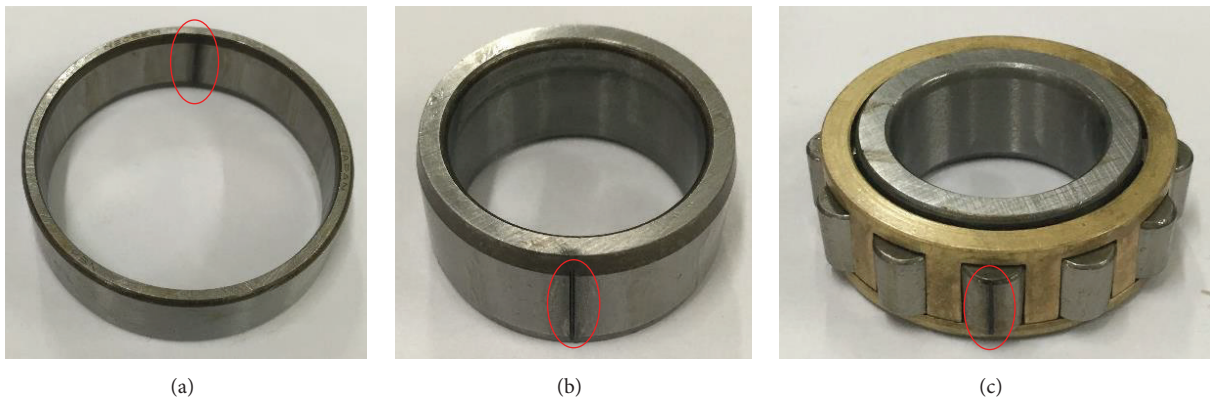


FIGURE 4: (a) Outer-race fault, (b) inner-race fault, and (c) rolling-element fault.

in Fourier domain is 2. Various matrices can be considered as measurement matrix, such as Gaussian random matrix, Bernoulli matrix, and Toeplitz matrix. Since the Gaussian random matrix can meet the requirement of RIP with the Fourier basis, it is selected as the measurement matrix in this study.

4. Application Cases

4.1. Test Rig. The vibration signals of roller bearing faults are measured through an accelerometer, and the faulty bearings are fixed in the fan system, as shown in Figure 3(a), which mainly consists of a motor, a belt, a fan, and a couple of bearings. The motor is a three phase induction motor, whose type is SF-JR with a rated power of 2.2 Kw. The fan, which has 48 blades, operates at a speed of 800 rpm. The flow diagram of the fan system is presented in Figure 3(b). The sensors are installed on the bearing housing, as shown in Figure 3(c), where the collected vibration signals might be valid and easily measured. The faulty bearings are shown in Figure 4, concluding outer-race fault, inner-race fault, and rolling-element fault, which are created through wire-electrode cutting. In all experiments, the sampling frequency is 100 KHz and the roller bearings are operated at a speed of 800 rpm. The fault characteristic frequencies can be computed according to (6)–(8) [23, 37] and the results are shown in Table 1.

TABLE 1: Fault characteristic frequency.

Fault location	Outer race	Inner race	Ball element
Fault characteristic frequency (Hz)	72.5	103.4	79.6

The fault characteristic frequency of outer race is

$$f_o = \frac{Z}{2} \left(1 - \frac{d}{D} \cos \alpha \right) f_r. \quad (6)$$

The fault characteristic frequency of inner race is

$$f_i = \frac{Z}{2} \left(1 + \frac{d}{D} \cos \alpha \right) f_r. \quad (7)$$

The fault characteristic frequency of ball element is

$$f_b = \frac{D}{2d} \left(1 - \left(\frac{d}{D} \cos \alpha \right)^2 \right) f_r, \quad (8)$$

where Z denotes the number of roller elements, f_r is the rotating frequency, d is the roller diameter, D represents the pitch diameter, and α is the contact angle.

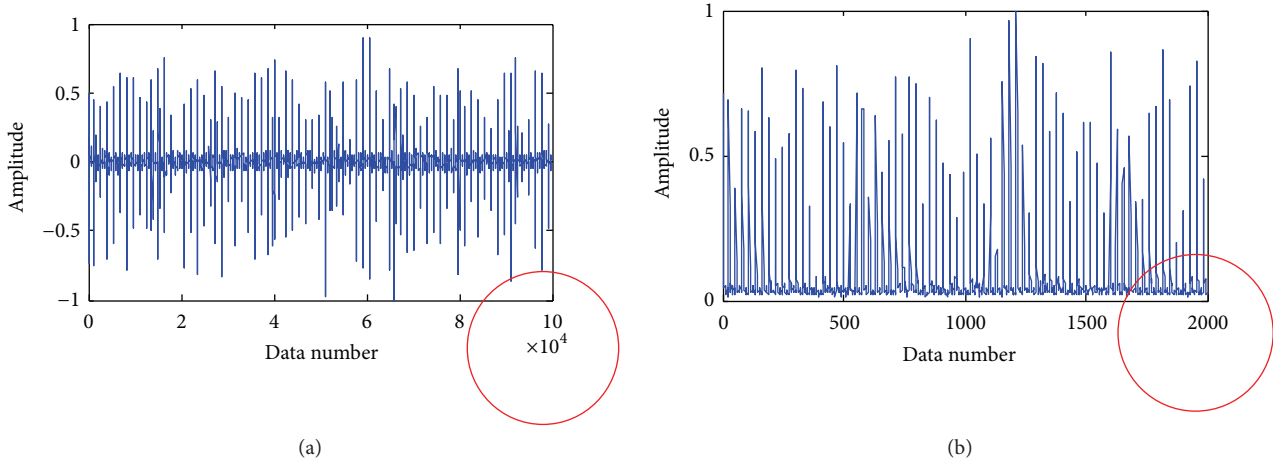


FIGURE 5: (a) Original signals and (b) symptom parameter wave using peak-to-peak value.

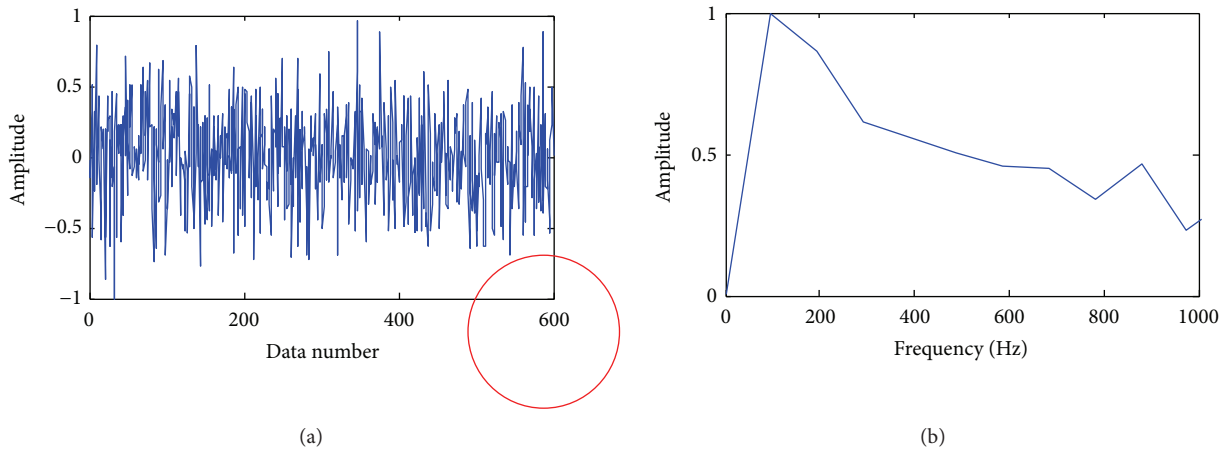


FIGURE 6: (a) Random sampling and (b) envelope spectrum of the original signals with 600 points.

4.2. Detection of the Bearing Fault in the Outer Race. The proposed method was employed to detect the bearing fault in the outer race. The peak-to-peak value, kurtosis, and shape factor are considered to represent the original signals, acquiring a symptom parameter wave, aiming at compressing the signals with the significant information preserved. The size of the sliding window is 50 points and the amount of the random sampling points is 600. All the data in this work are processed through the normalization.

4.2.1. Detecting the Outer-Race Fault Using Peak-to-Peak Value and Compressed Sensing. The first time-domain symptom parameter selected to compress the original signals is peak-to-peak value, which reflects the impact characteristic of the signals. The time-domain waveform of the original signals is presented in Figure 5(a), which contains plenty of impulses. However, the number of vibration signals sampled for fault diagnosis is 100000 points, which can be compressed to ease the pressure of signal processing. Then the peak-to-peak value is utilized to obtain the time-domain symptom parameter wave as shown in Figure 5(b), which retains the

impact characteristic of the original signals. Here, the size of the sliding window is 50 points. Thus, the samples are reduced 50 times and the samples are compressed from 100000 to 2000. Next, a Gaussian random matrix is selected as the measurement matrix to reduce the amount of the signals obtained from the envelope of the symptom parameter wave as in Figure 6(a). Envelope analysis is selected as a comparison to validate if it can extract the fault features from the random samples in Figure 6(a). However, it is difficult to find out the frequencies of interest in the envelope analysis of the original signals with only 600 points presented in Figure 6(b). Thus, the detection method based on the CS theory is applied to extract the fault features with the sparsity $K = 2$. With the matching pursuit, the fault features are detected successfully, as shown in Figures 7(a) and 7(b), which are almost equal to the theoretical values.

4.2.2. Detecting the Outer-Race Fault Using Kurtosis and Compressed Sensing. The original signals in this part are presented in Figure 8(a). The kurtosis is used to gain the time-domain symptom parameter wave, assisted by the sliding window

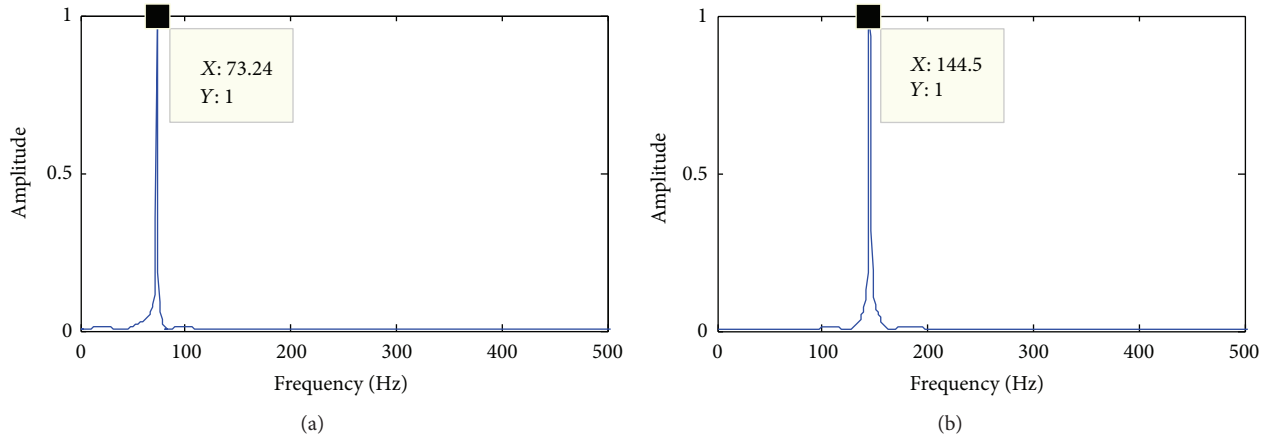


FIGURE 7: (a) Fault characteristic frequency and (b) twice the fault characteristic frequency.

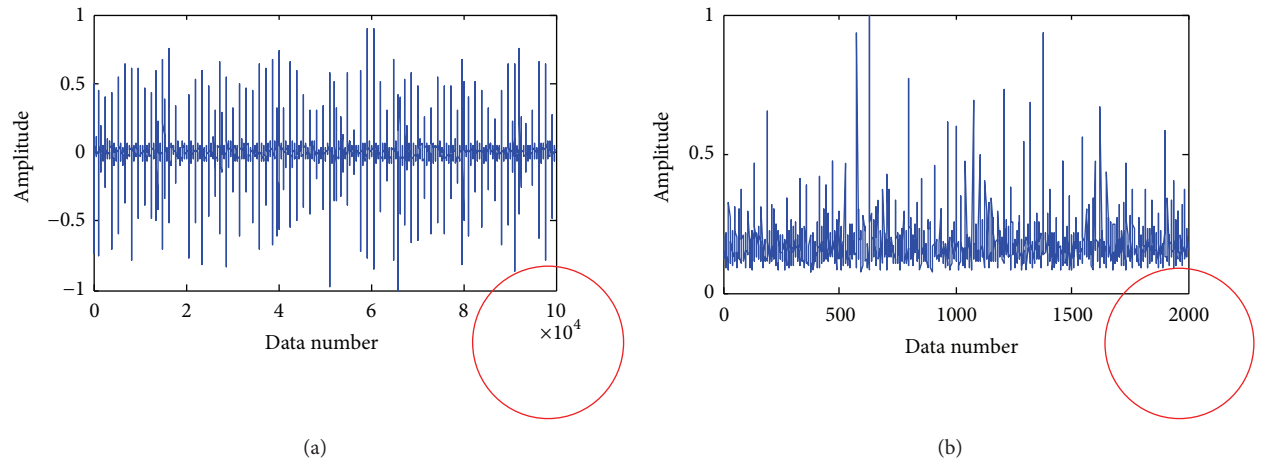


FIGURE 8: (a) Original signals and (b) symptom parameter wave using kurtosis.

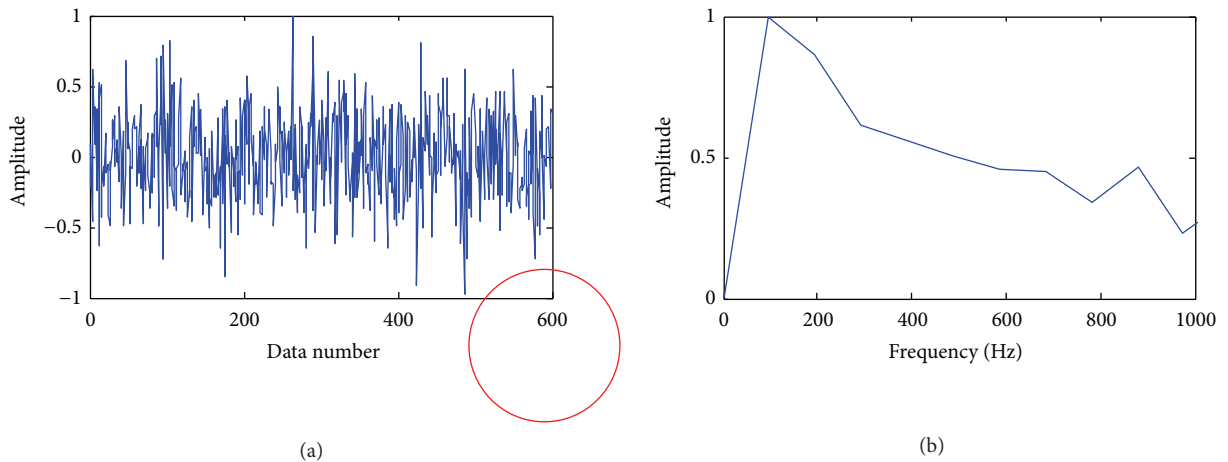


FIGURE 9: (a) Random sampling and (b) envelope spectrum of the original signals with 600 points.

with a fixed size of 50 points. The symptom parameter wave is shown in Figure 8(b), which presents that the number of the raw signals is shrunk 50 times. Compared to the symptom parameter wave in Figure 5(b), the impulses in

Figure 8(b) are much less. Then the random sampling was used to further reduce the amount of the symptom parameter wave envelope signals using a measurement matrix and the random sampling waveform is presented in Figure 9(a). The

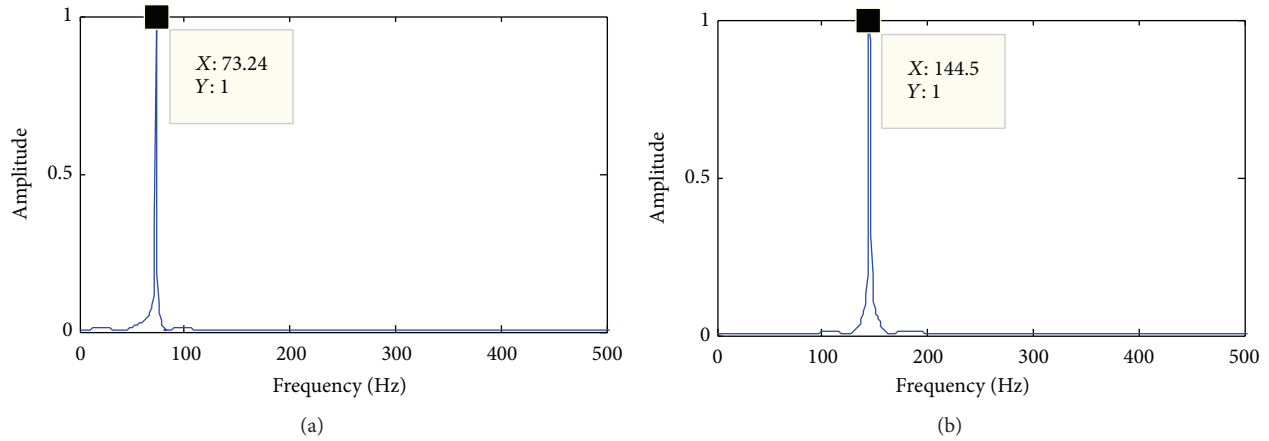


FIGURE 10: (a) Fault characteristic frequency and (b) twice the fault characteristic frequency.

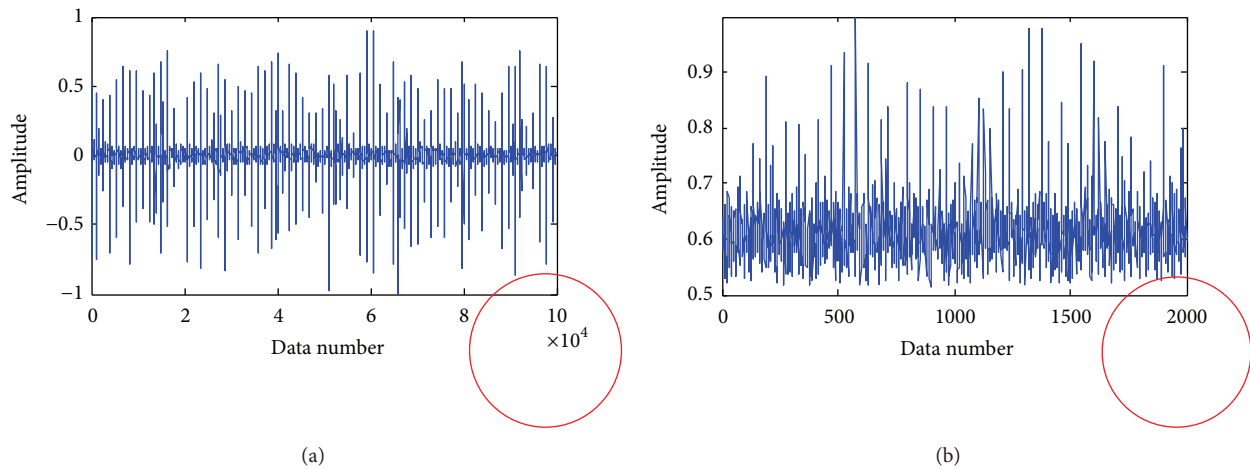


FIGURE 11: (a) Original signals and (b) symptom parameter wave using shape factor.

envelope analysis of the original signals in Figure 9(a) is presented in Figure 9(b), from which the status of the roller bearing is difficult to identify. However, the fault features are extracted successfully using the proposed method as shown in Figures 10(a) and 10(b), through which the conclusion that there is a fault in outer race can be drawn.

4.2.3. Detecting the Outer-Race Fault Using Shape Factor and Compressed Sensing. The original signals employed here are shown in Figure 11(a). The symptom parameter wave in Figure 11(b) obtained through the shape factor is worse than that in Figure 5(b), and the noise in Figure 11(b) was much more than that in Figure 5(b), since the peak-to-peak value is more sensitive to the impacts. The amount of the target signals is reduced from 100000 to 600 by random sampling, as presented in Figure 12(a). From Figure 12(b), it is difficult to identify the condition of the roller bearing. Finally, the fault features are extracted from the random sampling signals through the proposed method and the fault detection results are shown in Figures 13(a) and 13(b), which illustrate that there is a failure in the outer race.

5. Comparison between the Three Symptom Parameters

The amount of the faulty vibration signals is reduced by the time-domain symptom parameters and the CS theory. From the abovementioned results, the three symptom parameters selected to represent the raw vibration signals are all effective in detecting the faults in roller bearings. Here, the detection success ratio is considered as a criterion to compare the effectiveness of the three symptom parameters. The detection success ratio is calculated through 30 groups of vibration signals, containing outer-race fault, inner-race fault, and rolling-element fault. A suitable Gaussian random matrix is selected and it is utilized to detect the remaining samples. When the frequency of interest is detected, this fault detection belongs to a successful example. Different sizes of the sliding window and different dimensions of the measurement matrix are selected to assess the detection success ratio.

5.1. Different Sizes of the Sliding Window. Different sizes of the sliding window with a fixed dimension of the measurement

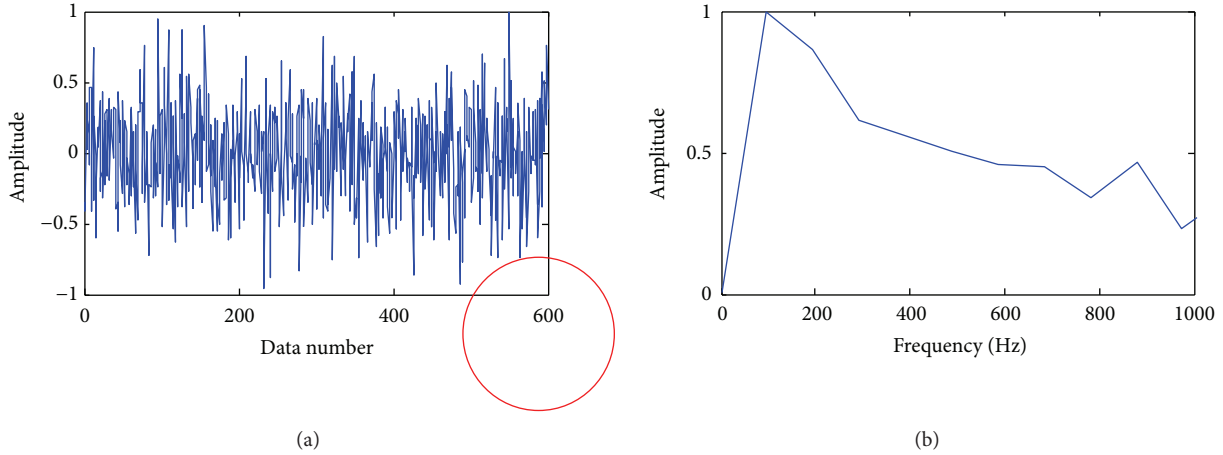


FIGURE 12: (a) Random sampling and (b) envelope spectrum of the original signals with 600 points.

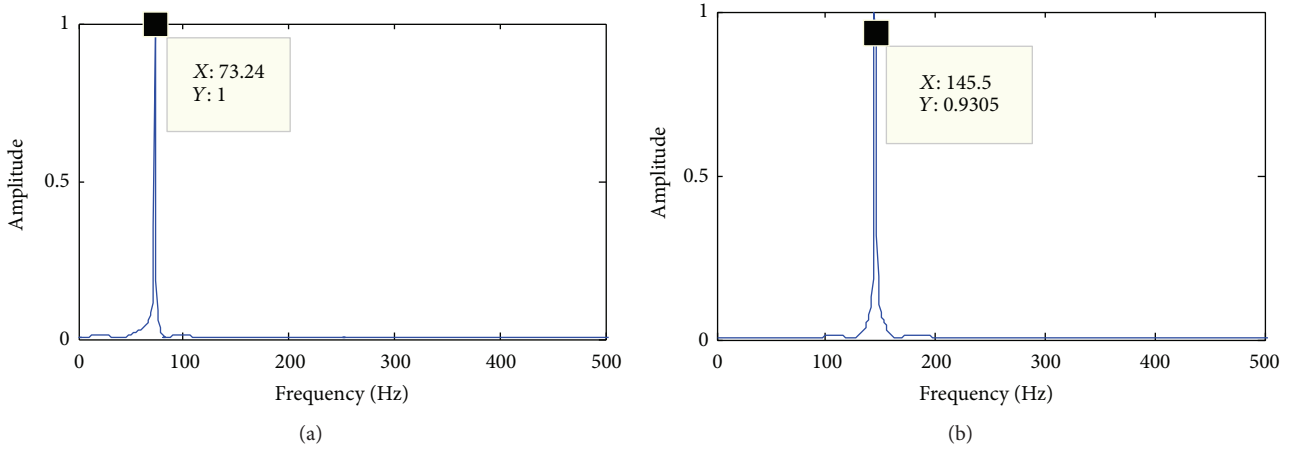


FIGURE 13: (a) Fault characteristic frequency and (b) twice the fault characteristic frequency.

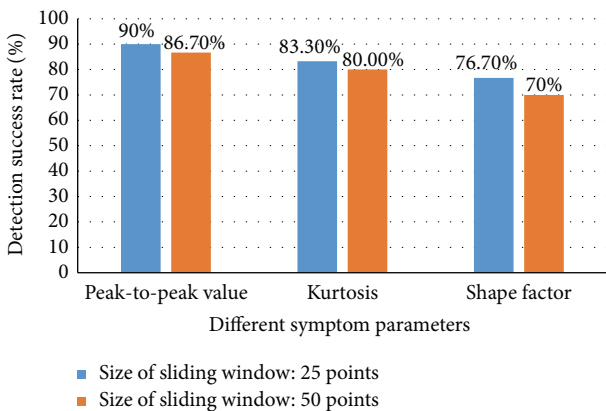


FIGURE 14: Size of sliding window: 25 points and 50 points.

matrix are utilized to assess the performance of the proposed method. A conclusion can be drawn that the detection success ratio of peak-to-peak value is higher than that of kurtosis and shape factor from Figure 14. Furthermore, the detection success ratio of the sliding window with a 25-point size is a

bit higher than that of the sliding window with a 50-point size. Thus, a conclusion can be drawn that more information related to the roller bearing faults may be collected when a smaller size of the sliding window is selected.

5.2. *Different Dimension of the Measurement Matrix.* Different dimensions of the measurement matrix with a predetermined size of the sliding window are also employed to evaluate the effectiveness of the proposed fault detection strategy. Also, the detection success ratio of peak-to-peak value is higher than that of kurtosis and shape factor as presented in Figure 15. Moreover, the detection success ratio rises with the increase of the measurement matrix’s dimension. This means that when a larger compression ratio is achieved, the detection success ration may decrease. Therefore, if a better compression result needs to be achieved, suitable sizes of the sliding window and measurement matrix should be cooperative.

6. Conclusion

In this study, a two-stage compression method is developed to reduce the large amount of the faulty vibration signals

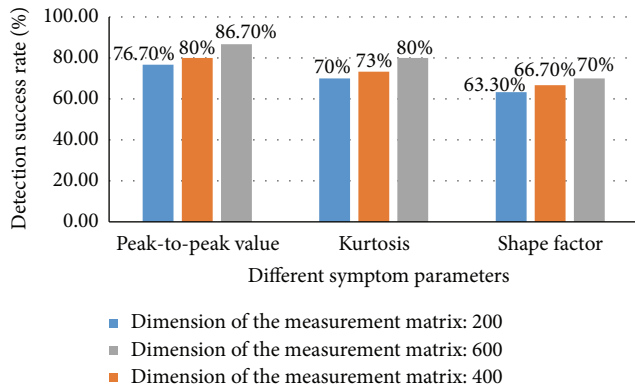


FIGURE 15: Dimension of the measurement matrix: 200, 400, and 600.

induced by the condition monitoring. First, three time-domain symptom parameters, namely, peak-to-peak value, kurtosis, and shape factor, are separately considered to gain the symptom parameter wave. In this way, the dimension of the original signals is reduced to a certain level but the fault features are reserved. Next, the measurement matrix works as a compressor to further shrink the amount of the symptom parameter wave. Finally, the fault features are extracted via the CS theory from a small number of samples, which were far below the Shannon sampling rate. Compared to the envelope analysis, the proposed method has an advantage in detection faults from limited samples. Detection success ratio is considered as a criterion to compare the three symptom parameters. From the comparing result, a conclusion can be made that the detection success ratio of peak-to-peak value ranked first, followed by that of kurtosis, and the ratio of shape factor was last.

Competing Interests

The authors declare that there is no conflict of interests regarding the publication of this paper.

Acknowledgments

This work is partially supported by the National Natural Science Foundation of China (Grant nos. 51405012 and 51375037) and Petro China Innovation Foundation.

References

- [1] Y. B. Li, M. Q. Xu, Y. Wei, and W. H. Huang, "Rotating machine fault diagnosis based on intrinsic characteristic-scale decomposition," *Mechanism and Machine Theory*, vol. 94, pp. 9–27, 2015.
- [2] O. Janssens, R. Schulz, V. Slavkovikj et al., "Thermal image based fault diagnosis for rotating machinery," *Infrared Physics and Technology*, vol. 73, pp. 78–87, 2015.
- [3] H. T. Zhou, J. Chen, G. M. Dong, H. C. Wang, and H. D. Yuan, "Bearing fault recognition method based on neighbourhood component analysis and coupled hidden Markov model," *Mechanical Systems and Signal Processing*, vol. 66–67, pp. 568–581, 2016.
- [4] A. Mahvash and A. A. Lakis, "Application of cyclic spectral analysis in diagnosis of bearing faults in complex machinery," *Tribology Transactions*, vol. 58, no. 6, pp. 1151–1158, 2015.
- [5] C. Ruiz-Cárcel, V. H. Jaramillo, D. Mba, J. R. Ottewill, and Y. Cao, "Combination of process and vibration data for improved condition monitoring of industrial systems working under variable operating conditions," *Mechanical Systems and Signal Processing*, vol. 66–67, pp. 699–714, 2016.
- [6] N. Saravanan, S. Cholairajan, and K. I. Ramachandran, "Vibration-based fault diagnosis of spur bevel gear box using fuzzy technique," *Expert Systems with Applications*, vol. 36, no. 2, pp. 3119–3135, 2009.
- [7] M. Strączkiewicz, P. Czop, and T. Barszcz, "The use of a fuzzy logic approach for integration of vibration-based diagnostic features of rolling element bearings," *Journal of Vibroengineering*, vol. 17, no. 4, pp. 1760–1768, 2015.
- [8] V. K. Rai and A. R. Mohanty, "Bearing fault diagnosis using FFT of intrinsic mode functions in Hilbert-Huang transform," *Mechanical Systems and Signal Processing*, vol. 21, no. 6, pp. 2607–2615, 2007.
- [9] N. Tandon and A. Choudhury, "Review of vibration and acoustic measurement methods for the detection of defects in rolling element bearings," *Tribology International*, vol. 32, no. 8, pp. 469–480, 1999.
- [10] M. Oltean, J. Picheral, E. Lahalle, H. Hamdan, and J. Griffaton, "Compression methods for mechanical vibration signals: application to the plane engines," *Mechanical Systems and Signal Processing*, vol. 41, no. 1–2, pp. 313–327, 2013.
- [11] V. Sugumaran and K. I. Ramachandran, "Automatic rule learning using decision tree for fuzzy classifier in fault diagnosis of roller bearing," *Mechanical Systems and Signal Processing*, vol. 21, no. 5, pp. 2237–2247, 2007.
- [12] J. H. Zhang, W. P. Ma, J. W. Lin, L. Ma, and X. J. Jia, "Fault diagnosis approach for rotating machinery based on dynamic model and computational intelligence," *Measurement*, vol. 59, pp. 73–87, 2015.
- [13] K. Li, P. Chen, S. Wang, and H. Wang, "Intelligent diagnosis method for bearing using non-dimensional symptom parameters and Ant colony optimization. International Information Institute (Tokyo)," *Information*, vol. 15, no. 2, pp. 867–877, 2012.
- [14] Y. J. Wang, Y. C. Jiang, and S. Q. Kang, "The applications of time domain and frequency domain statistical factors on rolling bearing performance degradation assessment," *Computer Modeling and New Technologies*, vol. 18, no. 8, pp. 192–198, 2014.
- [15] X. W. Niu, L. M. Zhu, and H. Ding, "New statistical moments for the detection of defects in rolling element bearings," *The International Journal of Advanced Manufacturing Technology*, vol. 26, no. 11–12, pp. 1268–1274, 2005.
- [16] R. B. W. Heng and M. J. M. Nor, "Statistical analysis of sound and vibration signals for monitoring rolling element bearing condition," *Applied Acoustics*, vol. 53, no. 1–3, pp. 211–226, 1998.
- [17] Y. Guo, J. Na, B. Li, and R.-F. Fung, "Envelope extraction based dimension reduction for independent component analysis in fault diagnosis of rolling element bearing," *Journal of Sound and Vibration*, vol. 333, no. 13, pp. 2983–2994, 2014.
- [18] H.-Q. Wang, W. Hou, G. Tang, H.-F. Yuan, Q.-L. Zhao, and X. Cao, "Fault detection enhancement in rolling element bearings via peak-based multiscale decomposition and envelope demodulation," *Mathematical Problems in Engineering*, vol. 2014, Article ID 329458, 11 pages, 2014.

- [19] H. Q. Wang and P. Chen, "A feature extraction method based on information theory for fault diagnosis of reciprocating machinery," *Sensors*, vol. 9, no. 4, pp. 2415–2436, 2009.
- [20] Q. Gao, C. Duan, H. Fan, and Q. Meng, "Rotating machine fault diagnosis using empirical mode decomposition," *Mechanical Systems and Signal Processing*, vol. 22, no. 5, pp. 1072–1081, 2008.
- [21] Z. K. Peng, P. W. Tse, and F. L. Chu, "A comparison study of improved Hilbert-Huang transform and wavelet transform: application to fault diagnosis for rolling bearing," *Mechanical Systems and Signal Processing*, vol. 19, no. 5, pp. 974–988, 2005.
- [22] J. Ma, J. Wu, and X. Yuan, "The fault diagnosis of the rolling bearing based on the LMD and time-frequency analysis," *International Journal of Control and Automation*, vol. 6, no. 4, pp. 357–376, 2013.
- [23] M. J. Li, H. Q. Wang, G. Tang, H. F. Yuan, and Y. Yang, "An improved method based on CEEMD for fault diagnosis of rolling bearing," *Advances in Mechanical Engineering*, vol. 2014, Article ID 676205, 10 pages, 2014.
- [24] J.-H. Ahn, D.-H. Kwak, and B.-H. Koh, "Fault detection of a roller-bearing system through the EMD of a wavelet denoised signal," *Sensors*, vol. 14, no. 8, pp. 15022–15038, 2014.
- [25] D. L. Donoho, "Compressed sensing," *IEEE Transactions on Information Theory*, vol. 52, no. 4, pp. 1289–1306, 2006.
- [26] A. S. Khwaja and J. Ma, "Applications of compressed sensing for sar moving-target velocity estimation and image compression," *IEEE Transactions on Instrumentation and Measurement*, vol. 60, no. 8, pp. 2848–2860, 2011.
- [27] S. Zhu, B. Zeng, and M. Gabbouj, "Adaptive sampling for compressed sensing based image compression," *Journal of Visual Communication and Image Representation*, vol. 30, pp. 94–105, 2015.
- [28] I. Kim and N.-L. Vu, "parallel compressed sensing method to accelerate MRI," in *Proceedings of the 12th International Conference on Control, Automation and Systems (ICCAS '12)*, pp. 1103–1107, Jeju Island, Republic of Korea, October 2012.
- [29] M. Ghahremani and H. Ghassemian, "Remote sensing image fusion using ripple transform and compressed sensing," *IEEE Geoscience and Remote Sensing Letters*, vol. 12, no. 3, pp. 502–506, 2015.
- [30] K. P. Zhu, X. Lin, K. X. Li, and L. L. Jiang, "Compressive sensing and sparse decomposition in precision machining process monitoring: from theory to applications," *Mechatronics*, vol. 31, pp. 3–15, 2015.
- [31] X. Chen, Z. Du, J. Li, X. Li, and H. Zhang, "Compressed sensing based on dictionary learning for extracting impulse components," *Signal Processing*, vol. 96, pp. 94–109, 2014.
- [32] G. Tang, Q. Yang, H.-Q. Wang, G.-G. Luo, and J.-W. Ma, "Sparse classification of rotating machinery faults based on compressive sensing strategy," *Mechatronics*, vol. 31, pp. 60–67, 2015.
- [33] Y. Wang, J. Xiang, Q. Mo, and S. He, "Compressed sparse time-frequency feature representation via compressive sensing and its applications in fault diagnosis," *Measurement*, vol. 68, pp. 70–81, 2015.
- [34] L. Stankovic, S. Stankovic, and M. Amin, "Missing samples analysis in signals for applications to L-estimation and compressive sensing," *Signal Processing*, vol. 94, no. 1, pp. 401–408, 2014.
- [35] S. Gishkori, G. Leus, and V. Lottici, "Compressive sampling based differential detection for UWB impulse radio signals," *Physical Communication*, vol. 5, no. 2, pp. 185–195, 2012.
- [36] G. Tang, W. Hou, H. Q. Wang, G. G. Luo, and J. W. Ma, "Compressive sensing of roller bearing faults via harmonic detection from under-sampled vibration signals," *Sensors*, vol. 15, no. 10, pp. 25648–25662, 2015.
- [37] H. Q. Wang, R. T. Li, G. Tang, H. F. Yuan, Q. L. Zhao, and X. Cao, "A Compound fault diagnosis for rolling bearings method based on blind source separation and ensemble empirical mode decomposition," *PLoS ONE*, vol. 9, no. 10, Article ID e109166, 2014.

Research Article

Feature Extraction and Selection Scheme for Intelligent Engine Fault Diagnosis Based on 2DNMF, Mutual Information, and NSGA-II

Peng-yuan Liu, Bing Li, Cui-e Han, and Feng Wang

Forth Department, Mechanical Engineering College, No. 97, Heping West Road, Shijiazhuang, Hebei 050003, China

Correspondence should be addressed to Bing Li; rommandy@163.com

Received 24 December 2015; Revised 20 March 2016; Accepted 27 March 2016

Academic Editor: Arturo Garcia-Perez

Copyright © 2016 Peng-yuan Liu et al. This is an open access article distributed under the Creative Commons Attribution License, which permits unrestricted use, distribution, and reproduction in any medium, provided the original work is properly cited.

A novel feature extraction and selection scheme is presented for intelligent engine fault diagnosis by utilizing two-dimensional nonnegative matrix factorization (2DNMF), mutual information, and nondominated sorting genetic algorithms II (NSGA-II). Experiments are conducted on an engine test rig, in which eight different engine operating conditions including one normal condition and seven fault conditions are simulated, to evaluate the presented feature extraction and selection scheme. In the phase of feature extraction, the *S* transform technique is firstly utilized to convert the engine vibration signals to time-frequency domain, which can provide richer information on engine operating conditions. Then a novel feature extraction technique, named two-dimensional nonnegative matrix factorization, is employed for characterizing the time-frequency representations. In the feature selection phase, a hybrid filter and wrapper scheme based on mutual information and NSGA-II is utilized to acquire a compact feature subset for engine fault diagnosis. Experimental results by adopted three different classifiers have demonstrated that the proposed feature extraction and selection scheme can achieve a very satisfying classification performance with fewer features for engine fault diagnosis.

1. Introduction

Engine is one of the core mechanical components in a wide range of industrial applications. Detecting and identifying the faults of engine at an early stage while the machine is still on operation can help to avoid serious accidents and reduce economic losses. For this reason, various intelligent techniques such as artificial neural networks (ANN), support vector machine (SVM), relevance vector machine (RVM), and extreme learning machines (ELM) have been successfully applied to automated detection and diagnosis of engine conditions over the past few years [1–6].

For any intelligent fault diagnosis systems, feature extraction and feature selection schemes can be regarded as the two most important steps. Feature extraction is a mapping process from the measured signal space to the feature space. Representative features associated with the conditions of machinery components should be extracted by using appropriate signal processing and calculating approaches. Various

techniques, such as wavelet analysis, empirical mode decomposition, multivariate statistics, morphological pattern spectrum, fractal theory, and nonnegative matrix factorization, have been applied in engine fault diagnosis in the past few years [7–11]. In this work, a new feature extraction approach based on *S* transform [12] and two-dimensional nonnegative matrix factorization (2DNMF), which has been used for bearing fault diagnosis in our earlier work [13], is employed for engine fault diagnosis. To the best of our knowledge, this feature extraction has never been utilized in engine fault diagnosis. The main advantage of 2DNMF to NMF is that it does not need to transform the 2D matrix to 1D vector, which will lead to a high-dimensional vector space and loss of some structure information hiding in original 2D matrices. Thus, the 2DNMF is capable of characterizing the time-frequency representations more effectively and efficiently for engine fault diagnosis.

Filter and wrapper methods can be regarded as the two main categories of feature selection approaches in the

literatures. Several researches have been done by utilizing the filter method or wrapper method for mechanical fault diagnosis utilizing Fisher's criterion [14], distance evaluation technique [15, 16], decision tree [17, 18], and evolution algorithm (EA) combined with ANN and SVM [19–24]. They have largely improved the efficiency and accuracy of mechanical fault diagnosis in practice. Despite the successive applications of filter or wrapper methods in fault diagnosis, it should be noted that the wrapper and filter methods can complement each other. The filter methods can search through the feature space efficiently but usually fail to obtain a good accuracy, while the wrappers can provide good accuracy but require much computation time. Therefore, it is very desirable to combine the filter and wrapper methods to achieve high efficiency and accuracy simultaneously [25–28]. In our earlier works [29, 30], the hybrid feature selection scheme combining filter and wrapper methods based on ReliefF, genetic algorithm (GA), mutual information, and nondominated sort genetic algorithm (NSGA-II) has been investigated for gear fault diagnosis. However, to the best of our knowledge, these schemes have not yet been used for engine fault diagnosis. Therefore, in this work, the hybrid feature selection scheme based on the mutual information and the improved nondominated sort genetic algorithm (NSGA-II) is employed and verified for engine fault diagnosis. Otherwise, a more detailed demonstration of the above-mentioned feature extraction and selection scheme, which has not been demonstrated in earlier works, is given in this work.

Experiments are conducted on an engine test rig, in which eight different engine operating states including normal state and seven fault states are simulated in the experiments. The performance of the proposed feature extraction and selection scheme is testified on the engine dataset. Experimental results have demonstrated the superiority of the proposed intelligent scheme on computation cost and classification accuracies in engine fault diagnosis. Figure 1 illustrates the flowchart of the intelligent engine fault diagnosis scheme presented in this work.

The remainder of this work is organized as follows. Section 2 describes the feature extraction method based on the S transform and 2DNMF. In Section 3, the hybrid filter and wrapper feature selection scheme based on mutual information and NSGA-II is detailed. Section 4 presents the application results of the proposed feature extraction and selection scheme for engine fault diagnosis. The conclusions of this paper are summarized in Section 5.

2. Feature Extraction Based on S Transform and Two-Dimensional Nonnegative Matrix Factorization

2.1. S Transform. The S transform, put forward by Stockwell et al. in 1996, can be regarded as an extension to the ideas of the Gabor transform and the wavelet transform. The S transform of signal $x(t)$ is defined as

$$S(\tau, f) = \int_{-\infty}^{+\infty} x(t) w(t - \tau) e^{-j2\pi ft} dt, \quad (1)$$

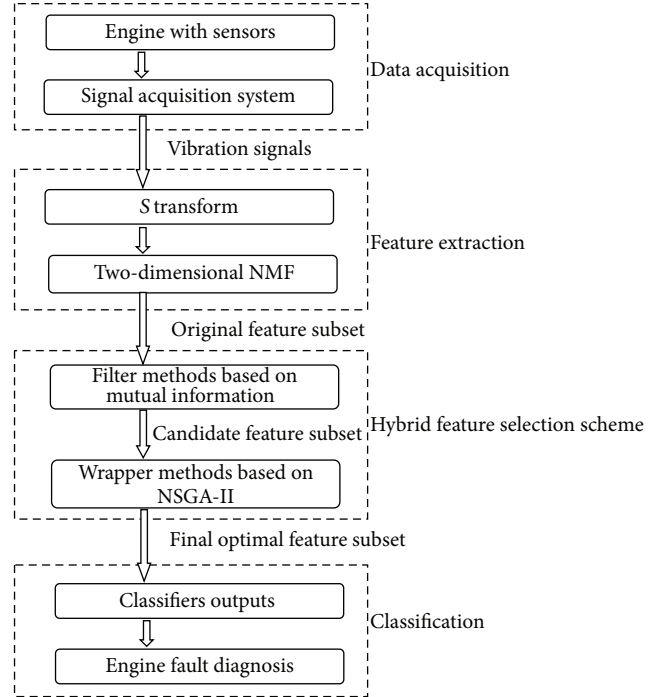


FIGURE 1: Flowchart of the presented feature extraction and selection scheme for intelligent engine fault diagnosis.

where

$$w(t) = \frac{1}{\sigma\sqrt{2\pi}} e^{-t^2/2\sigma^2}, \quad (2)$$

$$\sigma = \frac{1}{|f|}.$$

Then the S transform can be given by combining (1) and (2):

$$S(\tau, f) = \int_{-\infty}^{+\infty} x(t) \frac{|f|}{\sqrt{2\pi}} e^{-(t-\tau)^2 f^2 / 2} e^{-j2\pi ft} dt. \quad (3)$$

Since S transform is a representation of the local spectra, Fourier or time average spectrum can be directly obtained by averaging the local spectra as

$$\int_{-\infty}^{+\infty} S(\tau, f) d\tau = X(f), \quad (4)$$

where $X(f)$ is the Fourier transform of $x(t)$.

The inverse S transform is given by

$$x(t) = \int_{-\infty}^{+\infty} \int_{-\infty}^{+\infty} S(\tau, f) e^{j2\pi ft} d\tau df. \quad (5)$$

The main advantage of the S transform over the short-time Fourier transform (STFT) is that the standard deviation σ is actually a function of frequency f . Consequently, the window function is also a function of time and frequency. As the width of the window is controlled by the frequency, it can obviously be seen that the window is wider in the time domain at lower frequencies and narrower at higher

frequencies. In other words, the window provides good localization in the frequency domain for low frequencies while providing good localization in time domain for higher frequencies. It is a very desirable characteristic for accurate representation of nonstationary vibration signals in time-frequency domain.

2.2. Nonnegative Matrix Factorization (NMF)

2.2.1. Nonnegative Matrix Factorization. The NMF algorithm is a technique that compresses a matrix into a smaller number of basis functions and their encodings [31]. The factorization can be expressed as follows:

$$\mathbf{V}_{n \times m} \approx \mathbf{W}_{n \times r} \mathbf{H}_{r \times m}, \quad (6)$$

where \mathbf{V} denotes an $n \times m$ matrix and m is the number of examples in the dataset, each column of which contains an n -dimensional observed data vector with nonnegative values. This matrix then approximately factorized into $n \times r$ matrix \mathbf{W} and $r \times m$ matrix \mathbf{H} . The rank r of the factorization is usually chosen such that $(n + m)r < nm$, and hence the compression or dimensionality reduction is achieved. The key characteristic of NMF is the nonnegativity constraints imposed on the two factors, and the nonnegativity constraints are compatible with the intuitive notion of combining parts to form a whole.

2.2.2. Two-Dimensional Nonnegative Matrix Factorization (2DNMF). The key difference between 2DNMF and NMF is that the former adopt a novel representation for original time-frequency representations. In traditional NMF, the 2D time-frequency matrices must be previously transformed into 1D vector. The resulting vectors usually lead to a high-dimensional vector space, where it is difficult to find good bases to approximately reconstruct original time-frequency distributions. That is also called the ‘‘curse of dimensionality’’ problem, which is more apparent in small-sample-size cases. Another disadvantage of NMF is that such a matrix-to-vector transform may cause the loss of some structure information hiding in original 2D time-frequency representations [13].

Assume $p \times q$ matrix \mathbf{A}_k ($k = 1, 2, \dots, m$) denotes the time-frequency representation of k th training sample signal acquired from engine. In traditional NMF, a 2D time-frequency representation is first transformed into a 1D vector, and then the training databases are represented with $n \times m$ matrix \mathbf{V} , each column of which contains $n = pq$ nonnegative values of one of the m time-frequency representations. In 2DNMF, however, it never transforms the 2D time-frequency representations into their corresponding 1D vector. Instead, it will use a more straightforward way which views a time-frequency representation as a 2D matrix.

The procedure of 2DNMF method consists of two successive stages. At first it aligns m training TFR matrices into a $p \times qm$ matrix $\mathbf{X} = [\mathbf{A}_1 \ \mathbf{A}_2 \ \dots \ \mathbf{A}_m]$, where each \mathbf{A}_k denotes one of the m TFR matrices. Similar to NMF, 2DNMF first finds $p \times d_1$ nonnegative matrix \mathbf{L} and $d_1 \times qm$ nonnegative matrix \mathbf{H} such that

$$\mathbf{X} \approx \mathbf{LH}. \quad (7)$$

Here \mathbf{L} and \mathbf{H} are the basis functions and encoding coefficients, respectively. Since each column of \mathbf{X} corresponds to a column of original TFR matrix, \mathbf{L} is also named as column bases.

The second stage of 2DNMF involves computing the row bases. In this stage, it first constructs a new $q \times pm$ matrix $\mathbf{X}' = [\mathbf{A}'_1 \ \mathbf{A}'_2 \ \dots \ \mathbf{A}'_m]$, where each \mathbf{A}'_k denotes the transpose of \mathbf{A}_k . Similarly, 2DNMF seeks a $q \times d_2$ nonnegative matrix \mathbf{R} and a $d_2 \times pm$ nonnegative matrix \mathbf{C} such that

$$\mathbf{X}' \approx \mathbf{RC}. \quad (8)$$

Here \mathbf{R} and \mathbf{C} are the basis functions and encoding coefficients, respectively.

By now the $p \times d_1$ dimensional column bases \mathbf{L} and the $q \times d_2$ dimensional row bases \mathbf{R} are obtained. A new representation of TFR \mathbf{A}_k projected to the column bases \mathbf{L} and row bases \mathbf{R} can be denoted as

$$\mathbf{D}_k = \mathbf{L}^T \mathbf{A}_k \mathbf{R}, \quad k = 1, 2, \dots, m, \quad (9)$$

where \mathbf{D}_k is a $d_1 \times d_2$ matrix, which can be regarded as a reduced dimension representation of TFR \mathbf{A}_k and can be used as features for fault diagnosis of engine states.

3. Hybrid Filter and Wrapper Feature Selection Scheme Based on Mutual Information and NSGA-II

3.1. Hybrid Filter and Wrapper Feature Selection Scheme. Filters and wrappers are the two main categories of feature selection algorithms in the literatures. Filter methods evaluate the goodness of the feature subset by using the intrinsic characteristic of the data. They are relatively computationally cheap since they do not involve the induction algorithm. However, they also take the risk of selecting subsets of features that may not match the chosen induction algorithm. Wrapper methods, on the contrary, directly use the classifiers to evaluate the feature subsets. They generally outperform filter methods in terms of prediction accuracy, but they are generally computationally more intensive [32–35]. In summary, wrapper and filter methods can complement each other, in that filter methods can search through the feature space efficiently while the wrappers can provide good accuracy. It is desirable to combine the filter and wrapper methods to achieve high efficiency and accuracy simultaneously.

In this work, the hybrid feature selection combining filter and wrapper feature selection technique based on the mutual information and the improved nondominated sort genetic algorithm (NSGA-II) is employed [30]. In this hybrid filter and wrapper feature selection scheme, there are two steps involved. In the first stage, a candidate feature subset is chosen according to the max-relevance and min-redundancy (mRMR) criterion based on mutual information from the original feature set. Then at the second stage, classifier combined with NSGA-II is adopted to find a more compact feature subset from the candidate feature subset. In this stage, feature selection problem is defined as a multiobjective problem dealing with two competing objectives, mean lesser features and lower classification error rate.

3.2. Filter Method Based on Mutual Information

3.2.1. Mutual Information. Mutual information is one of the most widely used measures to define relevancy of variables [36]. In this section, the feature selection method based on mutual information is focused on. Given two random variables x and y , their mutual information can be defined in terms of their probabilistic density functions $p(x)$, $p(y)$, and $p(x, y)$:

$$I(x, y) = \iint p(x, y) \log \frac{p(x, y)}{p(x)p(y)} dx dy. \quad (10)$$

The estimation of the mutual information of two variables was detailed in [36].

In supervised classification, one can view the classes as a variable (named C) with L possible values (where L is the number of classes of the system) and the feature component as another variable (named X) with K possible values (where K is the number of parameters of the system). So one will be able to compute the mutual information $I(x_k, c)$ between the classes c and the feature x_k ($k = 1, 2, \dots, K$):

$$I(x_k, c) = \iint p(x_k, c) \log \frac{p(x_k, c)}{p(x_k)p(c)} dx_k dc. \quad (11)$$

Then the informative variables with larger $I(x_k, c)$ can be identified. A more compact feature subset can be obtained via selecting the d best features based on (12) from the original feature set.

Equation (12) provides us with a measure to evaluate the effectiveness of the ‘‘global’’ feature that is simultaneously suitable to differentiate all classes of signals. For a small number of classes, this approach may be sufficient. The more signal classes, the more ambiguous $I(x_k, c)$.

3.2.2. Max-Relevance and Min-Redundancy. Max-relevance means that the selected features x_i are required, individually, to have the largest mutual information $I(x_i, c)$. It means that the m best individual features should be selected according to this criterion. It can be represented as

$$\max D(S, c), \quad (12)$$

$$D = \frac{1}{|S|} \sum_{x_i \in S} I(x_i, c),$$

where $|S|$ denotes the number of features contained by S .

However, it has been proved that the simple combination of the best individual features does not necessarily lead to a good performance. In other words, ‘‘the m best features are not the best m features’’ [36, 37]. The most important problem of the max-relevance is that it neglects the redundancy between features and may cause the degradation of the classification performance.

So the min-redundancy criterion should be added to the selection of the optimal subsets. It can be represented as

$$\min R(S), \quad (13)$$

$$R = \frac{1}{|S|^2} \sum_{x_i, x_j \in S} I(x_i, x_j).$$

The criterion combining the above two constraints is called the ‘‘maximal relevance minimal redundancy’’ (mRMR) [36]. The operator $\Phi(D, R)$ is defined to optimize D and R simultaneously:

$$\max \Phi(D, R), \quad (14)$$

$$\Phi = D - R.$$

3.2.3. Candidate Feature Subset Obtained Based on Max-Relevance and Min-Redundancy. In practice, greedy search methods can be used to find the near-optimal features by Φ . Let F be the original feature sets and let S be the selected subsets. Suppose that S already has S_{m-1} , which means it has selected $m - 1$ features. The next work is to select m th feature from the set $\{F - S_{m-1}\}$. This is done according to the following criterion:

$$\max_{x_j \in F - S_{m-1}} \left[I(x_j, c) - \frac{1}{m-1} \sum_{x_i \in S_{m-1}} I(x_j, x_i) \right]. \quad (15)$$

The main steps can be represented as follows.

Step 1. Let F be the original feature set and let S be the selected subset. S is initialized to be an empty subset, $S \rightarrow \{\}$.

Step 2. Calculate the relevance of individual feature x_i with the target class c , denoted by $I(x_i, c)$.

Step 3. Find the feature x_k which has the maximum relevance:

$$I(x_k, c) = \max_{x_i \in F} I(x_i, c). \quad (16)$$

Let $F_1 \rightarrow \{F - x_k\}$, $S_1 \rightarrow \{S + x_k\}$.

Step 4. This step consists of the following:

for $m = 2 : N$

Let $x_j \in F_{m-1}$, $x_i \in S_{m-1}$, find the x_k according to the following criterion:

$$\max_{x_j \in F_{m-1}} \left[I(x_j, c) - \frac{1}{m-1} \sum_{x_i \in S_{m-1}} I(x_j, x_i) \right] \quad (17)$$

Let $F_m = \{F_{m-1} - x_k\}$, $S_m = \{S_{m-1} + x_k\}$

end

In this way, N sequential feature subsets can be obtained and satisfy $S_1 \subset S_2 \subset \dots \subset S_N$. In practice, the first d features can be selected as the feature subset S_d , which is the candidate feature subset for wrapper methods.

3.3. Wrapper Method Based on NSGA-II

3.3.1. A Brief Review on NSGA-II. The presence of multiple objectives in practical problems has given rise to the rapid

development of multiobjective evolutionary algorithms over the past few years. Nondominated sorting genetic algorithm (NSGA), which was suggested by Goldberg and implemented by Srinivas and Deb [38], has been proved to be an effective approach for multiobjective optimization problems. However, NSGA is still suffering three main drawbacks: the high computational complexity of nondominated sorting, lack of elitism, and requirement for specifying the sharing parameter.

As an improved version of the NSGA, NSGA-II was introduced by Deb et al. in 2002 [39]. The NSGA-II overcame the original NSGA defects by introducing the fast nondominated sorting algorithm to alleviate computational complexity, the elitist-preserving mechanism to speed up the evolution, and the crowded comparison operator to avoid specifying the sharing parameter. It has been verified that the NSGA-II is able to maintain a better spread of solutions and converges better in the obtained nondominated front compared to other similar elitist multiple objectives evolution algorithms (MOEAs). More details about the description and implementation can be found in [39].

3.3.2. Wrapper Feature Selection Using NSGA-II. In most cases of conventional wrapper methods for fault diagnosis, the feature selection problem was formulized as a single objective problem [19, 21, 22, 24, 40]. However, the feature selection is inherently a multiobjective problem, which deals with two competing objectives: the feature dimension and the classification accuracy. An optimal feature set has to be of a minimal number of features and has to produce the minimum classification error rate.

In this work, the feature selection problem for engine fault diagnosis is formulated to be a multiobjective problem. The NSGA-II mentioned above is utilized to optimize the two objectives: the minimal number of features and minimum classification error rate. A step-by-step procedure for solving the feature selection problem by utilizing the NSGA-II is illustrated in Figure 2.

3.3.3. Implementation Issues for Wrapper Feature Selection Using NSGA-II. For wrapper feature selection approach, there are several factors for controlling the process of NSGA-II while searching the suboptimal feature subsets for classifiers. To apply NSGA-II to feature selection, the following issues are focused on.

(1) Fitness Functions. Two competing objectives are defined as the fitness functions: the first was minimization of the number of used features and the second was minimization of the classification error rate. Three popular classifiers, that is, K nearest neighbor classifier (KNNC) [41], Naïve Bayes classifier (NBC) [42], and least-square support vector machine (LS-SVM) [43], are employed as induction algorithms to implement and evaluate the proposed feature selection approach. The KNNC and NMC are implemented by utilizing the MATLAB Toolbox for Pattern Recognition (PRTools 4.1) [44]. The LS-SVM was implemented by the LS-SVMlab1.5, which can be downloaded from [45].

TABLE 1: Engine operating states in experiment.

State code	Engine operating condition
1	Normal state
2	First cylinder misfire
3	Second cylinder misfire
4	First and second cylinder misfires
5	Too large clearance of intake valve
6	Too large clearance of exhaust valve
7	Air leakage of the intake valve
8	Air leakage of the exhaust valve

(2) Encoding Scheme. The binary coding system is used to represent the chromosome in this investigation. For chromosome representing the feature subsets, the bit with value “1” represents the feature being selected, and “0” indicates that feature is not selected, as shown in Figure 3.

(3) Genetic Operators. Genetic operator consists of two basic operators, that is, crossover and mutation. The used crossover technique is the uniform crossover consisting of replacing genetic material of the two selected parents uniformly in several points. The mutation operator used in this work is implemented as conventional mutation operator operating on each bit separately and changing randomly its value.

4. Results and Discussion

4.1. Engine Dataset Description. To evaluate the performance of the presented feature extraction and selection scheme, experiments are carried out on F3L912 engine with three cylinders to measure the vibration signals. Eight engine running conditions, including one healthy engine state and seven faulted states as summarized in Table 1, are tested in the experiments. All the valve defects are set on the first cylinder. The running speed is set to be 1200 rpm.

Vibration data is collected using accelerometers, which are attached to the cylinder head near first cylinder with magnetic bases. The sample frequency is 20 K. A working cycle of vibration signals is recorded as a sample, which include 4096 sample points. Forty samples are recorded for every condition of engine, where there are totally 320 samples. Figure 4 shows the waveform of vibration signal from the eight engine states.

4.2. Feature Extraction Based on S Transform and 2DNMF. The S transform is utilized to convert the vibration signals from time domain to time-frequency domain, which can provide more discriminative information on engine working states. Figure 5 illustrates the time-frequency representations of eight engine states obtained by S transform.

For each sample of the engine, a 2048×4096 time-frequency matrix can be obtained based on the S transform. The size of the matrix is too large for processing. So the matrix is firstly segmented to 256×512 blocks, where every block consists of an 8×8 submatrix. The mean value of the submatrix is calculated to represent the block. In this way

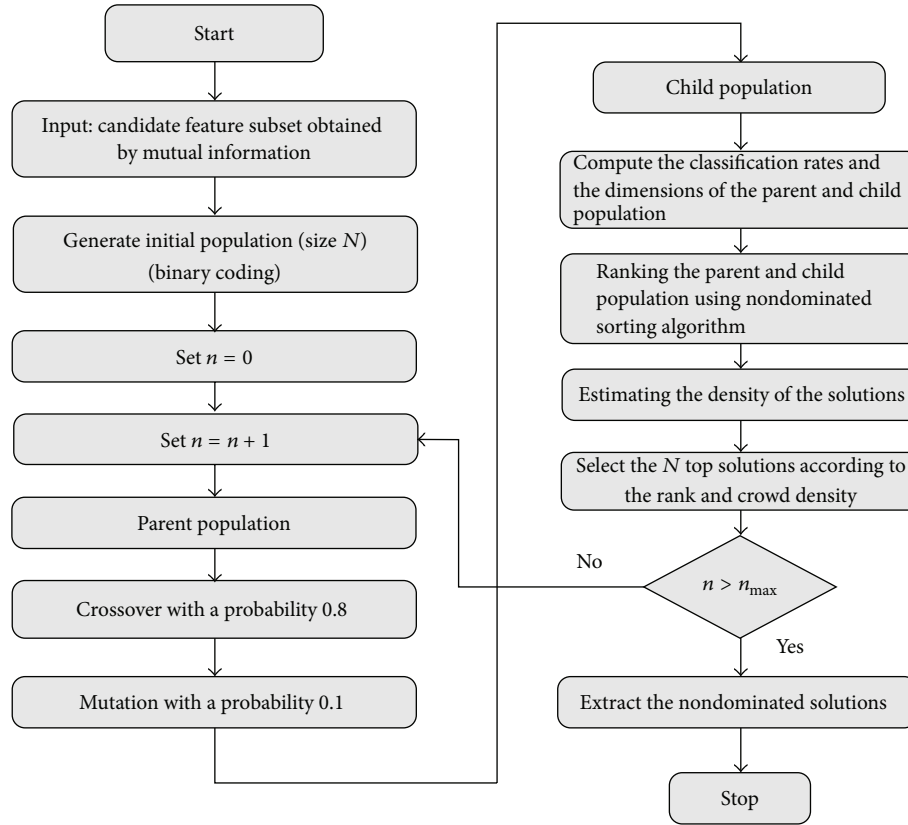


FIGURE 2: The schematic for applying the NSGA-II to the feature selection.

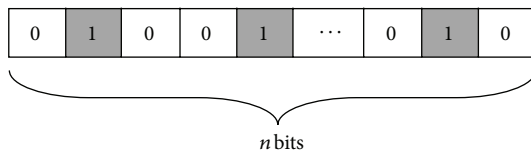


FIGURE 3: The binary coding system.

the time-frequency matrix reduced to 256×512 . The new matrix could provide enough information for classification of engine faults. But it is still not realistic to take all the elements of time-frequency distribution as features, where the dimension could be 131072. For this reason, it is very necessary to compress the feature dimensions from the time-frequency matrix. The 2DNMF, as described in Section 2.2, is used to characterize the time-frequency representations (TFRs) for engine fault diagnosis.

Based on the S transform, 320 TFRs in total can be obtained. Forty TFRs, five samples for each engine state, are selected as training samples to calculate the column basis matrix \mathbf{L} and row basis matrix \mathbf{R} for 2DNMF. The parameters d_1 and d_2 of the 2DNMF are both set to be 10. Figures 6 and 7 have shown the column basis matrix \mathbf{L} and row basis matrix \mathbf{R} obtained by 2DNMF for characterizing the TFRs of engine.

Then by mapping each TFR onto column basis matrix \mathbf{L} and row basis matrix \mathbf{R} based on (9), a 10×10 mapping coefficient matrix can be obtained. The feature matrices of

forty training TFRs are demonstrated in Figure 8, in which every row represents one engine state.

It can be found that the feature matrices obtained by 2DNMF can distinguish the eight engine operating states very effectively. The 100 elements of the feature matrix can be used as the original feature subset for engine fault diagnosis. The original feature subset is set to be F_{Original} .

4.3. Feature Selection Based on Mutual Information and NSGA-II. Although the original feature subset obtained by 2DNMF has shown to be effective in identifying the eight engine states, the dimension of the feature subset can be reduced and the classification accuracy can be improved via feature selection methods. In this subsection, the hybrid filter and wrapper scheme based on mutual information and NSGA-II is employed to find a more compact feature subset for engine fault diagnosis.

In the first stage, the filter method based on mutual information is used to obtain a candidate feature subset. Figures 9 and 10 show the relevance values of the 100 features and the redundancy values between the 100 features calculated by mutual information.

According to the relevance values and redundancy values calculated above, 100 sequential feature subsets $S_1 \subset S_2 \subset \dots \subset S_{100}$ can be obtained based on the mRMR criterion described in Section 3.2. The first 50 features, meaning half of the original feature subset, are selected as the candidate

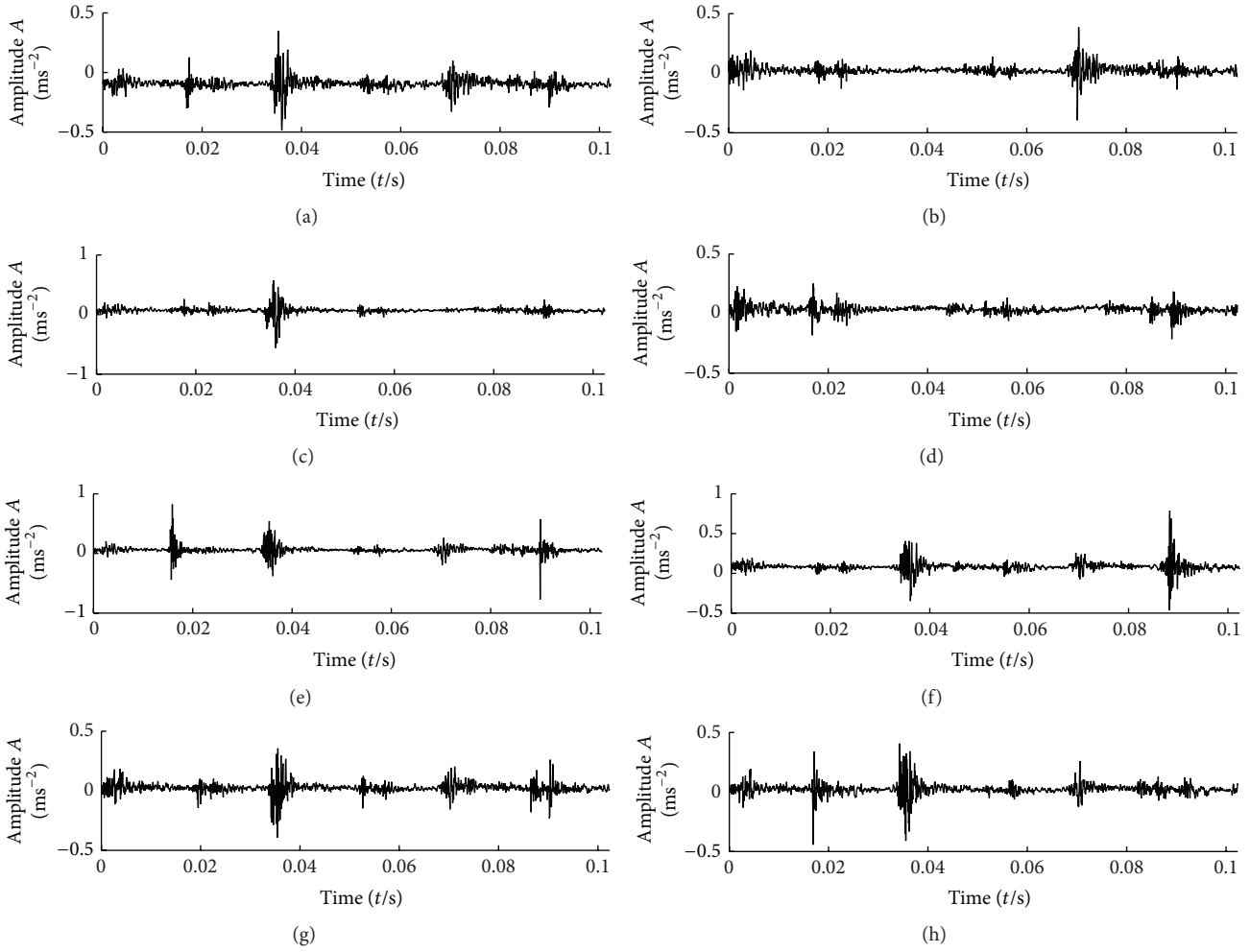


FIGURE 4: Vibration signals acquired from eight engine states: (a) normal state; (b) first cylinder misfire; (c) second cylinder misfire; (d) first and second cylinder misfire; (e) too large clearance of intake valve; (f) too large clearance of exhaust valve; (g) air leakage of the intake valve; (h) air leakage of the exhaust valve.

feature subset for wrapper methods in this work. This feature subset is denoted as F_{mRMR} .

In the second stage, the wrapper method based on NSGA-II is used to find a more compact feature subset based on the feature subset F_{mRMR} . An experiment is also conducted on applying the wrapper method directly on the original feature subset $F_{Original}$ for a comparison with the two-stage feature selection scheme.

Three classifiers, KNNC, NBC, and LS-SVM, as mentioned in Section 3.3, are employed to evaluate the presented two-stage feature selection scheme for engine fault diagnosis. The KNNC classifier is just selected to illustrate the wrapper method based on NSGA-II algorithm. For every chromosome created by NSGA-II, the dimension of features selected by this chromosome and the classification error rate based on KNNC classifier are regarded as the fitness functions. Other parameters of NSGA-II for feature selection are summarized in Table 2.

Figures 11 and 12 show the distributions of the solutions over the objective plane utilizing the NSGA-II and KNNC

TABLE 2: Parameters of NSGA-II for feature selection.

Parameters of NSGA-II	Parameter settings
Population size	200
Generation	60
Crossover probability	0.8
Mutation probability	0.01
Crossover method	Binary crossover
Mutation method	Binary mutation
Selection method	Tournament selection

based on the original feature subset $F_{Original}$ and the candidate feature set F_{mRMR} , respectively. In each figure, the solutions obtained by NSGA-II at generations 10, 20, 40, and 60 are shown. In the figures, all the solutions are marked as blue asterisks and the Pareto optimal solutions are marked with red circles. It can be observed that, with the increasing of generation, the Pareto fronts move toward the ideal

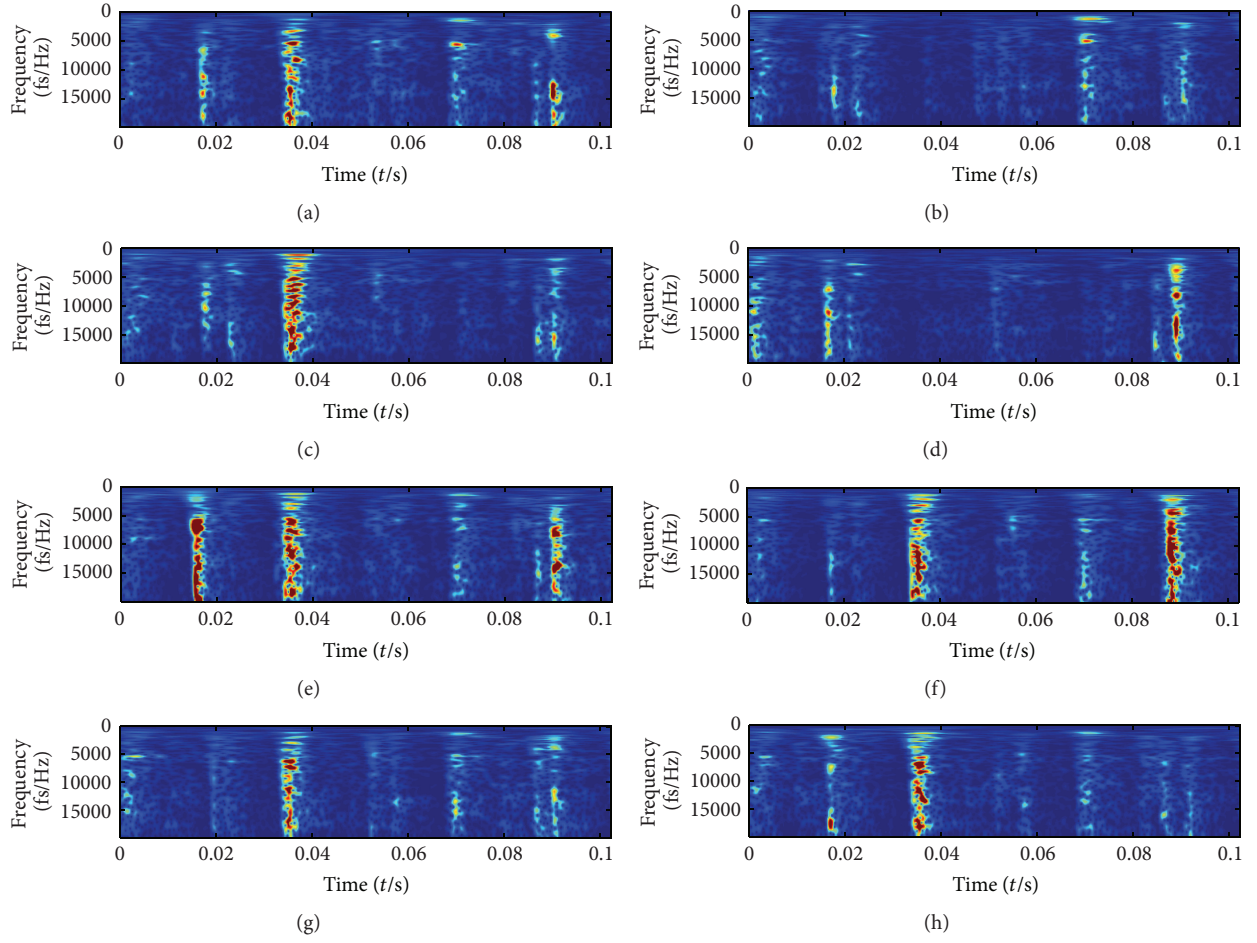


FIGURE 5: The S transform of the eight engine states: (a) normal state; (b) first cylinder misfire; (c) second cylinder misfire; (d) first and second cylinder misfire; (e) too large clearance of intake valve; (f) too large clearance of exhaust valve; (g) air leakage of the intake valve; (h) air leakage of the exhaust valve.

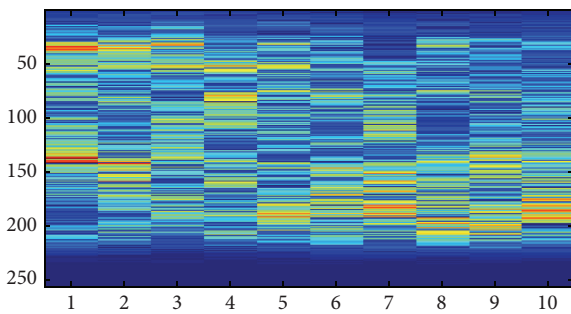


FIGURE 6: The column basis matrix obtained by 2DNMF.

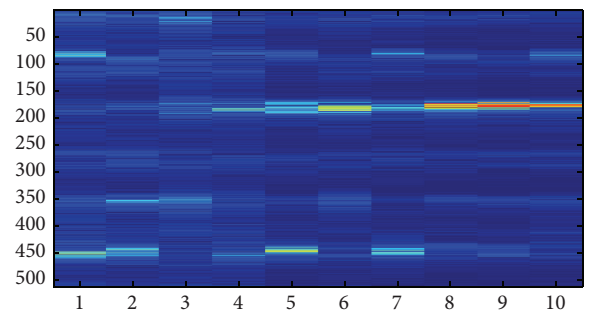


FIGURE 7: The row basis matrix obtained by 2DNMF.

solution, meaning the lower dimension of features and lower classification error rate, for the feature selection problem.

Furthermore, it can be obviously noted from Figures 11 and 12 that the hybrid feature selection scheme which conducts wrapper method on F_{mRMR} obtained better solutions than the wrapper method directly conducted on the original feature subset $F_{Original}$. The hybrid feature selection scheme

achieved a similar or lower classification error rate with much less features than the wrapper method.

4.4. Classification Performances of the Different Feature Subsets. In this section, the classification performance of four different feature subsets, the original feature subset ($F_{Original}$), the feature subset obtained by filter method based on mutual

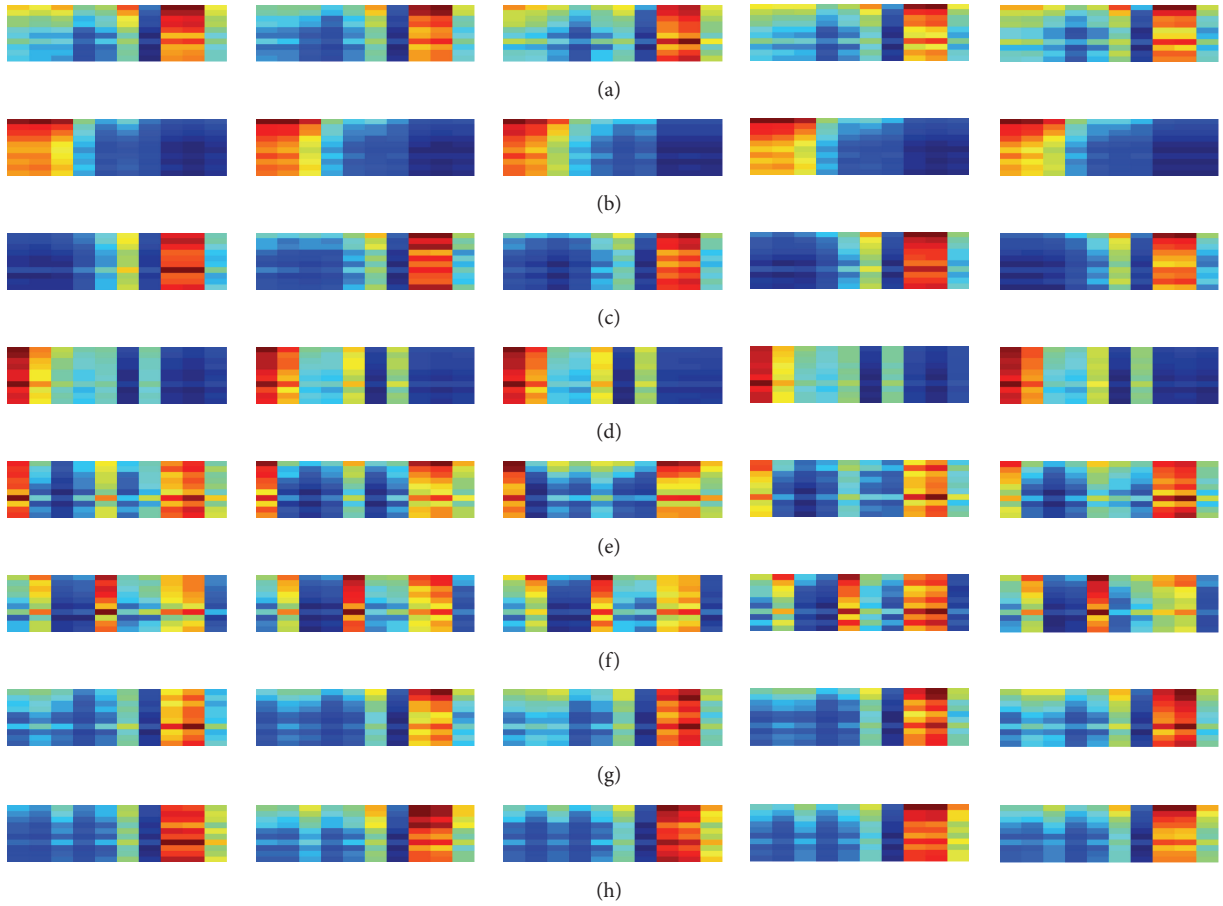


FIGURE 8: The feature matrices of eight engine states obtained by 2DNMF (every row represents one engine state and five samples of each engine state are displayed): (a) normal state; (b) first cylinder misfire; (c) second cylinder misfire; (d) first and second cylinder misfire; (e) too large clearance of intake valve; (f) too large clearance of exhaust valve; (g) air leakage of the intake valve; (h) air leakage of the exhaust valve.

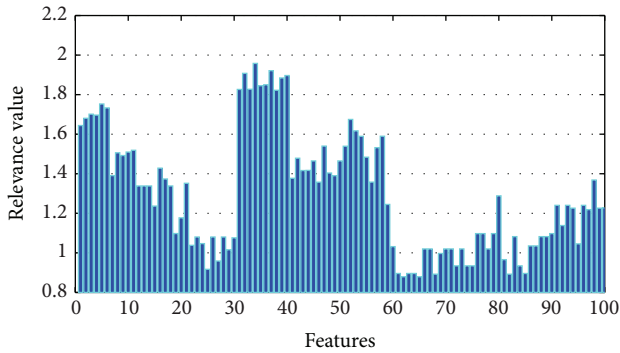


FIGURE 9: Relevance values of the features calculated by mutual information.

information (F_{mRMR}), the feature subset obtained by wrapper method based on NSGA-II (F_{NSGA}), and the feature subset obtained by the hybrid filter and wrapper method ($F_{\text{mRMR}+\text{NSGA}}$), is evaluated and compared. The computation time, feature subset dimensions, and the classification accuracy of different feature subsets based on three classifiers are shown in Table 3. All the experiments are conducted on a

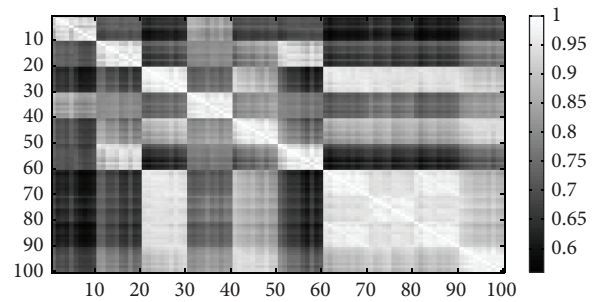


FIGURE 10: Redundancy values between the features calculated by mutual information.

personal computer with 2.93 GHz CPU and 512 M memory. The software used is MATLAB with version 7.1.

It can be found from Table 3 that the original feature subset F_{Original} , which consists of all the 100 features, obtained satisfactory classification performances by using all the three classifiers for engine fault diagnosis. It verifies the effectiveness of the presented feature extraction scheme based on S transform and 2DNMF.

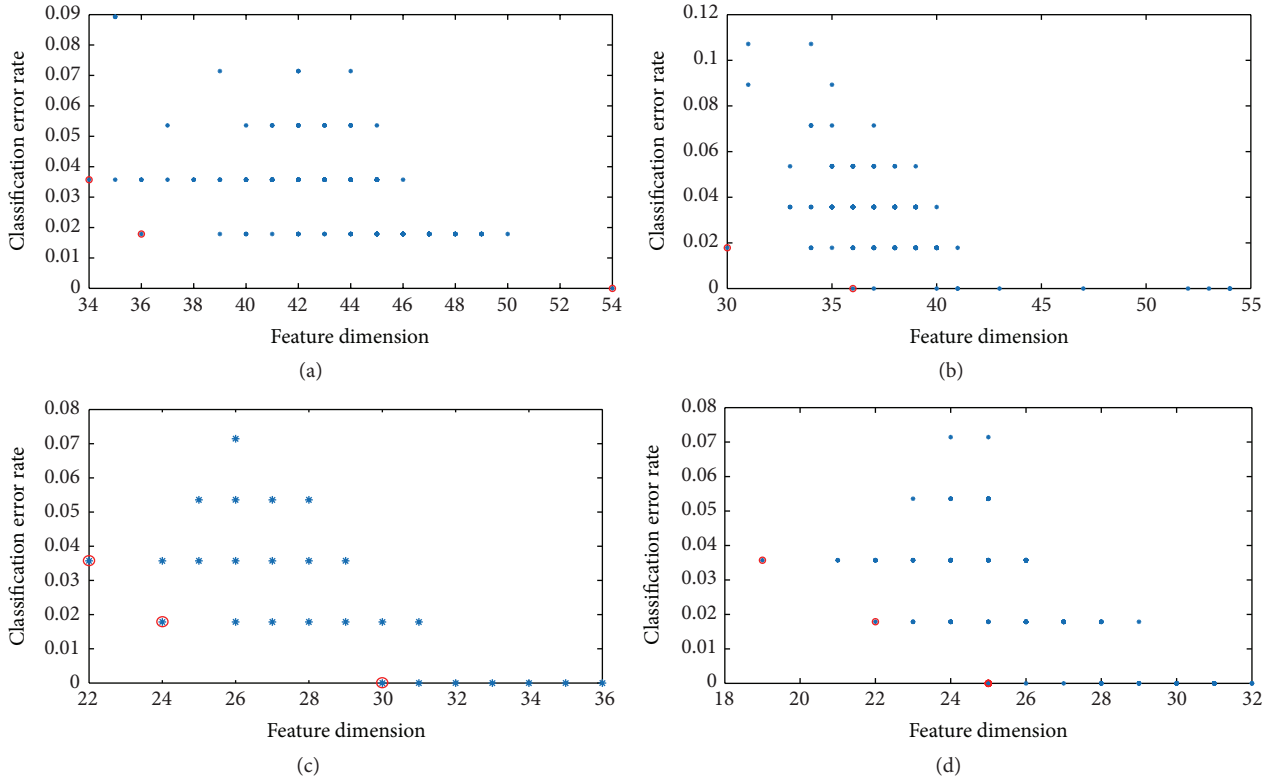


FIGURE 11: Distributions of the solutions at different generations over the objective plane utilizing the NSGA-II based on the original feature subset F_{Original} : (a) 10 generations; (b) 20 generations; (c) 40 generations; (d) 60 generations.

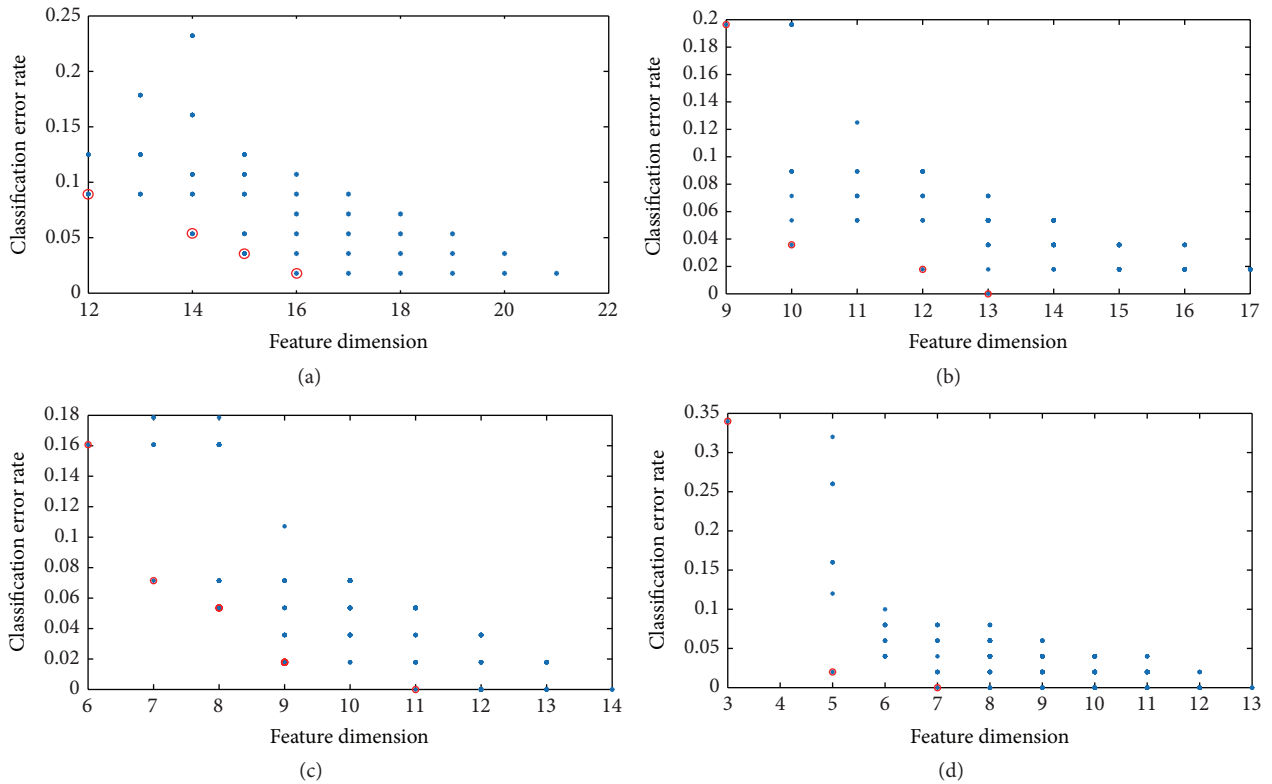


FIGURE 12: Distributions of the solutions at different generations over the objective plane utilizing the NSGA-II based on the candidate feature subset F_{mRMR} : (a) 10 generations; (b) 20 generations; (c) 40 generations; (d) 60 generations.

TABLE 3: Engine faults classification performances of four feature subsets F_{Original} , F_{mMMR} , F_{NSGA} , and $F_{\text{mRMR+NSGA}}$ based on three classifiers.

Classifiers	Feature subsets	Dimension of the feature subset	Computation time (s)	Classification accuracy (%)
KNNC	F_{Original}	100	—	92.5
	F_{mMMR}	40	2.54	96.25
	F_{NSGA}	25	102.3	100
	$F_{\text{mRMR+NSGA}}$	7	49.6	100
NBC	F_{Original}	100	—	87.5
	F_{mMMR}	40	2.54	88.75
	F_{NSGA}	24	148.25	96.25
	$F_{\text{mRMR+NSGA}}$	9	86.5	97.5
SVM	F_{Original}	100	—	96.25
	F_{mMMR}	40	2.54	97.5
	F_{NSGA}	27	496.4	100
	$F_{\text{mRMR+NSGA}}$	9	172.8	100

However, it also can be observed that the classification accuracies of F_{Original} are the lowest in the four feature subsets. It ascertains our assumption that there exist many irrelevant and redundant features, which will decrease the performances in the original feature subset. A feature selection procedure is indispensable before classification.

The performances of the feature subset F_{mRMR} showed to be better than F_{Original} . Otherwise, the dimension of F_{mRMR} is half of the original feature subset. However, the classification accuracies of F_{mRMR} are inferior to F_{NSGA} and $F_{\text{mRMR+NSGA}}$ obviously.

The feature subsets F_{NSGA} and $F_{\text{mRMR+NSGA}}$, which are obtained by wrapper method and hybrid filter and wrapper method, have demonstrated similar classification accuracies in our case. The $F_{\text{mRMR+NSGA}}$ achieved the highest classification rates by using KNNC and LS-SVM classifiers, while the F_{NSGA} gained the best performance by using NBC classifier. However, it can be found from Table 3 that the feature dimensions of $F_{\text{mRMR+NSGA}}$ are lower than F_{NSGA} . Moreover, the hybrid feature selection scheme required much less computation cost than the wrapper method. Therefore, it is very desirable to use hybrid filter and wrapper feature selection scheme to get a satisfactory refined feature subset for engine fault diagnosis.

It also can be found that very satisfactory classification performances can be achieved by the three classifiers with only 7, 9, and 9 features for engine fault diagnosis. It indicates that the presented feature extraction and selection scheme has provided a very effective and efficient approach for engine intelligent fault diagnosis.

5. Conclusion

This work has presented a new feature extraction and feature selection scheme for intelligent fault diagnosis of engine by utilizing S transform, 2DNMF, mutual information, and NSGA-II. Eight different engine operating states, which are simulated on an engine test rig, are employed to evaluate the effectiveness of the proposed methods.

In the phase of feature extraction, the S transform is firstly adopted to obtain time-frequency representations of vibration signals. Then the 2DNMF technique is applied to characterize the time-frequency representations. Experimental results revealed that the features extracted by S transform and 2DNMF obtain a very promising performance for identifying the eight engine states.

In the phase of feature selection, the hybrid filter and wrapper scheme based on mutual information and NSGA-II is employed to obtain a more compact feature subset and higher classification accuracy. And the performance of the hybrid method and the separate filter and wrapper methods is also compared. Experimental results have shown that the hybrid feature selection scheme achieved very promising performances with very few features for engine fault diagnosis. The faults classification accuracies of three different classifiers using the selected features by the presented scheme are consistently higher than those using original feature subset and feature subsets obtained by other feature selection methods. The dimension of the feature subset obtained by the hybrid feature selection scheme is lower than the filter or wrapper method. Furthermore, the computation cost of the hybrid feature selection is much less than the wrapper method.

This research demonstrates clearly that the presented feature extraction and feature selection scheme has great potential to be an effective and efficient tool for the fault diagnosis of engine and can be easily extended to be applied to other machineries.

Competing Interests

The authors declare that they have no competing interests.

References

- [1] Ş. Yildirim, S. Erkaya, I. Eski, and I. Uzmay, "Noise and vibration analysis of car engines using proposed neural network," *Journal of Vibration and Control*, vol. 15, no. 1, pp. 133–156, 2009.

- [2] J.-D. Wu, C.-K. Huang, Y.-W. Chang, and Y.-J. Shiao, "Fault diagnosis for internal combustion engines using intake manifold pressure and artificial neural network," *Expert Systems with Applications*, vol. 37, no. 2, pp. 949–958, 2010.
- [3] B. Li, R.-X. Hu, G.-Q. Ren, and J.-P. Fu, "Engine fault diagnosis based on a morphological neural network using a morphological filter as a preprocessor," *Proceedings of the Institution of Mechanical Engineers, Part D*, vol. 227, no. 4, pp. 490–505, 2013.
- [4] Y. S. Wang, Q. H. Ma, Q. Zhu, X. T. Liu, and L. H. Zhao, "An intelligent approach for engine fault diagnosis based on Hilbert-Huang transform and support vector machine," *Applied Acoustics*, vol. 75, no. 1, pp. 1–9, 2014.
- [5] Y. Liu, J. H. Zhang, F. R. Bi, J. W. Lin, and W. P. Ma, "A fault diagnosis approach for diesel engine valve train based on improved ITD and SDAG-RVM," *Measurement Science and Technology*, vol. 26, no. 2, Article ID 025003, 2014.
- [6] P. K. Wong, J. H. Zhong, Z. X. Yang, and C. M. Vong, "Sparse Bayesian extreme learning committee machine for engine simultaneous fault diagnosis," *Neurocomputing*, vol. 174, pp. 331–343, 2016.
- [7] B. Li, P.-L. Zhang, S.-B. Liang, Y.-T. Zhang, and H.-B. Fan, "Feature extraction for engine fault diagnosis utilizing the generalized S-transform and non-negative tensor factorization," *Proceedings of the Institution of Mechanical Engineers Part C: Journal of Mechanical Engineering Science*, vol. 225, no. 8, pp. 1936–1949, 2011.
- [8] B. Li, S.-S. Mi, P.-Y. Liu, and Z.-J. Wang, "Classification of time-frequency representations using improved morphological pattern spectrum for engine fault diagnosis," *Journal of Sound and Vibration*, vol. 332, no. 13, pp. 3329–3337, 2013.
- [9] X. Wang, C. W. Liu, F. R. Bi, X. Y. Bi, and K. Shao, "Fault diagnosis of diesel engine based on adaptive wavelet packets and EEMD-fractal dimension," *Mechanical Systems and Signal Processing*, vol. 41, no. 1-2, pp. 581–597, 2013.
- [10] S. M. Jafari, H. Mehdigholi, and M. Behzad, "Valve fault diagnosis in internal combustion engines using acoustic emission and artificial neural network," *Shock and Vibration*, vol. 2014, Article ID 823514, 9 pages, 2014.
- [11] Y. Liu, J. H. Zhang, and L. Ma, "A fault diagnosis approach for diesel engines based on self-adaptive WVD, improved FCBF and PECOC-RVM," *Neurocomputing*, vol. 177, pp. 600–611, 2016.
- [12] R. G. Stockwell, L. Mansinha, and R. P. Lowe, "Localization of the complex spectrum: the S transform," *IEEE Transactions on Signal Processing*, vol. 44, no. 4, pp. 998–1001, 1996.
- [13] B. Li, P.-L. Zhang, D.-S. Liu, S.-S. Mi, G.-Q. Ren, and H. Tian, "Feature extraction for rolling element bearing fault diagnosis utilizing generalized S transform and two-dimensional non-negative matrix factorization," *Journal of Sound and Vibration*, vol. 330, no. 10, pp. 2388–2399, 2011.
- [14] G. G. Yen, "Wavelet packet feature extraction for vibration monitoring," *IEEE Transactions on Industrial Electronics*, vol. 47, no. 3, pp. 650–667, 2000.
- [15] Q. Hu, Z. He, Z. Zhang, and Y. Zi, "Fault diagnosis of rotating machinery based on improved wavelet package transform and SVMs ensemble," *Mechanical Systems and Signal Processing*, vol. 21, no. 2, pp. 688–705, 2007.
- [16] Y. Lei, Z. He, Y. Zi, and Q. Hu, "Fault diagnosis of rotating machinery based on multiple ANFIS combination with GAs," *Mechanical Systems and Signal Processing*, vol. 21, no. 5, pp. 2280–2294, 2007.
- [17] V. Sugumaran, V. Muralidharan, and K. I. Ramachandran, "Feature selection using Decision Tree and classification through Proximal Support Vector Machine for fault diagnostics of roller bearing," *Mechanical Systems and Signal Processing*, vol. 21, no. 2, pp. 930–942, 2007.
- [18] V. Sugumaran and K. I. Ramachandran, "Automatic rule learning using decision tree for fuzzy classifier in fault diagnosis of roller bearing," *Mechanical Systems and Signal Processing*, vol. 21, no. 5, pp. 2237–2247, 2007.
- [19] L. B. Jack and A. K. Nandi, "Fault detection using support vector machines and artificial neural networks, augmented by genetic algorithms," *Mechanical Systems and Signal Processing*, vol. 16, no. 2-3, pp. 373–390, 2002.
- [20] Z. Chen, Y. He, F. Chu, and J. Huang, "Evolutionary strategy for classification problems and its application in fault diagnostics," *Engineering Applications of Artificial Intelligence*, vol. 16, no. 1, pp. 31–38, 2003.
- [21] B. Samanta, K. R. Al-Balushi, and S. A. Al-Araimi, "Artificial neural networks and support vector machines with genetic algorithm for bearing fault detection," *Engineering Applications of Artificial Intelligence*, vol. 16, no. 7-8, pp. 657–665, 2003.
- [22] B. Samanta, "Gear fault detection using artificial neural networks and support vector machines with genetic algorithms," *Mechanical Systems and Signal Processing*, vol. 18, no. 3, pp. 625–644, 2004.
- [23] B. Samanta, K. R. Al-Balushi, and S. A. Al-Araimi, "Artificial neural networks and genetic algorithm for bearing fault detection," *Soft Computing*, vol. 10, no. 3, pp. 264–271, 2006.
- [24] B. Samanta and C. Nataraj, "Use of particle swarm optimization for machinery fault detection," *Engineering Applications of Artificial Intelligence*, vol. 22, no. 2, pp. 308–316, 2009.
- [25] M. Danubianu, S. G. Pentiu, and D. M. Danubianu, "Data dimensionality reduction for data mining: a combined filter-wrapper framework," *International Journal Of Computers Communications & Control*, vol. 7, no. 5, pp. 824–831, 2012.
- [26] J. M. Cadenas, M. C. Garrido, and R. Martínez, "Feature subset selection Filter-Wrapper based on low quality data," *Expert Systems with Applications*, vol. 40, no. 16, pp. 6241–6252, 2013.
- [27] C. Peng, M. H. Wang, Y. Shen, H. Q. Feng, and A. Li, "Reconstruction and analysis of transcription factor-miRNA co-regulatory feed-forward loops in human cancers using filter-wrapper feature selection," *PLoS ONE*, vol. 8, no. 10, Article ID e78197, 2013.
- [28] Z. Y. Hu, Y. K. Bao, T. Xiong, and R. Chiong, "Hybrid filter-wrapper feature selection for short-term load forecasting," *Engineering Applications of Artificial Intelligence*, vol. 40, pp. 17–27, 2015.
- [29] B. Li, P. Zhang, G. Ren, and Z. Xing, "A two stage feature selection method for gear fault diagnosis using relief and GA-wrapper," in *Proceedings of the International Conference on Measuring Technology and Mechatronics Automation (ICMTMA '09)*, pp. 578–581, Zhangjiajie, China, April 2009.
- [30] B. Li, P.-L. Zhang, H. Tian, S.-S. Mi, D.-S. Liu, and G.-Q. Ren, "A new feature extraction and selection scheme for hybrid fault diagnosis of gearbox," *Expert Systems with Applications*, vol. 38, no. 8, pp. 10000–10009, 2011.
- [31] D. D. Lee and H. S. Seung, "Learning the parts of objects by non-negative matrix factorization," *Nature*, vol. 401, no. 6755, pp. 788–791, 1999.
- [32] M. Sebban and R. Nock, "A hybrid filter/wrapper approach of feature selection using information theory," *Pattern Recognition*, vol. 35, no. 4, pp. 835–846, 2002.

- [33] Ö. Uncu and I. B. Türkşen, "A novel feature selection approach: combining feature wrappers and filters," *Information Sciences*, vol. 177, no. 2, pp. 449–466, 2007.
- [34] Z. Zhu, Y.-S. Ong, and M. Dash, "Wrapper-filter feature selection algorithm using a memetic framework," *IEEE Transactions on Systems, Man, and Cybernetics, Part B: Cybernetics*, vol. 37, no. 1, pp. 70–76, 2007.
- [35] M.-C. Lee, "Using support vector machine with a hybrid feature selection method to the stock trend prediction," *Expert Systems with Applications*, vol. 36, no. 8, pp. 10896–10904, 2009.
- [36] H. Peng, F. Long, and C. Ding, "Feature selection based on mutual information: criteria of max-dependency, max-relevance, and min-redundancy," *IEEE Transactions on Pattern Analysis and Machine Intelligence*, vol. 27, no. 8, pp. 1226–1238, 2005.
- [37] R. Kohavi and G. H. John, "Wrappers for feature subset selection," *Artificial Intelligence*, vol. 97, no. 1-2, pp. 273–324, 1997.
- [38] N. Srinivas and K. Deb, "Multiobjective optimization using nondominated sorting in genetic algorithms," *Evolutionary Computation*, vol. 2, no. 3, pp. 221–248, 1994.
- [39] K. Deb, A. Pratap, S. Agarwal, and T. Meyarivan, "A fast and elitist multiobjective genetic algorithm: NSGA-II," *IEEE Transactions on Evolutionary Computation*, vol. 6, no. 2, pp. 182–197, 2002.
- [40] L. B. Jack and A. K. Nandi, "Genetic algorithms for feature selection in machine condition monitoring with vibration signals," *IEE Proceedings: Vision, Image and Signal Processing*, vol. 147, no. 3, pp. 205–212, 2000.
- [41] P. J. Grother, G. T. Candela, and J. L. Blue, "Fast implementations of nearest neighbor classifiers," *Pattern Recognition*, vol. 30, no. 3, pp. 459–465, 1997.
- [42] R. R. Yager, "An extension of the naive Bayesian classifier," *Information Sciences*, vol. 176, no. 5, pp. 577–588, 2006.
- [43] J. A. K. Suykens and J. Vandewalle, "Least squares support vector machine classifiers," *Neural Processing Letters*, vol. 9, no. 3, pp. 293–300, 1999.
- [44] P. J. R. P. W. Duin, P. Paclik, E. Pekalska, D. de Ridder, D. M. J. Tax, and S. Verzakov, *PRTools4.1, A Matlab Toolbox for Pattern Recognition*, Delft University of Technology, Delft, The Netherlands, 2007.
- [45] LS-SVMLab1.5, <http://www.esat.kuleuven.ac.be/sista/lssvmlab/>.

Research Article

Vibration Suppression for Improving the Estimation of Kinematic Parameters on Industrial Robots

David Alejandro Elvira-Ortiz,¹ Rene de Jesus Romero-Troncoso,²
Arturo Yosimar Jaen-Cuellar,¹ Luis Morales-Velazquez,¹ and Roque Alfredo Osornio-Rios¹

¹CA Mecatronica, Facultad de Ingenieria, Universidad Autonoma de Queretaro, Campus San Juan del Rio, Rio Moctezuma 249, Colonia San Cayetano, 76807 San Juan del Rio, QRO, Mexico

²CA Procesamiento Digital de Señales, CA Telematica, Division de Ingenierias, Universidad de Guanajuato, Campus Irapuato-Salamanca, Carretera Salamanca-Valle km 3.5+1.8, Comunidad de Palo Blanco, 36700 Salamanca, GTO, Mexico

Correspondence should be addressed to Roque Alfredo Osornio-Rios; raosornio@hspdigital.org

Received 12 December 2015; Revised 28 February 2016; Accepted 6 March 2016

Academic Editor: Konstantinos N. Gyftakis

Copyright © 2016 David Alejandro Elvira-Ortiz et al. This is an open access article distributed under the Creative Commons Attribution License, which permits unrestricted use, distribution, and reproduction in any medium, provided the original work is properly cited.

Vibration is a phenomenon that is present on every industrial system such as CNC machines and industrial robots. Moreover, sensors used to estimate angular position of a joint in an industrial robot are severely affected by vibrations and lead to wrong estimations. This paper proposes a methodology for improving the estimation of kinematic parameters on industrial robots through a proper suppression of the vibration components present on signals acquired from two primary sensors: accelerometer and gyroscope. A Kalman filter is responsible for the filtering of spurious vibration. Additionally, a sensor fusion technique is used to merge information from both sensors and improve the results obtained using each sensor separately. The methodology is implemented in a proprietary hardware signal processor and tested in an ABB IRB 140 industrial robot, first by analyzing the motion profile of only one joint and then by estimating the path tracking of two welding tasks: one rectangular and another one circular. Results from this work prove that the sensor fusion technique accompanied by proper suppression of vibrations delivers better estimation than other proposed techniques.

1. Introduction

Industry tries to automate most of its processes as part of an update that is focused on improving quality standards. This is done by developing tasks in which a robotic system can directly supervise that the process is taking out properly and correcting the problems that may arise along the way. High-precision and high-accuracy in robotics require the study of robot kinematics, dynamics, and control [1]. Forward kinematics is generally used to compute the position and orientation of the robot end-effector as a function of the angular position at each joint [2]. Through this forward kinematics it is possible to identify error parameters by measuring the complete pose of the robot end-effector [3]. Industrial robots are used in several tasks like pick-and-place, painting, welding, and machining operations, where

high positioning accuracy is required [4]. However, there are several factors that can affect the proper performance of a robotic manipulator, for example, resolution of the sensors, computer round-off, and one of the most important: vibration [5]. In this sense, it becomes relevant to develop methodologies that allow carrying out proper and reliable measurements by suppressing some error factors present on signals. Besides, all measurements from sensors are contaminated with noise. Noisy measurements are not desirable on the estimation of kinematic parameters because wrong values on the signal produce wrong estimations.

The estimation of kinematic parameters in industrial robots has been widely studied. There are many works focused on the improvement of the measurement of the pose of the manipulator end-effector. Artificial vision is one of the most common techniques used for this task

[6, 7]. One of the advantages of this technique is that it is a noninvasive system. However, this methodology requires much signal processing, and as the images are acquired in 2D, many assumptions must be done in order to obtain spatial information, which affects the accuracy in the estimation. Laser tracking is another technology that has been recently used to know the configuration of an industrial robot [5, 8]. Yet, it requires a device to be placed on the robot end-effector, so the dimensions of this device introduce an error factor. The solutions mentioned so far use only one sensor. On the other hand, sensor fusion is being used to obtain more accurate results because it tries to compensate for the problems and mistakes from a single sensor with the information provided by different sensors [2, 9–11]. Although all these techniques yield favorable results, they still can be improved. Good noise suppression leads into obtaining better accuracy in the estimation of kinematic parameters in industrial robots, where the acquired signals can be processed to fix some troubles due to manufacturing errors or some other undesired interferences such as vibrations.

Current researches reported in literature point out that the encoder in servomotors and the accelerometer are two of the most widely used sensors for monitoring motion dynamics and vibrations on computerized numeric control (CNC) machines and robotic manipulator arms [9]. The accelerometer is used to measure the inclination or angular position of several CNC and robotics systems [2, 9–13]. Nevertheless, accelerometers have been also used for monitoring vibrations in many structures like bridges [14], washing machines [15], CNC machines [16], and industrial robots [9]. The output signal of an accelerometer contains merged information from both, inclination with respect to gravity and vibrations; therefore, a separation of these parameters is desirable for further kinematics and vibration monitoring. Great effort has been done trying to suppress vibrations and noise components from the inclination signals in an accelerometer. In [17], a methodology using a classical linear filter and an orthogonal decomposition is presented. This methodology delivers good noise suppression but it introduces much delay to the system. The use of finite impulse response (FIR) filters [18] and infinite impulse response (IIR) filters [19] is well studied too for this application. The problem when using FIR filters is that it is common that a high order of the filter is required to obtain satisfactory results. This is translated in a high computational cost that turns the system slow. On the other hand, IIR filters generally produce phase distortion; that is, the phase is not linear with frequency. Moreover, IIR filters are prone to instabilities when implemented. In [20] the noise reduction is carried out by using genetic algorithms and wavelet decomposition. This is a novel technique but the mathematical analysis is quite complex and requires much computational effort, so the implementation for online applications is seriously compromised. Another very useful technique for noise reduction is the Kalman filter (KF). The popularity of KF rests in its capability for reducing errors in a least square sense [21]. According to [22] KF has many applications and among the most important are sensorless control, diagnosis, and fault-tolerant control of ac drives; distributed generation and storage systems; robotics,

vision, and sensor fusion techniques; applications in signal processing and instrumentation and real-time implementation of KF for industrial control systems. In this sense, KF represents one of the best options for vibration suppression on accelerometer signals.

As it can be seen from the aforementioned research works, many of them are focused on the estimation of kinematic parameters. In order to obtain a reliable estimation of these kinematic parameters, it is important to provide the system with a filtering stage for noise and undesired vibration suppression. The developed methodologies so far offer a good estimation of parameters such as angular position, velocity, and acceleration; nevertheless, the reported stages for noise and undesired vibration reduction require high computational effort, which is a major disadvantage for online applications. Additionally, most of the methodologies use only one sensor for estimating kinematic parameters so the limitations of the sensor are also limitations of the methodology.

The main contribution of this work is the vibration suppression using a KF to improve the accuracy on the estimation of industrial robot dynamics; the use of KF provides a technique that does not require high computational effort so the developed methodology can easily work for online applications. Moreover, the sensor fusion of accelerometer and gyroscope improves the results delivered by each sensor separately. This paper proposes a methodology to acquire signals from an accelerometer and a gyroscope; these signals contain information of the motion profile of every axis of the robot merged with noise due to vibration, which is attenuated by a KF. Another KF is used for signal fusion of both, accelerometer and gyroscope. Several study cases are developed to prove the efficiency of the methodology. First, the motion profile of only one link of the manipulator is studied; then, the industrial robot is programmed to perform a circular welding task and a rectangular welding task. The trajectory of the industrial robot is monitored to determine the motion error. A comparison of the results with the vibration components and without them is presented to prove that the results from the proposed methodology improve those results obtained from other reported methodologies. The proposed methodology is implemented in a Field Programmable Gate Array (FPGA) to obtain a hardware signal processor allowing a fast and reliable online system. The proposed methodology is implemented on an ABB IRB 140 industrial robot to prove its efficiency.

2. Theoretical Background

This section establishes the relationship between the estimated parameters and robot dynamics, where the accelerometer provides information about acceleration of an axis of the robot relative to gravity, while the gyroscope does the same but with the angular velocity.

2.1. Robot Kinematics. The parameters that describe the architecture of the industrial robot ABB IRB 140 [23] are shown in Figure 1, where x_i , y_i , and z_i are the axis name of

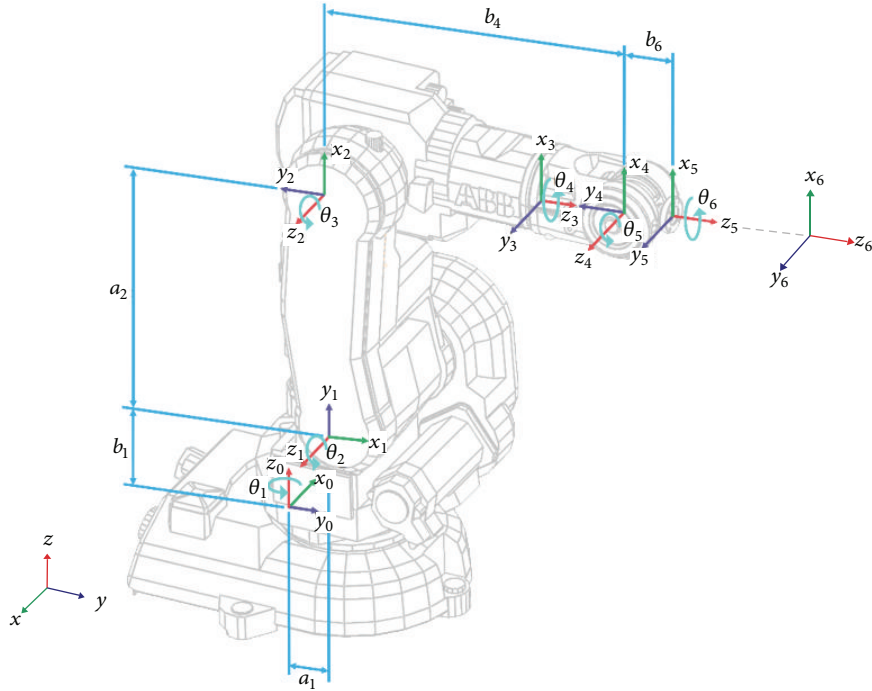


FIGURE 1: Architecture of the industrial robot ABB IRB 140.

TABLE 1: D-H parameters for the robot.

Joint i	a_i	b_i	α_i	θ_i
1	70	352	$-\pi/2$	θ_1
2	360	0	0	$\theta_2 - \pi/2$
3	0	0	$\pi/2$	$\theta_3 + \pi$
4	0	380	$-\pi/2$	θ_4
5	0	0	$\pi/2$	θ_5
6	0	65	$\pi/2$	$\theta_6 - \pi/2$

each joint, a_i is the distance between the axes z_i and z_{i+1} , and b_i is an offset measured along previous z_{i-1} to the common normal. From the diagram, the Denavit-Hartenberg (D-H) parameters are calculated and summarized in Table 1 where α_i is the angle between z_{i-1} and z_i and θ_i is the angle between x_{i-1} and x_i and denotes the rotation of the joint along the z_{i-1} axis, so it is the angular position of each joint.

The proposed system is able to obtain two measurements of the angular position of each joint, except for the first joint, where the movement is always perpendicular to gravity force, so an accelerometer cannot detect changes in this joint and only the data from the gyroscope is used. However, neither the accelerometer nor the gyroscope delivers information of the angular position directly, so it is necessary to process the signals to obtain a value for the current angular position.

2.1.1. Forward Kinematics. Forward kinematics provides the position and orientation (roll, pitch, and yaw) of the robot through the angular position of each joint. In this case, the forward kinematics is calculated through the standard

Denavit-Hartenberg notation. The notation is a transformation matrix T_i^0 relating the reference coordinate frame (X_0, Y_0, Z_0) with the coordinate frame of the joint (X_i, Y_i, Z_i). The notation requires obtaining the link parameters of the robot. Those parameters are the link length (a_i), the link twist (α_i), the joint distance (b_i), and the joint angle (θ_i) [23]. The mentioned parameters are summarized in Table 1. Those parameters are used to estimate the transformation matrix T_i^0 presented in

$$T_i^0 = \begin{bmatrix} M_i & d_i \\ 0 & 1 \end{bmatrix}, \quad (1)$$

where M_i (see (2)) contains the rotation information and d_i is a vector containing the position of the link i (see (3)):

$$M_i = \begin{bmatrix} m_{i,1,1} & m_{i,1,2} & m_{i,1,3} \\ m_{i,2,1} & m_{i,2,2} & m_{i,2,3} \\ m_{i,3,1} & m_{i,3,2} & m_{i,3,3} \end{bmatrix} \quad (2)$$

$$d_i = \begin{bmatrix} X_i \\ Y_i \\ Z_i \end{bmatrix}. \quad (3)$$

Therefore, forward kinematics can be calculated using (2) and (3). Position is directly estimated through (3). Orientation

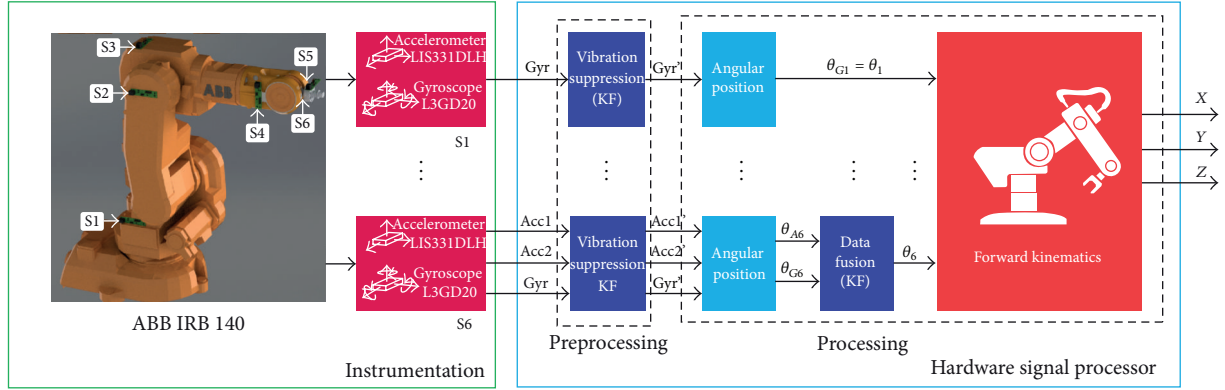


FIGURE 2: Methodology.

can be estimated using (4) to (6), where θ_i , β_i , and γ_i are the rotations along X_0 , Y_0 , and Z_0 axis, respectively:

$$\theta_i = \tan^{-1} \left(\frac{\sqrt{1 - m_{i,3,1}^2 - m_{i,3,3}^2}}{m_{i,3,3}} \right) \quad (4)$$

$$\beta_i = \tan^{-1} \left(-\frac{m_{i,3,1}}{\sqrt{1 - m_{i,3,1}^2}} \right) \quad (5)$$

$$\gamma_i = \tan^{-1} \left(\frac{\sqrt{1 - m_{i,3,1}^2 - m_{i,1,1}^2}}{m_{i,1,1}} \right). \quad (6)$$

2.2. Joint Angular Position. The joint angular position is calculated with both gyroscope and accelerometer sensors. Afterwards, the obtained information is fused through a Kalman filter. In the case of the gyroscopes, the angular joint position θ_{Gi} can be calculated using (7), where ω_i is the current measure from the gyroscope, S is the minimum value that can be measured with the gyroscope, and T is the sample period of the signal:

$$\theta_{Gi} = \theta_{G(i-1)} + \omega_i ST. \quad (7)$$

Concerning the estimation of the angular joint position using accelerometers (θ_{Ai}), the corresponding equations are summarized in Table 2. Such equations assume that the accelerometers provide a noise-free signal, which is unrealistic; thus, the signal requires a filtering stage before being used.

2.3. Kalman Filter. KF is a filter that is based on the use of stochastic variables for estimating the feedback gain K . The tasks in which it is used are many and varied. Its stochastic nature makes it very useful for working with noise suppression and system identification and even to fuse signals online. A Kalman filter works similarly to a feedback controller; the filter estimates the next state of the signal (predict) and then it obtains feedback in the form of

noisy measurements to modify the predicted state (correct). General equations for the “predict” stage are presented in

$$\begin{aligned} X_k^* &= SX_{k-1} + Bu_{k-1} \\ P_k^* &= SP_{k-1}S^T + Q, \end{aligned} \quad (8)$$

where S matrix relates the previous state X_{k-1} and the estimated current state X_k^* , u is an optional control input, and B defines the relation between u and X_k^* . Q is the signal covariance and P_k^* is the a priori estimated error covariance.

In the case of the “correct” stage, the required equations are summarized in (9), where R is the measurement noise covariance, H relates the measurements (Z_k) with the current state X_k , K_k is a gain factor that minimizes the a posteriori estimated error covariance (P_k), and I is the identity matrix:

$$\begin{aligned} K_k &= P_k^* H^T (HP_k^* H^T + R)^{-1} \\ X_k &= X_k^* + K_k (Z - HX_k^*) \\ P_k &= (I - K_k H) P_k^*. \end{aligned} \quad (9)$$

3. Methodology

A general diagram of the methodology is presented in Figure 2. The methodology is summarized in five stages: instrumentation and data acquisition system; vibration suppression that is the main module of this methodology and makes the difference between having good and accurate results or not; angular position estimation; data fusion and forward kinematics. Generally, the methodology is described as follows: 6 gyroscopes and 5 accelerometers are placed on the robot, signals from the sensors are acquired with an FPGA-based data acquisition system, and then the signals are filtered to suppress the vibration present on the signals; next, two angular positions for each joint are estimated: one from the accelerometer signals and another one from the gyroscope signals. The next step is the fusion of the two angular position signals for each link so only one signal is obtained for each link. Finally, the six angular positions are taken to estimate the position of the robot end-effector by its forward kinematics. So the system delivers three outputs

TABLE 2: Equations to estimate the angular position of each joint using accelerometers.

Joint i	Equation
1	—
2	$\theta_{A2} = \left(\tan^{-1} \frac{A_x}{A_y} \right) - 90^\circ$
3	$\theta_{A3} = \tan^{-1} \frac{A_y}{A_z}$
4	$\theta_{A4} = \left(\tan^{-1} \frac{A_y}{A_z} \right) - 90^\circ$
5	$\theta_{A5} = \left(\tan^{-1} \frac{A_y}{A_z} \right) + 90^\circ$
6	$\theta_{A6} = \tan^{-1} \frac{A_x}{A_z}$

X, Y, and Z that are the coordinates of the robot position. The data acquisition system and in general all the processing for this methodology are implemented in a hardware signal processor, which is a proprietary FPGA-based system, allowing implementing this methodology online. It is important to mention that KF is used for both, vibration suppression and data fusion. Nevertheless, two KF are used, one for vibration suppression and another one for data fusion. Although both are KF, the parameters of each one are different for every stage; that is why it is necessary to use two different KF. Following subsections describe each stage in detail.

3.1. Instrumentation. The use of accelerometers and gyroscopes on ABB IRB 140 robot requires placing them adequately in specific positions. The instrumentation of the robot consists of 5 triaxial accelerometers and 6 triaxial gyroscopes. In the case of gyroscopes only one axis per sensor is utilized. For the accelerometers two axes per sensor are used as can be seen in Table 2. Also, there is no accelerometer in joint 1 since in its case it does not provide information about the angular position. Therefore, the system has to filter and fuse the information from 16 sensor measurements. The data acquisition system (DAS) is FPGA-based. Data from sensors are acquired and stored in this DAS; then they can be sent to a personal computer or remain in the DAS to be processed.

3.2. Vibration Suppression. Since signals from accelerometers have merged information of vibration and inclination, it is necessary to eliminate the vibration components in order to correctly estimate the angular position of every link of the robot. Moreover, gyroscopes are not exempt from noise coming from the vibration, so every signal must be properly filtered before being used. KF is used for this purpose. For designing the filter, (8) to (9) are used. Concerning the vibration suppression stage, matrix S is an identity matrix; $B = 0$; $X = [A_{(i-1)X}^*, A_{(i-1)Y}^*, A_{(i-1)Z}^*]^T$ for accelerometers and $X = [V_{(i-1)}^*]^T$ for gyroscopes; $Z = [A_{(i-1)X}, A_{(i-1)Y}, A_{(i-1)Z}]^T$ for accelerometers and $Z = [V_{(i-1)}]^T$ for gyroscopes; Q is a diagonal matrix containing the covariance of each signal; likewise, R is a diagonal matrix with the noise covariance of each signal and H is an identity matrix. The correct

TABLE 3: Gyroscope axis used for estimating angular position.

Robot link	Gyroscope axis
1	Y
2	Z
3	Y
4	Y
5	Y
6	X

use of KF allows good vibration suppression. This vibration suppression is the key for having a good performance of the methodology, because the sensor fusion is fully exploited when the signals are properly filtered.

3.3. Angular Position Estimation. Once the signals are filtered to remove the vibration present on them, the angular position of the link is estimated using both, accelerometer and gyroscope. Since the gyroscope is a sensor that originally yields signals measuring angular velocity, it can be easily inferred that an integration must be done for obtaining the angular position from the data collected from this sensor. This integration is presented in (7). Concerning the gyroscope, the estimation of the angular position is carried out following the diagram shown in Figure 3. Gyroscope measurements are equal to zero when it is static, so it is necessary to establish an initial condition. In this particular case the initial condition is the first instantaneous measurement of the angular position from the accelerometer. It is noteworthy that this digital integration introduces a cumulative error in each iteration. This error is known as “drift.” The sensor fusion is intended to reduce such errors. For calculating the position with the gyroscope, the first step is to receive the input signal ω , which is the gyroscope signal after being filtered. The position value is initialized on a “init” value, (7) is applied, and an instantaneous value of angular position is obtained. If the task has already been completed, the final position signal is delivered; otherwise the process is repeated until the task is finished.

As the accelerometer is not used in axis 1, the initial position value for this axis must be taken from the robot controller. As mentioned, each sensor is triaxial, but for purposes of this work, only one axis of each gyroscope is used. Table 3 shows the relation of the axes of each gyroscope used for the estimation of the angular position.

To estimate the angular position of each link with the accelerometer, the vector components of the acceleration are used according to Table 2. The process to estimate the angular position with this sensor is very similar to the previous one shown in Figure 3. The first step is to receive the input signals from the accelerometer; the signal must be filtered before being used for estimating the angular position. The corresponding equation from Table 2 is applied and an instantaneous value of the angular position is estimated. If the task has already been completed the final position signal is delivered; otherwise the process is repeated until the task

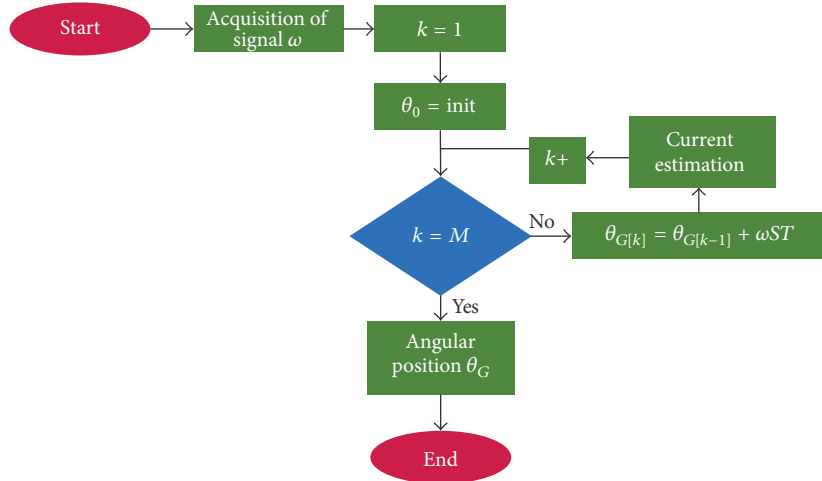


FIGURE 3: Angular position estimation with gyroscope.

is finished. It is necessary to remember that only two signals per accelerometer are used in this step.

3.4. Data Fusion. As aforementioned, KF can also be used for fusing signals. In this paper KF is used for this purpose because it can predict the future value of the signal with less delay than other filters. In this stage Kalman filter is designed for the sensor fusion of two signals; in this case the parameters of the general equations (8) to (9) are $S = 1$; $B = 0$; $X = \theta_i^*$; $Z = [\theta_{Ai}, \theta_{Gi}]^T$; Q is the covariance of the angular position; R is a diagonal matrix with the noise covariance of each input signal; and $H = [1, 1]^T$. To implement this filter, it is necessary to follow the diagram of Figure 3 but using the parameters described in this section.

3.5. Forward Kinematics Estimation. The forward kinematics is the last stage of this methodology. Through forward kinematics the position of the robot end-effector can be estimated. Figure 4 shows the process necessary to obtain this position. The signal θ_i of each link must be known. Once the angular position of the six axes is acquired, the transformation matrix T_0^6 is calculated. From this matrix the vector d_6 , containing the position of the robot end-effector, is obtained to give a current estimation; if the task has already been completed the final position signal is delivered; otherwise the process is repeated until the task is finished.

4. Experimental Setup

Figure 5 shows the experimental setup of this work. It consists of an ABB IRB-140 robot instrumented with accelerometers and gyroscopes. The desired trajectory is programed on the robot through the controller provided by the manufacturer. Both sensors, accelerometer and gyroscope, are mounted on a proprietary board, which sends the information via RS-485 protocol to the data acquisition system. All the signal processing is carried out using a proprietary FPGA-based hardware signal processor. It contains an FPGA SPARTAN-3E-1600; a

static Random Access Memory (RAM) IS61LV5128AL with capacity of 4 Mb and a dynamic RAM MT48LC16M16A2 of 256 Mb. So this system allows acquiring and storing the data to process them either online or offline. In order to validate the proposed measurement system two welding paths are performed in the robot since they are repetitive tasks commonly used in the industry. During the robot operation the set of sensors are monitored and sent to a hardware signal processor for their treatment. The information is sent to a PC for display and validation purposes.

4.1. Sensor Characteristics. The sensor characteristics are summarized in Table 4. Both sensors, the accelerometer and the gyroscope, provide the information in digital format.

4.2. Calibration. All sensors and the hardware signal processor are properly calibrated to validate the methodology proposed in this paper. The manufacturer calibrated the sensors and the parameters of that calibration appear on the data sheet of the accelerometer [24] and gyroscope [25], respectively. Some sensors required a correction factor because of the architecture of the robot. Figure 6 shows the home position of the robot and according to the robot controller, for this configuration, the angular position of every link must be zero. Nevertheless, due to the positioning of the sensors these values do not correspond to the expected values. Therefore, it was necessary to add the correction factors shown in Table 2 for correcting the values delivered by each accelerometer. For gyroscopes, this calibration was not necessary since they are initialized with the first value acquired by the accelerometer.

For the hardware signal processor, a calibration process as the one presented for the accelerometers is carried out. In this case, the correction factors are those due to the Denavit-Hartenberg parameters of the manipulator. From Table 1 it can be inferred that the values of θ_2 , θ_3 , and θ_6 must be corrected to obtain the expected results.

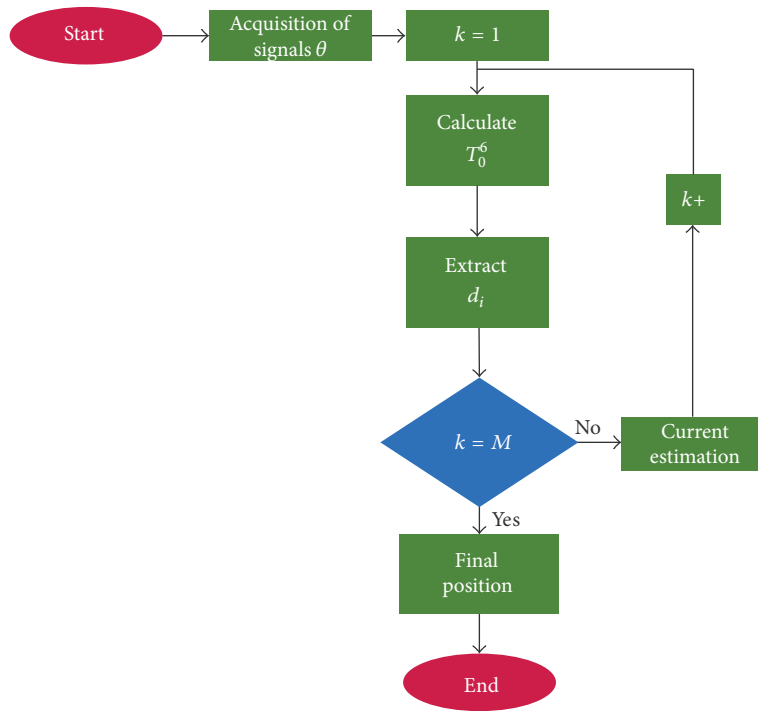


FIGURE 4: Forward kinematics estimation.

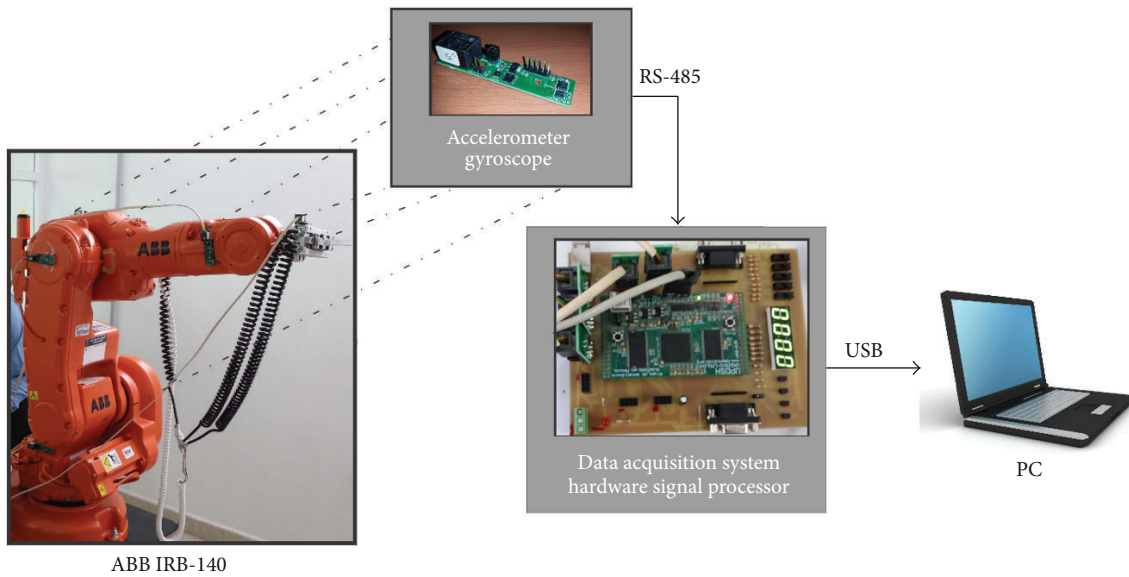


FIGURE 5: Experimental setup.

TABLE 4: Sensor characteristics.

Sensor	Description	Features
Accelerometer	LIS331DLH	Digital three-axis accelerometer, up to 1000 Hz user selectable bandwidth, user selectable scale of $\pm 2.0\text{ g}/4.0\text{ g}/8.0\text{ g}$ ($g = 9.81\text{ m/s}^2$), a 16-bit rate value data output, 1 mg/digit sensitivity, and communication protocol I2C and SPI.
Gyroscope	L3GD20	Digital three-axis gyroscope, up to 760 Hz user selectable bandwidth, user selectable scale of $\pm 250/500/2000\text{ dps}$, a 16-bit rate value data output, 8.75 mdps/digit sensitivity, and communication protocol I2C and SPI.

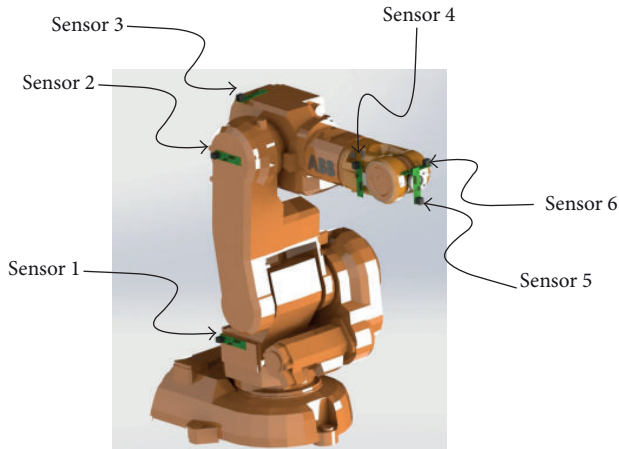


FIGURE 6: ABB IRB 140 home position.

Additionally, a kinematic calibration process is performed. This calibration process allows ensuring that the measurement and results are not affected by mechanical parameters of the robot such as flexion on the joints and links. For this work the recursive least square (RLS) algorithm is proposed. The principle of least squares states that the unknown parameters of a mathematical model must be calculated so that the overall solution minimizes the sum of the squares of the errors made in the results of every single equation.

5. Results and Discussion

Figure 7(a) shows the raw signal for one axis of one of the accelerometers. The motion profile can be easily seen. Nevertheless, it is clear that the signal contains noise. This noise is due to the vibration present on the robot and it affects the right estimation of the angular position on every axis. Figure 7(b) shows the spectrogram of the raw signal from the sensor. In this figure, the motion profile is clearly distinguished as a DC component, but also the components due to spurious vibration appear. Figure 7(b) shows that the vibration motion profile and spurious vibrations are in different frequency bands; that is why it is inferred that noise due to vibration can be reduced using the proper filter. Figure 7(c) presents a zoom to the vibration zone marked as 1 in Figure 7(b). In this zone it is possible to see that for the time between 2 and 6 seconds there are vibration components in the band from 10 to 20 Hz and the amplitude of these components is up to -40 dB. Looking at the time that the mentioned components appear, it can be inferred that these vibrations are due to the start of the motion, because the robot motors need a great effort to change the manipulator from rest to motion. On the other hand, Figures 7(d) and 7(e) show the time between 26 and 28 seconds. For this period there are vibrations comprised in two different bandwidths. Figure 7(d) shows that there are peaks of vibration in the band from 0 to 15 Hz with an amplitude of -30 dB, whereas Figure 7(e) shows that there is also vibration of high amplitude (up to -46 dB) at the

frequencies between 50 and 60 Hz. These components appear at the end of the motion task, so it can be assumed that they are due to the inertia needed to stop the manipulator. Some other components of vibration appear in Figure 7(b); these components are also comprised in frequencies lower than 25 Hz and they can be attributed to the changes on the direction followed by the robot. However, the amplitude is not as high as that amplitude present on the analyzed zones.

Conversely, Figure 8 shows the same signal of Figure 7 but after applying the filter. The motion profile in Figure 8(a) looks smoother than the one in Figure 7(a), proving that the filter really works and helps to diminish the vibration components present on the signal. Figure 8(b) shows the spectrogram of the signal after being filtered. Once again the motion profile appears as a DC component on the figure, while the noise appears spread on other frequencies. However, this time the zones presenting noise due to vibration are less than those in Figure 7(b), and also the amplitude of the components of vibration is higher in Figure 7(b) than in Figure 8(b), because of the filtering stage for reducing the spurious vibration levels; after this filtering stage, the acceleration signal presents some marginal spurious vibration in one zone. This zone is between 26 and 28 seconds at the bandwidth from 0 to 15 Hz, but the amplitude is highly attenuated when compared to the unfiltered signal. The zone described is the same marked as 2 in Figure 7(b), so Figure 8(c) presents a zoom of that zone but after applying KF. It is clear that the remaining spurious vibrations are greatly attenuated by the KF, highlighting the efficiency of the filtering stage. The amplitude of the vibration is reduced from -30 to -45 dB, which is a noticeable reduction. The other two zones that presented important levels of vibration before filtering are also marked in Figure 8(b), but now there are no visible spurious vibrations remaining on these zones, meaning that they are attenuated to levels below the background noise.

To have a better indicator on how the vibration signal is attenuated by the KF, Figure 9 shows the vibration levels extracted from the original signal of the accelerometer before and after the filtering stage. The signals used in the comparison are the same that are shown in Figures 7(a) and 8(a). The vibration level is obtained experimentally by using a high-pass IIR filter. It is important to mention that this filter is used only to show the magnitude of the vibration present in the acquired signals but it is not a part of the proposed methodology. Figure 9 corroborates the fact that the highest levels of vibration are present at the beginning and at the end of the task, and it is remarkable that the levels of vibration are almost imperceptible after applying the KF, indicating the right operation of the filtering stage.

The same analysis is performed to every link of the robot and for each axis of the sensor. Table 5 summarizes the extracted parameters. This table contains the peak amplitude, the mean value, and the RMS value of the vibrations. The KF clearly diminishes the peak values of the vibrations. The maximum amplitude of the vibration is high for some links (above 1g) without filtering. These peak values introduce high errors when estimating angular position so it is of great importance to suppress them. In addition, the RMS value is considerably lower after filtering; this RMS value

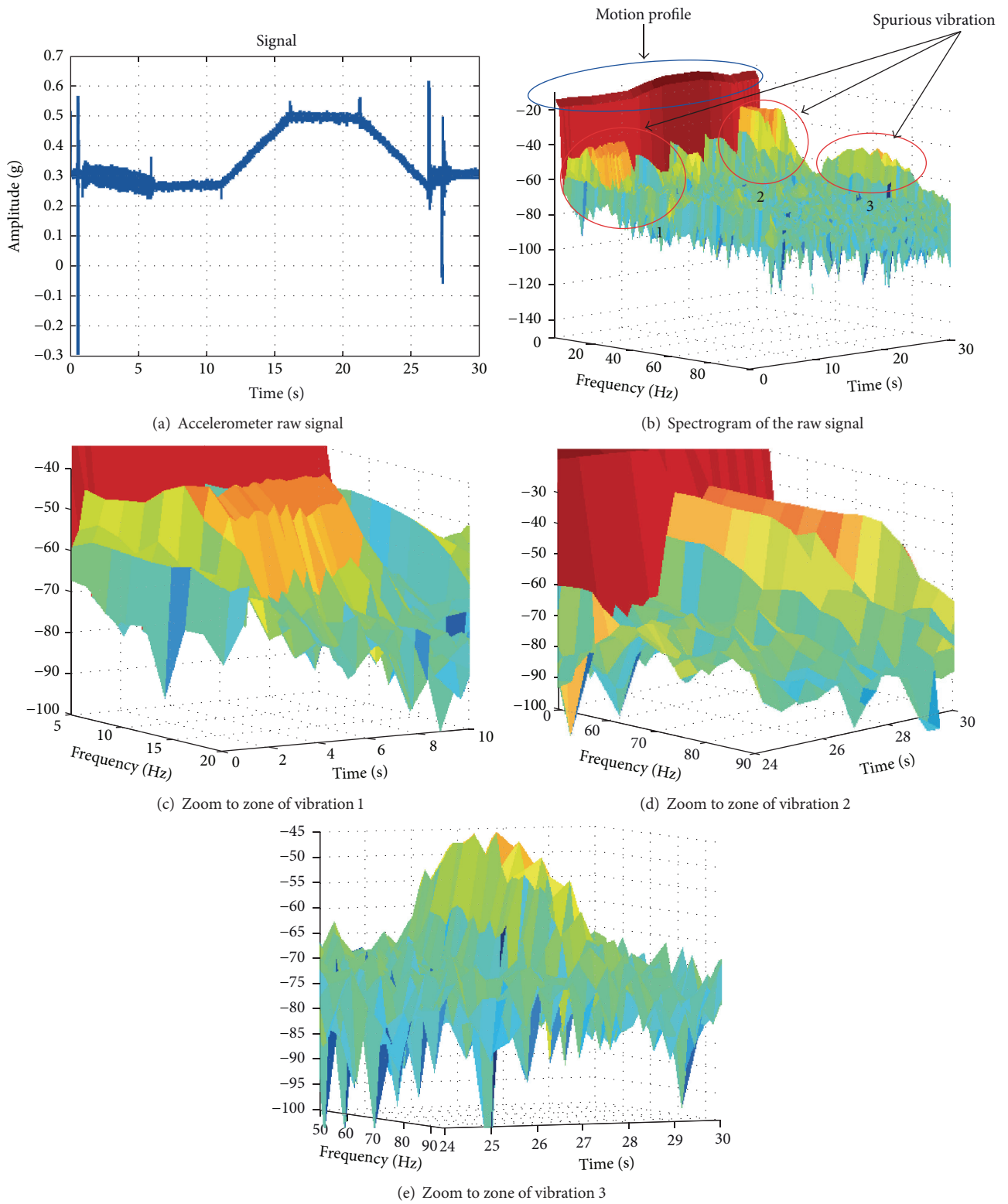


FIGURE 7: One axis motion profile with noise due to vibration.

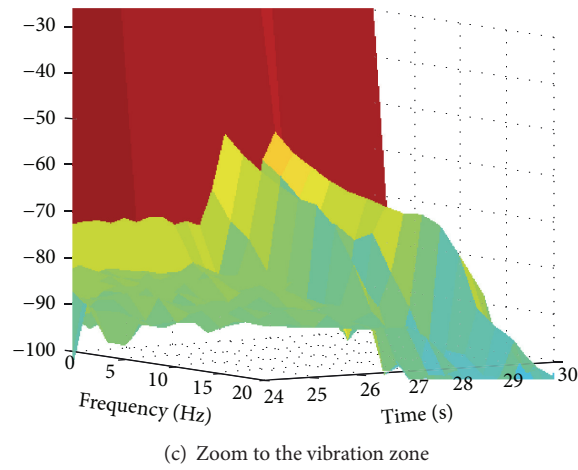
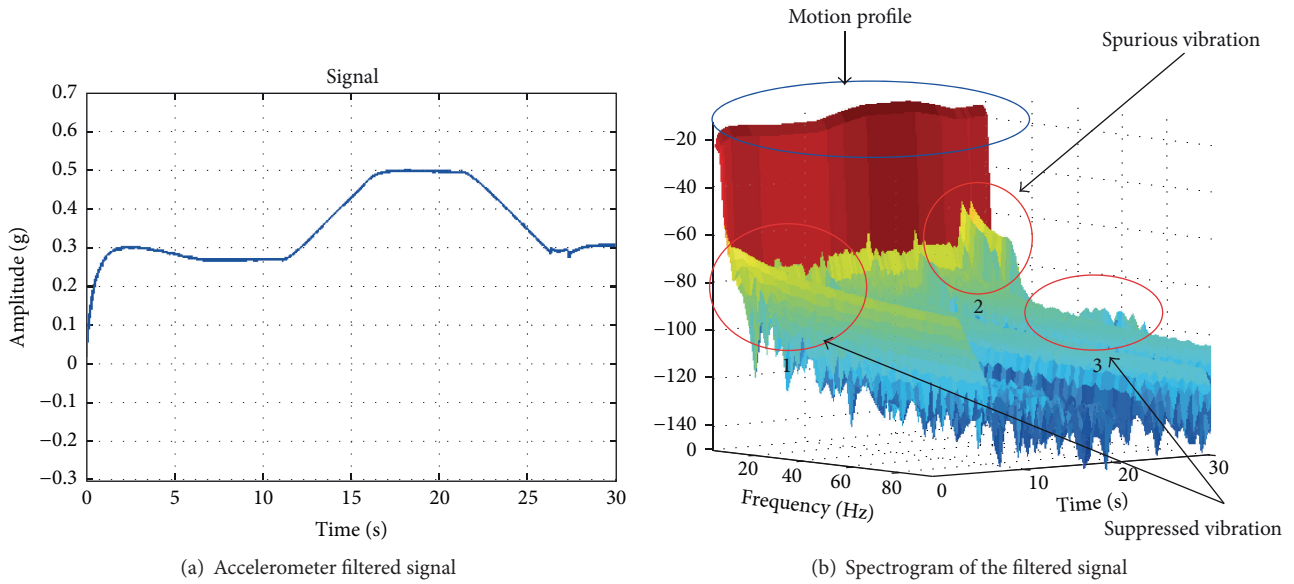


FIGURE 8: One axis motion profile without noise due to vibration.

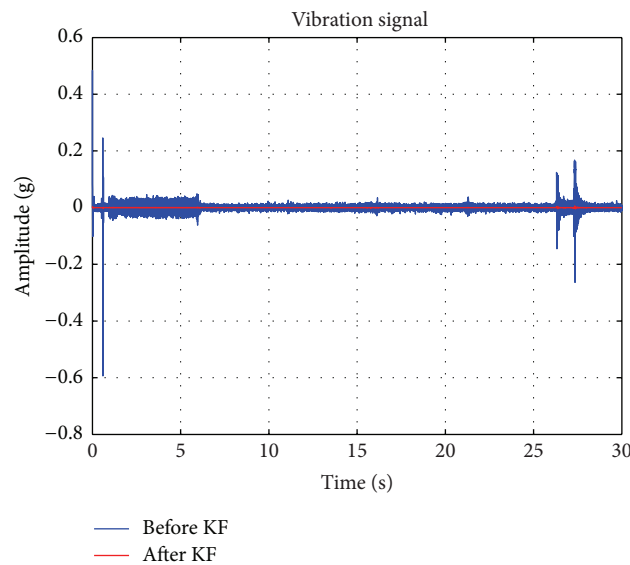


FIGURE 9: Comparison of the vibration levels before and after the KF from the acceleration signal.

TABLE 5: Analysis of the vibration parameters on each robot link.

Robot link	Sensor axis	Vibration level (g) $1\text{ g} = 9.81\text{ m/s}^2$					
		Before KF	After KF	Before KF	After KF	Before KF	After KF
		Peak	Mean	RMS	Peak	Mean	RMS
1	<i>x</i>	0.2571	6.61×10^{-5}	0.9799	0.0030	1.94×10^{-6}	0.0052
	<i>y</i>	0.5154	5.98×10^{-6}	0.3129	0.0060	-3.36×10^{-7}	0.0028
	<i>z</i>	0.2057	4.38×10^{-6}	0.5902	0.0017	2.90×10^{-7}	0.0036
2	<i>x</i>	0.9713	-4.53×10^{-7}	0.0150	0.0099	4.61×10^{-6}	0.0003
	<i>y</i>	1.6390	-6.34×10^{-7}	0.0178	0.0054	-2.78×10^{-9}	0.0003
	<i>z</i>	0.4696	5.86×10^{-7}	0.0087	0.0009	1.03×10^{-8}	0.0001
3	<i>x</i>	0.6392	3.63×10^{-7}	0.0940	0.0018	2.30×10^{-8}	0.0001
	<i>y</i>	0.5938	-1.32×10^{-7}	0.0152	0.0057	-2.19×10^{-8}	0.0003
	<i>z</i>	1.6423	-2.46×10^{-8}	0.0198	0.0100	-4.88×10^{-9}	0.0003
4	<i>x</i>	1.6434	-2.10×10^{-7}	0.0170	0.0051	2.71×10^{-9}	0.0003
	<i>y</i>	0.9624	9.98×10^{-8}	0.0189	0.0093	1.99×10^{-8}	0.0003
	<i>z</i>	0.2382	-1.52×10^{-7}	0.0096	0.0013	4.68×10^{-9}	0.0001
5	<i>x</i>	0.2733	8.15×10^{-8}	0.0140	0.0051	5.52×10^{-9}	0.0002
	<i>y</i>	0.3477	-3.29×10^{-7}	0.0183	0.0018	-1.80×10^{-9}	0.0002
	<i>z</i>	1.0015	-1.86×10^{-6}	0.0260	0.0120	-2.20×10^{-8}	0.0004
6	<i>x</i>	0.4371	3.71×10^{-8}	0.0150	0.0063	3.47×10^{-9}	0.0002
	<i>y</i>	0.4735	6.89×10^{-8}	0.0163	0.0015	1.78×10^{-9}	0.0002
	<i>z</i>	0.5328	2.37×10^{-7}	0.0230	0.0032	2.23×10^{-9}	0.0003

represents the deviation level of the vibrations from the mean and consequently, reducing the RMS value lowers the error introduced in the following processing stages.

A more complex and detailed analysis of the modes of vibration and the frequencies presented on each mode was carried out in [26] for a structure very similar to the one used for this methodology. Since both mechanisms are similar, the behavior of them is expected to be similar too. However, an analysis as complex as the aforementioned is left for future research.

For the gyroscope, Figure 10 shows the signal before and after applying the filter to suppress the vibration. It is easy to see that, before the filter, the signal contains noise and the information about the motion profile of the joint of the robot is not accurate. After applying the filter, the motion profile appears and the noise on the signal is greatly reduced.

As aforementioned, to prevent errors due to mechanical parameters of the manipulator, the RLS method is applied for calibration of the robot kinematic parameters. The first study case is a rectangular welding task. The tracking of the rectangular welding task without filtering the components of spurious vibration is shown in Figure 11(a). When trying to estimate the trajectory for this task, without filtering the components of vibration merged on data from sensors, the path estimated presents fluctuations and there are zones where the estimated value is far from the desired value. Furthermore, it is very notorious that the task starts and ends in different positions, which is not correct. This is a very inaccurate estimation, and any decision based on these results may not be correct. After applying the filter to suppress the vibration, the estimation of the trajectory is greatly improved (see Figure 11(b)). Now the estimated values are not so far

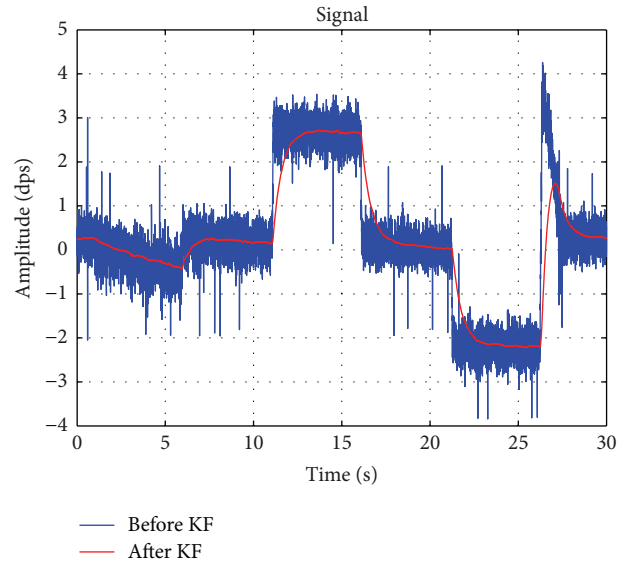


FIGURE 10: Signals from gyroscope before and after KF.

from the expected. The tracking of the path is smoother than when not applying the filter; there are still areas where the path does not match the expected but this is less marked than in previous case. In addition, it is easy to see that when the vibration is suppressed the trajectory starts and ends in the same position. These results clearly show the effect of vibration when trying to estimate the position of an industrial robot.

The second study case is a circular welding task. For this case there are also two different situations: the first one is

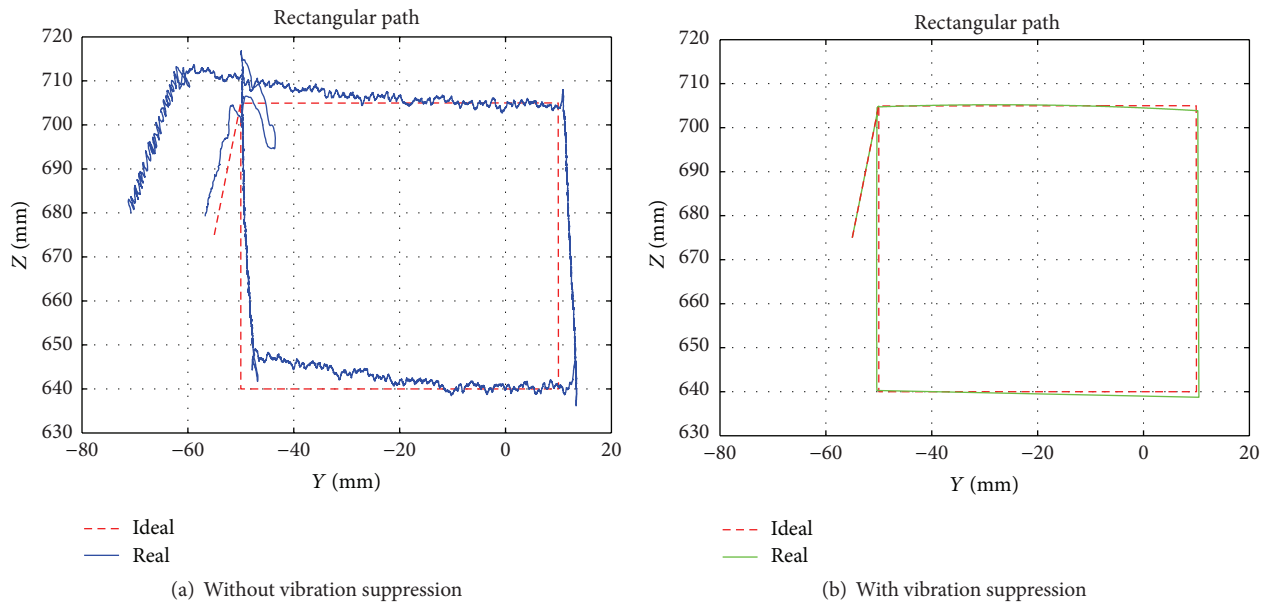


FIGURE 11: Tracking of the rectangular welding task.

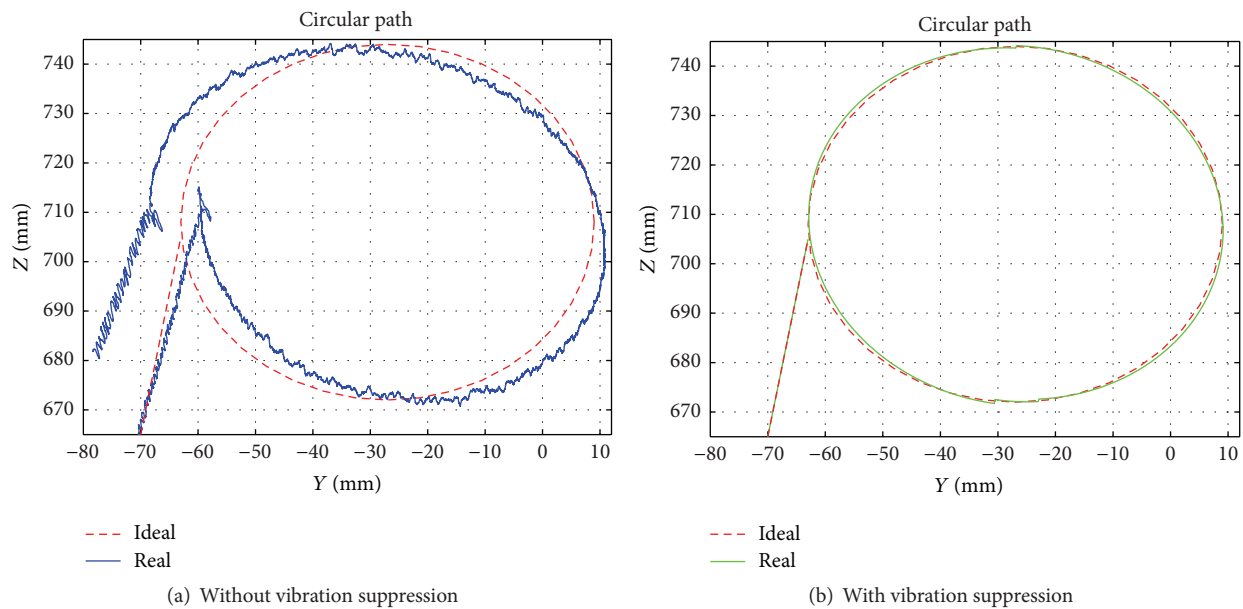


FIGURE 12: Tracking of circular welding task.

when the estimation of the trajectory is carried out with the data contaminated with spurious vibration and the second when the filter is used to diminish the noise present on the signals from sensors. In the case of circular welding task, the effect of vibrations is even more notorious than in the rectangular one (Figure 12(a)). The trajectory presents more fluctuations and the estimated values are further from the expected than in the previous case. It is more evident that the start and end of the trajectory are in different positions, which is erroneous. Nevertheless, after filtering the signals and repeating the estimation of the path for the circular trajectory, the results improve even more than in the

rectangular task (Figure 12(b)). Most of the estimated values match the expected; the trajectory is smooth and in this case the problem with the start and end positions is corrected, proving the good performance of the proposed methodology.

To have a better indicator of the efficiency of this work, the graphics of the evolution of the error on the estimations are presented. Figure 13 shows the error before and after applying the filter to suppress the vibration on rectangular welding task. When the filter is not applied, the maximum value of the error exceeds 20 mm. This error is unacceptable and it leads to a bad performance on the task programmed on the robot. When the vibration is reduced through the filter, the

TABLE 6: Mean square error and mean of the error for robot path tracking.

PATH	MSE (mm)		Mean (mm)	
	With vibration	Without vibration	With vibration	Without vibration
Rectangular	5.375	0.6274	5.5181	0.4353
Circular	43.7230	0.3325	28.4337	0.2086

TABLE 7: Comparison of error for different techniques.

PATH	MSE (mm)			Mean (mm)		
	Accelerometer	Gyroscope	Fusion	Accelerometer	Gyroscope	Fusion
Rectangular	1.0096	1.5053	0.6274	0.7160	1.1359	0.4353
Circular	0.9656	2.5431	0.3325	0.5951	1.6018	0.2086

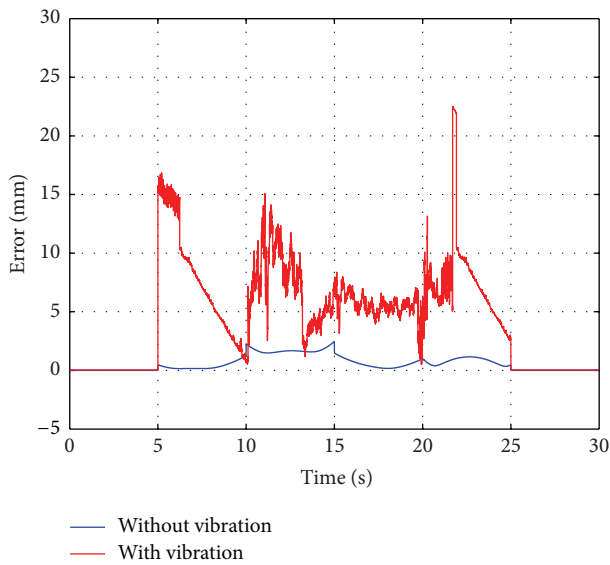


FIGURE 13: Error present on the estimation of the rectangular path.

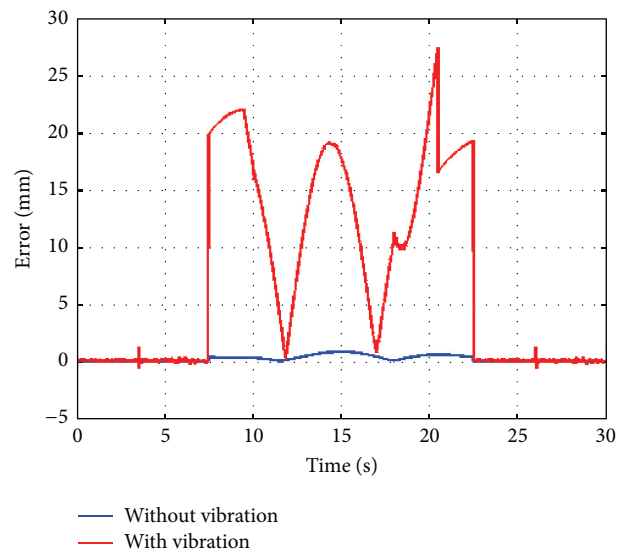


FIGURE 14: Error present on the estimation of the circular path.

maximum value of the error does not exceed the 2 mm, which means that filtering the noise due to vibration improves the performance over ten times. In the case of the error for the circular path it is clear that the error is higher than in the rectangular path (Figure 14). The highest value of the error is almost 30 mm when the vibration is present. When the filter removes the vibration, the maximum error is of less than 1 mm. Therefore, in order to have accurate measurements it is necessary to separate the noise from the relevant information.

Table 6 summarizes the values of the mean square error (MSE) and the mean of the error. This corroborates the results present in Figures 13 and 14. Both the MSE and the mean of the error are much higher when the vibration is present in the data. The error is clearly reduced when data is not contaminated with vibration.

Additionally, and in order to show that the estimation of kinematic parameters is better using the sensor fusion than with other techniques, Table 7 shows a comparative of the MSE and the mean error of the estimation using three different estimation techniques: accelerometer only, gyroscope

only, and the fusion of accelerometer and gyroscope. This analysis uses the values of the error considering that vibration is not present on the signals from sensors.

From results in Table 7, it is clear that the methodology that offers the best results is the fusion of signals. The worst results are obtained when using the gyroscope. This is because gyroscopes deliver very accurate results when they start working, but as the process progresses, the drift appears. This is an error introduced when estimating the position from the angular velocity data. Accelerometers offer better results than gyroscope. However, accelerometer only provides information about the acceleration relative to gravity and, in this particular case, the first joint of the robot under test does not present any variation of acceleration relative to gravity, so in order to obtain a value for the position of the robot, it is necessary to use expected data and not the real. The aforementioned problems can be corrected using the sensor fusion, and it is notorious that also the estimation of the kinematic parameters improves.

6. Conclusion

A system capable of providing complete joint kinematics and position of an industrial robot is proposed and tested in a 6 degrees of freedom robot. The system is based on KF technique for vibration suppression and for fusing the measurements of two primary sensors: gyroscopes and accelerometers. It is remarkable that although a calibration method is used to compensate errors due to external factors, vibration severely affects the estimation of the kinematic parameters of the manipulator. KF proves to be a great tool for suppressing vibration in order to obtain accurate results, and the introduced delay is not significant, so the task can be used online. Without this stage, all the results are meaningless so it is very important to carry out a proper suppression of the noise due to vibration. The fusion of these sensors adds improvements to measurements delivered by every sensor separately. By using these sensors and techniques, the estimation of robotic kinematic parameters is improved. Results from this work show that sensor fusion is not affected by the cumulative error caused by using the gyroscope or the accelerometer information. This cumulative error highly affects the results using another technique leading to a lack of accuracy which is traduced in undesired positioning problems. According to Table 6, fusion sensor technique delivers results up to 8 times better than gyroscope technique and 2 times better than accelerometer. This is a good improvement considering that industrial robots are designed to do repetitive and accurate tasks and a lack of any of these two aspects represents losses to the enterprise.

Competing Interests

The authors declare that they have no competing interests.

Acknowledgments

This research was partially supported by CONACyT scholarship 415315 and by projects SEP-CONACyT 222453-2013.

References

- [1] N. Reza, *Theory of Applied Robotics: Kinematics, Dynamics, and Control*, Springer, New York, NY, USA, 2nd edition, 2010.
- [2] C. Rodriguez-Donate, R. A. Osornio-Rios, J. R. Rivera-Guillen, and R. D. J. Romero-Troncoso, "Fused smart sensor network for multi-axis forward kinematics estimation in industrial robots," *Sensors*, vol. 11, no. 4, pp. 4335–4357, 2011.
- [3] A. Nubiola and I. A. Bonev, "Absolute robot calibration with a single telescoping ballbar," *Precision Engineering*, vol. 38, no. 3, pp. 472–480, 2014.
- [4] C. Dumas, S. Caro, S. Garnier, and B. Furet, "Joint stiffness identification of six-revolute industrial serial robots," *Robotics and Computer-Integrated Manufacturing*, vol. 27, no. 4, pp. 881–888, 2011.
- [5] A. Nubiola and I. A. Bonev, "Absolute calibration of an ABB IRB 1600 robot using a laser tracker," *Robotics and Computer-Integrated Manufacturing*, vol. 29, no. 1, pp. 236–245, 2013.
- [6] L. Lin, Y. Song, Y. Yang, H. Feng, Y. Cheng, and H. Pan, "Computer vision system R&D for EAST Articulated Maintenance Arm robot," *Fusion Engineering and Design*, vol. 100, pp. 254–259, 2015.
- [7] Y. Kwon and J. Hong, "Integrated remote control of the process capability and the accuracy of vision calibration," *Robotics and Computer-Integrated Manufacturing*, vol. 30, no. 5, pp. 451–459, 2014.
- [8] I.-W. Park, B.-J. Lee, S.-H. Cho, Y.-D. Hong, and J.-H. Kim, "Laser-based kinematic calibration of robot manipulator using differential kinematics," *IEEE/ASME Transactions on Mechatronics*, vol. 17, no. 6, pp. 1059–1067, 2012.
- [9] C. Rodriguez-Donate, L. Morales-Velazquez, R. A. Osornio-Rios, G. Herrera-Ruiz, and R. D. J. Romero-Troncoso, "FPGA-based fused smart sensor for dynamic and vibration parameter extraction in industrial robot links," *Sensors*, vol. 10, no. 4, pp. 4114–4129, 2010.
- [10] B. Munoz-Barron, J. R. Rivera-Guillen, R. A. Osornio-Rios, and R. J. Romero-Troncoso, "Sensor fusion for joint kinematic estimation in serial robots using encoder, accelerometer and gyroscope," *Journal of Intelligent and Robotic Systems*, vol. 78, no. 3-4, pp. 529–540, 2014.
- [11] G. Du and P. Zhang, "IMU-based online kinematic calibration of robot manipulator," *The Scientific World Journal*, vol. 2013, Article ID 139738, 10 pages, 2013.
- [12] X. Yao, G. Sun, W.-Y. Lin, W.-C. Chou, K. F. Lei, and M.-Y. Lee, "The design of an in-line accelerometer-based inclination sensing system," in *Proceedings of the IEEE International Symposium on Circuits and Systems (ISCAS '12)*, pp. 333–336, Seoul, South Korea, May 2012.
- [13] J. L. Han, X. Ma, and X. H. Yang, "Design of guided shell inclination measurement and display system based-on MEMS accelerometer," *Key Engineering Materials*, vol. 609, pp. 1040–1045, 2014.
- [14] M. R. Kaloop and J. W. Hu, "Stayed-cable bridge damage detection and localization based on accelerometer health monitoring measurements," *Shock and Vibration*, vol. 2015, Article ID 102680, 11 pages, 2015.
- [15] B. C. Yalçın and H. Erol, "Semiactive vibration control for horizontal axis washing machine," *Shock and Vibration*, vol. 2015, Article ID 692570, 10 pages, 2015.
- [16] X. Zhang, H. Gao, and H. Huang, "Screw performance degradation assessment based on quantum genetic algorithm and dynamic fuzzy neural network," *Shock and Vibration*, vol. 2015, Article ID 150797, 11 pages, 2015.
- [17] J. Benesty, J. Chen, Y. Huang, and T. Gaensler, "Time-domain noise reduction based on an orthogonal decomposition for desired signal extraction," *Journal of the Acoustical Society of America*, vol. 132, no. 1, pp. 452–464, 2012.
- [18] D.-W. Jee, Y. Suh, B. Kim, H.-J. Park, and J.-Y. Sim, "A fir-embedded phase interpolator based noise filtering for wide-bandwidth fractional-n PLL," *IEEE Journal of Solid-State Circuits*, vol. 48, no. 11, pp. 2795–2804, 2013.
- [19] B. Kamislioglu, T. Koza, S. Kockanat, and N. Karaboga, "Noise cancellation on mitral valve Doppler signal with IIR digital filter using harmony search algorithm," in *Proceedings of the IEEE International Symposium on Innovations in Intelligent Systems and Applications (IEEE INISTA '13)*, pp. 1–5, Albena, Bulgaria, June 2013.
- [20] X. Han and X. Chang, "An intelligent noise reduction method for chaotic signals based on genetic algorithms and lifting

- wavelet transforms,” *Information Sciences*, vol. 218, pp. 103–118, 2013.
- [21] S. Y. Chen, “Kalman filter for robot vision: a survey,” *IEEE Transactions on Industrial Electronics*, vol. 59, no. 11, pp. 4409–4420, 2012.
- [22] F. Auger, M. Hilairat, J. M. Guerrero, E. Monmasson, T. Orłowska-Kowalska, and S. Katsura, “Industrial applications of the kalman filter: a review,” *IEEE Transactions on Industrial Electronics*, vol. 60, no. 12, pp. 5458–5471, 2013.
- [23] J. Angeles, *Fundamentals of Robotic Mechanical Systems: Theory, Methods, and Algorithms*, Springer, New York, NY, USA, 2nd edition, 2003.
- [24] ST Microelectronics, “Datasheet LIS331DLH,” 2009, <http://www.st.com/web/en/resource/technical/document/datasheet/CD00213470.pdf>.
- [25] ST Microelectronics, “Datasheet L3GD20,” February 2016, <http://www.st.com/web/en/resource/technical/document/datasheet/CD00213470.pdf>.
- [26] S. Mejri, V. Gagnol, T.-P. Le, L. Sabourin, P. Ray, and P. Paultre, “Dynamic characterization of machining robot and stability analysis,” *International Journal of Advanced Manufacturing Technology*, vol. 82, no. 1, pp. 351–359, 2016.

Research Article

A Fault Feature Extraction Method for Rolling Bearing Based on Pulse Adaptive Time-Frequency Transform

Jinbao Yao,¹ Baoping Tang,¹ and Jie Zhao²

¹State Key Lab of Mechanical Transmission, Chongqing University, Chongqing 400030, China

²College of Mechanical Engineering, Chengdu University, Sichuan 610106, China

Correspondence should be addressed to Jinbao Yao; jbyao2001@163.com

Received 18 December 2015; Revised 27 February 2016; Accepted 2 March 2016

Academic Editor: Juan P. Amezcua-Sanchez

Copyright © 2016 Jinbao Yao et al. This is an open access article distributed under the Creative Commons Attribution License, which permits unrestricted use, distribution, and reproduction in any medium, provided the original work is properly cited.

Shock pulse method is a widely used technique for condition monitoring of rolling bearing. However, it may cause erroneous diagnosis in the presence of strong background noise or other shock sources. Aiming at overcoming the shortcoming, a pulse adaptive time-frequency transform method is proposed to extract the fault features of the damaged rolling bearing. The method arranges the rolling bearing shock pulses extracted by shock pulse method in the order of time and takes the reciprocal of the time interval between the pulse at any moment and the other pulse as all instantaneous frequency components in the moment. And then it visually displays the changing rule of each instantaneous frequency after plane transformation of the instantaneous frequency components, realizes the time-frequency transform of shock pulse sequence through time-frequency domain amplitude relevancy processing, and highlights the fault feature frequencies by effective instantaneous frequency extraction, so as to extract the fault features of the damaged rolling bearing. The results of simulation and application show that the proposed method can suppress the noises well, highlight the fault feature frequencies, and avoid erroneous diagnosis, so it is an effective fault feature extraction method for the rolling bearing with high time-frequency resolution.

1. Introduction

As the most common part in the rotating machinery, rolling bearing is most vulnerable to damage. The condition of the rolling bearing has a great effect on the working condition of the whole machine. Any defect in the rolling bearing may impair the normal working order of the machine, causing vibration in the machine, producing noises, and even resulting in fatal crashes. Therefore, it is necessary to perform fault diagnosis for defects in the rolling bearing. A damaged rolling bearing may produce regular shock pulses, and these components may be contained in the vibration signals. Besides, the shock modulation phenomenon may take place. However, as the operating condition of the rolling bearing is quite complex, in addition to the shock pulse components representing the fault information, the vibration signals produced by the rolling bearing always contain other signal components such as noise, rotation frequency, and its harmonic components, which usually interfere with the fault diagnosis of the rolling bearing. Hence, the key of the rolling

bearing fault diagnosis is to extract from the vibration signals the shock pulse representing the damage. Considering that the shock modulation is an important feature when any fault arises in the rolling bearing, the fault feature frequency can be extracted by demodulating the vibration signals, so as to realize the fault diagnosis of the rolling bearing. So the study on the vibration signal demodulation methods for the rolling bearing has for long become an attraction and also a difficulty in the area of rolling bearing fault diagnosis.

Present vibration signal demodulation methods for the rolling bearing mainly include the envelope demodulation method, resonance demodulation method (RDM), and shock pulse method (SPM). The envelope demodulation method uses a high frequency vibration sensor, acquires the high frequency vibration signals of the rolling bearing containing the low frequency shock components by setting a certain high frequency filtering bandwidth, and performs such processes as envelope interception and capture, demodulation, and low-pass filtering, so as to obtain the modulation frequency (rolling bearing fault feature frequency).

It mainly includes the generalized detection-filtering demodulation method [1], local mean decomposition demodulation method [2], wavelet analysis demodulation method [3–5], EMD/EMD demodulation method [6], and Hilbert demodulation method [7, 8]. Although the envelope demodulation methods in question have produced some results in the application study on the rolling bearing fault diagnosis, owing to their common limitations, the demodulated low frequency shock signals representing the fault information always contain noise and information of other vibration sources such as rotation axis and gear, which may badly interfere with the rolling bearing fault diagnosis, and the frequency domain information of the demodulation wave contains the frequency components that cannot be analyzed or may cause erroneous diagnosis. In addition, if the signal-to-noise ratio (SNR) of the shock signal is not raised, the envelope demodulation methods cannot be applied to the early fault diagnosis of the rolling bearing. Following the phenomenon that the shock signal of wide range may arouse resonance, and the vibration signal rarely produces resonance [9], SPM and RDM both modulate the low frequency shock signal to high frequency one, perform such processes as filtering and envelope demodulation, and then diagnose the working condition of the rolling bearing. Although both methods above solve the problems in the envelope demodulation method, they still have their own problems due to differences in the working principle. RDM modulates the shock signal to the resonance frequency of the mechanical system structure and employs the frequency domain information of the resonance demodulation wave to diagnose the working condition of the rolling bearing [10, 11]. It is able to accurately diagnose the faulty parts. But as the resonance frequency varies with the different mechanical system structures, it is hard for the method to select the filtering center frequency and bandwidth. And SPM modulates the shock signal to a fixed high frequency and uses the amplitude information of the resonance demodulation wave to diagnose the working condition of the rolling bearing [12, 13]. Though the method does not have the problem of RDM whose filtering center frequency and bandwidth can be hardly selected, as it adopts the fixed filtering center frequency and bandwidth, performs the envelope detection which is characterized by nonlinear transformation, and bases the diagnosis on the amplitude information of the resonance demodulation wave alone, without any further analysis or processing, it cannot arrive at desired diagnosis results in the presence of the strong background noise or other shock sources. To solve the problems as mentioned, the researchers proposed some improved methods such as shock pulse frequency analysis method [14], shock pulse time-frequency analysis method, and improved redundant lifting scheme method [15], but they just used the existing signal processing methods for analyzing frequency spectrum, time-frequency spectrum, and the like. Such proposed methods are still not suitable for the rolling bearing fault diagnosis in the presence of strong background noise, and they also lose the instantaneous time change feature of the shock.

For this reason, by integrating the advantages of RDM and SPM, this paper comes up with a pulse adaptive

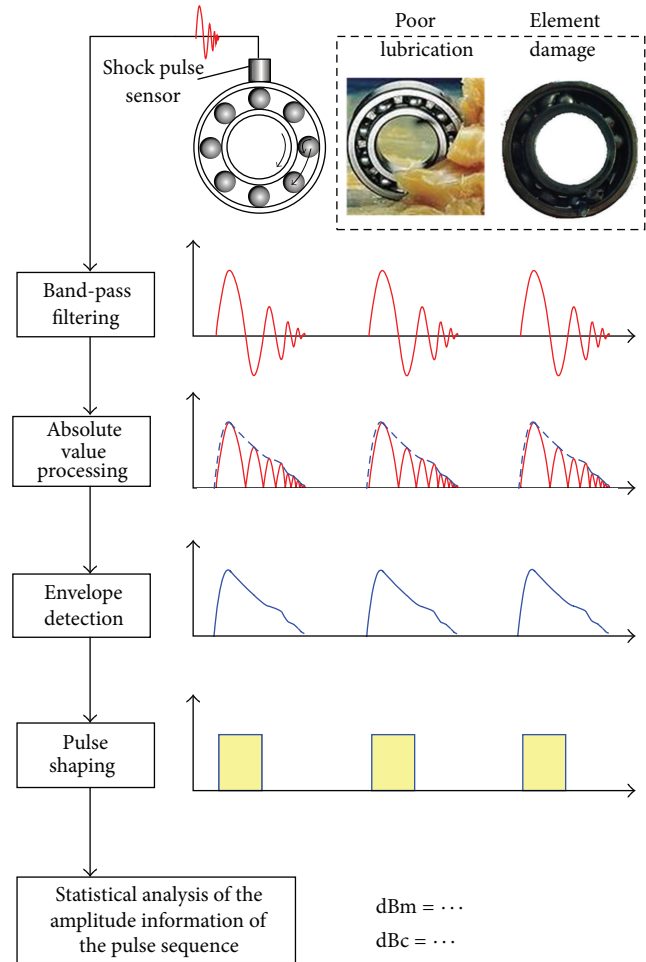


FIGURE 1: Block diagram of working principle of SPM.

time-frequency transform method (PATFTM). Like SPM, the proposed method uses the fixed filtering center frequency and bandwidth; and also like RDM, it is able to further process the extracted shock pulse, thus avoiding the problem existing in SPM.

The remainder of the paper is organized as follows: the working principle and diagnosis method of SPM are introduced in Section 2; on the basis of SPM, Section 3 proposes the PATFTM; through simulation and application analysis, PATFTM is validated in Section 4; and finally, based on the analysis results, Section 5 draws the study conclusions and makes suggestions for further studies in this regard.

2. Shock Pulse Method

SPM was first proposed in the 1970s [16], for diagnosing the failures in the rolling bearing, with its working principle shown in Figure 1. The rolling bearing in service, due to such reasons as poor lubrication, surface roughness, and element damage, may cause shock effect. And together with the mechanical and electrical tuning, the dedicated shock pulse sensor may be driven to resonate at a fixed frequency (usually within the range of 20 kHz~60 kHz) [17], so that the resonance signal amplitude acquired is obviously greater

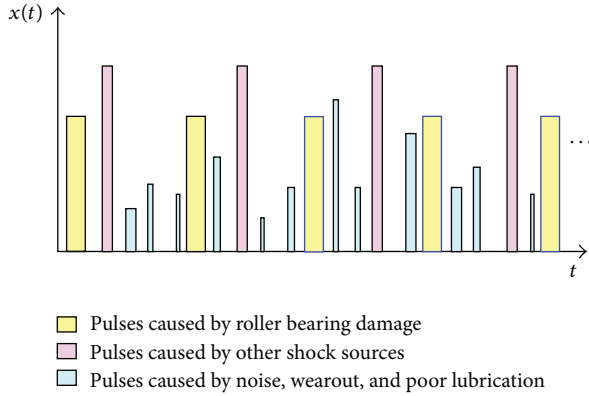


FIGURE 2: Schematic diagram of shock pulses extracted by SPM.

than the vibration signal amplitude collected by a common sensor. Then, the acquired resonance signals containing the amplitude modulation wave of the low frequency shock, random interference, and other shock sources are made to undergo such processes as band-pass filtering, absolute value processing, envelope detection, and pulse shaping, to obtain the pulse sequence. And the amplitude information of the pulse sequence is statistically analyzed, to finally diagnose the working condition of the rolling bearing.

After the pulse sequence is obtained, the statistical analysis of the amplitude information of the pulse sequence is the core of SPM. The statistical analysis means that dB-Maximum Value (dBm) and dB-Carpet Value (dBc), two physical quantities used for measuring the shock pulse amplitude, are defined, recorded, and analyzed, and then, according to the diagnosis rule of SPM, the failures in the rolling bearing are diagnosed. dBm denotes the strong pulse decibel value and corresponds to the low frequency pulse sequence amplitude. It is defined as the maximum shock peak value obtained with a single testing period and used for measuring the extent of damage of the rolling bearing component. dBc denotes the carpet decibel value and corresponds to the high frequency pulse sequence amplitude. It is defined as the mean value of lots of weak shock signals and used for measuring the lubrication, surface roughness, and degree of wear. The diagnosis rule of SPM is described as follows: if dBm and dBc both are often very low, this indicates that the bearing is well lubricated and free of damage; if dBm and dBc both are often very high, this indicates that the bearing is poorly lubricated; if the periodic peak value occurs and dBm rises, this indicates that the bearing is damaged [18].

The shock pulses extracted by SPM mainly consist of the pulses caused by such factors as rolling bearing damage, wearout failure, poor lubrication, other shock sources, and noise, as shown in Figure 2. SPM is well known for its simplicity and practicality and carries out the fault diagnosis of the rolling bearing through the statistical analysis of the pulse sequence amplitude. It is very accurate in diagnosing the wearout failure, poor lubrication, and so forth, and it is able to diagnose the damage in the rolling bearing. However, it is not capable of performing further diagnosis of the bearing damage, and in the presence of strong background

noise or other shock sources, it cannot arrive at desired diagnosis results [19].

Thus, for the sake of solving the problems in SPM, weeding out the pulse interference resulting from such factors as wearout failure, poor lubrication, other shock sources, and noise, extracting the pulses produced by the damage in the rolling bearing, and carrying out the further diagnosis of the damage in the rolling bearing, on the basis of SPM, PATFTM is proposed.

3. Pulse Adaptive Time-Frequency Transform Method

The basic idea of PATFTM is transforming the shock pulse sequence of one-dimensional time domain extracted by SPM into two-dimensional time-frequency domain, weeding out the interference from other factors through the effective instantaneous frequency extraction, highlighting the fault feature representing the rolling bearing damage, and finally realizing the fault diagnosis of the rolling bearing visually and effectively.

PATFTM mainly comprises such steps as amplitude threshold processing, shock pulse ordering, instantaneous frequency calculation, instantaneous frequency plane transformation, amplitude relevancy processing, and effective instantaneous frequency extraction, as shown in Figure 3.

In the following, with the application on the shock pulse sequence as shown in Figure 2, these processes will be discussed in detail.

(a) *Amplitude Threshold Processing.* In order to reduce the influences from such factors as background noise, wearout failure, and poor lubrication and raise the efficiency of PATFTM, the shock pulses extracted by SPM are made to experience the amplitude threshold processing by setting the threshold, in which the shock pulses whose amplitude is smaller than the threshold are excluded and those whose amplitude is greater than the threshold are retained. The threshold setting principle is regarding the average amplitude measured when the bearing is well lubricated and free of any damage as the threshold for amplitude threshold processing. Figure 4 shows the processing results of the shock pulse sequence as shown in Figure 2 through the amplitude threshold processing.

(b) *Shock Pulse Ordering.* As a basic physical quantity of communication signals, pulse arrival time is widely used in deinterleaving of radar pulses [20, 21]. Considering there is some similarity in regularity of pulse sequence between the radar pulses and the shock pulses to some extent, pulse arrival time is introduced into analyzing shock pulses. The shock pulses for which the amplitude threshold processing has been performed, as shown in Figure 4, are ranked in the order of pulse arrival time t_i , and the shock pulse sequence $\{x(t_i), i \in [1, N]\}$ is obtained, as shown in Figure 5. Here, i denotes the serial number of the shock pulse in the sequence, $i \in [1, N]$; N denotes the total number of the shock pulses, namely, the total length of the sequence; t_i denotes the arrival

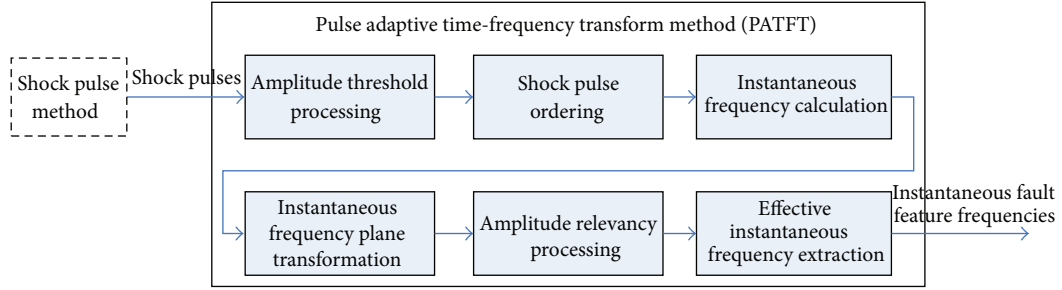


FIGURE 3: Steps of PATFTM.

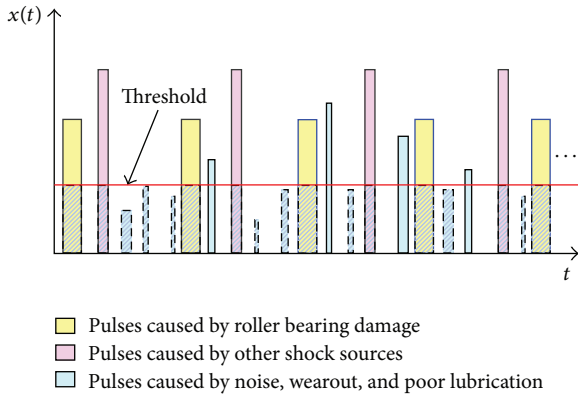


FIGURE 4: Schematic diagram of amplitude threshold processing.

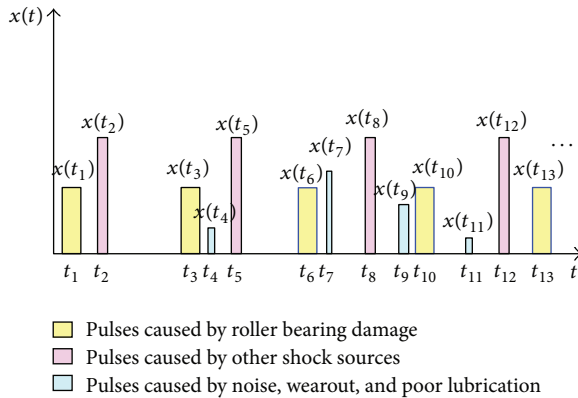


FIGURE 5: Schematic diagram of shock pulse ordering.

time of the i th shock pulse, with s as its unit; $x(t_i)$ denotes the amplitude of the i th shock pulse, with m/s^2 as its unit.

(c) *Instantaneous Frequency Calculation.* The shock pulse sequence $\{x(t_i), i \in [1, N]\}$ contains the shock information caused by all excitation sources, including the rolling bearing damage. The sequence has relatively high internal relevancy, and the rolling bearing fault feature cannot be accurately extracted by studying some pulse alone. Thus, this paper studies the pulse arrival time t_i and performs overall analysis of a group of pulses, to find the internal changing rule of pulses, obtain the instantaneous frequency components

contained in the moment t_i , and identify different excitation sources.

Considering that the pulse arrival times t_i and t_j correspond to the pulse occurrence moment, for the periodical shock sequence, if the shock at the moment t_i is produced by the damage in a rolling bearing, and the shock at the moment t_j is generated by the same damage in the rolling bearing next time or last time, then $|1/(t_j - t_i)|$ may be used for representing the feature frequency of the rolling bearing damage.

Thus, by reference to the feature frequency calculated from the periodical shock sequence, the instantaneous frequency component $f_{i,j}$ that may be contained in the moment t_i in the shock pulse sequence $\{x(t_i), i \in [1, N]\}$ can be calculated with the positive instantaneous frequency components expressed by (1) or the reverse instantaneous frequency components expressed by (2):

$$f_{i,j} = \begin{cases} \frac{1}{t_j - t_i}, & t_j - t_i \in \left[\frac{1}{f_u}, \frac{1}{f_d} \right], i \in [1, N], j \in (i, N) \\ 0, & \text{Others} \end{cases} \quad (1)$$

$$f_{i,j} = \begin{cases} \frac{1}{t_i - t_j}, & t_i - t_j \in \left[\frac{1}{f_u}, \frac{1}{f_d} \right], i \in [1, N], j \in (1, i) \\ 0, & \text{Others,} \end{cases} \quad (2)$$

where i and j denote the serial number of the i th shock pulse and the j th shock pulse, respectively; t_i and t_j denote the arrival time of the i th shock pulse and the j th shock pulse, respectively, with s as the unit; f_d and f_u denote the lower limit and the upper limit of $f_{i,j}$ (as the rolling bearing fault feature frequency can be obtained through theoretical calculation, and it tends to fall within a frequency range; the lower limit f_d and the upper limit f_u of $f_{i,j}$ can be defined in advance, to obtain the conditions for calculation termination of $f_{i,j}$), with Hz as the unit.

Taking the calculation of the positive and reverse instantaneous frequency components of the pulse sequence as shown in Figure 5 at the moment t_6 as an example, formulas (1) and (2) are used for the calculation, and the results obtained are shown in Figure 6.

Figure 6 clearly shows that the positive and reverse instantaneous frequency components calculated with (1) and

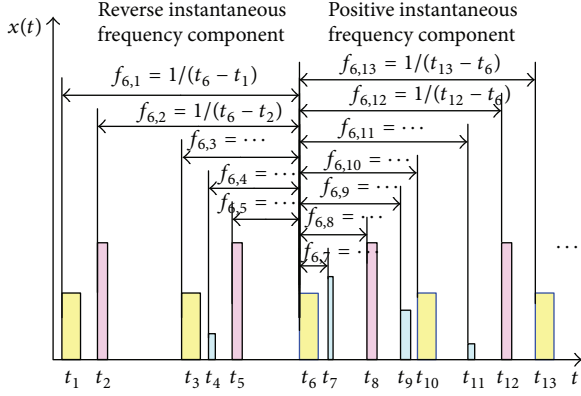


FIGURE 6: Schematic diagram of instantaneous frequency component calculation.

(2) have the instantaneous time change feature and that all instantaneous frequency components that may be contained in the shock pulse occurrence moment can be accurately and timely captured.

(d) *Plane Transformation of Instantaneous Frequency.* With i as the row and j as the column, the positive and reverse instantaneous frequency components $f_{i,j}$ both can be expressed by the matrix F in

$$F = \begin{pmatrix} 0 & f_{1,2} & \cdots & f_{1,i} & \cdots & f_{1,j} & \cdots & f_{1,N-1} & f_{1,N} \\ f_{2,1} & 0 & \cdots & f_{2,i} & \cdots & f_{2,j} & \cdots & f_{2,N-1} & f_{2,N} \\ \vdots & \vdots & \ddots & \vdots & & \vdots & & \vdots & \vdots \\ f_{i,1} & f_{i,2} & \cdots & 0 & \cdots & f_{i,j} & \cdots & f_{i,N-1} & f_{i,N} \\ \vdots & \vdots & \vdots & \vdots & \ddots & \vdots & & \vdots & \vdots \\ f_{j,1} & f_{j,2} & \cdots & f_{j,i} & \cdots & 0 & \cdots & f_{j,N-1} & f_{j,N} \\ \vdots & \vdots & & \vdots & \ddots & \vdots & & \vdots & \vdots \\ f_{N-1,1} & f_{N-1,2} & \cdots & f_{N-1,i} & \cdots & f_{N-1,j} & \cdots & 0 & f_{N-1,N} \\ f_{N,1} & f_{N,2} & \cdots & f_{N,i} & \cdots & f_{N,j} & \cdots & f_{N,N-1} & 0 \end{pmatrix}. \quad (3)$$

The elements $f_{i,j}$ ($i = j$) on the diagonal of the matrix F all equal zero.

The elements $f_{i,j}$ ($i \in [1, N], j \in (i, N]$) above the diagonal of the matrix F correspond to the positive instantaneous frequency components and are bound by the condition $t_i - t_j \in [1/f_u, 1/f_d]$. With j increasing, most elements above the diagonal are zero, and the number of the nonzero elements is smaller than or equal to $N - i$, and $f_{i,p} > f_{i,q}$ ($i < p < q \leq N$) is satisfied.

The elements $f_{i,j}$ ($i \in [1, N], j \in (1, i)$) below the diagonal of the matrix F correspond to the reverse instantaneous frequency components and are bound by the condition $t_j - t_i \in [1/f_u, 1/f_d]$. With j decreasing, most elements below the diagonal are zero, and the number of the nonzero elements is smaller than or equal to $j - 1$, and $f_{i,p} < f_{i,q}$ ($1 \leq p < q < i$) is satisfied.

The elements of the i th row above or below the diagonal of the matrix F mean the instantaneous frequency components

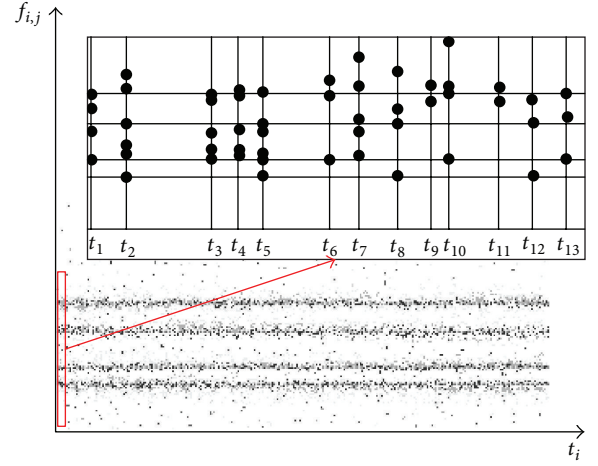


FIGURE 7: Schematic diagram of plane transformation of instantaneous frequency.

that may be contained in the vibration signal to which the shock pulse sequence $\{x(t_i), i \in [1, N]\}$ corresponds, at the moment t_i .

If the elements above the diagonal of the matrix F (positive instantaneous frequency components) are processed by the plane transformation method applied to the communication domain [20, 21], they will be displayed in the plane coordinates with t_i as horizontal coordinate and $f_{i,j}$ as vertical coordinate, and the instantaneous frequency component $f_{i,j}$ of the shock pulse sequence $\{x(t_i), i \in [1, N]\}$ and its changing rule will be shown with the arrival time t_i in a dynamic manner, the process which is called the plane transformation of instantaneous frequency. If the elements below the diagonal of the matrix F (reverse instantaneous frequency components) are made to experience the transformation above, the process is called the reverse plane transformation of instantaneous frequency. Figure 7 shows the results of plane transformation of instantaneous frequency of all pulse sequences as shown in Figure 5.

(e) *Amplitude Relevancy Processing.* After the pulse sequences extracted by SPM undergo the amplitude threshold processing, shock pulse ordering, instantaneous frequency calculation, and plane transformation of instantaneous frequency, the fault feature frequency has been extracted for qualitative fault diagnosis of the rolling bearing. However, as there is no amplitude information of all fault feature frequency components, further quantitative diagnosis and trend prediction cannot be carried out for the rolling bearing fault. Thus, the instantaneous frequency component $f_{i,j}$ needs to experience the amplitude relevancy processing.

The amplitude to which the instantaneous frequency component $f_{i,j}$ corresponds is expressed as $X(t_i, f_{i,j})$, and through (4) the instantaneous frequency component $f_{i,j}$ can be correlated with the amplitude $X(t_i, f_{i,j})$ as follows:

$$X(t_i, f_{i,j}) = \begin{cases} |x(t_j)|, & f_{i,j} \in [f_d, f_u] \\ 0 & \text{Others.} \end{cases} \quad (4)$$

If the amplitude is correlated with the positive instantaneous frequency component, then, in the formula above, $f_{i,j} = 1/(t_j - t_i)$, $i \in [1, N]$ and $j \in [i, N]$, while if the amplitude is correlated with the reverse instantaneous frequency component, then, in the formula, $f_{i,j} = 1/(t_i - t_j)$, $i \in [1, N]$ and $j \in (1, i]$.

Like the time-frequency spectrum of the time-frequency transformation, the processing result obtained from amplitude relevancy processing may also be expressed by the time-frequency spectrum; that is, the one-dimensional pulse sequence $\{x(t_i), i \in [1, N]\}$ is transformed into a two-dimensional plane in which the amplitude $X(t_i, f_{i,j})$ is expressed by the color space, with the pulse arrival time t_i as horizontal coordinate and the instantaneous frequency $f_{i,j}$ as vertical coordinate. Figure 8 presents the time-frequency spectrum after the Steps (a)–(e) above are applied to Figure 7.

(f) *Effective Instantaneous Frequency Extraction.* After the amplitude relevancy processing above, the instantaneous frequency components $f_{i,j}$ extracted at the moment t_i are not all effective instantaneous frequencies that help to diagnose the damage in the rolling bearing. Instead, they contain numerous ineffective instantaneous frequency components resulting from false interharmonic (see label A in Figure 8), cross-term interference (see label B in Figure 8), noise interference, wearout failure and poor lubrication inference (see label C in Figure 8), and other shock sources (see label D in Figure 8). Hence, it is necessary to weed out the ineffective instantaneous frequency components caused by these factors above, so as to highlight and extract the effective instantaneous frequency components.

(1) *False Interharmonic Weeding-Out.* The false interharmonic means the ineffective false instantaneous frequency component of the fraction times effective instantaneous frequency component produced by the reciprocal of the arrival time interval between several points on the pulse sequence with the time interval of T_1 , after the pulse sequence containing the periodical sequence component with the time interval of T_1 experiences PATFTM.

The ineffective instantaneous frequency caused by the false interharmonic can be weeded out by following the false interharmonic criterion below.

False interharmonic criterion: taking the judgment as to whether the positive instantaneous frequency $f_{i,j}$ is a false interharmonic as an example, suppose that δ_1 and δ_2 are minor tolerances; if there is k to make $|f_{i,j} - f_{i,k}/m| < \delta_1$ (wherein $f_{i,j} \neq 0$, $0 < i < k < j < N$, and the variable m is a positive integer and satisfies $1 < m < j - k$, which is used to demonstrate that $f_{i,j}$ is an interharmonic of $f_{i,k}$) and $|w_{i,k} - w_{i,j}| < \delta_2$ ($w_{i,j}$ and $w_{i,k}$ denote the pulse width at the moments t_j and t_k , resp.), then $f_{i,j}$ is an ineffective instantaneous frequency that is usually produced by the false interharmonic.

(2) *Removal of Cross-Term Interference and Noise Interference.* The cross-term interference means the ineffective instantaneous frequency component derived from the reciprocal of the arrival time interval between the staggered pulses

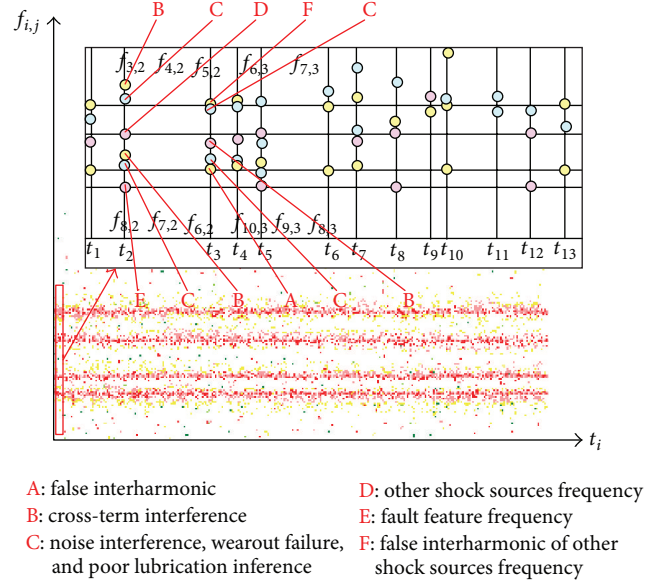


FIGURE 8: Schematic diagram of amplitude relevancy processing.

comprising several effective instantaneous frequency components, after the pulse sequence containing several effective instantaneous frequency components, experiences PATFTM.

The noise interference means the ineffective instantaneous frequency component comes from the reciprocal of the arrival time interval between the different noise pulses as well as between the noise pulse and other pulses, after the pulse sequence containing noise pulse experiences PATFTM.

As the rolling bearing fault feature frequencies can be calculated ahead, by defining the frequency domain bandwidth $[f_d, f_u]$ of the instantaneous frequency component $f_{i,j}$, the ineffective instantaneous frequencies produced by the cross-term interface and noise interface, which fall out of the frequency domain bandwidth, can be preliminarily removed.

The ineffective instantaneous frequencies produced by the cross-term interface and noise interface, which fall within the frequency domain bandwidth, can be weeded out by following the cross-term and noise interference criterion.

Cross-term and noise interference criterion: suppose that δ_3 is a minor tolerance, if there is no k to make $|f_{i,j} - f_{i,k}| < \delta_3$ (wherein $f_{i,j} \neq 0$, $0 < k < i < j < N$), then $f_{i,j}$ is an ineffective instantaneous frequency that is usually produced by the cross-term and noise interference.

This is because the positive instantaneous frequency component and the reverse instantaneous frequency component are obtained from the same pulse sequence in the same way, while the only difference between them lies in the direction of the calculation adopted in obtaining the instantaneous frequency components. As the shock pulse produced by the cross-term and noise interference within the same pulse sequence takes place at random (excluding the cross-term interference caused by several effective instantaneous frequency components in which the common multiple relationship exists), the instantaneous frequency components $f_{i,j}$ and $f_{i,k}$ produced by the cross-term and noise interference within the positive instantaneous frequency components

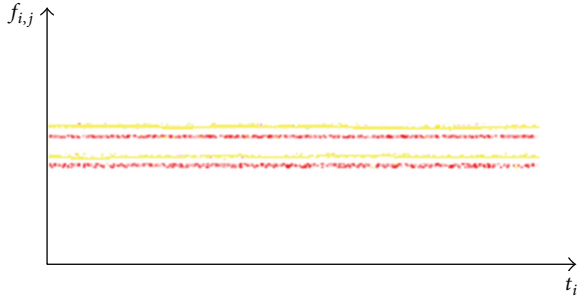


FIGURE 9: Schematic diagram of extraction of effective instantaneous frequency components.

and the reverse instantaneous frequency components are necessarily irrelevant, and as a rule, no k is available for making $|f_{i,j} - f_{i,k}| < \delta_3$ (wherein $f_{i,j} \neq 0, 0 < k < i < j < N$). However, for the shock pulse produced by the rolling bearing damage within the same pulse sequence, its occurring rule remains unchanged within a short time, and a certain phase shift alone takes place. Therefore, the changing rules of the instantaneous frequency components $f_{i,j}$ and $f_{i,k}$ produced by the rolling bearing damage within the positive instantaneous frequency components and the reverse instantaneous frequency components remain the same within a short time, and there is generally k available for making $|f_{i,j} - f_{i,k}| < \delta_3$ (wherein $f_{i,j} \neq 0, 0 < k < i < j < N$). Hence, the cross-term and noise interference criterion may be followed for weeding out the ineffective instantaneous frequencies, without excluding those instantaneous frequency components arising from the rolling bearing damage.

(3) *Removal of Wearout Failure and Poor Lubrication Interference.* The wearout failure and poor lubrication interference mean the ineffective instantaneous frequency component produced by the arrival time interval between the different shock pulses resulting from wearout failure and poor lubrication as well as between the shock pulse and other pulses, after the pulse sequence containing the shock pulse arising from wearout failure and poor lubrication, experiences PATFTM.

The removal process of the wearout failure and poor lubrication interference is similar to that of the noise interference, and so the description thereof is here omitted.

(4) *Removal of Other Shock Sources.* The ineffective instantaneous frequency components produced by other shock sources, if not falling within the set frequency domain bandwidth $[f_d, f_u]$, may be directly removed. Or else, like the rolling bearing damage, they will produce the fault feature frequencies of specific physical significance and may be weeded out by analyzing the fault feature frequencies.

In general, when the effective instantaneous frequency components are extracted, the smaller δ_1, δ_2 , and δ_3 value adopted leads to the greater time resolution and frequency resolution of the time-frequency spectrum obtained. The results of extraction of the effective instantaneous frequency components from the time-frequency spectrum as shown in Figure 8 are shown in Figure 9.

To sum up, the process of the amplitude threshold processing, shock pulse ordering, instantaneous pulse ordering,

plane transformation of instantaneous frequency, amplitude relevancy processing, and effective instantaneous frequency extraction is referred to as PATFTM.

After experiencing PATFTM, the instantaneous frequency component $f_{i,j}$ and its amplitude $X(t_i, f_{i,j})$ directly reflect the time change feature of the analyzed vibration signals, and they can be used for real-time and quantitative fault diagnosis for the rolling bearing.

In addition, as the instantaneous frequency component $f_{i,j}$ is indirectly calculated from the pulse arrival time, the maximum resolution of time and frequency of the time-frequency spectrum obtained from PATFTM is no longer bound by Heisenberg's uncertainty principle [22] but depends upon the measuring precision of the pulse arrival time t_i .

4. Simulation and Application Analysis

4.1. *Analysis of Simulation Signals.* If any local damage comes into existence in the inner ring, outer ring, or rolling elements of the rolling bearing, the signal demodulated by SPM (i.e., the envelope signal obtained after band-pass filtering) may contain the periodical shock components. Besides, if these signals so demodulated also contain the strong background noise or other shock sources, then SPM will cause an erroneous diagnosis. However, PATFTM can extract the fault feature well and complete the fault diagnosis. Therefore, in the following the simulation signal $x(t)$, as shown in (5), containing the signal components produced by the inner ring damage, strong background noise, and other shock sources is made, and then it is processed by SPM, shock pulse frequency spectrum analysis method, shock pulse time-frequency analysis method, and PATFTM, respectively. The results of analysis are then compared, to validate the effectiveness of PATFTM:

$$x(t) = x_1(t) + x_2(t) + x_3(t), \quad (5)$$

where $x_1(t)$ is the simulated shock signal caused by the inner ring damage; $x_2(t)$ is the simulated shock signals caused by other shock sources; $x_3(t)$ is the simulated Gaussian white noise, with the mean value being $0 \text{ mm}\cdot\text{s}^{-2}$ and the variance being $1.1 \times 10^{-4} \text{ mm}\cdot\text{s}^{-2}$.

$x_1(t)$ may be expressed as the following pulse shock signals of periodical exponential attenuation, with the period being T_1 :

$$x_1(t) = \sum_{k=-\infty}^{k=+\infty} A_1 e^{-\alpha_1(t-kT_1)} \cos[2\pi f_1(t-kT_1) + \varphi_{1k}] \cdot U(t-kT_1), \quad (6)$$

where A_1 denotes the peak amplitude and equals $0.05 \text{ mm}\cdot\text{s}^{-2}$; α_1 denotes the damping factor and equals 0.01; f_1 denotes the resonance frequency and equals 30,000 Hz; φ_{1k} denotes the initial phase, falling within $[0^\circ, 360^\circ]$; $U(t)$ denotes the unit step function; T_1 denotes the period of occurrence of shock and equals 0.0075 s.

$x_2(t)$ may be expressed as the following pulse shock signals of periodical exponential attenuation, with the period being T_2 :

$$x_2(t) = \sum_{k=-\infty}^{k=+\infty} A_2 e^{-\alpha_2(t-kT_2)} \cos [2\pi f_2(t-kT_2) + \varphi_{2k}] \cdot U(t-kT_2), \quad (7)$$

where A_2 denotes the peak amplitude and equals $0.07 \text{ mm}\cdot\text{s}^{-2}$; α_2 denotes the damping factor and equals 0.02; f_2 denotes the resonance frequency and equals 30,000 Hz; φ_{2k} denotes the initial phase, falling within $[0^\circ, 360^\circ]$; $U(t)$ denotes the unit step function; T_2 denotes the period of occurrence of shock and equals 0.005 s.

Figure 10(a) shows the time domain waveform of $x(t)$. It indicates that both positive transition and negative transition take place in the sporadic high frequency fading signal, and the initial phase changes with time. No periodical component representing the fault feature can be seen in the time domain waveform, and thus the fault diagnosis is impossible. Figure 10(b) shows the amplitude spectrum of the simulation signal $x(t)$.

Figure 10(c) shows the results of processing of the simulation signal $x(t)$ by SPM. As there is strong background noise, the statistical values dBm and dBc are generally high, as shown in the figure. If, based on this, it is judged that the rolling bearing is not well lubricated, it is obviously an erroneous diagnosis.

Figure 10(d) shows the frequency spectrum obtained after the simulation signal $x(t)$ is processed by shock pulse frequency spectrum analysis method. As shown in the figure, the visible feature frequencies are seen around 131.80 Hz and at its multiple frequency (corresponding to the shock signal with the period of 0.0075 s) and around 200.20 Hz and at its multiple frequency (corresponding to the shock signal with the period of 0.005 s). Based on this, it can be correctly judged that a fault happens. However, as the discrete sampling and interception of the continuous signal cause the frequency spectrum leakage and barrier effect, the feature frequencies extracted by shock pulse frequency spectrum analysis method have some errors. Besides, the method cannot display the shock occurring time. In addition, the method also produces the unwanted 66.89 Hz difference frequency signal component.

Figure 10(e) shows the time-frequency spectrum obtained after the simulation signal $x(t)$ is processed by shock pulse time-frequency analysis method, with the short-time Fourier transform being used and the 0.16 s wide Gaussian window being selected. As shown in the figure, within the time period analyzed, the visible feature frequencies are seen around 131.80 Hz and at its multiple frequency (corresponding to the shock signal with the period of 0.0075 s) and around 200.30 Hz and at its multiple frequency (corresponding to the shock signal with the period of 0.005 s). Based on this, it can be correctly judged that a fault happens. In comparison with shock pulse frequency spectrum analysis method, time-frequency analysis method can analyze two dimensions, that is, time and frequency,

at the same time. However, as the method is restricted by the Heisenberg uncertainty principle, a certain width is present in the feature lines as shown in Figure 10(e), and the high time resolution and frequency resolution cannot be simultaneously achieved. Besides, the instantaneous feature frequencies extracted in this way have some resolution errors, and the shock sequence causes too many feature lines, which are thus not eye-striking enough.

Figure 10(f) shows the time-frequency spectrum obtained after the simulation signal $x(t)$ is processed by PATFTM (the amplitude threshold is set to be $0.03 \text{ mm}\cdot\text{s}^{-2}$, f_d 0 Hz, f_u 500 Hz, δ_1 1 Hz, δ_2 0.00005 s, and δ_3 $0.006 \text{ mm}\cdot\text{s}^{-2}$). The visible feature frequencies are seen at 133.30 Hz and 200.00 Hz (corresponding to the shock signals with the periods of 0.0075 s and 0.005 s, resp.), and thus the shock occurring frequency is accurately and clearly reflected. Based on this, it can be correctly judged that a fault happens. In contrast with the shock pulse frequency spectrum analysis method, which makes errors in the extracted feature frequencies due to such problems as frequency spectrum leakage and barrier effect and cannot supply high time resolution and frequency resolution at the same time owing to its restriction by the Heisenberg uncertainty principle, the PATFTM may, by setting minor tolerances δ_1 , δ_2 , and δ_3 , make the extracted instantaneous feature frequencies approach the theoretical value (as shown in Figure 10(f)) and provide high time-frequency resolution.

To sum up, PATFTM is capable of extracting the feature frequencies representing the rolling bearing damage effectively even in the presence of the strong background noise and other shock sources, and the feature frequency resolution supplied by the proposed method is higher than that by shock pulse frequency spectrum analysis method and shock pulse time-frequency analysis method.

To further validate the effectiveness of PATFTM and obtain the range of applicability of the method in the white noise environment, on the basis of the simulation signal $x_1(t)$, the simulation signals with different SNR (0 dB, -7 dB, -10 dB, and -11 dB) are made and used to do a comparative analysis experiment with shock pulse time-frequency analysis method.

In the experiment, short-time Fourier transform with a 40.96 ms wide Gaussian window is used for shock pulse time-frequency analysis method, while the parameters of the amplitude threshold, f_d , f_u , δ_1 , δ_2 , and δ_3 , are set the same as the parameters adopted in Figure 10(f) for PATFTM. The experimental results are shown in Figure 11.

Figure 11(a) shows the time domain waveform of the simulation signals with different SNR as above, and Figures 11(b) and 11(c) show the results of processing of these simulation signals by shock pulse time-frequency analysis method and PATFTM. The results show that, with the decrease in SNR, PATFTM receives little effect. When SNR is -10 dB, the method remains able to suppress noise and extract the instantaneous feature frequencies with high time resolution and frequency resolution. However, when SNR is -7 dB, the white noise will interfere with the performance of shock pulse time-frequency analysis method. Although the frequency resolution of the method can be improved through increasing

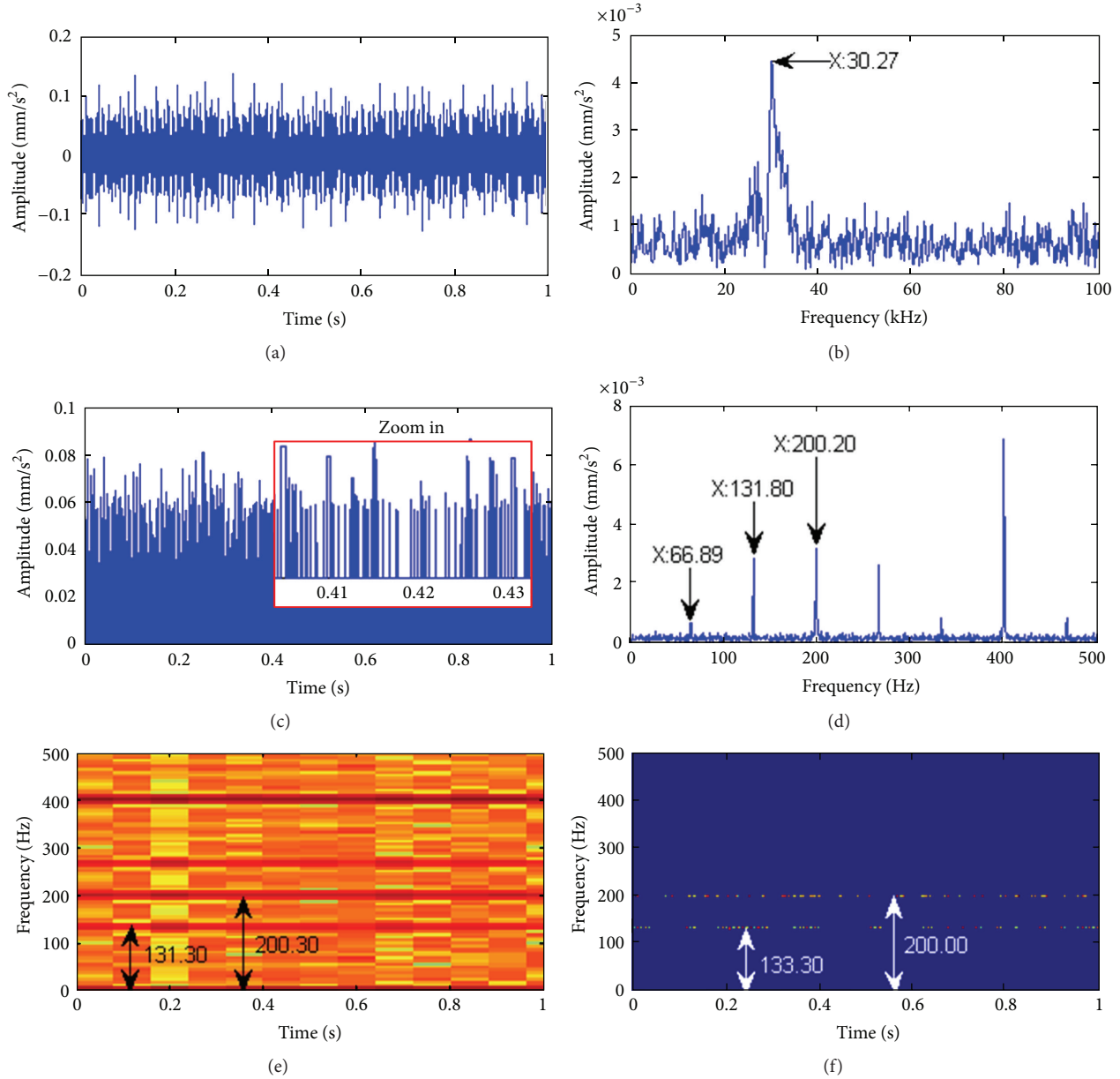


FIGURE 10: (a) The time domain waveform of $x(t)$; (b) the amplitude spectrum of $x(t)$; (c) the processing result of $x(t)$ by SPM; (d) the processing result of $x(t)$ by shock pulse frequency spectrum analysis method; (e) the processing result of $x(t)$ by shock pulse time-frequency analysis method; (f) the processing result of $x(t)$ by PATFTM.

the window width, the time resolution of the method will be lost.

In conclusion, the antinoise performance of the proposed method is much better than that of shock pulse time-frequency analysis method. Compared with shock pulse time-frequency analysis method, PATFTM can effectively suppress noise and extract the instantaneous feature frequencies with high time resolution and frequency resolution.

4.2. Analysis of Measured Data. To further validate the feasibility of PATFTM, the method is employed for processing and analyzing the measured data, and the results of processing and analysis are then compared with those of SPM, shock

pulse frequency spectrum analysis method, and shock pulse time-frequency analysis method. Figure 12(a) shows the time domain waveform of the acceleration signal acquired by the shock pulse sensor at the pedestal of the Timken 566 bearing with a faulty inner ring. Figure 12(b) shows the time domain waveform of the envelope signal obtained after measured data was demodulated. In the test, the device's rotation frequency is 2.0417 Hz. With reference to the structural parameters of the bearing and through the theoretical calculation [11], the fault feature frequency of the cage, rolling elements, outer ring, and inner ring of the bearing is obtained, that is, 0.89 Hz, 7.58 Hz, 17.77 Hz, and 23.06 Hz, respectively. Figures 12(c), 12(d), 12(e), and 12(f) show the results of processing

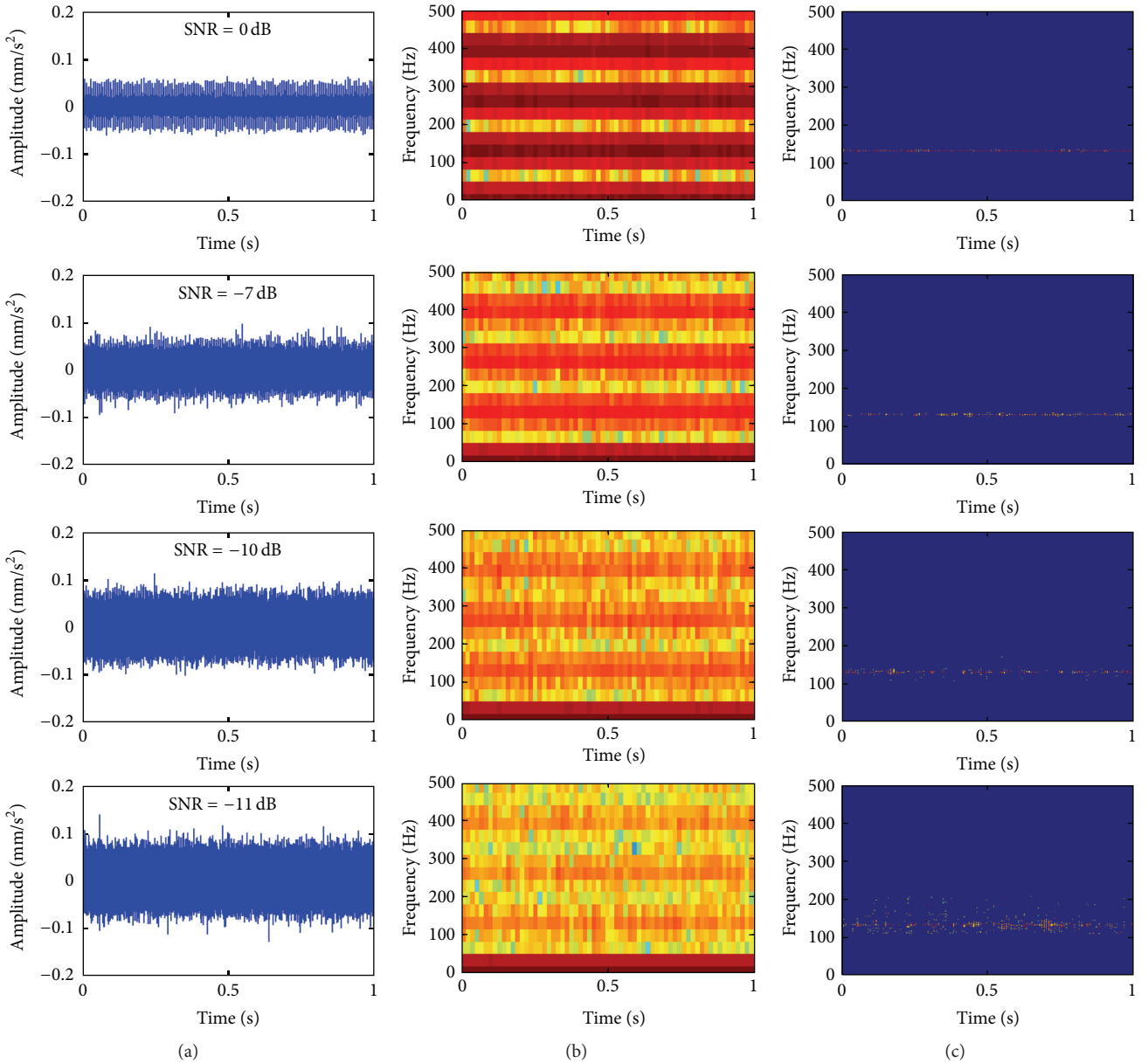


FIGURE 11: (a) The time domain waveforms of $x_1(t)$ with different SNR; (b) the processing results of $x_1(t)$ with different SNR by shock pulse time-frequency analysis method; (c) the processing results of $x_1(t)$ with different SNR by PATFTM.

of the signal as shown in Figure 12(a) by SPM, shock pulse frequency spectrum analysis method, shock pulse time-frequency analysis method, and PATFTM.

As shown in Figure 12(c), the periodical peak value takes place, and the value is great. So it can be judged that the bearing is damaged; however, which part of the bearing is damaged cannot be further judged. A series of 22.25 Hz harmonic frequencies and 22.25 Hz sideband frequencies, as shown in Figure 12(d), are close to the fault feature frequency of the inner ring obtained through theoretical calculation. Based on this, it can be judged that the inner ring of the bearing is damaged. In the frequency spectrum as shown in both Figures 12(e) and 12(f), the visible feature frequencies arise around 22.25 Hz, which are close to the fault feature frequency of the inner ring obtained through theoretical

calculation. So it can be judged that the inner ring of the bearing is damaged. However, with the almost same time resolution, Figure 12(f) can highlight the feature frequencies better than Figure 12(e) does, as well as with more accurate fault feature frequency extracted and higher resolution.

To sum up, PATFTM can be used for processing and analyzing the measured data well and extracting the fault feature frequencies representing the rolling bearing damage with high time resolution and frequency resolution.

5. Conclusions

(1) Conclusion of theoretical study analysis: PATFTM performs such processes as amplitude threshold processing, shock pulse ordering, instantaneous frequency calculation,

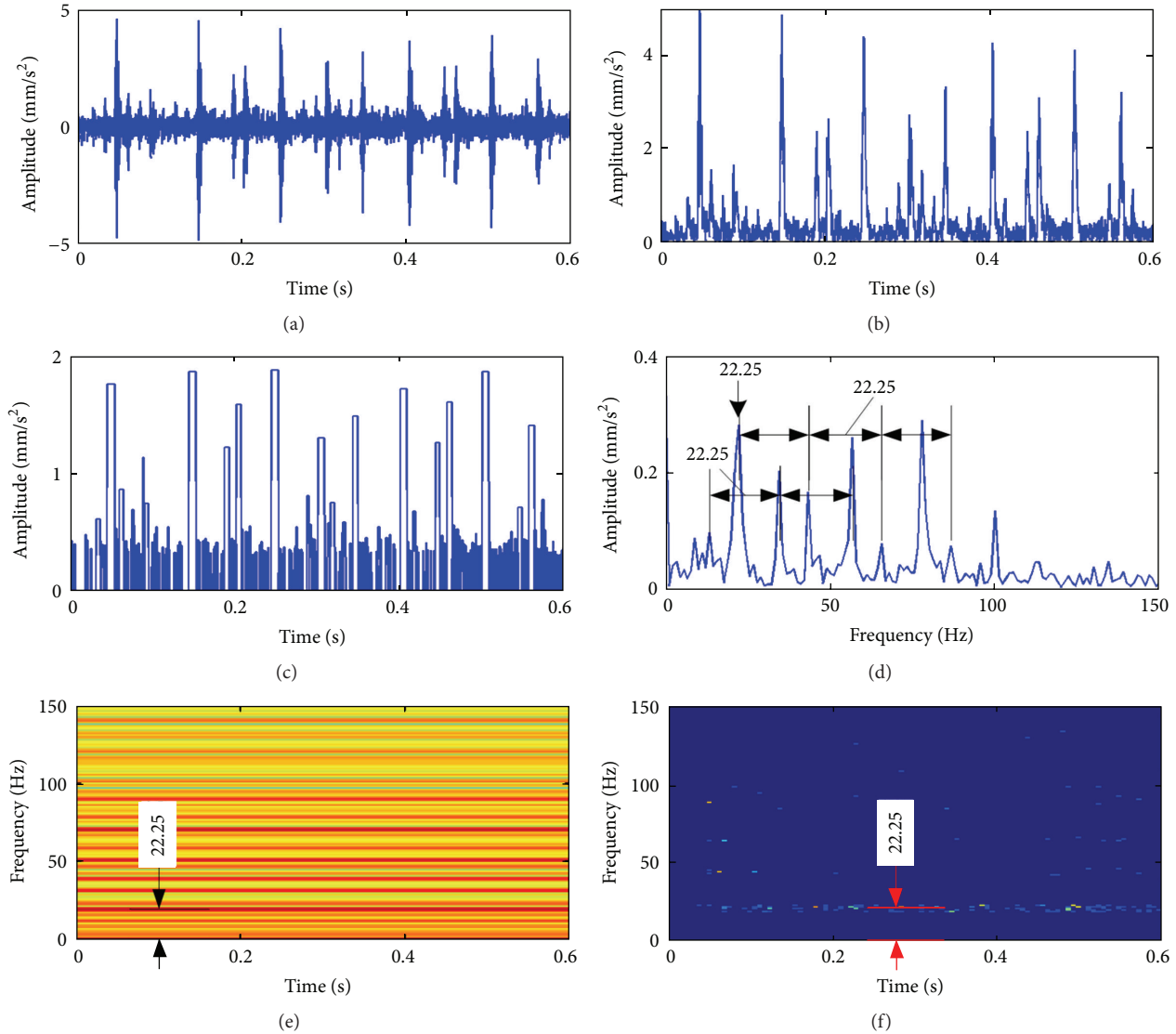


FIGURE 12: (a) The time domain waveform of the measured data; (b) the time domain waveform of the envelope signal of the measured data; (c) the processing result of the measured data by SPM; (d) The processing result of the measured data by shock pulse frequency spectrum analysis method; (e) the processing result of the measured data by shock pulse time-frequency analysis method; (f) the processing result of the measured data by PATFTM.

plane transformation of instantaneous frequency, and amplitude relevancy processing to the shock pulses extracted by SPM and transforms the shock pulse sequence of one-dimensional time domain into the two-dimensional time-frequency domain. Through the extraction of the effective instantaneous frequencies, it excludes the influences from other interference factors and highlights and extracts the fault feature representing the rolling bearing damage. The results of theoretical analysis show that the maximum time and frequency resolution of PATFTM is no longer restricted by the Heisenberg uncertainty principle but depends upon the measuring precision of the pulse arrival time. PATFTM can obtain the time-frequency spectrum with the high time and frequency resolution, and by extracting the effective instantaneous frequencies, it can greatly suppress the noises, accurately extract the feature frequencies,

and complete the rolling bearing fault diagnosis as desired.

(2) Conclusion of simulation experiment analysis: the results of the comparative simulation experiment in which the simulation signal produced by the inner ring damage, strong background noise, and other shock sources is made show that PATFTM is able to effectively extract the feature frequencies representing the rolling bearing damage even in the presence of the strong background noise and other shock sources, and the feature frequency resolution supplied by the method is higher than that by shock pulse frequency spectrum analysis method and shock pulse time-frequency analysis method. The results of the simulation experiment in which the simulation signals with different SNR are made show that PATFTM is little affected by noises and that when the SNR is -10 dB, the method can still suppress noises well

and extract the instantaneous feature frequencies with high time resolution and frequency resolution.

(3) Conclusion of measured data analysis: the results of measured data analysis show that PATFTM can effectively extract the fault feature representing the rolling bearing damage, and the extracted fault feature frequency accords with the theoretically calculated fault feature frequency. In addition, the same conclusion as that drawn in the simulation experiment is reached; that is, the resolution of the feature frequencies extracted by PATFTM is superior to that by shock pulse frequency spectrum analysis method and shock pulse time-frequency analysis method.

To sum up, the results of simulation and application analysis come in agreement with the results of theoretical analysis, and they both show that PATFTM can effectively suppress noises, highlight the feature frequencies, and avoid erroneous diagnosis. Thus, it is an effective method for extracting the rolling bearing fault features with high time and frequency resolution.

However, in the presence of strong background noise, although PATFTM is able to accurately diagnose the rolling bearing damage, it cannot qualitatively diagnose the wearout failure and poor lubrication in the rolling bearing. For this reason, PATFTM needs to be further studied and perfected.

Competing Interests

The authors declare no competing interests.

Acknowledgments

This work was supported in study design by the National Natural Science Foundation of China (Grant no. 51275546) and the Natural Science Foundation Project of Chongqing CSTC (Grant no. CQ cstc2011jjjq70001).

References

- [1] F. Zhang and K. Ding, "Research on the three algorithms and limitations of generalized detection-filtering demodulation analysis," *Journal of Vibration Engineering*, vol. 15, no. 2, pp. 243–248, 2002.
- [2] Y. B. Li, M. Q. Xu, H. Y. Zhao, Y. Wei, and W. Huang, "A new rotating machinery fault diagnosis method based on improved local mean decomposition," *Digital Signal Processing*, vol. 46, pp. 201–214, 2015.
- [3] C. T. Yiakopoulos and I. A. Antoniadis, "Wavelet based demodulation of vibration signals generated by defects in rolling element bearings," *Shock and Vibration*, vol. 9, no. 6, pp. 293–306, 2002.
- [4] R. Yan, R. X. Gao, and X. Chen, "Wavelets for fault diagnosis of rotary machines: a review with applications," *Signal Processing*, vol. 96, 15 pages, 2014.
- [5] H. C. Wang, J. Chen, and G. M. Dong, "Feature extraction of rolling bearing's early weak fault based on EEMD and tunable Q-factor wavelet transform," *Mechanical Systems and Signal Processing*, vol. 48, no. 1-2, pp. 103–119, 2014.
- [6] M. Zhao, J. Lin, X. Xu, and X. Li, "Multi-Fault detection of rolling element bearings under harsh working condition using imf-based adaptive envelope order analysis," *Sensors*, vol. 14, no. 11, pp. 20320–20346, 2014.
- [7] Y.-T. Sheen, "On the study of applying Morlet wavelet to the Hilbert transform for the envelope detection of bearing vibrations," *Mechanical Systems and Signal Processing*, vol. 23, no. 5, pp. 1518–1527, 2009.
- [8] Y. Qin, J. X. Wang, and B. P. Tang, "Multicomponent demodulation based on iterated Hilbert transform and its application," *Journal of Mechanical Engineering*, vol. 45, no. 8, pp. 37–44, 2009.
- [9] J. R. Stack, R. G. Harley, and T. G. Habetler, "An amplitude modulation detector for fault diagnosis in rolling element bearings," *IEEE Transactions on Industrial Electronics*, vol. 51, no. 5, pp. 1097–1102, 2004.
- [10] I. Moumene and N. Ouelaa, "Application of the wavelets multiresolution analysis and the high-frequency resonance technique for gears and bearings faults diagnosis," *The International Journal of Advanced Manufacturing Technology*, vol. 83, no. 5, pp. 1315–1339, 2016.
- [11] S. Patidar and P. K. Soni, "An overview on vibration analysis techniques for the diagnosis of rolling element bearing faults," *International Journal of Engineering Trends and Technology*, vol. 4, no. 5, pp. 1803–1809, 2013.
- [12] R. Yang, J. Kang, J. Zhao, J. Li, and H. Li, "A case study of bearing condition monitoring using SPM," in *Proceedings of the Prognostics and System Health Management Conference (PHM '14)*, pp. 695–698, Zhangjiajie, China, August 2014.
- [13] N. Tandon, G. S. Yadava, and K. M. Ramakrishna, "A comparison of some condition monitoring techniques for the detection of defect in induction motor ball bearings," *Mechanical Systems and Signal Processing*, vol. 21, no. 1, pp. 244–256, 2007.
- [14] H. Q. Sang, "Application on bearing detection in coal mine production," *Shanxi Coking Coal Science & Technology*, vol. 34, pp. 14–16, 2010.
- [15] L. Zhen, H. Zhengjia, Z. Yanyang, and C. Xuefeng, "Bearing condition monitoring based on shock pulse method and improved redundant lifting scheme," *Mathematics and Computers in Simulation*, vol. 79, no. 3, pp. 318–338, 2008.
- [16] D. E. Butler, "The Shock-pulse method for the detection of damaged rolling bearings," *Non-Destructive Testing*, vol. 6, no. 2, pp. 92–95, 1973.
- [17] V. Barzdaitis, V. Žemaitis, K. Žebelys, Z. Pocius, and P. Mažeika, "Condition monitoring of roller bearings using different diagnostic methods," *Diagnostyka*, vol. 30, no. 1, pp. 53–60, 2004.
- [18] Y. Zhang, L. Y. Lv, and S. T. Wan, "The shock pulse method applied on fault diagnosis of rolling bearing," *Petro-Chemical Equipment Technology*, vol. 28, no. 4, pp. 60–64, 2007.
- [19] J. Yan, "Research on diagnosing the fault in rolling bearing based on shock pulse method," *Compressor Blower & Fan Technology*, vol. 2, pp. 78–80, 2009.
- [20] W.-H. Yang and M.-G. Gao, "Deinterleaving of pulse signal based on plane transformation," *Transaction of Beijing Institute of Technology*, vol. 25, no. 2, pp. 151–154, 2005.
- [21] A. W. Ata'a and S. N. Abdullah, "Deinterleaving of radar signals and PRF identification algorithms," *IET Radar, Sonar and Navigation*, vol. 1, no. 5, pp. 340–347, 2007.
- [22] R. Parhizkar, Y. Barbotin, and M. Vetterli, "Sequences with minimal time-frequency uncertainty," *Applied and Computational Harmonic Analysis*, vol. 38, no. 3, pp. 452–468, 2015.

Research Article

Multiple-Fault Detection Methodology Based on Vibration and Current Analysis Applied to Bearings in Induction Motors and Gearboxes on the Kinematic Chain

Juan Jose Saucedo-Dorantes,¹ Miguel Delgado-Prieto,² Juan Antonio Ortega-Redondo,² Roque Alfredo Osornio-Rios,¹ and Rene de Jesus Romero-Troncoso³

¹CA Mecatronica, Facultad de Ingenieria, Campus San Juan del Rio, Universidad Autónoma de Querétaro, Rio Moctezuma 249, Colonia San Cayetano, 76807 San Juan del Rio, QRO, Mexico

²Technical University of Catalonia (UPC), Department of Electronic Engineering, MCIA Research Center, Rambla San Nebridi No. 22, Gaia Research Building, 08222 Terrassa, Spain

³CA Procesamiento Digital de Señales, CA Telematica, Division de Ingenierias, Campus Irapuato-Salamanca, Universidad de Guanajuato, Carretera Salamanca-Valle km 3.5 + 1.8, Comunidad de Palo Blanco, 36700 Salamanca, GTO, Mexico

Correspondence should be addressed to Rene de Jesus Romero-Troncoso; troncoso@hspdigital.org

Received 12 November 2015; Accepted 23 February 2016

Academic Editor: Konstantinos N. Gyftakis

Copyright © 2016 Juan Jose Saucedo-Dorantes et al. This is an open access article distributed under the Creative Commons Attribution License, which permits unrestricted use, distribution, and reproduction in any medium, provided the original work is properly cited.

Gearboxes and induction motors are important components in industrial applications and their monitoring condition is critical in the industrial sector so as to reduce costs and maintenance downtimes. There are several techniques associated with the fault diagnosis in rotating machinery; however, vibration and stator currents analysis are commonly used due to their proven reliability. Indeed, vibration and current analysis provide fault condition information by means of the fault-related spectral component identification. This work presents a methodology based on vibration and current analysis for the diagnosis of wear in a gearbox and the detection of bearing defect in an induction motor both linked to the same kinematic chain; besides, the location of the fault-related components for analysis is supported by the corresponding theoretical models. The theoretical models are based on calculation of characteristic gearbox and bearings fault frequencies, in order to locate the spectral components of the faults. In this work, the influence of vibrations over the system is observed by performing motor current signal analysis to detect the presence of faults. The obtained results show the feasibility of detecting multiple faults in a kinematic chain, making the proposed methodology suitable to be used in the application of industrial machinery diagnosis.

1. Introduction

Condition monitoring and fault diagnosis in rotating machinery are important topics in industrial applications. The most common rotating machines are induction motors and the associated kinematic chains which include gearboxes and are widespread in different applications. This topic has attracted the attention of many researchers over the last few years [1, 2], emphasizing the necessity of health monitoring and maintenance procedures in manufacturing operations in order to ensure equipment availability, product quality, on-time deliveries, and plant safety [3–6]. In many applications,

induction motors are connected to gearboxes [7, 8], and it is important to identify faulty conditions at an early stage while these elements are under operation along with the related kinematic chain. Although it has been shown that about 41% of the induction motor faults are due to bearing defects, this condition does not usually cause an immediate breakdown. In gearboxes, however, the possibility of gear fault appearing is lower, around 26%, but an early stage fault, as uniform wear, may cause severe consequences [9, 10]. Indeed, induction motors, gearboxes, and bearings represent critical components in the kinematic chain, and the presence of incipient faults may lead to unexpected interruptions

and nonproper operation in industrial processes [11–13]. Thus, the necessity of health monitoring schemes to consider multiple-fault sources is generating new investigations and methods based upon the condition monitoring field.

Condition monitoring applied to rotating machinery can be based on different physical magnitudes such as vibration, stator currents, and sound signals. Nevertheless, vibration based monitoring and motor current signature analysis represent the most accepted strategies. More than 82% of fault diagnosis methodologies have been done using vibration analysis [9, 14, 15]. Vibration analysis for monitoring rotating machines has been used during the last decades because of the dynamic forces within a rotating machine that produce a vibration force and the vibration pattern changes when a fault appears, even at an early stage. Thus, vibration analysis is a useful and reliable tool to assess the machinery condition [16–18]. Stator current based analysis has been also adopted by many researchers for condition monitoring in electrical rotating machines due to its advantages of being noninvasive and easy to use. Although vibration analysis is better suited for mechanical fault identification, the mechanical fault effects can also be detected by means of current analysis since the induction motor current consumption is modified by the mechanical efforts and vibrational modes in rotating machines [19–21]. Sound analysis is related to the use of acoustic emission signals; it has been applied during the last year in many research works and, similar to current analysis, it represents a noninvasive technique. Yet, due to the nature of the acoustic emission signals, the related processing is more complex, and the required sensors are more expensive than acceleration and Hall effect sensors. Therefore, mechanical faults detection can be addressed by means of vibration and current analysis, offering high reliability and moderate costs. In this regard, the fusion of both vibration and current analysis is expected to increase the multifault occurrence detection capabilities [22–25].

Many methodologies based on vibration analysis have been used for identifying specific faults in both induction motors and gearboxes. The most common analysis techniques are based on statistical time domain, frequency domain, and the joint time-frequency domain. The time domain analysis involves the extraction of specific features such as Root Mean Square (RMS), skewness, kurtosis, and crest factor. The best known methods regarding frequency domain and time-frequency domain analysis are the Fast Fourier Transform (FFT), Short-Time Fourier Transform (STFT), Continuous Wavelet Transform (CWT), and Hilbert Huang Transform (HHT) [26, 27]. In general, the specific technique is chosen according to the application. For instance, FFT is preferred when the analysis is performed over stationary signals having a low computational cost. Other methods are better suited when the signal is non-stationary. Regrettably, most of the condition monitoring techniques for early fault detection focus on the detection of single specific faults. For instance, in [28], a single fault in bearings is diagnosed and detected using HHT and Support Vector Machines (SVM) applied to the vibration signal. In [29] an incipient bearing fault classification was done using a vibration spectrum imaging under low signal to noise

ratio conditions. Also, some researchers are looking for the development of systems including monitoring and diagnosis capabilities; in this case, in [30], the authors developed a system for vibration signal monitoring in a rotating machine; with this system a classification between bearing defect and eccentricity was found. Other kinds of signal processing methods can be used; in [31] a method where the Kurtogram is obtained for a specific frequency band and the bearing condition is proposed. The detection of specific mechanical faults can be conducted by the use of different signals to those of vibration; bearing defect is one of the most common faults detected by performing a current signal processing; for instance, in [12] a method based on current analysis by performing also a Kurtogram extraction for detecting bearing faults in induction motors is proposed. The interest in studying the effects caused by bearing defects has increased during the last years, even new research and comparisons between vibrational and current signals have been carried out. In this sense, the works presented in [14, 18] proposed some techniques in which the bearing defect is detected and the vibration effects are reflected in current signals; their studies were focused on the relation between mechanical and electrical frequencies.

Unfortunately, most of the researches in condition monitoring around gearboxes are focused on the detection of discrete faults as broken teeth, and few works are related to the diagnosis and the identification of early stage faults as uniform wear. Li et al. [32] proposed a method for detecting advanced faults in gear based systems; the method was based on the vibration analysis using the HHT and the empirical mode decomposition. Nowadays, common applications are associated with gearboxes in their kinematic chain; for this reason condition monitoring in gearboxes is a current and important topic [33–35]. In this case, in [16], a spectral analysis is performed to monitor the amplitude increasing and the demodulation along the meshing frequency; these effects were produced by the pitting on the surface of the gear teeth studied. In [36] the gear condition is established using a frequency analysis applied to vibration signals; besides, a demodulation effect due to gear tooth damage is observed. Because a kinematic chain is composed of several elements, it may be possible that different faults caused by different elements would appear. However, there are just a few research works dealing with multiple faults occurrence and even fewer developments considering incipient stages in such multifault scenarios, as, for instance, the appearance of an incipient stage fault in a gearbox based on a uniform gear wear and its combination with a bearing defect. Some specific cases when multiple faults are analyzed exist because the studied faults are too severe; for instance, in [25], a technique based on vibration analysis for fault detection in a mechanical system is proposed; the considered faults were gear and bearing faults, but both are in an advanced fault stage.

It is possible to identify some lack of accuracy in a few of the aforementioned researches because in most of them a single fault in a specific element is studied; yet, in the presence of multiple faults, the use of different approaches is required to improve, or at least to maintain, the diagnosis capabilities. Furthermore, the use of techniques such as vibration and

current analysis represents the best option in multiple-fault detection because each technique has the ability of detecting a specific fault. Besides, with the monitoring of the most significant physical magnitudes in a specific process, it is possible to ensure its efficiency because any change presented in the signals patterns can be related to the fault appearance; these provide the motivation for conducting the present research. Furthermore, the combination of incipient faults with other faults in the kinematic chain has not been sufficiently studied. The novelty of this work lies in the proposal of a methodology based on vibration and current analysis for the diagnosis of uniform wear in a gearbox and the detection of bearing defect in an induction motor, both linked to the same kinematic chain.

Because there are not established schemes around the considered multifault scenario, the contribution of this work is the proposal and validation of a methodology for multiple faults identification in a kinematic chain and the knowhow of both uniform wear in a gearbox and induction motor bearings in a faulty stage, which produce changes along the kinematic chain behavior such as speed variations, current consumptions in the induction motor, the addition of nonlinear frequency components, or the transmission of vibration modes. The vibration analysis is done by means of a spectral analysis; part of the proposed methodology is based on extracting some characteristic frequency components from a theoretical model. The analysis is based on the amplitude increase and the spectral modulation in order to quantify the uniform wear level in the gearbox and the bearing defect presence. Similarly, the current analysis is confronted by the motor current signal spectral analysis in order to identify and corroborate the presence of the faults while observing the vibrational effects. Thus, the presence of multiple faults can be detected by using two different signatures in a condition monitoring process; the use of different signals makes the methodology more reliable in the diagnosis and detection of multiple faults. The obtained results from the proposed methodology show that it is possible to identify the frequency components associated with the studied faults and their mixing.

2. Theoretical Background

2.1. Vibration in Rotating Machinery with Gears. The mechanical vibrations in the study of rotating machinery with gears are inherent to its operation because these are generated by the backlash or the excitation of the dynamic forces induced when the gear teeth enter in contact; consequently, at higher backlash, the vibration amplitude is higher. Moreover, variations at speed and load also contribute to vibrations in systems with gears, when the gear teeth enter in contact producing an impact frequency called mesh frequency (f_m) and it is the main frequency at which gearing induces vibrations and it is given by

$$f_m = N \cdot f_r, \quad (1)$$

where N is the teeth number and f_r is the rotational frequency of the input or output shaft to analyze. It is useful

to note that several gear meshing frequencies are present in a complex gear train [36–38].

The most common gear fault is a discrete gear tooth irregularity such as a broken or chipped tooth. With a single discrete fault, the increase in levels of noise and vibrations can be expected at the shaft rotational frequency and its corresponding associated harmonics. These narrowband peaks are in addition to the various gear meshing frequencies and their associated harmonics. Also, discrete faults tend to produce low-level, flat, sideband spectra around the mesh frequency and its harmonics.

For gearboxes in good condition, the vibration spectra commonly show the input and output shaft frequencies as well as the mesh frequency with sideband frequencies (f_{sideband}) (2) around the mesh frequency and its corresponding harmonics. A theoretical spectrum vibration for a healthy gearbox is shown in Figure 1(a):

$$f_{\text{sideband}} = f_m \pm f_r. \quad (2)$$

Such f_{sideband} typically arises from the modulation of the tooth meshing waveform by the gear rotational frequency. When the teeth are in good condition and the gears are concentric, the amplitude of f_m and f_{sideband} and its harmonics are low. On the other hand, an increase of amplitude in f_m and f_{sideband} and its harmonics is associated with uniform wear as shown in Figure 1(b); the increase of these frequency components and their associated harmonics is typical criterion for fault detection. Given that for a pair of gears, f_m is the same, then the information contained in f_{sideband} allows knowing which one is the worn gear; this is determined since each gear has different f_r .

Gearboxes are considered as a complex system in rotating machines; this consideration is due to the appearance of nonlinear vibration and the addition of unexpected frequency components, along with the combination of higher operating speeds [38]. Additionally, the modulation and the appearance of nonlinear frequencies in gearboxes also depend on and can be generated by the material used in their construction and the linked elements inside the gearbox like bearings. In this sense, the existence of theoretical mechanical models with actual approaches may lead to understanding the behavior of these phenomena in gearbox systems [39].

2.2. Bearing Defect. In machine condition monitoring, much attention is generally given to bearing condition because it is the most common component; the rotational movement in bearing elements generates vibrational excitation at a series of discrete frequencies. Some researches give a review of the causes and expected frequencies of vibration due to bearing defects [11, 17, 18]. The characteristic frequencies regarding bearing defect are theoretically well known; these frequencies are mainly computed from the rotational frequency and the bearing geometry. These characteristic frequencies are the inner and outer race elements pass frequencies (f_{BPIF} , f_{BPOF}),

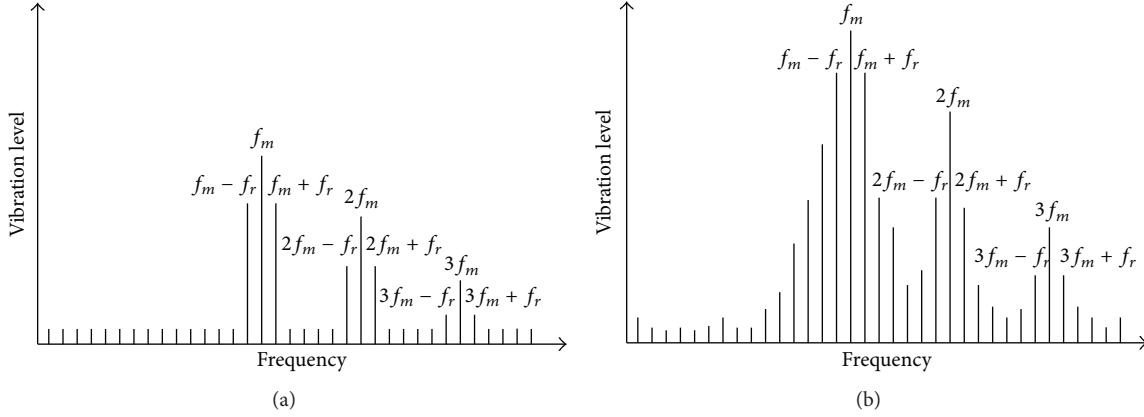


FIGURE 1: Typical vibration spectrum of a gearbox in (a) healthy condition and (b) with uniform wear.

the frequency of rotation for the cage (f_{FTF}), and rolling element spin frequency (f_{BSF}). Their corresponding expressions are as follows:

$$f_{\text{BPIF}} = \frac{f_r}{2} N_b \left(1 + \frac{D_B}{D_C} \cos \theta \right), \quad (3)$$

$$f_{\text{BPOF}} = \frac{f_r}{2} N_b \left(1 - \frac{D_B}{D_C} \cos \theta \right), \quad (4)$$

$$f_{\text{FTF}} = \frac{f_r}{2} \left(1 - \frac{D_B}{D_C} \cos \theta \right), \quad (5)$$

$$f_{\text{BSF}} = \frac{D_C}{2D_B} f_r \left(1 - \left(\frac{D_B}{D_C} \right)^2 (\cos \theta)^2 \right), \quad (6)$$

where f_r is the rotational frequency at which the inner raceway rotates, D_C is the cage diameter measured from a ball center to the opposite ball center, D_B is the ball diameter, N_b is the number of balls, and θ is the contact angle between the bearing surfaces.

The excitation of the previous frequencies can be used in bearing fault detection because these frequencies would appear in the vibration spectrum. The primary source of noise and vibration in rotating machinery with bearing defects is due to the mechanical impact produced by the rolling elements over the bearing races. When the bearing defect is located in the outer race it will cause an impulse each time the rolling elements contact the defect; sometimes the modulation effect is present in the vibration signal; this phenomenon can be explained by different causes such as nonuniform load, flexural bearing modes, and vibrations induced by other elements in rotating machinery [17].

The vibration component effect on the current is modeled as a static eccentricity; in this case bearing faults generate stator currents at predictable frequencies related to the mechanical characteristic frequencies (f_{BPIF} , f_{BPOF} , f_{FTF} , f_{BSF}) and electrical supply frequency (f_s); for this study the following equation represents the link between vibration and current components [14]:

$$f_{\text{BE}} = f_s \pm k f_{\text{BPOF}}, \quad (7)$$

where $k = 1, 2, 3, \dots$

3. Methodology and Experimental Setup

This section shows the proposed methodology and the description of the experimental setup for the diagnosis of wear in a gearbox and the detection of bearing defect in an induction motor; both faults are over the same kinematic chain.

3.1. Methodology. The flow chart of Figure 2 depicts the proposed methodology. This work is focused on the detection of different faults. First, the different studied conditions are defined as healthy, three levels of wear on the gearbox, the bearing defect, and the blending of each wear level with the bearing defect. These faults are artificially made, and the damaged elements are replaced in a specific kinematic chain for carrying out different experiments. Also, different rotating frequencies for each experiment are used in order to observe the speed dependencies for every studied fault.

Afterwards, vibration data are acquired from a triaxial accelerometer placed on the top of the gearbox. Besides, the motor current and the rotating speed are acquired from the Hall effect sensors and a digital encoder, respectively. In order to obtain the kinematic chain vibration, the motor current, and the rotational frequency, all the data are captured during the operation of the kinematic chain in each studied condition for all the different experiments executed. Then, the spectral analysis is performed consisting in applying a Hanning time window to the vibration and current signals to reduce the spectral leakage. The FFT and the Power Spectral Density (PSD) are then computed to get the vibration and current spectra to be analyzed.

After that, with the aim of locating a specific bandwidth to find the spectral frequency components that are related to each studied condition, the theoretical frequencies are computed. Therefore, these values are obtained by replacing the speed acquired, the characteristics of the gearbox, and the bearing geometry in (1), (4), and (7). The computed frequencies are summarized in Table 1. It is important to mention that these values correspond to approximations and are subjected to suffer variations (not greater than 3% of the expected value) due to the operating conditions.

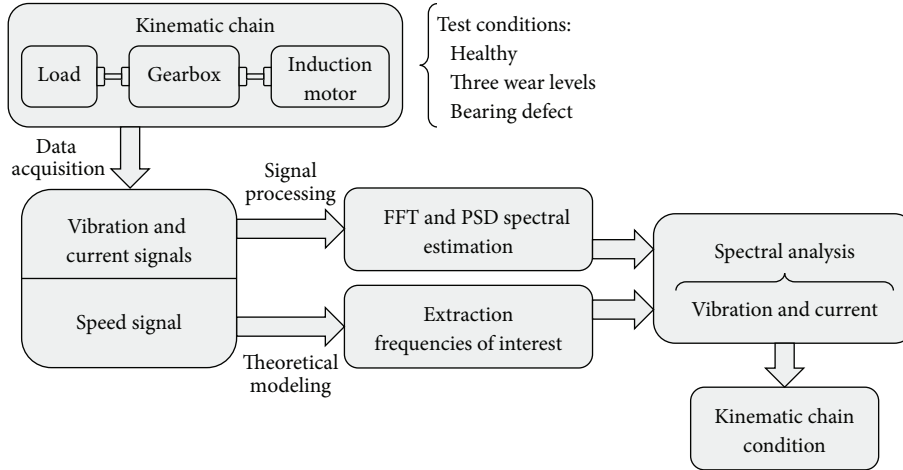


FIGURE 2: Flow chart of the proposed methodology.

TABLE 1: Computed frequencies of interest.

Rotational speed (rpm)	Frequencies of interest (Hz)					
	f_m	$2f_m$	f_{BPOF}	$2f_{\text{BPOF}}$	f_{BE}	f_r
293.4	88.02	176.04	17.50	35	21.99	4.89
889.28	266.79	533.58	53.06	106.12	67.88	14.82
2984.4	895.32	1790.65	178.09	356.18	227.83	49.74

Then, the frequencies of interest associated with the studied cases are located in both vibration and current spectra. For the purpose of quantifying the severity of the fault, a comparison in the amplitude increase between related frequencies in the healthy and faulty stage is performed. Finally, for each different experiment, the kinematic chain condition is given according to the proposed criteria of evaluation.

3.2. Test Bench. The test bench used for testing the kinematic chain with different faults and the acquisition system used to capture the vibration and current signals is shown in Figure 3. The test bench consists of a 1492-W, three-phase induction motor (WEG 00236ET3E145T-W22), with its rotational speed controlled through a variable frequency drive (VFD) (WEG CFW08), set to different frequencies. A 4:1 ratio gearbox (BALDOR GCF4X01AA) is used for testing the different levels of uniform wear studied in this work, and a DC generator (BALDOR CDP3604) is used as the mechanical load comprising around 20% of the nominal load. The vibration signals are acquired using a triaxial accelerometer (LIS3L02AS4), mounted on a board with the signal conditioning and antialias filtering, and the current signals are acquired by using a Hall effect sensor (L08P050D15), from Tamura Corporation. Two 12-bit 4-channel serial-output sampling analog-to-digital converters (ADS7841) are used on board of data acquisition system (DAS), with a sampling frequency of 3 kHz for vibration signal acquisition and a sampling frequency of 4 kHz for current signal acquisition, obtaining 60 kS and 80 kS, respectively, during 20 seconds of

the induction motor from start-up to steady state. The DAS is a proprietary low-cost design based on field programmable gate array technology (FPGA). The output rotational speed is captured using a digital encoder; the motor start-up is controlled by a relay in order to automatize the test run. All the aforementioned data are stored in a personal computer (PC) and analyzed under MATLAB, which is used for signal processing to compute the spectra of the vibration and current signals for each studied condition. The proposed method, implemented under MATLAB, consists of two Hanning filters so as to filter each of the acquired signatures; then, two 4096-point FFT are applied over the complete range of frequency for each signal and finally for the current signal the PSD is computed. These processing methods represent low computational cost and they are standard procedures that can be easily implemented in embedded systems for online operation, such as field programmable gate arrays. Some instances of the implementation of FFT and other standard signal processing methods can be found in [40, 41].

3.3. Description of the Studied Faults. As aforementioned, wear in gears and bearing defect are the studied faults. The considered fault in gears is a uniform wear due to the nonexistence of reported scientific studies using vibration analysis in gradual faults monitoring like uniform wear. Three levels of worn gears, which have 72 teeth, are used in this work to analyze different vibration effects in the kinematic chain and validate the ability of the proposed methodology to distinguish different levels of wear on the gears. The three levels of wear are artificially made at the gear factory, and it was induced for all teeth in a uniform way. Figures 4(a)–4(d) show the gears studied in this work: healthy and 25%, 50%, and 75% of wear, respectively. As mentioned, the vibration characteristic-defect frequencies are calculated using the gearbox characteristics and the speed acquired in (1).

Regarding the bearing defect, an artificial damage is produced by drilling a hole with 1.191 mm of diameter on the bearing outer race using a tungsten drill bit. This fault

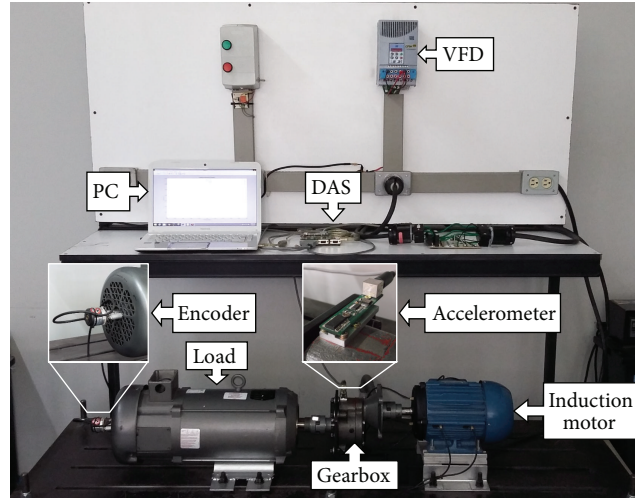


FIGURE 3: Test bench used for experimentation.

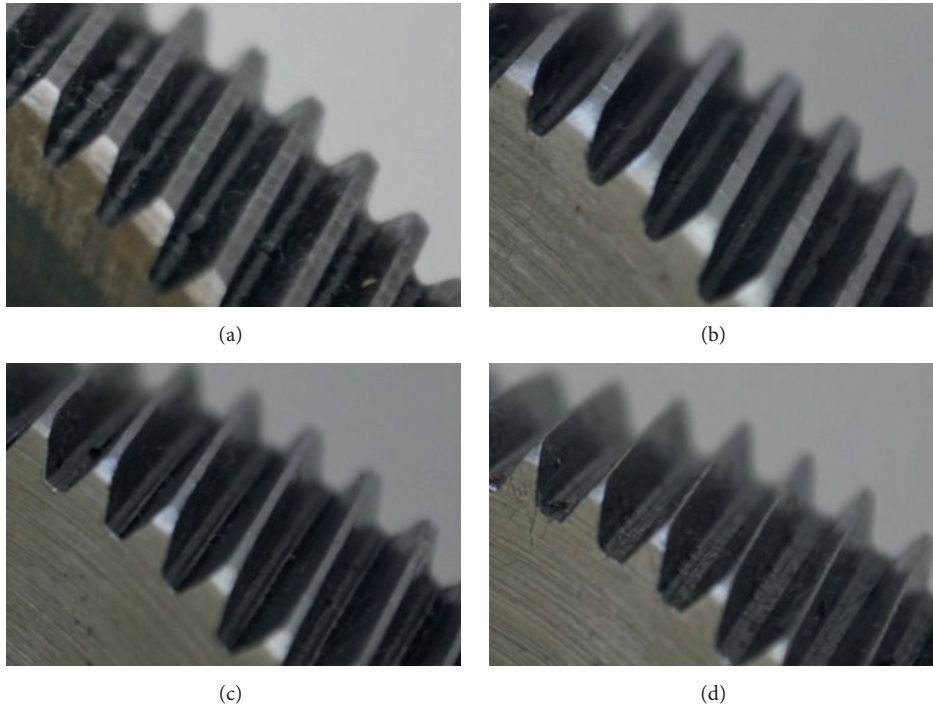


FIGURE 4: Treated gears: (a) healthy and (b) 25%, (c) 50%, and (d) 75% of wear.

has been used and reported in different studies [5, 11], and the artificial damaged bearing model 6205-2ZNR used in this experimentation is shown in Figure 5. Using (4) the vibration characteristic-defect frequency of the rolling element bearing outer race is calculated; then using f_{BPOF} into (7) the current characteristic-defect frequency related to the vibration defect is also calculated. The induction motor has different rotor frequencies; the test bearing has nine balls of 7.9 mm diameter and the cage diameter of the bearing is 39 mm with a contact angle $\theta = 0^\circ$.

4. Results and Discussion

The results provided in this section are obtained by applying the proposed methodology. The experiments were carried out by replacing the healthy gear with one of the worn gears iteratively and combining each gear wear level with the bearing defect. As it has been mentioned, for each experiment, vibration, current, and speed signals are acquired. In this sense, the operational rotating frequency is computed through the speed signal given by the digital encoder. Although



FIGURE 5: Outer race damaged bearing.

some specific frequencies such as 5 Hz, 15 Hz, and 50 Hz are established in the VFD, the output operational frequency for each case is slightly below the set-point frequency because of the slip in the rotor, as it is shown in Table 1. The main purpose of the research is the vibration analysis and the current analysis of the fault-related components as calculated from the theoretical model. Then, the diagnosis in rotating machinery at different fault stages through signal processing is made. The nature of the considered faults implies generation of shock impulses along the kinematic chain, which means that time domain based vibration analysis is not suitable for detection. Thus, the acquired vibration data are analyzed with the FFT and the acquired motor current data are analyzed with the PSD. The FFT technique has some disadvantage in the analysis of signals when the characteristic frequencies of the system are nonstationary. The use of VFD to feed the motor implies that the system can operate at different supply frequencies. The FFT is suited for analyzing the signals from this system, as long as the operating frequency at the VFD is set and the steady state is reached because the system is stationary under these conditions. Yet, under these steady state operating conditions, if the mechanical load varies during the operations, the performance of the FFT method can be affected. For this study, the conditions are kept to avoid load variations during steady state operation.

Considering the vibration signal, the best results are obtained from the perpendicular plane to the shaft; this is due to the fact that treated faults tend to generate radial forces that are converted into vibration motion in this direction. Consequently, vibration spectra shown in Figure 6 correspond to the healthy stage and a 50% of uniform wear when the VFD is set to 15 Hz. In these spectra it is possible to detect significant frequencies such as the rotational frequency ($f_r = 14.65$ Hz), the mesh frequency ($f_m = 267.3$ Hz), the ball pass outer race frequency ($f_{\text{BPOF}} = 52.73$ Hz), and their corresponding second harmonic ($2f_m = 534.7$ Hz, $2f_{\text{BPOF}} = 104$ Hz, and $4f_{\text{BPOF}} = 208$ Hz). Figure 6(a) shows the spectrum for the healthy condition; in this spectrum the related frequencies are present with a low amplitude level; also the appearance of unexpected vibration components is present in the spectrum; specifically around the second harmonic in the $2f_m$,

the lateral sidebands are full of additional frequency components. On the other hand, Figure 6(b) shows the spectrum for the experiment with 50% of uniform wear; the frequency amplitude increases significantly in this case. As well as in the healthy stage, the addition of frequency components appears around f_m and $2f_m$, but in this spectrum these frequencies have higher amplitude than the additional components.

A relevant feature of both spectra is the appearance of the sideband frequencies, related to the rotating speed, near the mesh frequency and its harmonics. The amplitude increase in these regions allows the identification of the gearbox frequency and fault presence. Besides, bearing frequencies are present with lower amplitudes because the bearing vibration amplitude is lower in comparison with gearbox vibration amplitude; yet, the bearing-related frequencies appear in the spectrum.

Figure 7 shows some of the obtained spectra of the vibrational behavior when the healthy stage, 75% of wear, bearing defect, and their mixing are tested at 5 Hz. For each of these vibration spectra it is possible to identify the fault-related frequency components, which are associated with the rotating frequency ($f_r = 4.83$ Hz), the mesh frequency ($f_m = 87.89$ Hz), the ball pass outer race frequency ($f_{\text{BPOF}} = 17.21$ Hz), and their corresponding harmonics ($2f_m = 176.1$ Hz, $3f_m = 264.8$ Hz, $2f_{\text{BPOF}} = 34.06$ Hz, and $3f_{\text{BPOF}} = 53.1$ Hz).

For the spectrum in the healthy condition shown in Figure 7(a) it is possible to notice that the fault-related frequencies have low amplitude in comparison with all of the others spectra, especially the gearbox frequencies. In the presence of the bearing fault when the gear is in a good condition as Figure 7(b) shows, the amplitudes of the frequencies remain on the same approximated level. However, the appearance of frequency components in both spectra is inevitable in the closest region to the mesh frequency sidebands and its harmonics.

On the other hand, the spectrum in Figure 7(c) corresponds to a faulty gear with 75% of uniform wear; the increases in $2f_m$ and $3f_m$ are revealing the wear presence in the gearbox. Moreover, when 75% of uniform wear and bearing defect are mixed the fault-related frequencies have an amplitude increase as spectrum of Figure 7(d) shows; in this spectrum the wear presence is detected by the increase in their harmonics of f_m . Also the appearance of frequency components inherent to the gearbox operation is a problem for the bearing defect identification due to bearing vibrations which have lower amplitude.

Although the accelerometer sensor is placed on the top of the gearbox, bearing vibration is transmitted through the kinematic chain and acquired by the accelerometer. Aside the principal frequencies of interest, all the spectra show different frequency components that do not correspond directly to some fault-related component; the reason is that complex elements as gearboxes and bearings both linked to a kinematic chain tend to generate nonlinear vibrations [39]. Once the tests were performed, they are analyzed through vibration spectra and similar increase in the amplitude is obtained. Results are summarized numerically from Tables 2 to 7, where tables are split up according to the operating

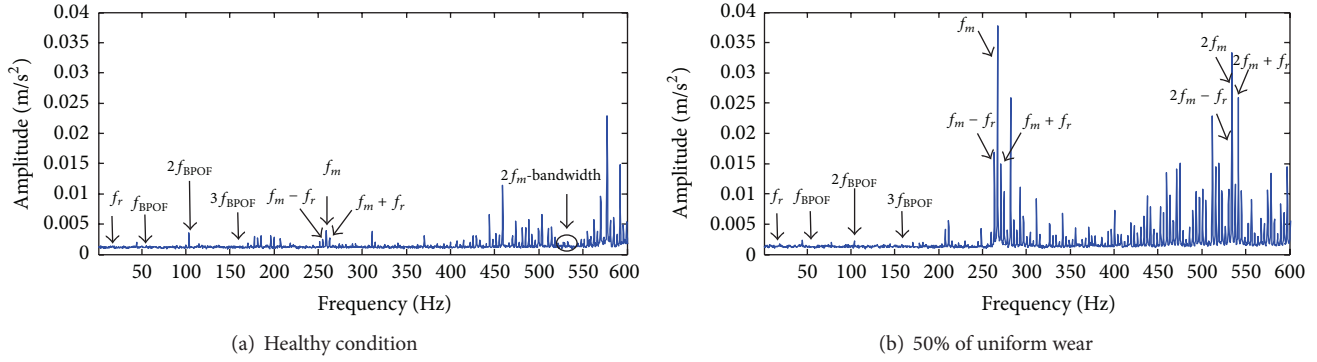


FIGURE 6: Vibration spectra of the experiment with VFD set to 15 Hz.

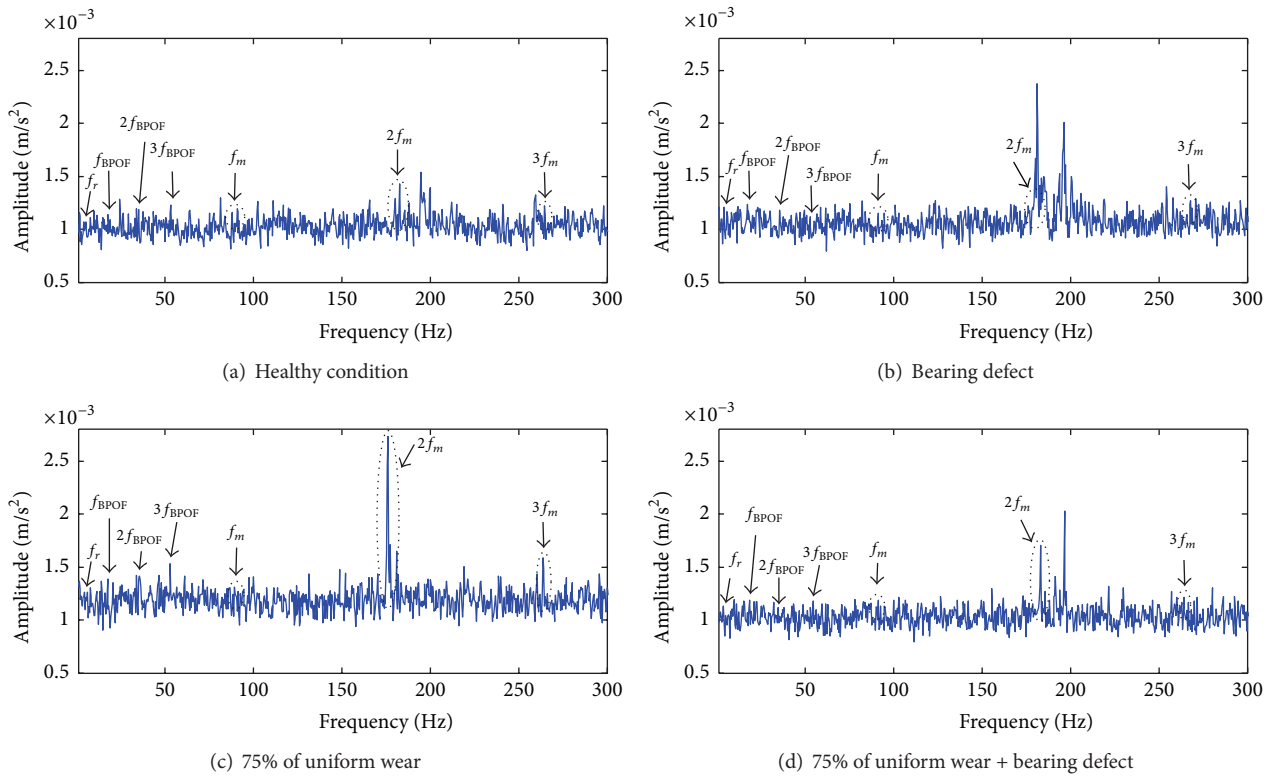


FIGURE 7: Vibration spectra of the experiment with VFD set to 5 Hz.

frequency and each one of these is divided by the bearing defect appearance.

By carrying out different experiments at different conditions and according to results, lower operating frequencies like 5 Hz and 15 Hz allow knowing gear condition by the amplitude increase in f_m , $2f_m$, and $3f_m$ when the bearing defect is not considered, where the most significant results are given by $2f_m$ amplitude increase. On the contrary, in the presence of bearing defect, the amplitude increases in f_m and its harmonics also increase and appear in an irregular way; this phenomenon is generated by the combination and transmission of vibration through the kinematic chain. A low-level increase in amplitude is not expected in f_{BPOF} frequency; for this reason, the bearing defect appearance is

not evident in each treated case, but sometimes it is possible to be detected by the amplitude increase in its second and third harmonics. It is clear that the bearing vibration tends to modify the behavior in the kinematic chain; furthermore, any kind of defect included in the kinematic chain adds components in the vibration spectrum.

Spectral analysis at lower operating frequencies is suitable in the detection of uniform wear in gearboxes since the quantification of the vibration levels in the frequencies of interest has a monotonic behavior, which grants the diagnosis of the levels of wear in the gearbox. In Figures 8(a)–8(c) the vibration spectra are shown for all levels of wear in the first, second, and third harmonics when the operating frequency is set to 15 Hz and the bearing defect is not

TABLE 2: Amplitude at the frequencies of interest for each gear condition without bearing defect and VFD set to 5 Hz.

Condition	Amplitude ($\times 10^{-3}$ m/s ²)					
	f_m	$2f_m$	$3f_m$	f_{BPOF}	$2f_{BPOF}$	$3f_{BPOF}$
Healthy	1.160	1.291	1.223	1.141	1.197	1.226
25%	1.193	1.372	1.805	1.252	1.228	1.198
50%	1.146	1.454	2.694	1.218	1.265	1.284
75%	1.131	2.737	1.588	1.387	1.424	1.530

TABLE 3: Amplitude at the frequencies of interest for each gear condition with bearing defect and VFD set to 5 Hz.

Condition	Amplitude ($\times 10^{-3}$ m/s ²)					
	f_m	$2f_m$	$3f_m$	f_{BPOF}	$2f_{BPOF}$	$3f_{BPOF}$
Healthy	1.155	1.220	1.271	1.123	1.177	1.111
25%	1.203	1.275	1.397	1.212	1.169	1.223
50%	1.206	1.364	2.774	1.217	1.170	1.338
75%	1.188	1.708	1.215	1.190	1.111	1.178

TABLE 4: Amplitude at the frequencies of interest for each gear condition without bearing defect and VFD set to 15 Hz.

Condition	Amplitude ($\times 10^{-3}$ m/s ²)					
	f_m	$2f_m$	$3f_m$	f_{BPOF}	$2f_{BPOF}$	$3f_{BPOF}$
Healthy	3.979	2.095	6.050	1.182	1.144	1.305
25%	15.96	7.438	6.821	1.322	1.178	1.363
50%	37.75	33.31	28.46	1.347	1.405	1.347
75%	42.29	34.48	30.09	1.461	1.322	1.345

TABLE 5: Amplitude at the frequencies of interest for each gear condition with bearing defect and VFD set to 15 Hz.

Condition	Amplitude ($\times 10^{-3}$ m/s ²)					
	f_m	$2f_m$	$3f_m$	f_{BPOF}	$2f_{BPOF}$	$3f_{BPOF}$
Healthy	2.482	4.673	8.622	1.204	1.352	1.427
25%	6.522	6.016	9.611	1.276	1.381	1.233
50%	13.93	9.154	13.11	1.432	1.414	1.427
75%	5.154	6.235	6.344	1.375	1.284	1.412

TABLE 6: Amplitude at the frequencies of interest for each gear condition without bearing defect and VFD set to 50 Hz.

Condition	Amplitude ($\times 10^{-3}$ m/s ²)			
	f_m	f_{BPOF}	$2f_{BPOF}$	$3f_{BPOF}$
Healthy	26.73	2.491	5.538	8.179
25%	31.67	1.551	1.721	8.298
50%	40.92	1.659	4.265	17.15
75%	19.69	2.628	3.474	12.49

present. An important part of these spectra is the amplitude increase at f_m , $2f_m$, and $3f_m$ due to wear influence, and the difference between each one of these and their side bands is approximately f_r of the wear with damage.

Spectral analysis at high operating frequencies somewhat limits the ability to detect faults; the disadvantage is that at

TABLE 7: Amplitude at the frequencies of interest for each gear condition with bearing defect and VFD set to 50 Hz.

Condition	Amplitude ($\times 10^{-3}$ m/s ²)			
	f_m	f_{BPOF}	$2f_{BPOF}$	$3f_{BPOF}$
Healthy	28.79	3.832	1.248	3.326
25%	10.27	4.005	1.527	7.018
50%	58.26	5.194	1.609	5.52
75%	23.79	6.364	1.811	5.857

higher operating frequencies f_m value increases considerably and sometimes the bandwidth in the accelerometer is not enough to acquire high frequencies generated by mechanical components such as gearboxes.

Another disadvantage is that at higher operating frequencies the addition of frequency components is inherent in the kinematic chain, causing the vibration concealing related to some specific fault. Results obtained by experimental tests at 50 Hz of operating frequency do not allow detecting the wear appearance in the gearbox because the amplitude does not exhibit a monotonic behavior for any of the related gearbox frequencies. Also, the bearing defect is not perfectly identified through spectral analysis. Although the treated faults are not perfectly detected at higher operating frequencies, the appearance of amplitude oscillations is generated by both treated faults.

The proposed methodology involves a current analysis, in order to observe the effects caused by vibrations and to identify different behaviors related to the studied faults. In this sense, for each experiment carried out, the PSD is obtained from the motor current signals. The current analysis is mainly focused on f_s ; both studied faults have influence in the motor consumption. When the experiments are carried out and the VFD is set to 5 Hz the current analysis lacks information connected to the studied faults. Otherwise, when the VFD is set to 15 Hz and 50 Hz, by performing a current analysis, it is possible to identify changes in the PSD for each studied condition.

The studied faults have their fault-related frequencies in the vibration analysis; therefore the bearing defect has a defined effect in the motor current signal, as Section 2 describes. On the other hand, the gearbox fault presence does not have a specific effect defined; however, according to [33], the appearance of any incipient gear fault may not consistently affect the amplitude of rotating and mesh frequencies in the electrical signal but give rise to those of rotation harmonics and the lateral components appearance. Thus, in Figure 9(a) is shown the PSD for the healthy stage and all levels of uniform wear, with the VFD set to 15 Hz as f_s . It is possible to observe some sidebands around the central frequency; the modified behavior in each one of these sidebands is generated due to uniform wear influence. In the spectra of Figure 9(b) it is possible to observe and compare the healthy stage, bearing defect, 75% of wear, and their mixing tested at 15 Hz because in the presence of uniform wear when the bearing defect appears, an increase is observed in these sidebands, as well as a change in the waveform.

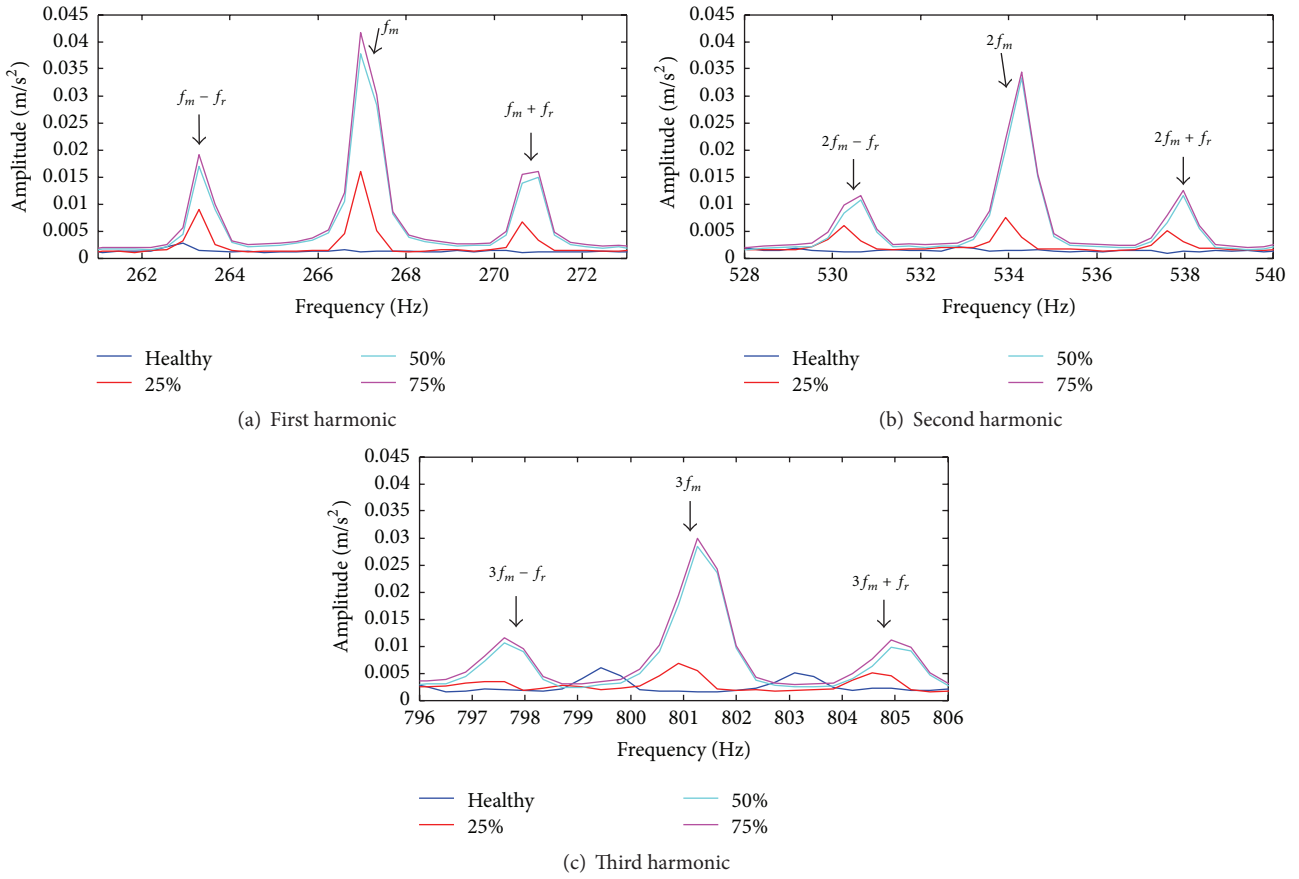


FIGURE 8: Vibration spectra for all gear conditions with VFD set to 15 Hz.

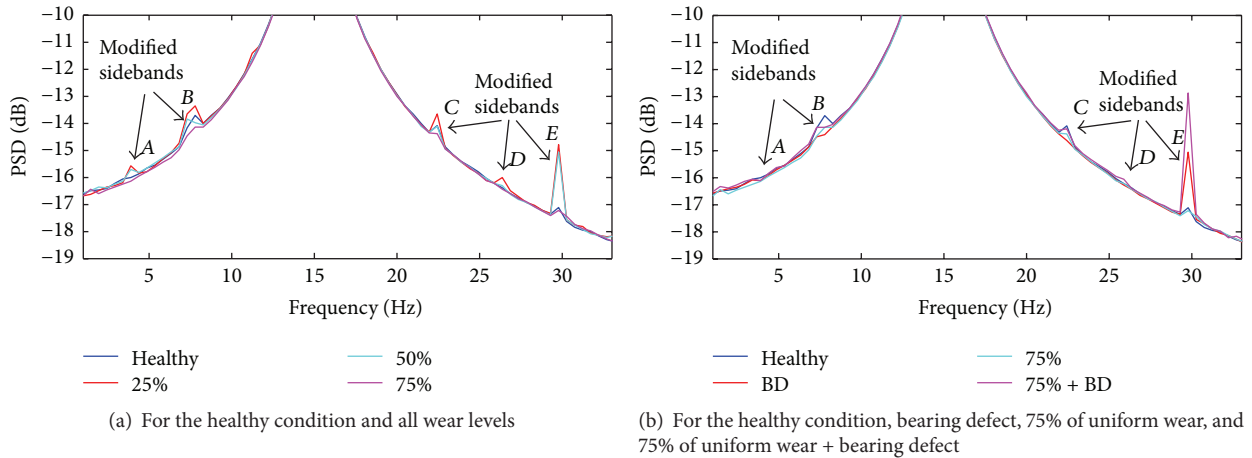


FIGURE 9: PSD spectrum from current signal when VFD is set to 15 Hz.

The studied faults have more influence when the VFD is set to 50 Hz; then in the spectra of Figure 10(a) the health condition and all the wear levels are shown. It is possible to notice the uniform wear effects; in these spectra the sideband frequencies appear and one of these is related to the f_r of the worn gear; although the amplitude increase is not present in monotonic way, the amplitude modification allows

knowing the presence of incipient faults as uniform wear. In spectra of Figure 10(b) the healthy condition, bearing defect, 75% of wear, and their mixing are depicted. In these spectra the bearing defect modified the amplitude in the sideband frequencies. Furthermore, by performing the current analysis in the bearing defect related frequency f_{BE} , it is possible to detect the bearing defect; due to the direct appearance of

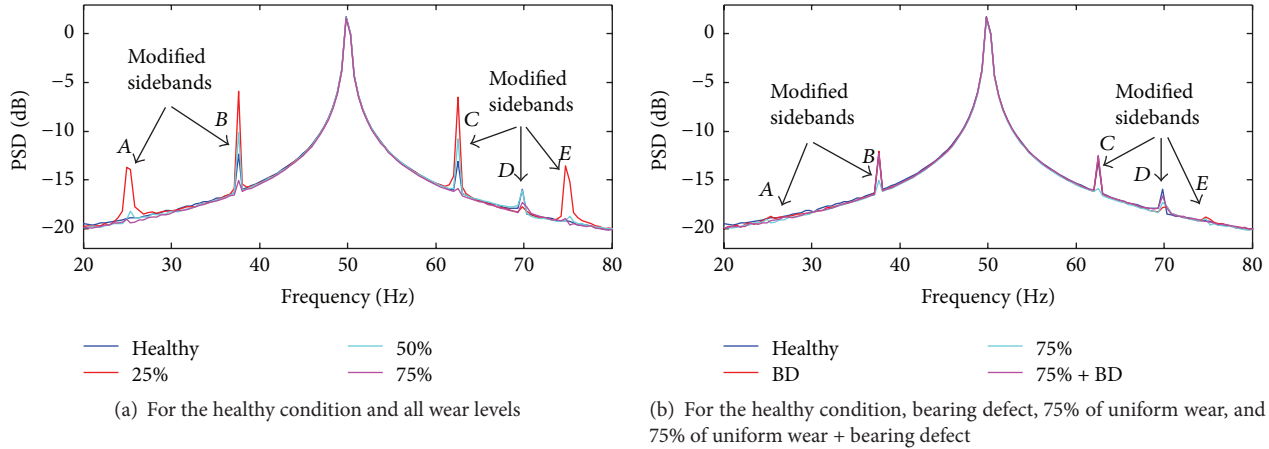


FIGURE 10: PSD spectrum from current signal when VFD is set to 50 Hz.

TABLE 8: Principal frequency components to be analyzed in current spectra.

Frequency set in VFD (Hz)	Frequencies around the supply frequency (Hz)						
	f_s	A	B	C	D	E	f_{BE}
15	15.14	3.90	7.81	22.46	26.37	29.79	83.02
50	49.81	25.39	37.60	62.50	69.82	74.71	277.64

TABLE 9: Amplitude of the current analysis frequencies for each gear condition without bearing defect and VFD set to 15 Hz.

Frequency set in VFD (Hz)	Frequencies around the supply frequency (Hz)						
	f_s	A	B	C	D	E	f_{BE}
Healthy	2.48	-16.01	-13.71	-14.09	-16.40	-17.12	-24.06
25%	2.44	-15.58	-13.36	-13.62	-16.01	-14.79	-23.66
50%	2.44	-15.70	-13.84	-14.13	-16.31	-15.06	-23.59
75%	2.41	-14.14	-14.16	-14.39	-16.45	-17.24	-24.32

TABLE 10: Amplitude of the current analysis frequencies for each gear condition with bearing defect and VFD set to 15 Hz.

Frequency set in VFD (Hz)	Frequencies around the supply frequency (Hz)						
	f_s	A	B	C	D	E	f_{BE}
Healthy	2.48	-16.12	-14.49	-14.63	-16.28	-15.08	-23.32
25%	2.44	-15.80	-13.78	-14.09	-16.18	-17.36	-22.56
50%	2.44	-15.53	-13.34	-13.40	-15.98	-15.93	-21.71
75%	2.41	-16.11	-14.15	-14.20	-16.08	-12.87	-23.17

bearing fault in the induction motor, it is a severe problem which can modify the machine operating condition.

In order to simplify the results, the numerical location of the principal frequency components are summarized in Table 8, in which it is possible to find f_s , five additional frequencies (A, B, C, D, E), and the bearing defect related frequency f_{BE} . And from Tables 9 to 12 the amplitudes for these frequencies are summarized.

TABLE 11: Amplitude of the current analysis frequencies for each gear condition without bearing defect and VFD set to 50 Hz.

Frequency set in VFD (Hz)	Frequencies around the supply frequency (Hz)						
	f_s	A	B	C	D	E	f_{BE}
Healthy	1.75	-18.86	-12.34	-13.13	-15.99	-19.16	-28.39
25%	1.68	-13.93	-5.90	-6.50	-17.74	-13.59	-27.76
50%	1.68	-18.22	-10.13	-10.76	-16.00	-18.73	-27.30
75%	1.58	-19.40	-15.02	-15.9	-17.33	-18.97	-27.97

TABLE 12: Amplitude of the current analysis frequencies for each gear condition with bearing defect and VFD set to 50 Hz.

Frequency set in VFD (Hz)	Frequencies around the supply frequency (Hz)						
	f_s	A	B	C	D	E	f_{BE}
Healthy	1.66	-18.74	-12.03	-12.55	-17.85	-18.84	-26.46
25%	1.67	-13.27	-6.00	-6.54	-17.94	-13.24	-21.74
50%	1.63	-15.65	-8.48	-9.01	-17.98	-15.82	-24.28
75%	1.67	-19.16	-12.25	-12.51	-16.64	-19.24	-26.34

For this study, it is proved that vibrations originated by mechanical faults affect the current consumption and the operating frequency is not a problem for the identification of faults. According to these results a good quantification of uniform wear in gearbox can be done by the vibration analysis focused on the gearbox frequencies given by theory; this analysis must be carried out at lower operating frequencies to ensure the detection. The detectability of uniform wear for all the experiments carried out with and without the presence of the bearing defect is around 83% through vibration analysis, and for the bearing defect detection in the presence of uniform wear comprises around 58%. Although bearing defect is not as well detected as the uniform wear effect from vibration analysis, it is possible to observe its effects in the vibration and current spectra. In this sense, the current analysis allows knowing the bearing defect appearance in the 83% of the experiments carried out and a 66% for the uniform wear detection. Therefore, for this research, the methodology

found upon different physical magnitudes such as vibration and stator current improves the condition monitoring in the kinematic chain; this is due to the advantages of each technique based on different physical magnitudes.

5. Conclusions

This work proposes a methodology based on vibration analysis and current analysis for the diagnosis of different levels of uniform wear in a gearbox and the detection of bearing defect both linked to the same kinematic chain. The methodology is based on the acquisition of vibration signals that are generated in the kinematic chain and induction motor current signals, along with an adequate signal processing to analyze the amplitude at the frequencies of interest given by theory, to provide reliable results of fault diagnosis. The vibration analysis results show that the amplitude increase in the mesh frequency component and its corresponding harmonics are related to the presence of wear in the gearbox. The analysis at lower operating frequencies perfectly detects the presence of wear in the gearbox because of the monotonic increase in all the mesh frequencies. Although at higher operating frequency it is not suitable for detecting uniform wear, it is possible to consider the nonmonotonic amplitude change in the mesh frequency as an indicator of the uniform wear presence.

As [38] mentions, the most common complex mechanical systems are gearboxes and bearings; therefore, nonlinear vibrations are inherent to their operation. For the present case, the presence of uniform wear in the gearbox and the remote location of the accelerometer make it difficult to determine perfectly the presence of the bearing defect based on the vibration analysis. Furthermore, the vibration effects on the kinematic chain are corroborated by doing the analysis to the induction motor current signals, which also detect the uniform wear effect by the sideband modification related to the rotational frequency of the worn gear, and the bearing fault presence by performing an analysis in the fault-related frequency component associated with the vibration effect. Additionally, with this study, it is demonstrated that any modification in the kinematic chain has effects capable of modifying the operation process. Furthermore, with the acquisition of more than one physical magnitude in the condition monitoring and fault detection in rotating machinery, the detection of multiple faults can be performed with better results.

From an industrial perspective, the proposed method can be extended and improved for further development. The structure of the proposed methodology makes it suitable for online monitoring and fault detection using embedded systems such as FPGA. The hardware implementation for online operation is possible because the Hanning filters and FFT modules can be easily integrated in FPGA devices as low-cost high-performance units. Also, the use of acceleration and current signals with an automatic classification system could produce an improved methodology based on the data fusion for multiple-fault detection in kinematic chains. For further improvement of the analysis method, there are other

techniques that can be used that are able to deal with nonstationary signals for analyzing the case of variable loads during operation.

Competing Interests

The authors declare that they have no competing interests.

Acknowledgments

This research was partially supported by CONACyT Scholarship 278033, FOMIX QRO-2014-C03-250269, and SEP-CONACyT 222453-2013 Grants.

References

- [1] G. Niu, B.-S. Yang, and M. Pecht, "Development of an optimized condition-based maintenance system by data fusion and reliability-centered maintenance," *Reliability Engineering & System Safety*, vol. 95, no. 7, pp. 786–796, 2010.
- [2] A. Bellini, F. Filippetti, C. Tassoni, and G.-A. Capolino, "Advances in diagnostic techniques for induction machines," *IEEE Transactions on Industrial Electronics*, vol. 55, no. 12, pp. 4109–4126, 2008.
- [3] V. T. Tran and B.-S. Yang, "An intelligent condition-based maintenance platform for rotating machinery," *Expert Systems with Applications*, vol. 39, no. 3, pp. 2977–2988, 2012.
- [4] M. Ayad, D. Chikouche, N. Boukazzoula, and M. Rezki, "Search of a robust defect signature in gear systems across adaptive Morlet wavelet of vibration signals," *IET Signal Processing*, vol. 8, no. 9, pp. 918–926, 2014.
- [5] L. Frosini, C. Harlisca, and L. Szabó, "Induction machine bearing fault detection by means of statistical processing of the stray flux measurement," *IEEE Transactions on Industrial Electronics*, vol. 62, no. 3, pp. 1846–1854, 2015.
- [6] J. Antonino-Daviu, M. Riera-Guasp, J. Pons-Llinares et al., "Detection of broken outer-cage bars for double-cage induction motors under the startup transient," *IEEE Transactions on Industry Applications*, vol. 48, no. 5, pp. 1539–1548, 2012.
- [7] D. A. Tobon-Mejia, K. Medjaher, and N. Zerhouni, "CNC machine tools wear diagnostic and prognostic by using dynamic Bayesian networks," *Mechanical Systems and Signal Processing*, vol. 28, pp. 167–182, 2012.
- [8] H. Henaou, G.-A. Capolino, M. Fernandez-Cabanas et al., "Trends in fault diagnosis for electrical machines: a review of diagnostic techniques," *IEEE Industrial Electronics Magazine*, vol. 8, no. 2, pp. 31–42, 2014.
- [9] P. Henríquez, J. B. Alonso, M. A. Ferrer, and C. M. Travieso, "Review of automatic fault diagnosis systems using audio and vibration signals," *IEEE Transactions on Systems, Man, and Cybernetics: Systems*, vol. 44, no. 5, pp. 642–652, 2014.
- [10] P. Bangalore and L. B. Tjernberg, "An artificial neural network approach for early fault detection of gearbox bearings," *IEEE Transactions on Smart Grid*, vol. 6, no. 2, pp. 980–987, 2015.
- [11] V. Mien, K. Hee-Jun, and S. Kyoo-Sik, "Rolling element bearing fault diagnosis based on non-local means de-noising and empirical mode decomposition," *IET Science, Measurement and Technology*, vol. 8, no. 6, pp. 571–578, 2014.
- [12] V. C. M. N. Leite, J. G. Borges da Silva, G. F. C. Veloso et al., "Detection of localized bearing faults in induction machines by

- spectral kurtosis and envelope analysis of stator current,” *IEEE Transactions on Industrial Electronics*, vol. 62, no. 3, pp. 1855–1865, 2015.
- [13] T. Wang, M. Liang, J. Li, W. Cheng, and C. Li, “Bearing fault diagnosis under unknown variable speed via gear noise cancellation and rotational order sideband identification,” *Mechanical Systems and Signal Processing*, vol. 62–63, pp. 30–53, 2015.
- [14] A. Bellini, F. Immovilli, R. Rubini, and C. Tassoni, “Diagnosis of bearing faults in induction machines by vibration or current signals: a critical comparison,” in *Proceedings of the IEEE Industry Applications Society Annual Meeting (IAS '08)*, pp. 1–8, IEEE, Edmonton, Canada, October 2008.
- [15] P.-L. Zhang, B. Li, S.-S. Mi, Y.-T. Zhang, and D.-S. Liu, “Bearing fault detection using multi-scale fractal dimensions based on morphological covers,” *Shock and Vibration*, vol. 19, no. 6, pp. 1373–1383, 2012.
- [16] S. Guoji, S. McLaughlin, X. Yongcheng, and P. White, “Theoretical and experimental analysis of bispectrum of vibration signals for fault diagnosis of gears,” *Mechanical Systems and Signal Processing*, vol. 43, no. 1–2, pp. 76–89, 2014.
- [17] P. A. Delgado-Arredondo, A. Garcia-Perez, D. Morinigo-Sotelo et al., “Comparative study of time-frequency decomposition techniques for fault detection in induction motors using vibration analysis during startup transient,” *Shock and Vibration*, vol. 2015, Article ID 708034, 14 pages, 2015.
- [18] B. Trajin, J. Regnier, and J. Faucher, “Comparison between vibration and stator current analysis for the detection of bearing faults in asynchronous drives,” *IET Electric Power Applications*, vol. 4, no. 2, pp. 90–100, 2010.
- [19] K. Shin and S.-H. Lee, “Machinery fault diagnosis using two-channel analysis method based on fictitious system frequency response function,” *Shock and Vibration*, vol. 2015, Article ID 561238, 7 pages, 2015.
- [20] J.-C. Urresty, J.-R. Riba, L. Romeral, and J. A. Ortega, “Mixed resistive unbalance and winding inter-turn faults model of permanent magnet synchronous motors,” *Electrical Engineering*, 2014.
- [21] J. Uddin, M. Kang, D. V. Nguyen, and J.-M. Kim, “Reliable fault classification of induction motors using texture feature extraction and a multiclass support vector machine,” *Mathematical Problems in Engineering*, vol. 2014, Article ID 814593, 9 pages, 2014.
- [22] M. Amarnath and I. R. Praveen Krishna, “Empirical mode decomposition of acoustic signals for diagnosis of faults in gears and rolling element bearings,” *IET Science, Measurement and Technology*, vol. 6, no. 4, pp. 279–287, 2012.
- [23] R. Li and D. He, “Rotational machine health monitoring and fault detection using EMD-based acoustic emission feature quantification,” *IEEE Transactions on Instrumentation and Measurement*, vol. 61, no. 4, pp. 990–1001, 2012.
- [24] Y. Qu, D. He, J. Yoon, B. Van Hecke, E. Bechhoefer, and J. Zhu, “Gearbox tooth cut fault diagnostics using acoustic emission and vibration sensors—a comparative,” *Sensors*, vol. 14, no. 1, pp. 1372–1393, 2014.
- [25] D. P. Jena and S. N. Panigrahi, “Automatic gear and bearing fault localization using vibration and acoustic signals,” *Applied Acoustics*, vol. 98, pp. 20–33, 2015.
- [26] I. Bediaga, X. Mendizabal, A. Arnaiz, and J. Munoa, “Ball bearing damage detection using traditional signal processing algorithms,” *IEEE Instrumentation and Measurement Magazine*, vol. 16, no. 2, pp. 20–25, 2013.
- [27] R. G. Teixeira de Almeida, S. A. da Silva Vicente, and L. Rodrigues Padovese, “New technique for evaluation of global vibration levels in rolling bearings,” *Shock and Vibration*, vol. 9, no. 4–5, pp. 225–234, 2002.
- [28] A. Soualhi, K. Medjaher, and N. Zerhouni, “Bearing health monitoring based on hilbert-huang transform, support vector machine, and regression,” *IEEE Transactions on Instrumentation and Measurement*, vol. 64, no. 1, pp. 52–62, 2015.
- [29] M. Amar, I. Gondal, and C. Wilson, “Vibration spectrum imaging: a novel bearing fault classification approach,” *IEEE Transactions on Industrial Electronics*, vol. 62, no. 1, pp. 494–502, 2015.
- [30] E. T. Esfahani, S. Wang, and V. Sundararajan, “Multisensor wireless system for eccentricity and bearing fault detection in induction motors,” *IEEE/ASME Transactions on Mechatronics*, vol. 19, no. 3, pp. 818–826, 2014.
- [31] X. Zhang, J. Kang, L. Xiao, J. Zhao, and H. Teng, “A new improved kurtogram and its application to bearing fault diagnosis,” *Shock and Vibration*, vol. 2015, Article ID 385412, 22 pages, 2015.
- [32] H. Li, H. Zheng, and L. Tang, “Gear fault detection based on teager-huang transform,” *International Journal of Rotating Machinery*, vol. 2010, Article ID 502064, 9 pages, 2010.
- [33] S. Hedayati Kia, H. Henao, and G.-A. Capolino, “Trends in gear fault detection using electrical signature analysis in induction machine-based systems,” in *Proceedings of the IEEE Workshop on Electrical Machines Design, Control and Diagnosis (WEMDCD '15)*, pp. 297–303, Torino, Italy, March 2015.
- [34] J. J. Saucedo-Dorantes, A. G. Garcia-Ramirez, J. C. Jauregui-Correa, R. A. Osornio-Rios, A. Garcia-Perez, and R. J. Romero-Troncoso, “Reliable methodology for gearbox wear monitoring based on vibration analysis,” in *Proceedings of the 40th Annual Conference of the IEEE Industrial Electronics Society (IECON '14)*, pp. 3381–3385, IEEE, Dallas, Tex, USA, October–November 2014.
- [35] T. Geramitcioski, L. Trajcevski, I. Vilos, and V. Mitrevski, “Early gear tooth damage diagnostic from the vibration signatures,” in *Proceedings of the 3rd International Conference (Power Transmissions '09)*, Thessaloniki, Greece, 2009.
- [36] W. D. Mark, “Time-synchronous-averaging of gear-meshing-vibration transducer responses for elimination of harmonic contributions from the mating gear and the gear pair,” *Mechanical Systems and Signal Processing*, vol. 62–63, pp. 21–29, 2015.
- [37] M. P. Norton and D. G. Karczub, *Fundamental of Noise and Vibration Analysis for Engineers*, Cambridge University Press, Cambridge, UK, 2nd edition, 2003.
- [38] J. C. Jauregui-Correa and O. M. Gonzales, *Mechanical Vibrations of Discontinuous Systems*, Nova Science, New York, NY, USA, 1st edition, 2009.
- [39] J. C. Jauregui-Correa, “The effect of nonlinear traveling waves on rotating machinery,” *Mechanical Systems and Signal Processing*, vol. 39, no. 1–2, pp. 129–142, 2013.
- [40] J. A. Vite-Frias, R. D. J. Romero-Troncoso, and A. Ordaz-Moreno, “VHDL core for 1024-point radix-4 FFT computation,” in *proceedings of the IEEE International Conference on Reconfigurable Computing and FPGAs (RECONFIG '05)*, Puebla, Mexico, September 2005.
- [41] J. D. J. Rangel-Magdalen, R. D. J. Romero-Troncoso, R. A. Osornio-Rios, E. Cabal-Yepez, and A. Dominguez-Gonzalez, “FPGA-based vibration analyzer for continuous CNC machinery monitoring with fused FFT-DWT signal processing,” *IEEE Transactions on Instrumentation and Measurement*, vol. 59, no. 12, pp. 3184–3194, 2010.

Research Article

Experimental Investigation into Vibration Characteristics for Damage Minimization in a Lapping Process

J. Suwatthikul,¹ S. Sornmuang,¹ T. Yaemglin,² I. Cheowanish,² and C. Supavasuthi²

¹Advanced Automation and Electronics Research Unit, National Electronics and Computer Technology Center, Pathum Thani 12120, Thailand

²Western Digital (Thailand) Co., Ltd., Ayutthaya 13160, Thailand

Correspondence should be addressed to J. Suwatthikul; jittiwut.suwatthikul@nectec.or.th

Received 21 December 2015; Revised 9 February 2016; Accepted 14 February 2016

Academic Editor: Arturo Garcia-Perez

Copyright © 2016 J. Suwatthikul et al. This is an open access article distributed under the Creative Commons Attribution License, which permits unrestricted use, distribution, and reproduction in any medium, provided the original work is properly cited.

Lapping machines are used in a hard disk rough lapping process where a workpiece (a wafer row bar) is locked with a robot arm and rubbed on a lap plate. In this process, the lap plate's condition and lifetime are among important concerned factors. The lifetime can be too short due to the plate being accidentally scratched by the workpiece during lapping. This problem leads to undesired consequences such as machine downtime and excessive plate material usage. This paper presents an experimental investigation into vibration characteristics of passed and failed lapping scenarios and discusses a potential solution to minimize the serious damage so-called "plate scratch" which intermittently occurs in such process. The experimental results show that, by in situ monitoring vibration and utilizing artificial intelligence, damage minimization can be possible.

1. Introduction

Lapping or polishing is a process that produces a smooth and lustrous surface finish. This shiny smooth appearance results from the action of abrasive power and a polishing tool. It has been widely used in the production of optical lenses, metallic bearing surfaces, and products requiring excellent finishes [1–5]. In the silicon wafer and the hard disk drive (HDD) industry, removing materials from slider bars together with controlling the strip height (SH) variation to the minimum value is the major purpose of the lapping process [6–12].

Figure 1 shows a schematic view of a lapping machine used in an HDD manufacturing process. It basically consists of a plate, a moving arm (or slider arm), a clamping tool (CT), and a place where a workpiece is fitted. The machine is controlled by proprietary software to operate in defined steps and some feedback signals, for instance, RPM and resistance, are used in the control loop. The process is finished when the resistance meets the specified value. Normally, wear from normal use does occur; therefore, plate replacement or refinishing is required.

A previous study reported that a plate replacement accounted for 16.2% of lapping machine downtime [13]. The replacement usually results from normal wear and, being focused on in this paper, the undesired damage so-called "plate scratch" (PS) as illustrated in Figure 2. So far, root causes of such damage have not yet been identified in any research or engineering studies since the damage occurs randomly and the available feedback signals are not a good indicator to pinpoint such causes. One of the suspected root causes is an improper wedge angle or a sudden angle change during lapping. Conventional damage prevention is the careful checks of machine configurations and the continuous manual observation by an operator during lapping. Nonetheless, once the damage becomes visible to the naked eye, the scratched surface has already been too serious and costly to be refinished.

The objective of this investigation is to find a solution to PS minimization by recognizing vibration patterns of the lapping machine during lapping. A hypothesis has been the fact that there should be aggressive abrasion between the workpiece and the plate when PS is beginning, thereby

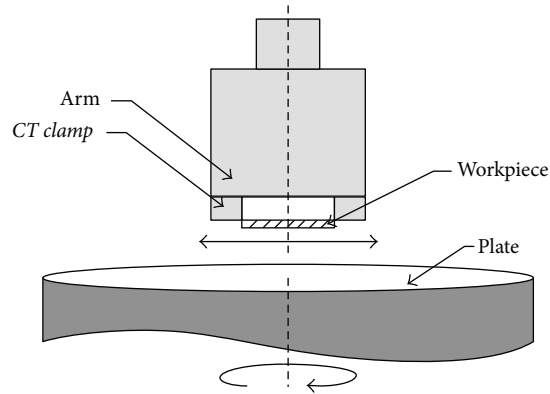


FIGURE 1: Schematic view of a lapping machine.

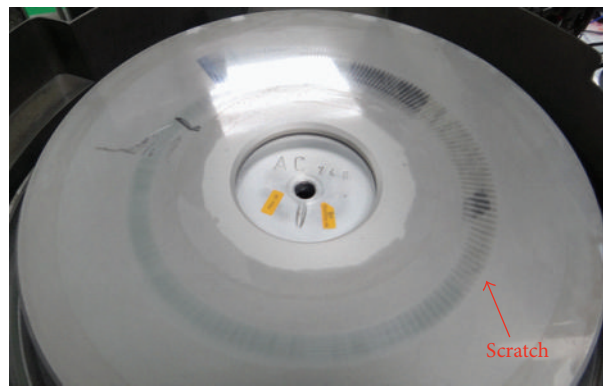


FIGURE 2: Plate scratch.

causing some abnormal vibration. If the vibration (if any) can be detected early enough, the machine would be stopped in time and the damage should be minimized.

The paper firstly presents an experimental investigation into vibration characteristics of passed and failed lapping scenarios (with and without damage). Then, a potential solution such as an AI-based detection system to minimize the damage is discussed. Kalman filter (KF) is used as a filter to eliminate the background noise of the signal. The signal spectra are generated and analyzed by using Fast Fourier Transform (FFT) technique. Finally, the conclusion of the paper is provided.

2. Validation of the Vibration Sensor and Sensing Position

Vibration is a repetitive, periodic, or oscillating response of a mechanical system [14]. Applications of vibration analysis have been found in many areas of engineering such as aeronautical and aerospace, civil, manufacturing, mechanical, and electrical applications [15–28]. In this work, in situ measurements of vibration using piezoelectric accelerometers are conducted to obtain vibration signals at the nearest position where the plate touches and rubs the workpiece. This section discusses basic understanding and validation of sensing positions on the machine and signals from the sensors.

2.1. Movement of the Vibration Sensor. A vibration sensor is originally designed by a manufacturer to be mounted firmly to a target and the DC bias voltage is set very close to zero. However, if the sensor is moved during operation for any reason, the bias level will change in relation to the direction and the magnitude of the movement. This section provides test results of the relationship between the sensor movement and the bias levels and directions. This behavior is found in “CT clamp in” and “CT clamp out” steps of the lapping process in the experiment section.

Sensor movements, as shown in Figure 3, are divided into two steps by moving the sensor in counterclockwise and clockwise directions between 0 and 360 degrees divided into four quarters and shifting every one quarter.

Test results of sensor movement are illustrated in Figure 4. It can be summarized that changes in the bias signal can indicate the sensor movement. The negative change occurs when the sensor moves either counterclockwise or clockwise between 0 and 180 degrees. However, the change is positive when moving sensor for both directions during 180–360 degrees.

2.2. Sensing Position. After considering the mechanical structure and the movement of the concerned machine, measurement points were defined and vibration sensors were attached to test the response as shown in Figure 5. The defined measurement positions are as follows:

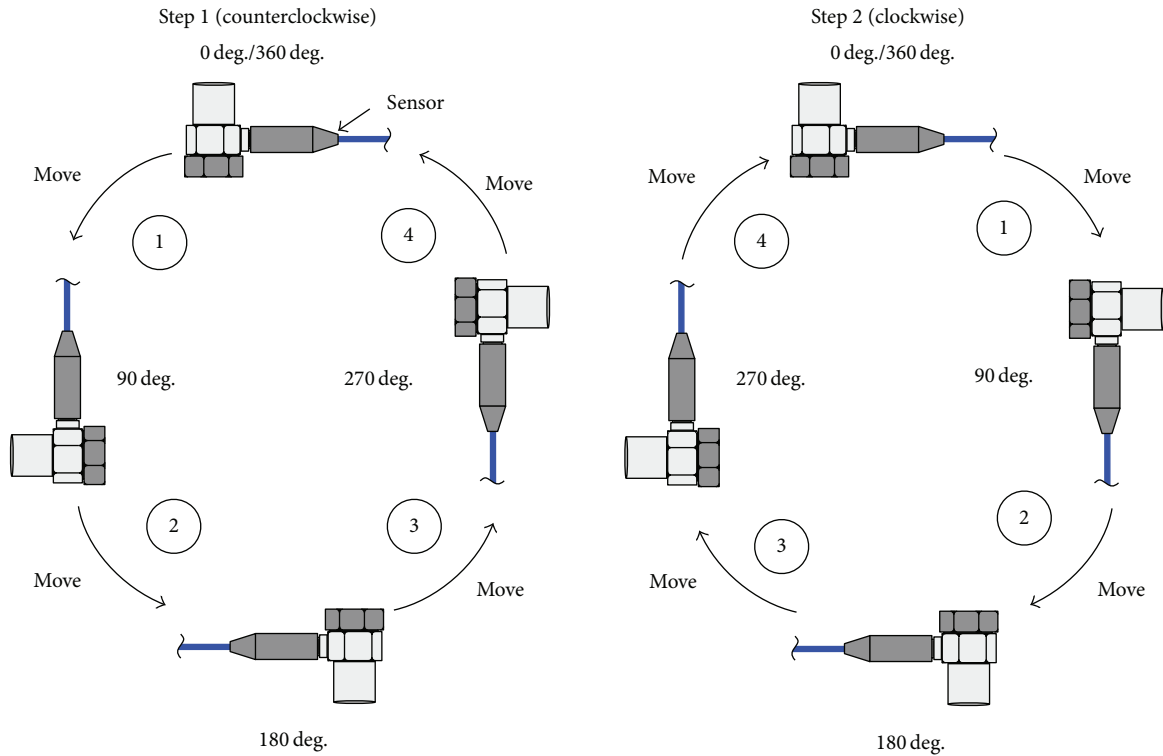


FIGURE 3: Sensor movement tests.

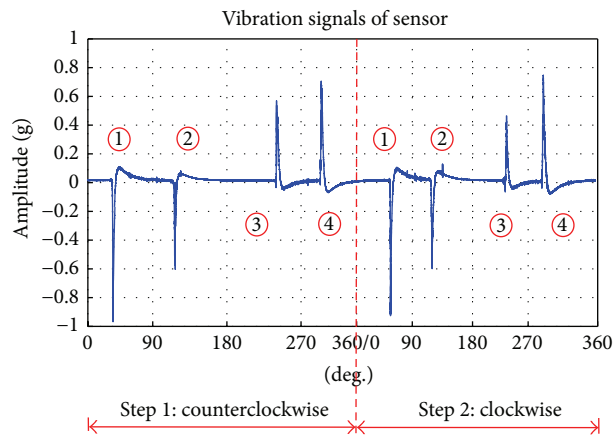


FIGURE 4: Signals from sensor movement tests.

- (i) Row Tool (RT): the closest location to the original abrasion point between the plate and the workpiece.
- (ii) Frame (Frame): at the arm which is a moving part of the machine.
- (iii) Base (Base): the stationary part of the machine.

Step-by-step movement tests were then conducted to record and understand vibration signals. The machine was tested with the normal operating steps:

- Step 1: *Stationary*, the machine is stationary.
- Step 2: *CT clamp in*, the clamp moves to lock the workpiece to the arm.

Step 3: *Landing*, the arm moves and lands to touch the plate.

Step 4: *Lapping*, lapping starts and the plate rotates at the programmed speed.

Step 5: *Lifting*, the arm moves upwards and goes back.

Step 6: *CT clamp out*, the clamp is released to unload the workpiece.

The position test results are shown in Figures 6 and 7. For “*Stationary*” in Figure 6(a), no major vibration changes were detected. This can be regarded as background noise. Next, a sensor movement was detected in “*CT clamp in*” and “*CT*”

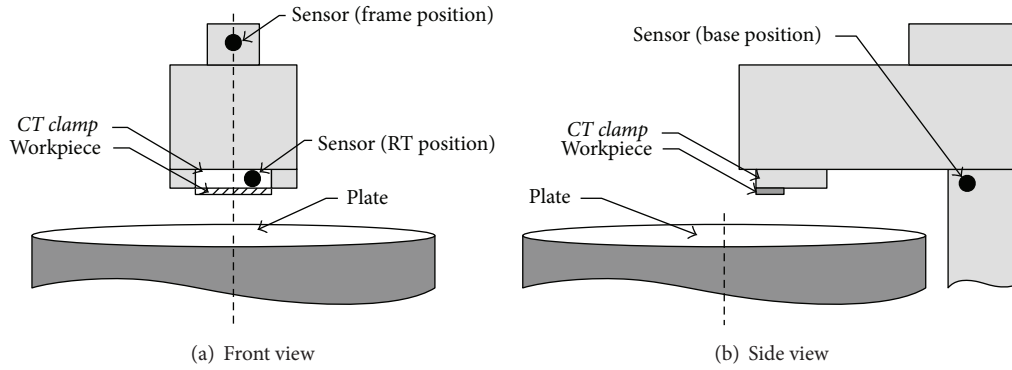


FIGURE 5: Schematic view of sensor position tests.

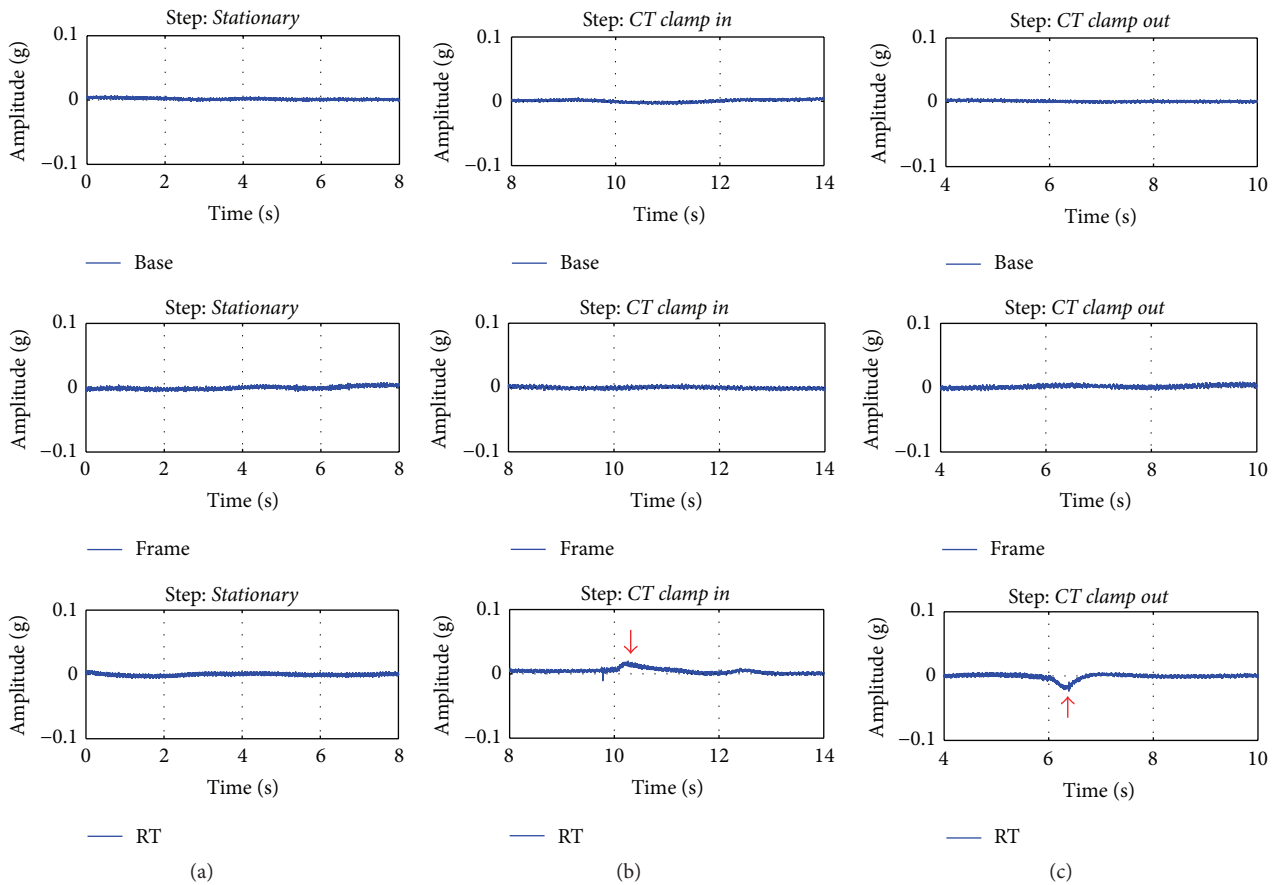


FIGURE 6: Vibration signals for “Stationary,” “CT clamp in,” and “CT clamp out” steps.

clamp out” steps at RT position as shown in Figures 6(b) and 6(c), respectively. In “CT clamp in” step, the positive change in the bias voltage can be measured when the clamp is moving to lock the workpiece, and this causes the sensor to move up slightly (as discussed in Section 2.1). Similarly, the negative signal occurs when the workpiece is moving down by the clamp release in “CT clamp out” step.

The vibration signals of “Landing” and “Lifting” steps can be measured at all sensing positions. For “Landing” step as shown in Figure 7(a), the arm moves to the position above the plate and then moves downward to touch it. In this step,

vibration occurs and is damped down over time. Figure 7(b) shows the signals of the “Lifting” step; the behaviors are the same as “Landing” step but in reverse order.

According to the results, Base and Frame positions are sensitive to signals of the arm movement only. At RT position, in contrast, the sensor can sense all the test signals. Therefore, RT was finally selected to install the sensor for the experiment.

2.3. Kalman Filter (KF). The Kalman filter is a set of mathematical equations that provide an efficient computational

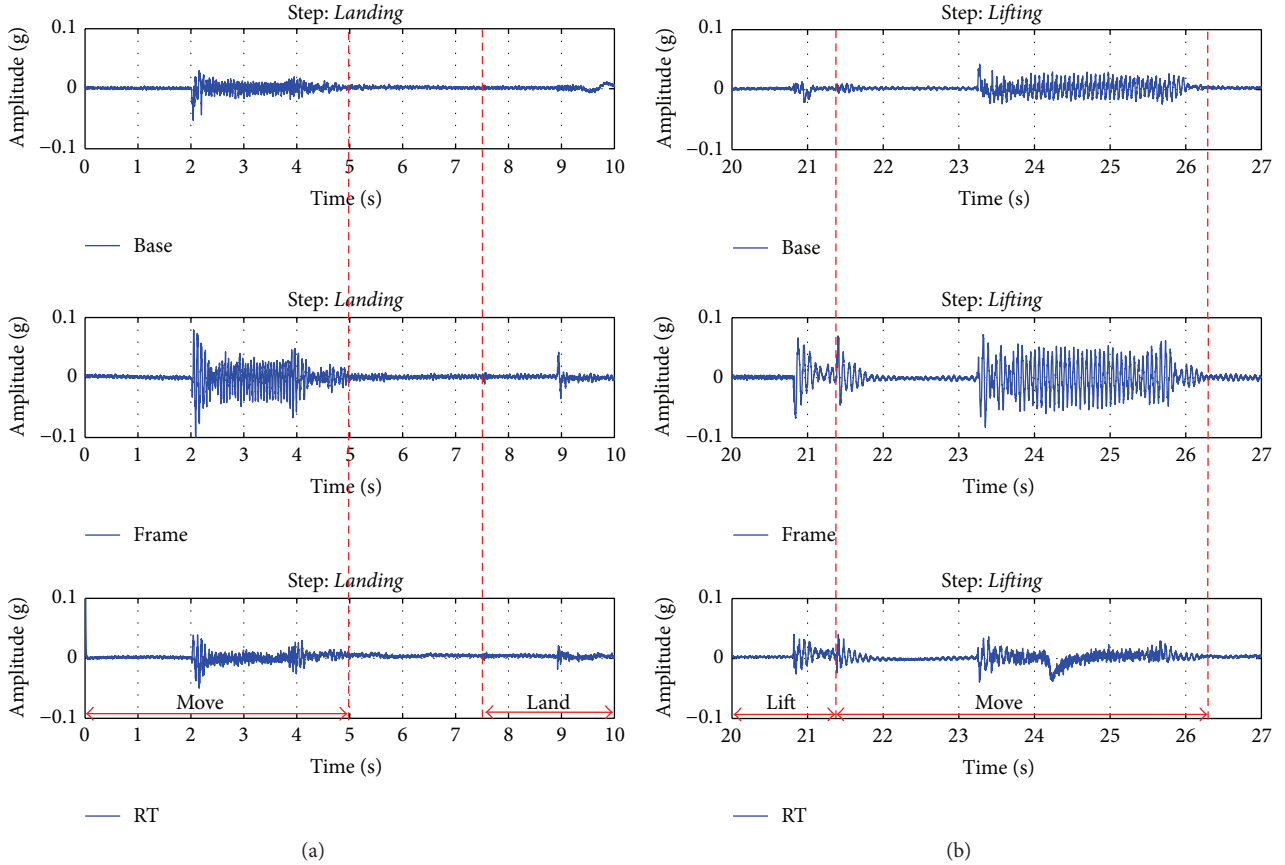


FIGURE 7: Vibration signals of “Landing” step.

means to estimate the state of a process, in a way that minimizes the mean of the squared error [29, 30]. The filter is very powerful in several aspects: it supports estimations of past, present, and even future states, and it can do so even when the precise nature of the modeled system is unknown. The Kalman filter equations can be divided into two groups: time update equations and measurement update equations. The time update equations project forward the current state and error covariance estimates to obtain a priori estimates for the next step. The measurement update equations are responsible for incorporating a new measurement into a priori estimate to obtain an improved posterior estimate.

The time update equations can also be considered as predictor equations, while the measurement update equations can be considered as corrector equations. Mathematically, prediction of the state ahead (\hat{x}_k^-) and the error covariance (P_k^-) may be represented as

$$\begin{aligned}\hat{x}_k^- &= A\hat{x}_{k-1} + Bu_{k-1}, \\ P_k^- &= AP_{k-1}A^T + Q,\end{aligned}\quad (1)$$

where Q is the process noise covariance. A and B are the form of linear stochastic difference equation.

The Kalman gain (K_k), update estimate with measurement (\hat{x}_k), and update error covariance (P_k) are defined in (2), (3), and (4), respectively. Consider

$$K_k = P_k^- H^T (HP_k^- H^T + R)^{-1}, \quad (2)$$

$$\hat{x}_k = \hat{x}_k^- + K_k (z_k - H\hat{x}_k^-), \quad (3)$$

$$P_k = (1 - K_k H) P_k^-, \quad (4)$$

where R , z_k , and H are measurement noise covariance, the actual measurements of the process, and measurement Jacobian matrix at step k , respectively.

In this case, our noisy measurement is of the state directly; hence, $H = 1$. The Kalman filter algorithm is described in the flowchart in Figure 8.

The flowchart summarizes the algorithm of Kalman filter which includes two main parts: the measurement part for computing the Kalman gain, updating the estimate of the measurement, and updating the error covariance and the time update part for prediction and estimation of state and error covariance.

A comparison of the collected vibration signal with and without using the filter is shown in Figure 9. The filtered signal (bottom) appears considerably smoother than the raw measured signal.

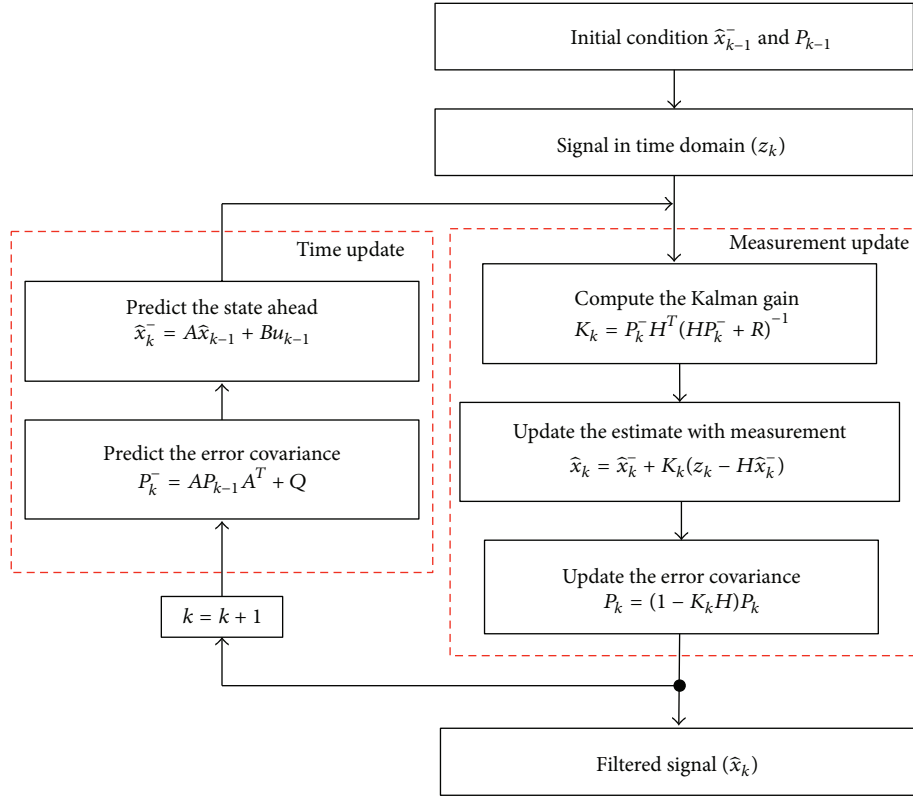


FIGURE 8: Flowchart of Kalman filter.

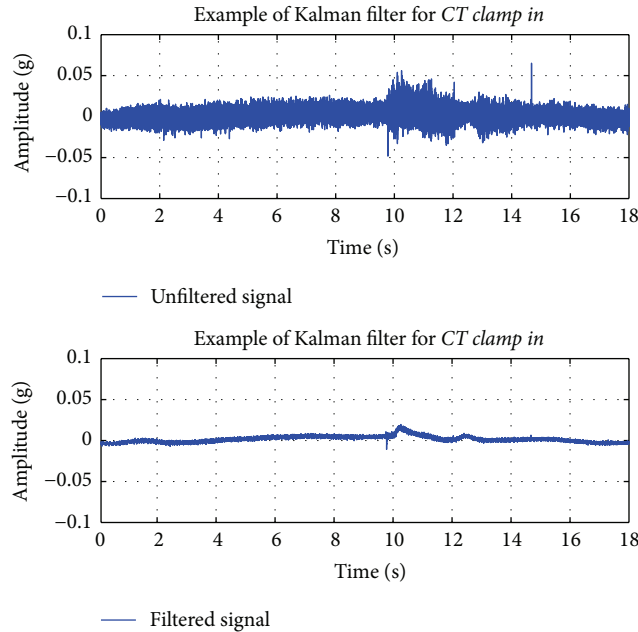


FIGURE 9: Example of filtered signal.

3. Experimental Apparatus and Procedure

Experiments with parameters listed in Table 1 to observe vibration and damage in rough lapping processes were conducted. The total workpieces were divided into two groups.

The first group was tested in a “healthy” (no damage) lapping process, and the other group was in an “unhealthy” (with damage) lapping process. In addition, the “unhealthy” process was tested under two conditions that have been suspected as the potential root causes of the damage: mechanical problem

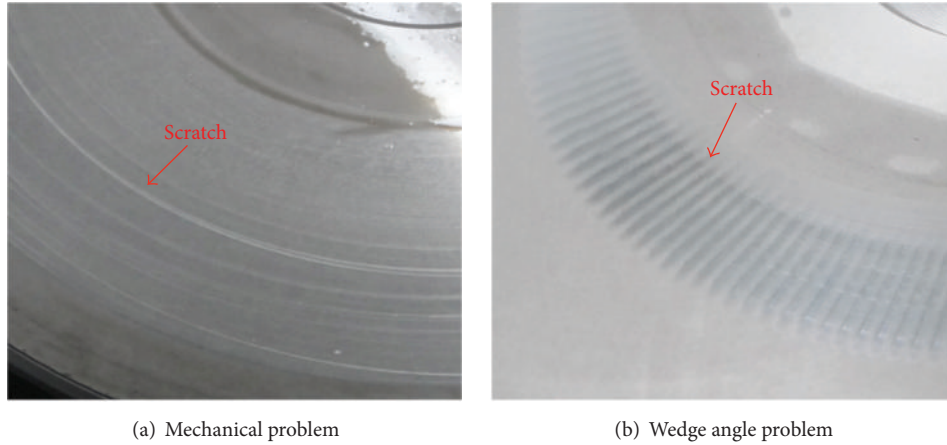


FIGURE 10: Scratches occurred in “*unhealthy*” lapping processes.

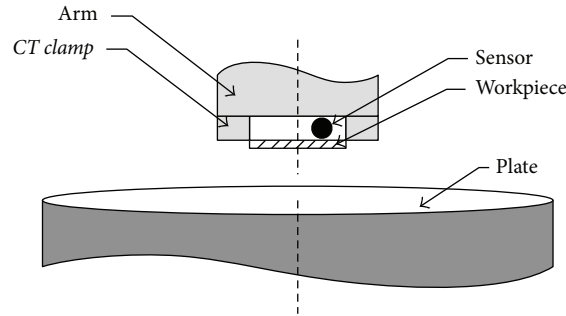


FIGURE 11: Schematic view of the experiment.

TABLE 1: Lapping parameters in the experiments.

Lapping parameters	Details
Lapping control	Constant lapping pressure, varying lap plate speed for removal rate control
Workpiece material	Composite alumina oxide titanium carbide (AlTiC)
Diamond powder	Monocrystalline submicron diamond size

and wedge angle problem. These can result in scratches which are different in appearance as shown in Figure 10.

The mechanical problem was simulated by applying an impact at the back of the slider arm. This case is nonetheless interesting as the lapping process managed to continue and finish despite having the scratch. The wedge angle problem was simulated by swapping a workpiece that had been specifically assigned a wedge angle with another workpiece such that the angle became improper for lapping. In this case, if an operator cannot stop the machine in time, the problem will cause more severe damage to the plate than that of the mechanical problem.

The schematic view of the machine under the experiments is given in Figure 11. The sensor was firmly fitted at RT position which can best sense signals for all movements as previously discussed in Section 2. The rough lapping

process was controlled by proprietary software to continuously operate the six major steps as presented above: *Stationary*, *CT clamp in*, *Landing*, *Lapping*, *Lifting*, and *CT clamp out*.

4. Results and Discussion

The test results include both “*healthy*” and “*unhealthy*” processes in which vibration signals were measured at RT position. The vibration characteristics of the “*healthy*” and “*unhealthy*” processes are summarized in Figures 12 and 13, respectively.

For the “*healthy*” process, the vibration in “*Stationary*” step can be considered as background noise as shown in Figure 12(a). In Figures 12(b) and 12(f), the vibration of “*CT clamp in*” and “*CT clamp out*” steps has opposite directions due to the sensor movement. The vibration signals of “*Landing*” and “*Lifting*” steps are illustrated in Figures 12(c) and 12(e), respectively. When the arm moves in, downward, upward, and out, the vibration can be clearly detected. Lastly and most importantly, smooth vibration signal of “*Lapping*” step in this “*healthy*” process was measured as depicted in Figure 12(d). The signal has similar amplitude level to that of the background noise in “*Stationary*” step but some high frequency components were detected.

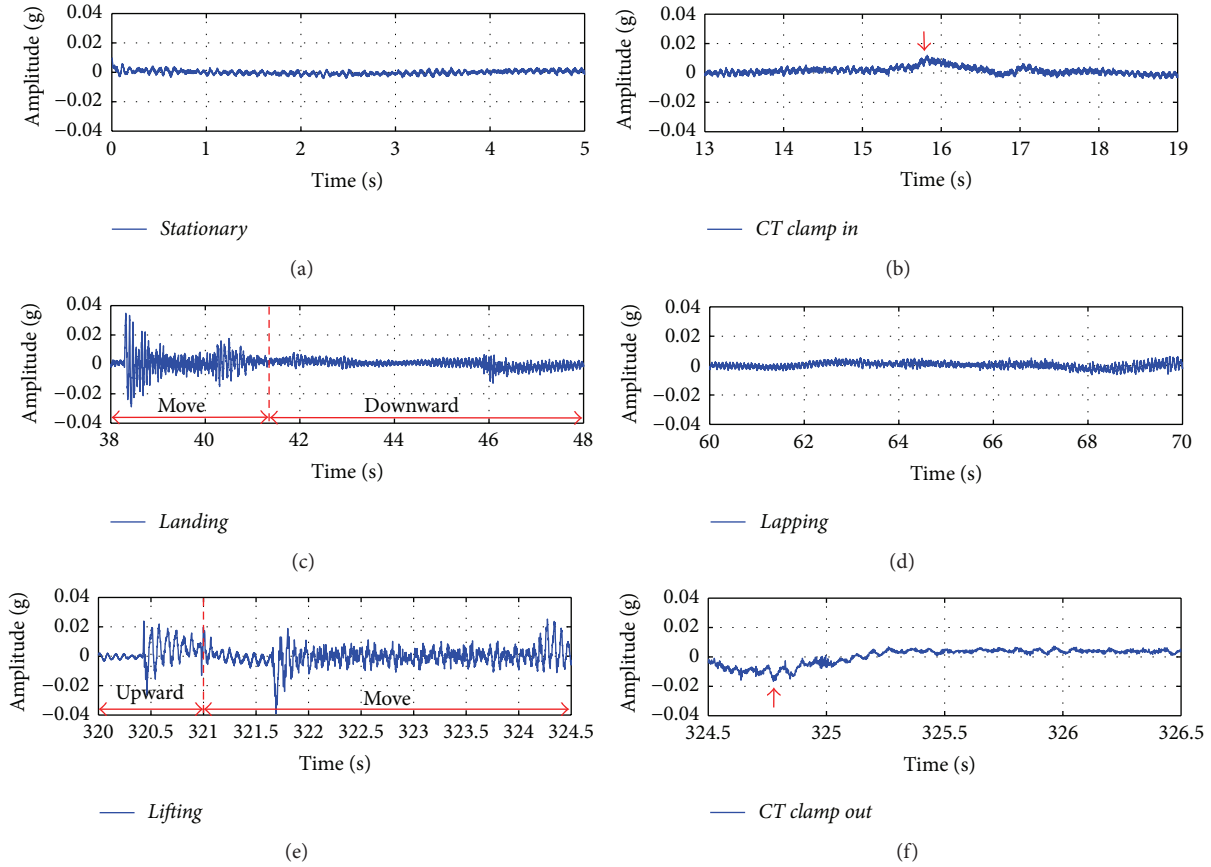


FIGURE 12: Vibration of the “healthy” lapping process.

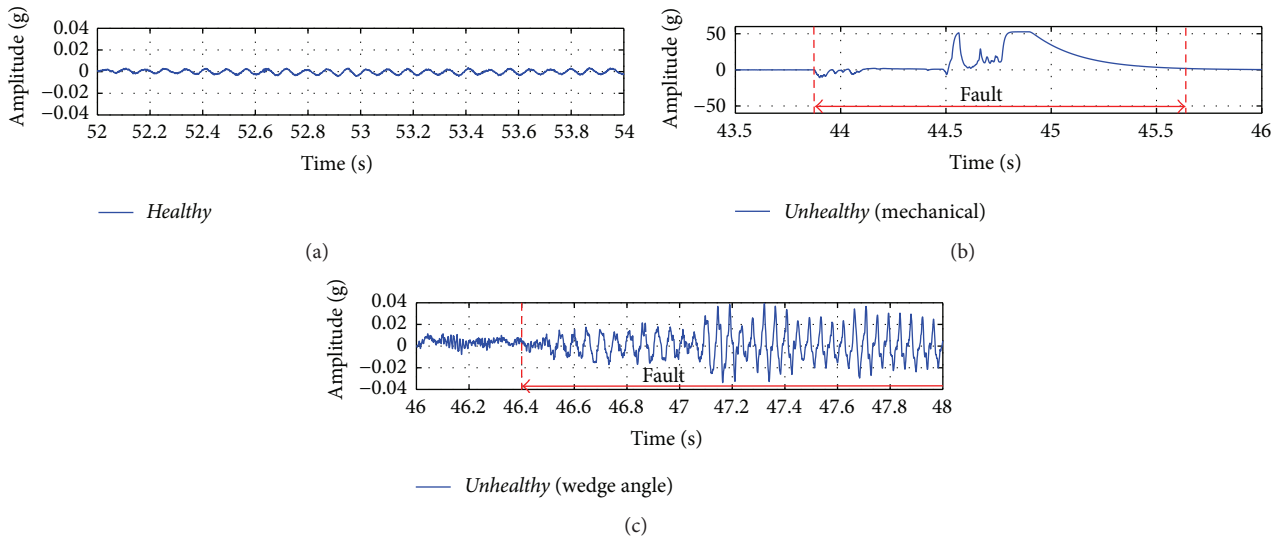


FIGURE 13: Vibration during lapping of the “healthy” and “unhealthy” processes.

For the “unhealthy” process, vibration characteristics in all steps except “Lapping” were similar to those of the “healthy” process. Figure 13 only compares the vibration signals in “Lapping” steps where scratches on the plates occurred during the “unhealthy” process. It can be clearly seen that the signals in “Lapping” of the “unhealthy” process

are different from those of the “healthy” process. The test with the mechanical problem shows strong vibration as seen in Figure 13(b). According to an additional video record, PS was visible to the naked eye about 15 seconds afterward. This case is nonetheless interesting as the lapping process managed to continue and finish the process despite having

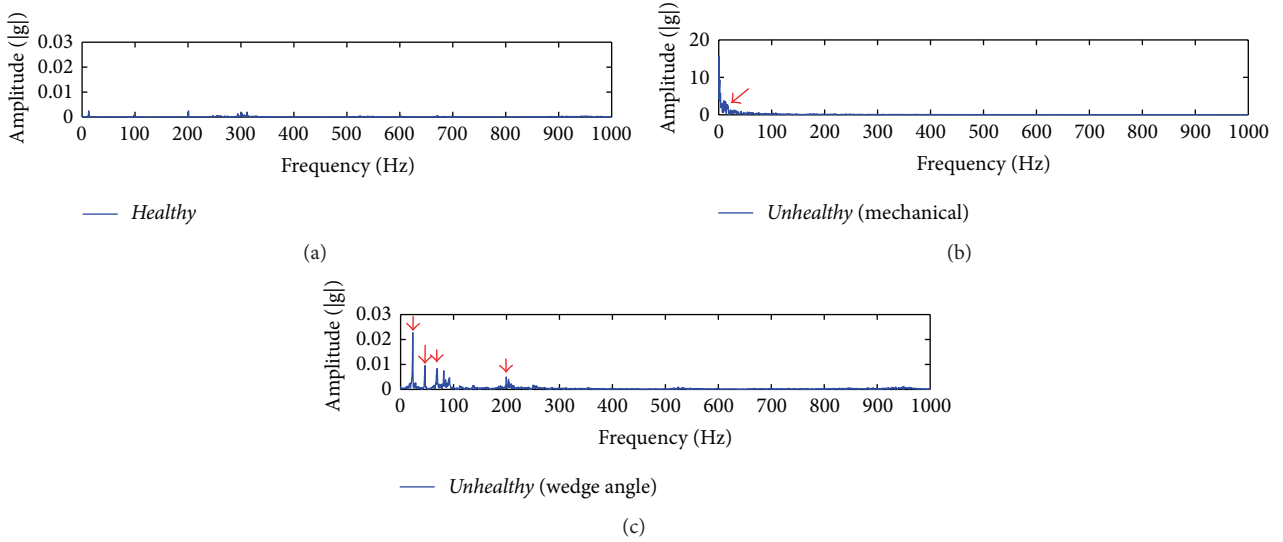


FIGURE 14: Vibration spectra of the “healthy” and “unhealthy” lapping processes.

PS. This may have been because the scratch was not repeated so that the machine was able to control lapping force to achieve the desired SH. Abnormal vibration of the test with the wedge angle problem can be measured at the beginning of the lapping and kept oscillating until the machine was stopped. The damage on the plate can be clearly discerned at 3 seconds later. In this case, the lapping failed to finish.

Frequency spectra of the vibration signals in “Lapping” steps are shown in Figure 14. The spectrum of the mechanical problem has higher peaks in low frequency than the “healthy” process and the wedge angle problem’s spectra.

5. Simulation of Scratch Detection by Using Neural-Expert Systems

According to the experiments, the vibration signals are important components to identify whether a process is “healthy” or “unhealthy.” The signals of the “unhealthy” process are different from the baseline characteristics in both time and frequency domains. Those signals can be classified by an artificial intelligence technique. This section demonstrates a simulation of scratch detection in the “Lapping” steps of the above experimental lapping processes by using a neural-expert system technique. Detection results show that it is possible to detect PS much earlier before it is visible to the naked eye; thus, the damage can be minimized.

5.1. Neural-Expert Systems. Expert systems and neural networks share common goals in attempting to imitate human intelligence and eventually create an intelligent machine [31]. However, they use very different means to achieve their goals. An expert system is used to diagnose and classify raw data before sending them to a neural network. This increases accuracy and reduces time in the neural process. The flowchart of the method for PS detection is summarized in Figure 15. The expert system part is designed to classify raw

TABLE 2: Subranges and thresholds for the neural-expert system.

Range	Vibration signals		Threshold
	Frequency (Hz)	Time (s)	
1	0–25	—	0.015
2	25–100	—	0.008
3	150–200	—	0.015
4	—	All (positive)	0.03
5	—	All (negative)	0.03

data into a set of logic 0 or logic 1 by comparing input signals with specific thresholds. The logic set is then sent to the neural network which then calculates the output with parameters from training data and judges the output to be healthy or unhealthy by comparing with another threshold.

5.1.1. Expert System Part. As seen in Figures 13 and 14, the magnitudes of the “unhealthy” process are different from those of the “healthy” process. The different maximum values in each range ($|g|$ = amplitude) and threshold levels were used by the neural-expert system to make a decision. The range of interest was classified as shown in Table 2.

Referring to Figure 15, the expert system part calculates maximum values of subranges which are represented by logic 0 or logic 1 from the threshold of each range. The output is defined as

$$p = [p_1 \ p_2 \ p_3 \ p_4 \ p_5], \quad (5)$$

where p_i represents logic 0 or logic 1 which are used as inputs of the neural network part.

5.1.2. Neural Network Part. A neural network can be trained with historical data to perform a desired function by adjusting the weights (w) and bias (b) of the connections such that the outputs match the inputs. A set of neurons are combined

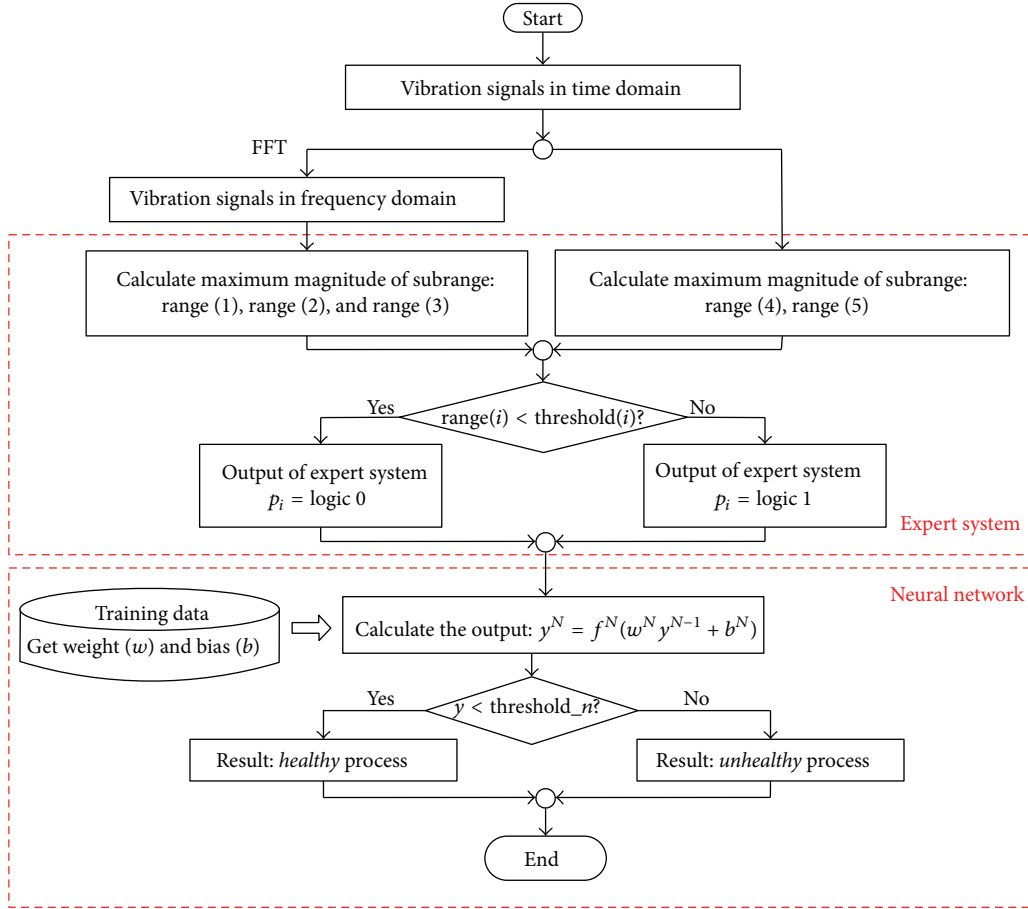


FIGURE 15: Flowchart of neural-expert systems.

in a layer and a network can consist of single or multiple layers, as shown in Figure 16. The general equations of ANNs are as follows:

$$\begin{aligned}
 y^1 &= f^1(w^1 p + b^1) \\
 y^2 &= f^2(w^2 y^1 + b^2) \\
 &\vdots \\
 y^N &= f^N(w^N y^{N-1} + b^N),
 \end{aligned} \tag{6}$$

$$\begin{aligned}
 b &= \begin{bmatrix} b_1 \\ b_2 \\ \vdots \\ b_S \end{bmatrix}, \\
 w &= \begin{bmatrix} w_{11} & w_{12} & \cdots & w_{1R} \\ w_{21} & w_{22} & \cdots & w_{2R} \\ \vdots & \vdots & & \vdots \\ w_{S1} & w_{S2} & \cdots & w_{SR} \end{bmatrix}.
 \end{aligned} \tag{7}$$

where

$$p = \begin{bmatrix} p_1 \\ p_2 \\ \vdots \\ p_R \end{bmatrix},$$

The neural network model is trained with the experimental data by using Levenberg-Marquardt (LM) algorithm which is the fastest back-propagation algorithm and one of the efficient methods [32]. A feed-forward neural network is used and consists of an input layer (5 neurons), a 1-node output layer, and a hidden layer (35 neurons). The transfer functions are *tansig*, *logsig*, and *logsig*, respectively.

The detection system was implemented in a LabView and Matlab environment. An example of the user interface is depicted in Figure 17 where measured vibration signals,

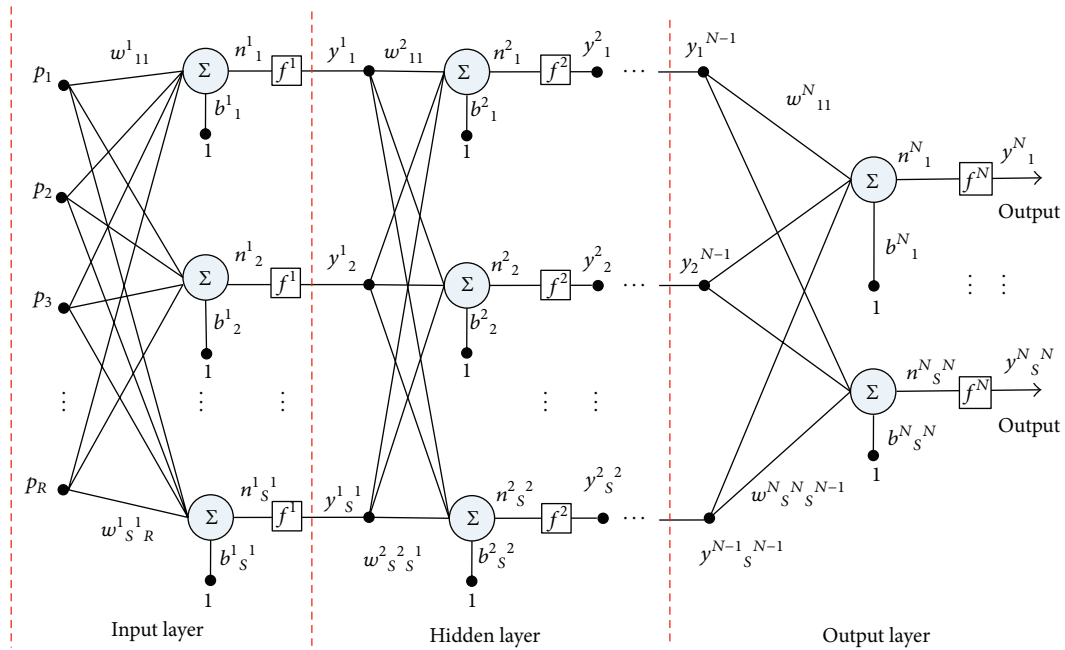


FIGURE 16: General structure of an artificial neural network.

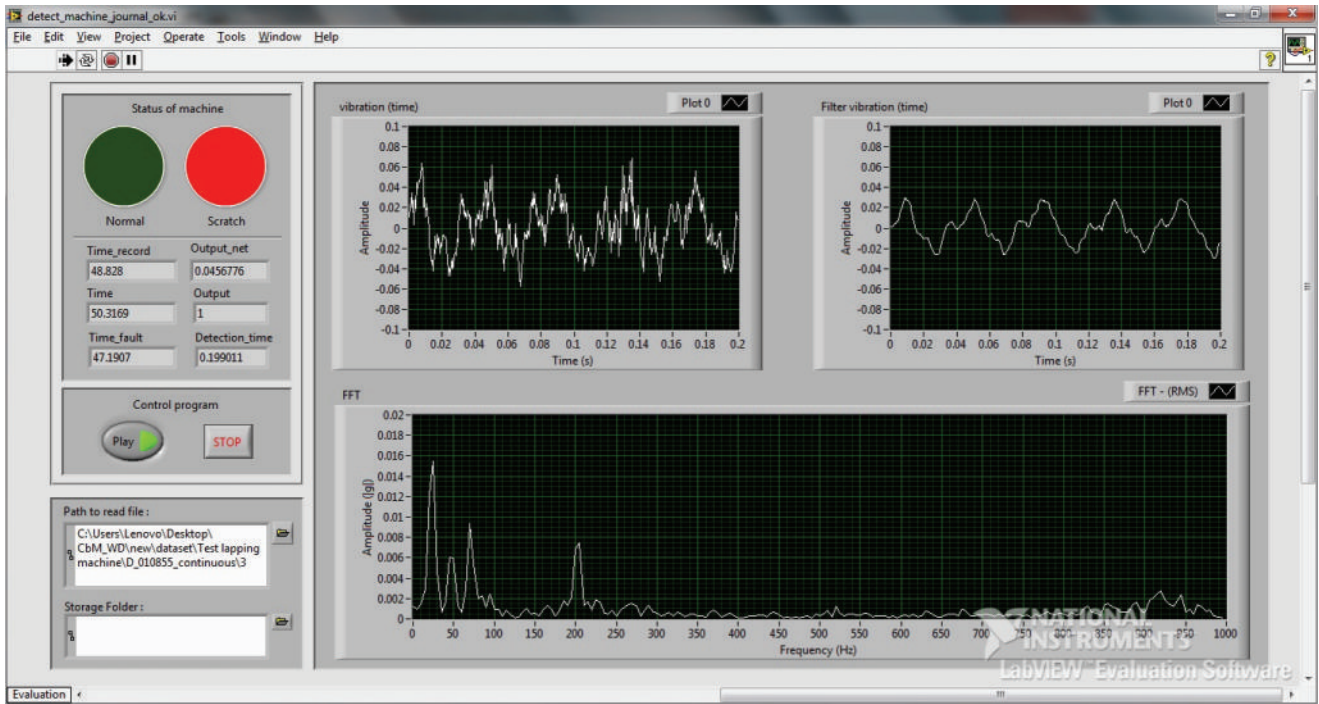


FIGURE 17: PS detection system.

fault messages, and detection times can be monitored and recorded.

5.2. *Detection Results.* Detection results are summarized in Tables 3 and 4. Twenty-two datasets were tested. The accuracy of the detection system is 98% on average and the detection time is in the range of 0.2 s. The 5% detection error came from

the fact that the system was unable to classify the “healthy” input signals with high confidence so that they were declared as unknown. The system performed early detection before the two damage incidents were visible to the naked eye, which were recorded as 3 seconds for the mechanical problem and 15 seconds for the wedge angle problem (on average) as shown in Table 4. The time recording started immediately after the

TABLE 3: Detection results.

Lapping process	Accuracy (%)	Detection time (s)
Healthy	95	—
Unhealthy (mechanical problem)	100	0.21
Unhealthy (wedge angle problem)	100	0.20
Total	98.33	0.205

TABLE 4: Visible PS.

Appearance	Type	Averaged time to be visible (s)
	Mechanical	3
	Wedge angle	15

problem was applied. As such, it is possible that the process can be stopped by the detection system to prevent further serious damage.

6. Conclusions

This paper has presented an experimental investigation into vibration characteristics of a lapping machine in an HDD lapping process. The objective is to find a solution to PS minimization by recognizing vibration patterns of the lapping machine during lapping. The vibration signals in each normal operating step have their own patterns as presented and discussed above. Any anomalies that deviate from the baselines will potentially indicate undesired impacts or abrasion between the plate and the workpiece. In both “unhealthy” test cases conducted in this paper, abnormal vibration patterns are related to the original root causes and can be detected by the vibration sensor significantly earlier than being visible to an operator. It can be concluded in this investigation that there are detectable vibration signals at RT, generated by aggressive abrasion or impacts before PS occurs. Being able to detect and characterize the signals can enable us to stop lapping and to prevent further serious damage. Early detection of the anomalies can be achieved by a condition monitoring and fault detection system.

Competing Interests

The authors declare that there are no competing interests regarding the publication of this paper.

Acknowledgments

This work is sponsored by Western Digital (Thailand). The authors would like to thank the students from King Mongkut's University of Technology North Bangkok for their great support: Ms. Sumittra Viriyakitpattana and Ms. Kunjalin Sangrunruang.

References

- [1] Y.-C. Chiou, R.-T. Lee, and C.-L. Yau, “A novel method of composite electroplating on lap in lapping process,” *International Journal of Machine Tools and Manufacture*, vol. 47, no. 2, pp. 361–367, 2007.
- [2] M. P. Groover, *Fundamental of Modern Manufacturing*, John Wiley & Sons, New York, NY, USA, 2002.
- [3] N. J. Brown, “Some speculations on the mechanisms of abrasive grinding and polishing,” *Precision Engineering*, vol. 9, no. 3, pp. 129–138, 1987.
- [4] T. K. Doy, “Colloidal silica polishing based on micromechanical removal action and its applications,” *Sensors and Materials*, vol. 3, pp. 153–167, 1988.
- [5] T. Kasai, K. Horio, and A. Kobayashi, “Improvement of conventional polishing conditions for obtaining super smooth surfaces of glass and metal works,” *CIRP Annals—Manufacturing Technology*, vol. 39, no. 1, pp. 321–324, 1990.
- [6] Z. J. Pei, G. R. Fisher, and J. Liu, “Grinding of silicon wafers: a review from historical perspectives,” *International Journal of Machine Tools and Manufacture*, vol. 48, no. 12–13, pp. 1297–1307, 2008.
- [7] X. Zhu, C. Chung, C. S. Korach, and I. Kao, “Experimental study and modeling of the effect of mixed size abrasive grits on surface topology and removal rate in wafer lapping,” *Wear*, vol. 305, no. 1–2, pp. 14–22, 2013.
- [8] Y. Mei and K. A. Stelson, “Lapping control of hard disk drive heads,” *Journal of Dynamic Systems, Measurement and Control*, vol. 123, no. 3, pp. 439–448, 2001.
- [9] H. H. Gatzert, J. Christoph Maetzig, and M. K. Schwabe, “Precision machining of rigid disk head sliders,” *IEEE Transactions on Magnetics*, vol. 32, no. 3, pp. 1843–1849, 1996.
- [10] M. Jiang, S. Hao, and R. Komanduri, “On the advanced lapping process in the precision finishing of thin-film magnetic recording heads for rigid disc drives,” *Applied Physics A: Materials Science and Processing*, vol. 77, no. 7, pp. 923–932, 2003.
- [11] P. Wonglersak, P. Youngkong, and I. Cheowanish, “Classification of initial stripe height patterns using radial basis function neural network for proportional gain prediction,” in *Proceedings of the International Conference on Machine Learning and Data Analysis*, Venice, Italy, April 2011.
- [12] P. Wonglersak, P. Youngkong, and I. Cheowanish, “PD compensator for lapping process of hard disk drive heads,” in *Proceedings of the International Conference on Computer, Electrical, and Systems Sciences, and Engineering*, Paris, France, December 2011.
- [13] P. Maprachong and W. Tharmmapornphilas, “Increasing availability of lapping machine in a hard disk read/write head production process,” in *Proceedings of the IRES 4th International Conference*, Kuala Lumpur, Malaysia, July 2015.
- [14] W. Clarence, *Vibration Fundamentals and Practice*, CRC Press, 2000.
- [15] S. Nandi, H. A. Toliyat, and X. Li, “Condition monitoring and fault diagnosis of electrical motors—a review,” *IEEE Transactions on Energy Conversion*, vol. 20, no. 4, pp. 719–729, 2005.

- [16] F. P. Kopsaftopoulos and S. D. Fassois, "Vibration based health monitoring for a lightweight truss structure: experimental assessment of several statistical time series methods," *International Journal of Machine Tool & Manufacture*, vol. 24, pp. 1977–1997, 2010.
- [17] H. Wang, S. To, C. Y. Chan, C. F. Cheung, and W. B. Lee, "A theoretical and experimental investigation of the tool-tip vibration and its influence upon surface generation in single-point diamond turning," *International Journal of Machine Tools and Manufacture*, vol. 50, no. 3, pp. 241–252, 2010.
- [18] F. Wu, T. Wang, and J. Lee, "An online adaptive condition-based maintenance method for mechanical systems," *Mechanical Systems and Signal Processing*, vol. 24, no. 8, pp. 2985–2995, 2010.
- [19] P. K. Kankar, S. C. Sharma, and S. P. Harsha, "Fault diagnosis of ball bearings using continuous wavelet transform," *Applied Soft Computing Journal*, vol. 11, no. 2, pp. 2300–2312, 2011.
- [20] S. Sornmuang and J. Suwatthikul, "Detection of a motor bearing shield fault using neural networks," in *Proceedings of the 50th Annual Conference on Society of Instrument and Control Engineers (SICE '11)*, pp. 1260–1264, Tokyo, Japan, September 2011.
- [21] J. Suwatthikul and S. Sornmuang, "Fault detection and diagnosis of a motor bearing shield," in *Proceedings of the 6th IEEE International Conference on Intelligent Data Acquisition and Advanced Computing Systems (IDAACS '11)*, pp. 332–335, Prague, Czech Republic, September 2011.
- [22] H. Su, K. T. Chong, and R. R. Kumar, "Vibration signal analysis for electrical fault detection of induction machine using neural networks," *Neural Computing and Applications*, vol. 20, no. 2, pp. 183–194, 2011.
- [23] D. Zenunovic, M. Topalovic, and R. Folic, "Identification of modal parameters of bridges using ambient vibration measurements," *Shock and Vibration*, vol. 2015, Article ID 957841, 21 pages, 2015.
- [24] J. Huang, Q. Su, T. Liu, and X. Wang, "Vibration and long-term performance analysis of pile-plank-supported low subgrade of ballastless track under excitation loads," *Shock and Vibration*, vol. 2015, Article ID 404627, 12 pages, 2015.
- [25] A. Soleimani and S. E. Khadem, "Early fault detection of rotating machinery through chaotic vibration feature extraction of experimental data sets," *Chaos, Solitons & Fractals*, vol. 78, pp. 61–75, 2015.
- [26] D. Bayram and S. Şeker, "Anfis model for vibration signals based on aging process in electric motors," *Soft Computing*, vol. 19, no. 4, pp. 1107–1114, 2015.
- [27] T. Natsuki, N. Matsuyama, and Q. Ni, "Vibration analysis of carbon nanotube-based resonator using nonlocal elasticity theory," *Applied Physics A*, vol. 120, no. 4, pp. 1309–1313, 2015.
- [28] C. Ruiz-Cárcel, V. H. Jaramillo, D. Mba, J. R. Ottewill, and Y. Cao, "Combination of process and vibration data for improved condition monitoring of industrial systems working under variable operating conditions," *Mechanical Systems and Signal Processing*, vol. 66–67, pp. 699–714, 2016.
- [29] R. E. Kalman, "A new approach to linear filtering and prediction problems," *Journal of Basic Engineering*, vol. 82, no. 1, pp. 35–45, 1960.
- [30] G. Welch and G. Bishop, *An Introduction to the Kalman Filter*, UNC-Chapel Hill, 2006.
- [31] M. Negnevitsky, *Artificial Intelligence*, Addison Wesley, 2001.
- [32] H. Yu and B. M. Wilamowski, "Levenberg-marquardt training," in *Industrial Electronics Handbook*, CRC Press, 2011.

Research Article

Bearing Fault Diagnosis Using a Novel Classifier Ensemble Based on Lifting Wavelet Packet Transforms and Sample Entropy

Lei Zhang, Long Zhang, Junfeng Hu, and Guoliang Xiong

School of Mechatronics Engineering, East China Jiaotong University, Nanchang 330013, China

Correspondence should be addressed to Long Zhang; longzh@126.com

Received 21 October 2015; Revised 25 January 2016; Accepted 27 January 2016

Academic Editor: Konstantinos N. Gyftakis

Copyright © 2016 Lei Zhang et al. This is an open access article distributed under the Creative Commons Attribution License, which permits unrestricted use, distribution, and reproduction in any medium, provided the original work is properly cited.

In order to improve the fault detection accuracy for rolling bearings, an automated fault diagnosis system is presented based on lifting wavelet packet transform (LWPT), sample entropy (SampEn), and classifier ensemble. Bearing vibration signals are firstly decomposed into different frequency subbands through a three-level LWPT, resulting in a total of 8 frequency-band signals throughout the third layers of the LWPT decomposition tree. The SampEn's of all the 8 components are then calculated as feature vectors. Such a feature extraction paradigm is expected to depict complexity, irregularity, and nonstationarity of bearing vibrations. Moreover, a novel classifier ensemble is proposed to alleviate the effect of initial parameters on the performance of member classifiers and to improve classification effectiveness. Experiments were conducted on electric motor bearings considering various set of fault categories and fault severity levels. Experimental results demonstrate the proposed diagnosis system can effectively improve bearing fault recognition accuracy and stability in comparison with diagnosis methods based on a single classifier.

1. Introduction

Rolling element bearings are among the most critical components in various machines, and their faults are the main causes of breakdowns in rotating machinery. It was reported that rolling bearing faults accommodate 45–55% of asynchronous motor failures. A variety of fault diagnosis methods have been developed and exploited effectively to detect bearing faults at an early stage for the purpose of keeping machinery performing at its best and avoid unplanned downtime and economical loss. In order for the large machines used in current industry to operate in a safe and efficient mode, a number of sensors of which the number might be up to several thousands are employed to collect dynamical signals [1, 2]. The amount of signals to be processed is such vast that it must resort to automated fault diagnosis systems instead of manual analysis. Vibrations emitted from industry machinery like asynchronous motors usually contain signatures of multiple resources and are affected by operation parameters including speed and load. Accordingly, bearing fault diagnosis is not a trivial task in terms of signal

processing and fault identification. As an antecedent step of machine prognostics and health management (PHM), it needs to not only find the faulty bearings but also locate faulty components, as different fault location follows different fault development mode. As such, the objective of the present work is to identify bearing health condition and locate faulty bearing components with emphases on feature extraction and faulty component recognition.

When local faults such as cracks, pitting, and indentions occur to bearings, the fault signature is represented by repeating impulses in vibrations. The interval and intensity of impulses vary with speed or load fluctuation and slipping between bearing parts. As such, bearing vibrations could be considered to be nonstationary. Various methods have been employed to deal with the nonstationary characteristics of vibration signals for fault diagnosis of rolling bearings [3, 4]. For nonstationary signals, it is desired to examine how their energies vary with time and frequency. Such a demand impels the development of time-frequency or time-scale signal processing methods, among which wavelet packet transform (WPT) has proven effective in feature extraction

and been exploited for fault diagnosis of rolling bearings [5]. Selection of wavelet basis has a significant effect on the results of wavelet transform. During the past decades, many methods for constructing wavelet basis have been proposed, providing a rich variety of wavelet function for fault diagnosis in practice. These traditional wavelet functions were normally constructed by Fourier transform in the frequency domain, and hence the traditional wavelet transform was also known as the first-generation wavelet transform [6]. The WPT of a vibration signal results in a set of frequency-band signals locating in independent frequency bands by means of orthogonal or biorthogonal wavelet packet basis. The frequency-band signals are multiscale representation of original signals and able to highlight the information related to health condition of machinery. As frequency-band signals have the same length as original signal, it is therefore necessary to extract some features to represent each frequency-band signal and eventually result in a feature vector of original signals. The energies of each frequency-band signal at the bottom layer of the WPT decomposition tree are extracted as feature vector to depict bearing vibrations in [7]. Reference [8] extracts the standard deviations (STD) of the WPT coefficients as features for gear vibrations, where the experimental results indicate the STD can lead the neural networks to converge more rapidly than the aforementioned energy features.

Although feature extraction methods based on WPT preprocessing have reported considerable success in those works, more attention is deserved to be paid on the nonlinear information due to factors such as discontinuous stiffness, damping, surface friction, and impacts in defective bearings. The nonlinearity enriched by the presence of faults will render the traditional extraction methods based on the assumption of linear system less effective [9]. As such, it is important to extract nonlinear features for bearing fault diagnosis. With the development of the nonlinear theory, a lot of nonlinear dynamic parameters have found applications in fault diagnosis. Those nonlinear dynamic parameters, taking fractal dimension (FrD), for example, effectively describe the irregularity and complexity of the vibration signals and reflect the change in mechanical systems' health condition. Reference [10] decomposes vibration signals by WPT and utilizes FrD as a parameter to depict the irregularity and complexity of each frequency-band signal. The combined use of WPT and FrD can characterize not only the nonstationarity but also the irregularity and complexity of vibration signals.

In order to further improve the application of the WPT and nonlinear dynamic parameters, two items deserve more attention. On the one hand, the aforementioned feature extraction methods are all based on the first-generation wavelet packet transform preprocessing. However, WPT has limited number of wavelet functions and the adaptive construction of wavelet basis is difficult in practice. Lifting wavelet packet transform (LWPT) proposed by Sweldens, also known as the second-generation wavelet packet transform, is an alternative scheme for building wavelet function which was constructed by means of the lifting scheme. The wavelet function construction is no longer based on Fourier transform but is obtained completely in time domain [11]. Lifting wavelet packet transform therefore has a deal of

merits over the traditional WPT, including the flexibility of wavelet function construction and less computational effort and memory. As such, the LWPT is positively appreciated in mechanical fault diagnosis. On the other hand, the calculation of some nonlinear dynamic parameters like fractal dimension (FrD) requires a long noise-free data set which is not beneficial for online diagnosis and difficult to obtain particularly under nonstationary conditions. Due to such shortcomings, approximate entropy (ApEn) is proposed to assess regularity of time series by means of statistical methods and applied to dealing with physiological signals and vibration signals [12]. Sample entropy (SampEn) proposed by Richman and Moorman is a modified version of ApEn [13, 14]. In comparison with ApEn, SampEn is less dependent on data quantity and at certain extent robust to noises. Therefore, SampEn can exactly reflect the complexity and irregularity of signals with wide applications in biomedical signal processing [15, 16]. Motivated by the similarities between mechanical vibration signals and biomedical signals, SampEn is expected to effectively describe the complexity and irregularity of bearing vibrations. For these reasons, the present study investigates the joint use of LWPT and SampEn for feature extraction of bearings fault diagnosis.

In order to reduce manual intervention and human subjectivity, signals are analyzed in an automatic fashion in the form of intelligent diagnosis [17]. In recent years, artificial neural networks (ANNs) have been widely used in intelligent fault diagnosis to conduct pattern classification. The performance of a single neural network is usually affected by initial parameters like weights and node number in middle layer, and thus its recognition accuracy is unstable [18]. Aimed at such a dilemma, many methods of the multiple classifier fusion have been applied in the field of pattern recognition. Multiple classifiers fusion harnesses the advantages of different neural networks and avoids the shortcomings of a single neural network. Reference [19] utilizes the multiclassifier fusion which consists of seven different classifiers and combined by majority voting scheme (MVS) to classify four different patterns, which can acquire significantly higher classification accuracy than a single neural network. When more than one class wins the highest number of votes, classification decision was solved by comparing the sum of the posterior probability of each class. Reference [20] exploits the result from the highest rate of the member of multiclassifier in order to solve the problem that more than one class gets the highest number of votes. All of the above multiclassifier fusion can effectively improve the recognition accuracy in comparison with the diagnosis method based on a single classifier. However, these aforementioned methods not only employ a large number of classifiers which will increase computation burden and decrease recognition accuracy but also failed to fully resolve the problem that MVS become invalid when more than one classification wins the highest number of votes. For these reasons, the present study investigates a multiclassifier fusion algorithm using the form of binary tree for fault classification, where a multiclassification issue turns into a series of binary classification problems.

Based on the aforementioned discussions, a new approach is proposed for efficient bearing fault diagnosis by

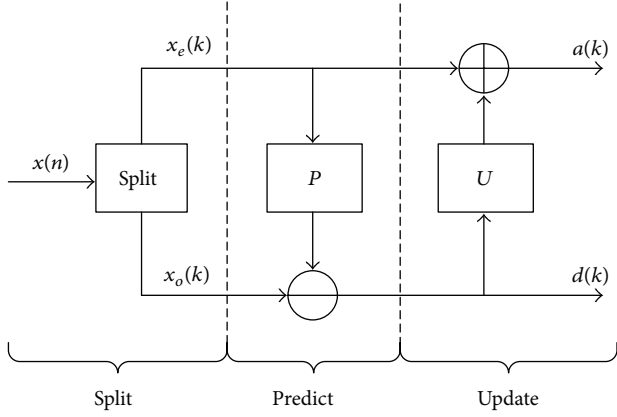


FIGURE 1: Decomposition steps of the second-generation wavelet transform.

conjunct use of the LWPT, SampEn, and binary tree structure based classifier ensemble. The novelties and contributions of the present work are twofold. Firstly, feature extraction is performed by LWPT and SampEn in order to exploit the nonstationarity, irregularity, and complexity of bearing vibrations. Secondly, a binary tree structure based classifier ensemble is proposed to mitigate the requirement on the number of member classifiers as well as improve classification accuracy and stability.

The paper is organized as follows. Section 2 introduces the theoretical backgrounds of LWPT, SampEn and presents the proposed binary tree structure based classifier ensemble. Section 3 shows the architecture of the proposed fault diagnosis system. The experimental setup is described in Section 4. In Section 5, the experimental results and discussions are given followed by a conclusion of the current paper in Section 6.

2. Theoretical Background

2.1. Lifting Wavelet Packet Transform. Wavelet packet transform can be implemented using lifting scheme in an easy understanding and efficient way [21]. The wavelet basis is determined by the prediction operator and update operator. Selecting different prediction operator $P = [p_1, p_2, \dots, p_M]$ and update operator $U = [u_1, u_2, \dots, u_{\bar{M}}]$ is equivalent to determining different wavelet function, which can obtain different signal decompositions. The decomposition process of the LWPT consists principally of three steps: split, predict, and update, as shown in Figure 1.

In the split step, the original signal $\{x(n), n = 0, 1, \dots, N - 1\}$ is decomposed into even samples $\{x_e(k), k = 0, 1, \dots, \lfloor N/2 \rfloor - 1\}$ and odd samples $\{x_o(k), k = 0, 1, \dots, \lfloor N/2 \rfloor - 1\}$. The symbol $\lfloor N/2 \rfloor$ is the smallest integer greater than or equal to $N/2$, $\lfloor N/2 \rfloor$ is the largest integer smaller than or equal to $N/2$, and

$$\begin{aligned} x_e(k) &= x(2k), \quad k = 0, 1, \dots, \left\lfloor \frac{N}{2} \right\rfloor - 1, \\ x_o(k) &= x(2k + 1), \quad k = 0, 1, \dots, \left\lfloor \frac{N}{2} \right\rfloor - 1. \end{aligned} \quad (1)$$

In the prediction step, using the adjacent M even samples to predict one odd sample (M is an even number) and the resulting error $d = \{d(k), k = 0, 1, \dots, \lfloor N/2 \rfloor - 1\}$ is defined as the detail coefficients of the wavelet transform. The processing of prediction is as follows:

$$\begin{aligned} d(k) &= x_o(k) - \sum_{i=1}^M p_i x_e\left(k - \frac{M}{2} + i\right), \\ k &= 0, \dots, \left\lfloor \frac{N}{2} \right\rfloor - 1, \end{aligned} \quad (2)$$

where $P = [p_1, p_2, \dots, p_M]$ is the prediction operator and its length is M .

In the update step, a designed update operator is applied on the detail coefficients obtained at the above step to update the even samples, which enable them to maintain a global nature of the original signal $x(n)$, such as energy, the mean, or vanishing moments. The update operator $U = [u_1, u_2, \dots, u_{\bar{M}}]$ is applied to the detail coefficients resulting from the prediction step and added to the even sample $x_e(k)$; the concrete processing of update step is as follows:

$$\begin{aligned} a(k) &= x_e(k) - \sum_{j=1}^{\bar{M}} u_j d\left(k - \frac{\bar{M}}{2} - 1 + j\right), \\ k &= 0, \dots, \left\lfloor \frac{N}{2} \right\rfloor - 1, \end{aligned} \quad (3)$$

where \bar{M} , an even number, is the length of the update operator. The above formula indicates that \bar{M} detail coefficients were used to update an even sample, and the obtained $a = \{a(k), k = 0, 1, \dots, \lfloor N/2 \rfloor\}$ is defined as the approximated factor of the original signal $x(n)$.

The above three steps complete the processing of the first decomposition of the lifting wavelet packet transform. In order to acquire approximation and detail coefficients for $x(n)$ at different scales, constantly repeat these three steps to approximation and detail coefficients which are calculated at each scale. The LWPT reconstruction can be performed by simple algebraic transformation from (2) and (3); the reconstruction processing of the LWPT consists of three steps: undo update, undo prediction, and merge, as shown in Figure 2.

In the undo update step, the even sample $x_e(k)$ is recovered using approximate coefficient a and detail coefficient d :

$$\begin{aligned} x_e(k) &= a(k) - \sum_{j=1}^{\bar{M}} u_j d\left(k - \frac{\bar{M}}{2} - 1 + j\right), \\ k &= 0, \dots, \left\lfloor \frac{N}{2} \right\rfloor - 1. \end{aligned} \quad (4)$$

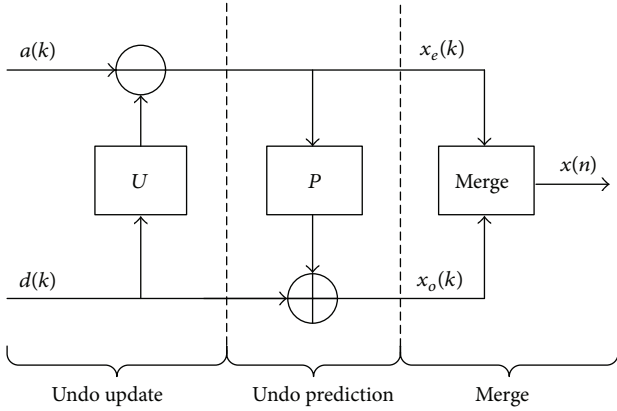


FIGURE 2: Reconstruction steps of the second-generation wavelet transform.

In the undo prediction step, the odd sample $x_o(k)$ is recovered using the above even sample $x_e(k)$ and detail coefficient d :

$$x_o(k) = d(k) - \sum_{i=1}^M p_i x_e\left(k - \frac{M}{2} + i\right), \quad (5)$$

$$k = 0, \dots, \left\lfloor \frac{N}{2} \right\rfloor - 1.$$

In the merge step, the original signal $x(n)$ is recovered using the above even sample $x_e(k)$ and odd sample $x_o(k)$:

$$x(2k) = x_e(k), \quad k = 0, 1, \dots, \left\lfloor \frac{N}{2} \right\rfloor - 1, \quad (6)$$

$$x(2k+1) = x_o(k), \quad k = 0, 1, \dots, \left\lfloor \frac{N}{2} \right\rfloor - 1.$$

2.2. Sample Entropy. Provided a time series containing N points $\{x(1), x(2), \dots, x(N)\}$, the step of calculating its sample entropy is as follows [13, 14].

- (I) Given the dimension of the space m , the original time series is composed of m dimension vector:

$$X(i) = [x(i), x(i+1), \dots, x(i+m-1)], \quad (7)$$

$$(i = 1, 2, \dots, N - m + 1).$$

- (II) Define the distance between two vectors $X(i)$ and $X(j)$:

$$d(i, j) = \max(|x(i+k) - x(j+k)|_{k=0, \dots, m-1}). \quad (8)$$

- (III) Given the threshold r , the number which satisfied the inequality $d(i, j) < r$ is counted for each value i , the ratio of this number, and the total number of distances $N - m + 1$ which is denoted by $B_i^m(r)$:

$$B_i^m(r) = \frac{[d(i, j) < r]}{N - m - 1}, \quad (9)$$

where $i \leq j \leq N - m$, $j \neq i$ and the average of all i is counted as

$$B^m(r) = \frac{1}{N - m} \sum_{i=1}^{N-m} B_i^m(r). \quad (10)$$

- (IV) The above three steps are repeated for $m + 1$, and then $B^{m+1}(r)$ is obtained.

- (V) Theoretically, SampEn(m, r) is defined as

$$\text{SampEn}(m, r) = \lim_{N \rightarrow \infty} \left[-\ln \frac{B^{m+1}(r)}{B^m(r)} \right] \quad (11)$$

and when N is a finite value, the SampEn of a time series containing N points is defined as

$$\text{SampEn}(m, r, N) = -\ln \frac{B^{m+1}(r)}{B^m(r)}. \quad (12)$$

2.3. Binary Tree Structure Based Classifier Ensemble. In pattern recognition, it is impossible to achieve good recognition results for all samples by only one classifier, and different classifiers may lead to different results. As the performance of a single neural network is susceptible to its initial parameters, the recognition accuracy is unstable and volatile. Therefore, the results obtained by using a single neural network are limited. For these reasons, multiple classifiers fusion has potentials to improve the results due to the fact that classifier ensemble combines the advantages and overcomes the shortcomings of member classifiers.

When majority voting scheme (MVS) is employed to build a classifier ensemble system, the number of the required member classifiers needs to be larger than that of the patterns to be recognized. In order to tackle such an issue, a multiclassifier fusion system is proposed by dividing the classification of multiple classes into a series of binary recognition issues. The member classifiers constructing the classifier ensemble system include BP neural network, Elman neural network, and RBF neural network.

BP neural network known as a feed-forward artificial neural network is proposed by Rumelhart, Hinton, and Williams in 1986 which belongs to supervised learning and consists of nonlinear transformation units [22]. A BP neural network has a three-layer or over three-layer structure with strong nonlinear mapping ability and self-learning, self-organization, and adaptive ability, which is currently the most widely used network in many fields.

Elman neural network, a well-known recurrent topology, is proposed by Jeffrey Elman in 1990. This network is more sensitive to the historical data, which enable it to handle the dynamic information. Furthermore, the network does not utilize state variable as the input or training signals due to the fact that its internal connections depict its dynamic characteristic, which makes it more suitable for the modeling of time-varying system [23].

RBF neural network, a feed-forward neural network with three layers, is proposed by Broomhead and Lowe in 1988. It is composed of input layer, hidden layer, and output layer

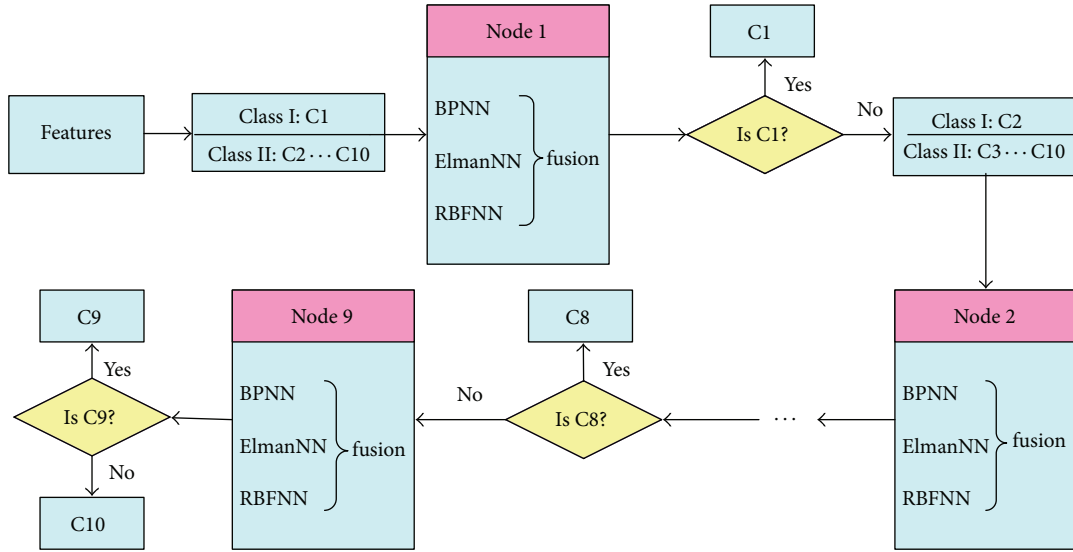


FIGURE 3: Binary tree structure based multiple classifier fusion.

where the input and output consist of linear neurons and the hidden layer node is a Gaussian kernel. The most important characteristics of the RBF network lie in the fact that its hidden layer neurons have only local reactions of input function, which is in the middle of the basis function. RBF neural network is characterized by simple structure, concise training, and fast learning convergence with the ability to approximate any nonlinear function [24].

Classifier ensemble gives a final result by combining the output of each member classifier through certain fusion algorithm. A lot of fusion algorithms are available like voting scheme and DS evidence theory. The present study exploits MVS to build a multiclassifier fusion system. The MVS is a simple and effective method at decision level, of which the final decision is the one that the majority of the member classifiers support. Although the final decision is not necessary to be the best decision rule, it is the decision with highest relative reliability. Nevertheless, for effective utilization of MVS, the number of the member classifiers is usually bound to be larger than that of the patterns to be recognized. Otherwise, it is difficult to achieve decision fusion in certain cases. For example, if 3 classifiers are applied to classify 10 patterns, the 3 classifiers may give a result different with each other. In this case, the MVS is unable to give a reasonable result. Aimed at such a problem, the present study puts forward a classifier ensemble algorithm performed in the form of binary tree, where the multiclassification problem is divided into a sequence of binary classification. Figure 3 shows the procedure of the proposed classifier ensemble. Patterns are grouped into two categories at each node, and the first category contains only one fault type while the rest of the fault types are considered as the other category. Taking a total of 10 fault types for example, at the first node of the binary tree, the bearing condition C1 is treated as the first category, while the remaining 9 bearing health conditions are packed together as the other category. This process is repeated until the last node contains only two bearing fault types, that is, C9 and C10.

Such a trick transforms the multiclassification problem into a series of binary classification problems, which is beneficial for performing multiclassifier fusion based on the MVS with only three member classifiers on each node.

3. Architecture of the Proposed Fault Diagnosis System

Figure 4 depicts the procedure of the proposed fault diagnosis system. Firstly, the signals are decomposed into different frequency subbands through a three-level LWPT, resulting in a total of 8 node signal components. Later on, the SampEns of all the 8 components were calculated as a feature input to a binary tree structure based classifier ensemble. The trained binary tree based classifier ensemble was finally utilized to recognize the testing set.

4. Experimentation

4.1. Experimental Setup. Experiments were conducted on rolling bearings to testify the proposed fault diagnosis method. The test rig is a motor-driven mechanical system as shown in Figure 5 which is composed of a three-phase induction motor on the left, a torque sensor in the middle, and a dynamometer on the right [25]. Because a big load can facilitate fault diagnosis of rolling bearing, the vibration signals of rolling bearing were collected under a load free state which can serve as a better metric to measure the effectiveness of the fault diagnosis method. The tested bearings are 6205-2RS JEM SKF, deep-groove ball bearings, which are fixed in the motor drive end to brace the motor shaft. Faults are preseeded on one element of rolling bearings involving ball, outer race, and inner race by means of electric discharge machining. The levels of fault severity for each fault type include (0.1778 mm, 0.2794 mm), (0.3556 mm, 0.2794 mm), and (0.5334 mm, 0.2794 mm) in fault diameter and depth, respectively.

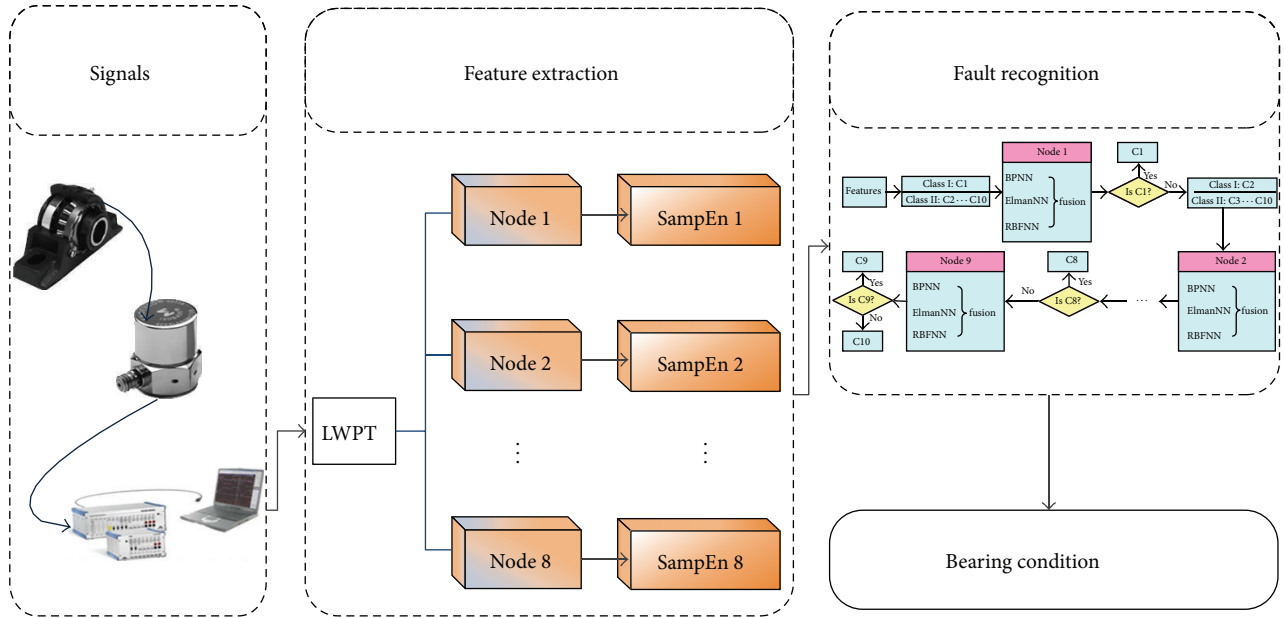


FIGURE 4: The structure of the proposed fault diagnosis system.

TABLE 1: Experimental data condition.

Bearing condition	Defect size (mm)	Number of samples	Condition number
Normal	0	60	C1
Inner race fault	0.1778×0.2797	60	C2
	0.3556×0.2797	60	C3
	0.5334×0.2797	60	C4
Outer race fault	0.1778×0.2797	60	C5
	0.3556×0.2797	60	C6
	0.5334×0.2797	60	C7
Rolling ball fault	0.1778×0.2797	60	C8
	0.3556×0.2797	60	C9
	0.5334×0.2797	60	C10

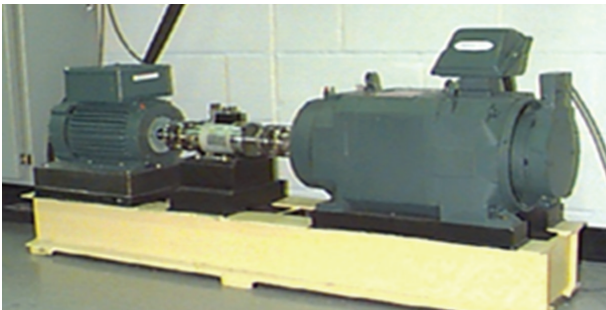


FIGURE 5: Rolling bearing fault test sets.

The vibration signals were obtained by means of a 16-channel DAT recorder at the sampling frequency of 12 000 Hz, and the shaft rotating speed was set approximately 1797 rpm. In order to acquire vibration signals of various bearing health conditions, an accelerometer was attached to

the motor housing at the drive end and fixed at 12 o'clock position. The experimental data set is depicted in Table 1 in detail, including a total of 10 bearing conditions considering various fault types and different severity levels. Each bearing condition was collected with 60 samples, and each data sample contains 2000 data points. Examples for the time waveforms of the 10 bearing conditions are shown in Figure 6, where conditions C3, C5, and C7 are characterized by obvious impulses.

4.2. Feature Extraction. Features extracted from bearing vibrations should characterize not only the nonstationarity but also the irregularity and complexity embedded in the data. Lifting wavelet packet transform takes advantage of the local relevance in signal data structure to perform wavelet function construction completely in the time domain, so it is suitable for processing vibration signals of rolling bearings. The lifting wavelet function is determined by the prediction and update operators which are produced by the interpolating subdivision method (ISM) introduced in [11]. When the

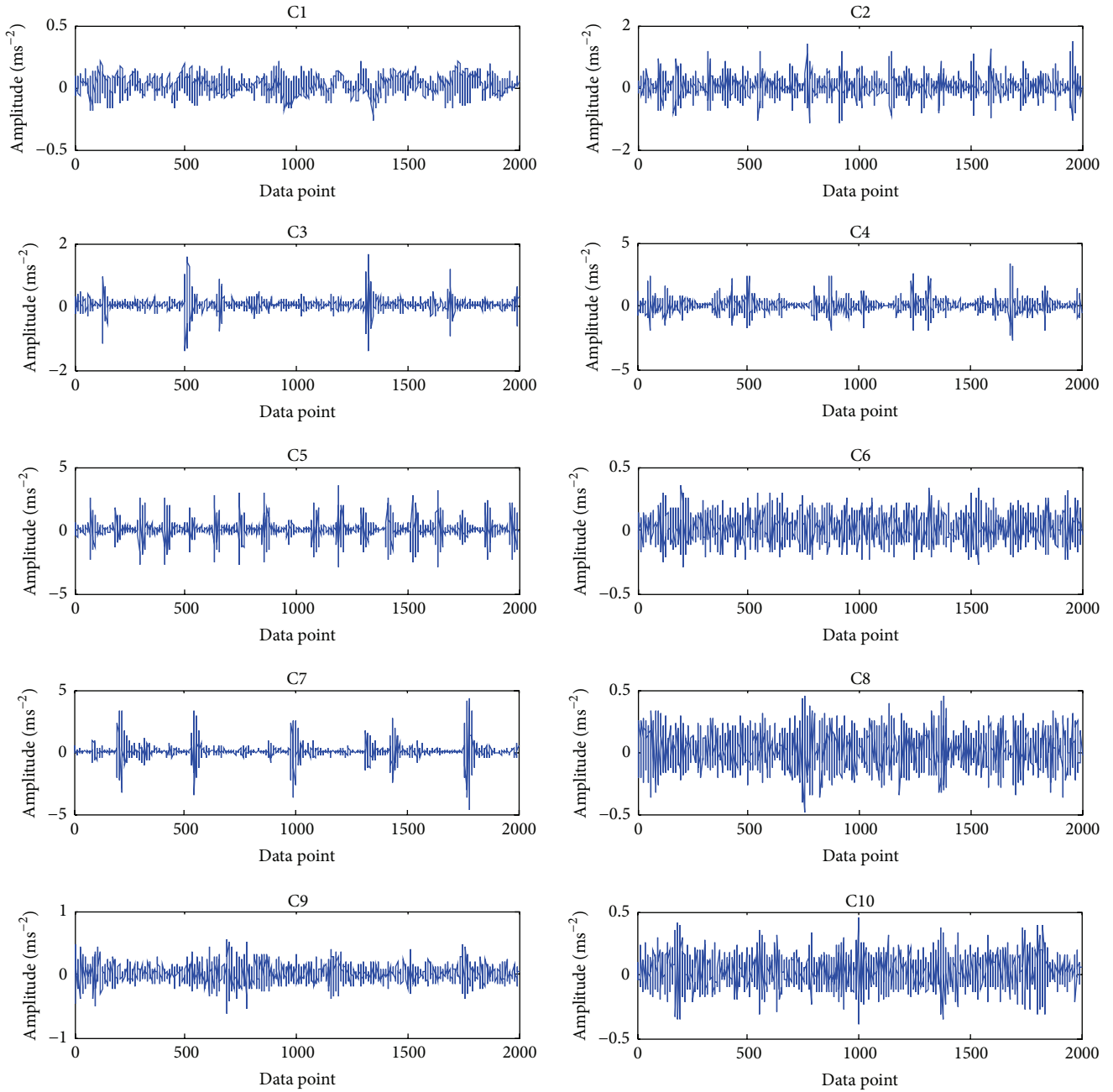


FIGURE 6: Vibration signals of 10 bearing conditions.

order of both prediction and update operators is 12, operators P and U as well as the waveforms of scale and wavelet function are as follows. It is observed from Figure 7 that the wavelet function is in a considerable agreement with bearing shocks:

$$\begin{aligned}
 P = & [-0.1202, 1.6155, -10.3855, 43.6192, \\
 & -145.3972, 610.6682, 610.6682, \\
 & -145.3972, 43.6192, -10.3855, 1.6155, -0.1202] \\
 & \times 10^{-3},
 \end{aligned}$$

$$\begin{aligned}
 U = & [-0.0601, 0.8078, -5.1928, 21.8096, \\
 & -72.6986, 305.3341, 305.3341, \\
 & -72.6986, 21.8096, -5.1928, 0.8078, -0.0601] \\
 & \times 10^{-3}.
 \end{aligned}$$

(13)

SampEn is an improved version of approximate entropy with the ability to reflect the complexity and irregularity of a time series. For calculation of SampEn, the dimension m and the tolerance level r should be determined a priori. Herein,

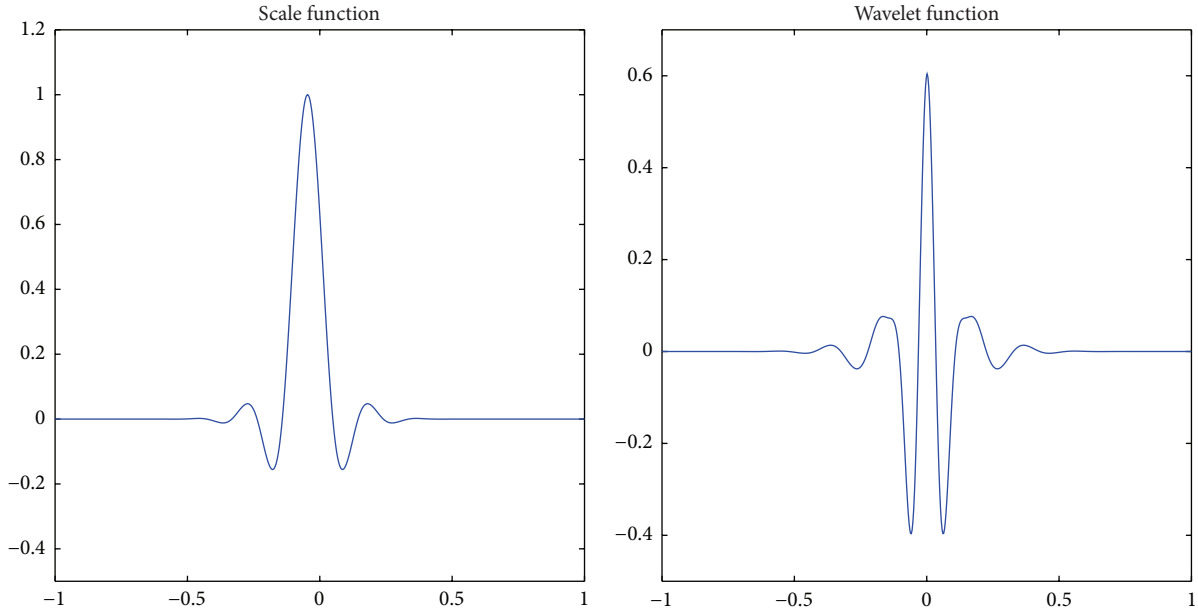


FIGURE 7: Scale and wavelet function when $M = 12$, $\tilde{M} = 12$.

the tolerance level r is selected as 0.2 times the standard deviations of the inspected data and the dimension of the space m is chosen as 2.

With above selected parameters, the bearing signals are first decomposed by the three-level LWPT (with $M = 12$, $\tilde{M} = 12$). The SampEns of all the 8 components are then calculated as a feature vector to depict the irregularity and complexity of the bearing vibration signals. By the joint use of the LWPT and SampEn, the features of the signals shown in Figure 6 are obtained. It is seen from Figure 8 that the extracted features can effectively distinguish among different bearing fault types and severity levels.

4.3. Experimental Data and Parameter Preparation. As shown in Table 1, 10 types of bearing conditions have $60 \times 10 = 600$ data samples in total. The data set was divided into a training set and a testing set, where the training set was 40 randomly selected samples from each kind of health conditions and the testing set was constituted by the remaining data samples. That is, the training set comprised $40 \times 10 = 400$ data samples and the testing set contained $20 \times 10 = 200$ data samples. The testing set serves the purpose of measuring the performance of the trained binary tree structure based classifier ensemble. Each sample is represented by a feature vector consisting of the SampEns of all the 8 node signal components throughout the third layer of the LWPT decomposition tree. In the present experiment, the bearing signals are first decomposed by a (12, 12) three-level LWPT. The SampEns of all the 8 components are then calculated as a feature vector to characterize the complexity of the bearing vibration signals and then input to binary tree structure based classifier ensemble to train each classifier involving BP neural network and Elman neural network as well as RBF neural network. The transfer function of hidden layer and output layer neurons of BP neural network employs Logsig and

Purelin, respectively. The largest amount of training and the minimum mean square error are chosen as 1000 and 10^{-8} , respectively. The hidden layer node number is selected as 10 for BP neural network. The transfer function of hidden layer and output layer neurons of Elman neural network is Tansig and Purelin, respectively. The largest amount of training is chosen as 1000, the minimum mean square error is set as 10^{-8} , and the hidden layer nodes number is 10 for Elman neural network. For RBF neural network, the correlation function adopts Newrbe and the value of spread of radial basis function is chosen as 1.

5. Results and Discussion

5.1. Diagnostic Results from Binary Tree Structure Based Classifier Ensemble. Due to the advantages of binary tree structured classifier ensemble, the fusion algorithm shown in Figure 3 is adopted. In this context, the bearing condition C1 is treated as one category, while the remaining 9 types of bearing health condition are grouped into the other category in the first node of the binary tree. The tree node employs three different neural networks and MVS fusion strategy to separate condition C1 from other 9 conditions. In the second node, the bearing condition C2 is distinguished from other 8 conditions excluding condition C1 by means of classifier ensemble based on three classifiers and MVS. The above steps are repeated until all the 10 bearing conditions are differentiated.

Given that the initial connection weights and thresholds have an effect on the performance of each member classifier, 100 runs for binary tree structure based classifier ensemble using the same training set and testing set were conducted. The recognition accuracy of 100 runs for binary tree system is shown in Figure 9, where the highest accuracy, the average accuracy, and the lowest accuracy are 100%, 99.53%, and

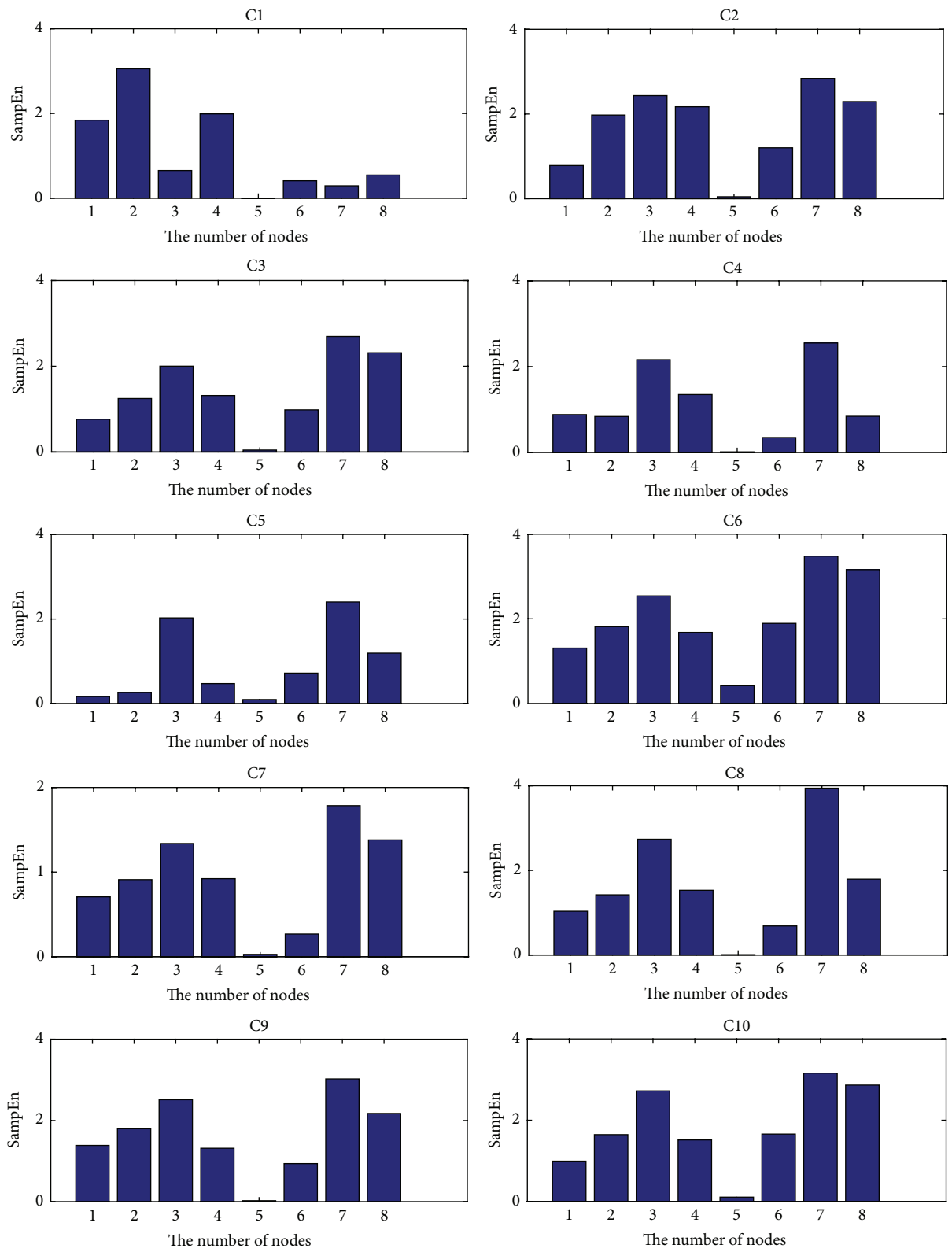


FIGURE 8: Features of 10 bearing conditions extracted by LWPT and SampEn.

TABLE 2: Averaged confusion matrix over 100 tests (%).

True condition	Assigned condition (%)									
	C1	C2	C3	C4	C5	C6	C7	C8	C9	C10
C1	100.0	0	0	0	0	0	0	0	0	0
C2	0	100.0	0	0	0	0	0	0	0	0
C3	0	0	100.0	0	0	0	0	0	0	0
C4	0	0	0	100.0	0	0	0	0	0	0
C5	0	0	0	0	100.0	0	0	0	0	0
C6	0	0	0	0	0	100.0	0	0	0	0
C7	0	0	0	0	0	0	100.0	0	0	0
C8	0	0	0	0	0	0	0	100.0	0	0
C9	0	0	0	0	0	0	3.5	0.2	96.3	0
C10	0	0	0.7	0	0	0	0	0.3	0	99.0

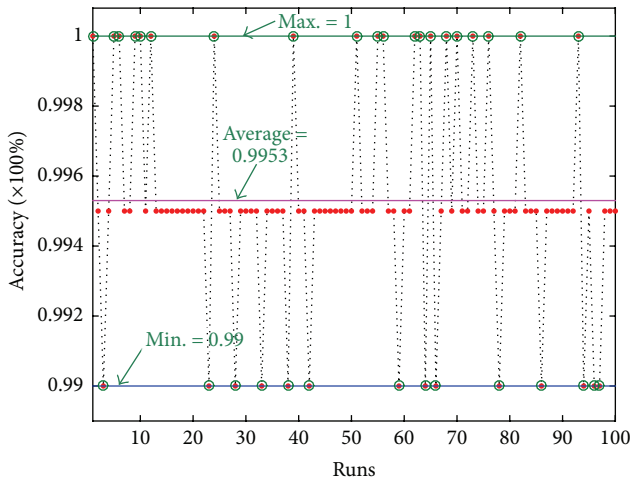


FIGURE 9: Testing results of 100 runs for binary tree system.

99.00%, respectively. The recognition accuracy is considerably stable which implies that the classifier ensemble has a good adaptability and high stability. It is demonstrated that the effect of initial connection weights and thresholds on the final recognition accuracy is small and negligible. The proposed binary tree structure based classifier ensemble can effectively judge bearing fault type and severity.

In order to further examine the details of the classification results, the confusion matrix averaged over the 100 tests is shown in Table 2. The cells along the diagonal of the 10×10 matrix indicate the percentage of accurately sorted samples, while the other cells of the diagonal reveal the misclassified samples. Utilizing the cells at the second row from the bottom of the matrix in Table 2, for example, it is shown that the samples belonging to bearing condition C9 are misclassified into conditions C7 and C8 by the proportion of 3.5% and 0.2%, respectively. On the other hand, the value 96.3% indicates the proportion of exactly classified samples. Therefore, the values of the cells along the diagonal are expected to be as large as possible. A small value of the cell along the diagonal in the first line indicates a higher risk for a healthy condition misdiagnosed as that with fault, which will lead to unnecessary production downtime. It is observed in

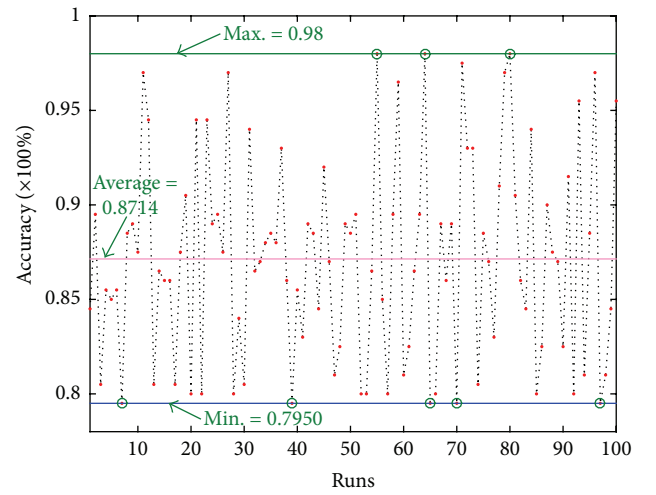


FIGURE 10: Testing results of 100 runs using BP neural network.

Table 2 that false identifications just occurred with conditions C9 and C10 and the remaining conditions are able to be identified correctly.

5.2. Comparison with a Single Neural Network. In order to verify the advantages of the binary tree structured classifier ensemble in fault classification, single classifier was utilized for comparison purpose including BP network, Elman network, and RBF network. The training set, testing set, and the initial settings except weights and thresholds of each member classifier are identical with those used in above classifier ensemble. Considering the initial connection weights and thresholds have an effect on the performance of BP neural network and Elman neural network, the test was repeated 100 times for each classifier using the same training set and testing set, but the weights and thresholds are randomly obtained. Figures 10 and 11 show the 100 test results for the BP neural network and Elman neural network, respectively. The results of RBF neural network vary with its ‘‘Spread’’ value. With the ‘‘Spread’’ varying from 1 to 100 with a step of 1, the test using RBF was repeated 100 times with results shown in Figure 12.

Figure 10 shows that the maximum accuracy, the averaged accuracy, and the minimum accuracy of BP neural network

TABLE 3: Classification results using different classifiers of 100 runs ($\times 100\%$).

Classifiers	Minimum accuracy	Average accuracy	Maximum accuracy
BP	0.7950	0.8714	0.9800
Elman	0.7000	0.8046	0.9350
RBP	0.8400	0.8606	0.9200
Binary tree system	0.9900	0.9953	1

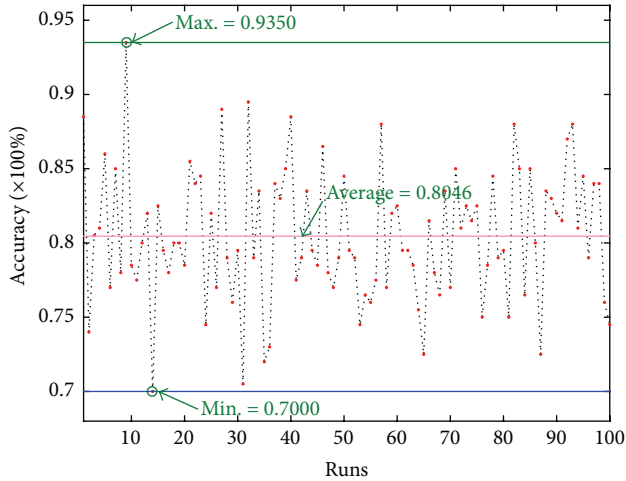


FIGURE 11: Testing results of 100 runs using Elman neural network.

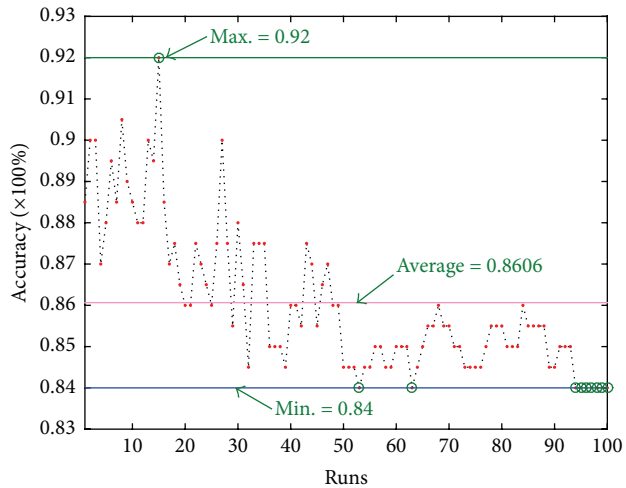


FIGURE 12: Testing results of 100 runs using RBF neural network.

are 98.00%, 87.14%, and 79.50%, respectively. The test results show the initial connection weights and thresholds have a substantial effect on the performance of BP neural network and lead the accuracy to fluctuate significantly. It is seen from Figure 11 that the maximum, averaged, and minimum recognition accuracy are 93.50%, 80.46%, and 70.00% for Elman neural network. The test results demonstrate that randomly selected initial connection weights and thresholds may result in an unfavorable accuracy. Figure 12 exhibits that the maximum accuracy is up to 92.00% when the “Spread” of radial basis function is 15, while the averaged accuracy

is 86.07%. The recognition rate gets its minimum values of 84.00% when the value of “Spread” is 53, 63, or within 94 to 100. The test results illustrate that the recognition accuracy is highly sensitive to the “Spread” of radial basis function. The results of classifier ensemble and member classifiers are summarized in Table 3 in the form of minimum, average, and maximum diagnosis accuracy. It is seen that the performance of classifier ensemble is superior to any member classifier in the sense that the classifier fusion has a high average accuracy and the difference between maximum and minimum accuracy is small. The small variation of diagnosis accuracy means the classifier ensemble paradigm is robust to initial parameter selection of member classifiers, which is important for intelligent diagnosis to be used in the fields. The accuracy of member classifier is necessary to be larger than a random assignment in the framework of multiple classifier fusion. The fusion philosophy can give a reasonable result by synthesizing results of the member classifiers. The excellent performance of classifier ensemble can also be ascribed to the conjunct use of the LWPT and SampEn to characterize not only the nonstationarity but also the irregularity and complexity of bearing vibration signals.

The confusion matrixes averaged over the 100 tests are shown in Tables 4, 5, and 6 when only using BP neural network, Elman neural network, and RBF neural network, respectively. Table 4 shows that conditions C8, C9, and C10 show high misidentified probability and poor diagnostic reliability with BP neural network. Table 5 indicates that high misclassifications also lie in conditions C8, C9, and C10 by Elman neural network with the average diagnostic accuracy of 10.35%, 67.75%, and 31.10%, respectively. Such results imply that BP and Elman neural networks have trouble in distinguishing between the three levels of fault severity on rolling element. The false identifications of RBF networks mostly appear in conditions C8 and C10 as shown in Table 6 where the samples belonging to condition C8 are misclassified into conditions C4 and C9 by the proportion of 74.4% and 0.15% and the samples belonging to condition C10 are misclassified into conditions C4, C7, and C9 by the proportion of 62.05%, 0.05%, and 0.2%, respectively. Above comparison indicates that classifier ensemble is robust to initial parameters of networks and can recognize both fault type and fault severity level with a satisfied accuracy by resorting to the effective feature extraction using the LWPT and SampEn.

6. Conclusions

The current paper presents an intelligent diagnosis method for rolling bearings by integrating the LWPT, SampEn, and

TABLE 4: Averaged confusion matrix of 100 tests for BP neural network (%).

True condition	Assigned condition (%)									
	C1	C2	C3	C4	C5	C6	C7	C8	C9	C10
C1	100.0	0	0	0	0	0	0	0	0	0
C2	0	99.95	0	0.05	0	0	0	0	0	0
C3	0	0	100.0	0	0	0	0	0	0	0
C4	0	0	0	100.0	0	0	0	0	0	0
C5	0	0	0	0	99.95	0	0	0	0.05	0
C6	0	0	0	0	0	100.0	0	0	0	0
C7	0	0	0	0	0	0	100.0	0	0	0
C8	0	0	0	64.75	0	0	0	34.95	0.3	0
C9	0.05	0	0.85	1.25	0	0.05	1.85	0.2	95.75	0
C10	0	0.1	0.1	58.4	0.05	0	0	0	0.55	40.8

TABLE 5: Averaged confusion matrix of 100 tests for Elman neural network (%).

True condition	Assigned condition (%)									
	C1	C2	C3	C4	C5	C6	C7	C8	C9	C10
C1	100.0	0	0	0	0	0	0	0	0	0
C2	0	99.6	0	0.4	0	0	0	0	0	0
C3	0	0.55	95.8	0.05	0	0	2.9	0	0	0.7
C4	0	0	0	100.0	0	0	0	0	0	0
C5	0	0	0	0	100.0	0	0	0	0	0
C6	0	0	0	0	0	99.95	0	0	0	0.05
C7	0	0	0	0	0	0	100.0	0	0	0
C8	0	0	0	89.65	0	0	0	10.35	0	0
C9	0	0	1.1	25.45	0	0	4.9	0.75	67.75	0.05
C10	0	0.1	0.3	67.9	0.45	0.05	0	0.05	0.05	31.1

TABLE 6: Averaged confusion matrix of 100 tests for RBF neural network (%).

True condition	Assigned condition (%)									
	C1	C2	C3	C4	C5	C6	C7	C8	C9	C10
C1	100.0	0	0	0	0	0	0	0	0	0
C2	0	100.0	0	0	0	0	0	0	0	0
C3	0	0	100.0	0	0	0	0	0	0	0
C4	0	0	0	100.0	0	0	0	0	0	0
C5	0	0	0	0	100.0	0	0	0	0	0
C6	0	0	0	0.15	0	99.8	0	0	0.05	0
C7	0	0	0	0	0	0	100.0	0	0	0
C8	0	0	0	74.4	0	0	0	25.45	0.15	0
C9	0	0	0.3	0.65	0	0	1.15	0.2	97.7	0
C10	0	0	0	62.05	0	0	0.05	0	0.2	37.7

binary tree structure based classifier ensemble. The distinct merits of the diagnosis method lie in the feature extraction methods combining the LWPT with the SampEn as well as the recognition methods by binary tree system based classifier ensemble. Given that bearing vibrations especially in fault conditions demonstrate not only nonstationarity but also irregularity and complexity, vibration signals are decomposed by a three-level LWPT followed by the application of the SampEnS to all the 8 components as feature vectors to represent the bearing vibration signals. A multiclassifier

fusion algorithm is presented using the form of binary tree, due to the fact that initial connection weights and thresholds have a significant effect on the performance for a single neural network classifier and traditional fusion algorithms for multiple classifier not only require a large number of member classifiers leading to increase of computation effort and decrease of recognition accuracy but also fail to resolve the problem with more than one class winning the highest number of votes. Experimental data are composed of 10 kinds of bearing health conditions including various fault types

and severity levels. The results demonstrate the proposed method can effectively improve the recognition accuracy and performance stability for rolling bearing fault diagnosis in comparison with the diagnosis method based on a single classifier.

Conflict of Interests

The authors declare that there is no conflict of interests regarding the publication of this paper.

Acknowledgments

This work was financially supported by the Natural Science Foundation of China (51205130, 51265010) and the Foundation of Jiangxi Association for Science and Technology (YHG2014-154) as well as the Postgraduate Innovation Funds of Jiangxi Province (YC2014-S244, YC2015-S239).

References

- [1] X. Zhang, J. Kang, L. Xiao, J. Zhao, and H. Teng, "A new improved Kurtogram and its application to bearing fault diagnosis," *Shock and Vibration*, vol. 2015, Article ID 385412, 22 pages, 2015.
- [2] W. Wen, Z. Fan, D. Karg, and W. Cheng, "Rolling element bearing fault diagnosis based on multiscale general fractal features," *Shock and Vibration*, vol. 2015, Article ID 167902, 9 pages, 2015.
- [3] P. H. Nguyen and J.-M. Kim, "Multifault diagnosis of rolling element bearings using a wavelet kurtogram and vector median-based feature analysis," *Shock and Vibration*, vol. 2015, Article ID 320508, 14 pages, 2015.
- [4] X. Jin, M. Zhao, T. W. S. Chow, and M. Pecht, "Motor bearing fault diagnosis using trace ratio linear discriminant analysis," *IEEE Transactions on Industrial Electronics*, vol. 61, no. 5, pp. 2441–2451, 2014.
- [5] R. Yan, M. Shan, J. Cui, and Y. Wu, "Mutual information-assisted wavelet function selection for enhanced rolling bearing fault diagnosis," *Shock and Vibration*, vol. 2015, Article ID 794921, 9 pages, 2015.
- [6] I. Daubechies and W. Sweldens, "Factoring wavelet transform into lifting steps," *Journal of Fourier Analysis and Applications*, vol. 4, no. 3, pp. 245–267, 1998.
- [7] Y. Pan, J. Chen, and L. Guo, "Robust bearing performance degradation assessment method based on improved wavelet packet-support vector data description," *Mechanical Systems and Signal Processing*, vol. 23, no. 3, pp. 669–681, 2009.
- [8] J. Rafiee, F. Arvani, A. Harifi, and M. H. Sadeghi, "Intelligent condition monitoring of a gearbox using artificial neural network," *Mechanical Systems and Signal Processing*, vol. 21, no. 4, pp. 1746–1754, 2007.
- [9] E. Cabal-Yepez, M. Valtierra-Rodriguez, R. J. Romero-Troncoso et al., "FPGA-based entropy neural processor for online detection of multiple combined faults on induction motors," *Mechanical Systems and Signal Processing*, vol. 30, pp. 123–130, 2012.
- [10] C.-H. Chen, R.-J. Shyu, and C.-K. Ma, "Rotating machinery diagnosis using wavelet packets-fractal technology and neural networks," *Journal of Mechanical Science and Technology*, vol. 21, no. 7, pp. 1058–1065, 2007.
- [11] W. Sweldens, "The lifting scheme: a construction of second generation wavelets," *SIAM Journal on Mathematical Analysis*, vol. 29, no. 2, pp. 511–546, 1998.
- [12] S. M. Pincus, "Approximate entropy as a measure of system complexity," *Proceedings of the National Academy of Sciences of the United States of America*, vol. 88, no. 6, pp. 2297–2301, 1991.
- [13] J. S. Richman and J. R. Moorman, "Physiological time-series analysis using approximate entropy and sample entropy," *American Journal of Physiology—Heart and Circulatory Physiology*, vol. 278, no. 6, pp. H2039–H2049, 2000.
- [14] N.-K. Hsieh, W.-Y. Lin, and H.-T. Young, "High-speed spindle fault diagnosis with the empirical mode decomposition and multiscale entropy method," *Entropy*, vol. 17, no. 4, pp. 2170–2183, 2015.
- [15] V. Bari, A. Marchi, B. de Maria et al., "Low-pass filtering approach via empirical mode decomposition improves short-scale entropy-based complexity estimation of QT interval variability in long QT syndrome type 1 patients," *Entropy*, vol. 16, no. 9, pp. 4839–4854, 2014.
- [16] Q. Wei, Q. Liu, S.-Z. Fan et al., "Analysis of EEG via multivariate empirical mode decomposition for depth of anesthesia based on sample entropy," *Entropy*, vol. 15, no. 9, pp. 3458–3470, 2013.
- [17] V. A. Sotiris, P. W. Tse, and M. G. Pecht, "Anomaly detection through a Bayesian support vector machine," *IEEE Transactions on Reliability*, vol. 59, no. 2, pp. 277–286, 2010.
- [18] L. Zhang, G. L. Xiong, L. P. Liu, and Q. S. Cao, "Gearbox health condition identification by neuro-fuzzy ensemble," *Journal of Mechanical Science and Technology*, vol. 27, no. 3, pp. 603–608, 2013.
- [19] B. Yang, Z. J. Liu, and Y. Xing, "Integration of multiple classifiers for remote sensing image classification," *Remote Sensing Information*, vol. 27, no. 6, pp. 17–20, 2012.
- [20] B. B. Tang, X. W. Wang, and W. H. Wang, "Network traffic classification based on combination of multi-classifiers," *Computer Engineering and Applications Journal*, vol. 49, pp. 82–84, 2013.
- [21] W. Sweldens, "Bulding your own wavelet at home," in *Proceedings of the ACM SIGGRAPH Wavelets in Computer Graphics*, pp. 16–87, 1996.
- [22] C. C. Ma, X. D. Gu, and Y. Y. Wang, "Fault diagnosis of power electronic system based on fault gradation and neural network group," *Neurocomputing*, vol. 72, no. 13–15, pp. 2909–2914, 2009.
- [23] B. Fan, Z. M. Du, X. Q. Jin, X. B. Yang, and Y. B. Guo, "A hybrid FDD strategy for local system of AHU based on artificial neural network and wavelet analysis," *Building and Environment*, vol. 45, no. 12, pp. 2698–2708, 2010.
- [24] Q. Yi, L. Zhan-Ming, and L. Er-Chao, "Fault detection and diagnosis for non-Gaussian stochastic distribution systems with time delays via RBF neural networks," *ISA Transactions*, vol. 51, no. 6, pp. 786–791, 2012.
- [25] K. A. Loparo, "Bearing Vibration Data: Case Western Reserve University Bearing Data Center Website," January 2015, <http://csegroups.case.edu/bearingdatacenter/pages/welcome-case-western-reserve-university-bearing-data-center-website>.

Research Article

A New Feature Extraction Technique Based on 1D Local Binary Pattern for Gear Fault Detection

Zrar Kh. Abdul,¹ Abdulbasit Al-Talabani,² and Ayub O. Abdulrahman³

¹Department of Computer, Charmo University, Sulaymaniyah, Iraq

²Department of Software Engineering, Koya University, Erbil, Iraq

³Halabja Institution, Halabja, Iraq

Correspondence should be addressed to Zrar Kh. Abdul; eng.zrar1394@gmail.com

Received 8 November 2015; Revised 12 January 2016; Accepted 17 January 2016

Academic Editor: Arturo Garcia-Perez

Copyright © 2016 Zrar Kh. Abdul et al. This is an open access article distributed under the Creative Commons Attribution License, which permits unrestricted use, distribution, and reproduction in any medium, provided the original work is properly cited.

Gear fault detection is one of the underlying research areas in the field of condition monitoring of rotating machines. Many methods have been proposed as an approach. One of the major tasks to obtain the best fault detection is to examine what type of feature(s) should be taken out to clarify/improve the situation. In this paper, a new method is used to extract features from the vibration signal, called 1D local binary pattern (1D LBP). Vibration signals of a rotating machine with normal, break, and crack gears are processed for feature extraction. The extracted features from the original signals are utilized as inputs to a classifier based on k -Nearest Neighbour (k -NN) and Support Vector Machine (SVM) for three classes (normal, break, or crack). The effectiveness of the proposed approach is evaluated for gear fault detection, on the vibration data obtained from the Prognostic Health Monitoring (PHM'09) Data Challenge. The experiment results show that the 1D LBP method can extract the effective and relevant features for detecting fault in the gear. Moreover, we have adopted the LOSO and LOLO cross-validation approaches to investigate the effects of speed and load in fault detection.

1. Introduction

It is a big challenge in fault detection and diagnostics to ensure the safe running of rotating machines. Vibration signal analysis has been widely used for fault diagnostics. With increasing improvements in vibration signal analysis, more accurate fault-detection techniques are being developed. In the area of gear fault detection, researchers are constantly investigating techniques for relevant features of fault detection.

Among several signal analysis methods, fast Fourier transform (FFT) is one of the most widely used and well-established methods. For instance, Pan and Sas in [1] conducted two tests, one to measure transient vibration signals and another to analyse the nonstationary vibration response of a rotor-dynamic system with both clutch and brake. Unfortunately, FFT-based methods are not suitable for nonstationary signal analysis and are not able to reveal the inherent information of nonstationary signals [1]. On the other hand,

both wavelet scalogram and wavelet transform are effective methods for extracting relevant features of vibration signal for fault diagnostics of rotating machinery and are suitable for nonstationary signal analysis. In [2], statistical feature vectors were obtained using Morlet wavelet coefficients, which were utilized as the input into Support Vector Machine (SVM) classifiers. Al-Atat et al. in [3] developed a model that built specific fault signatures more visibly by applying wavelet decomposition into the row signal. However, the wavelet scalogram is incapable of achieving good time and spectral concentration in both the time and frequency space. Moreover, the wavelet transform cannot fully estimate the “good” features, because the vibration signal generates the structure of components, which makes it difficult to identify features for each component by wavelet transform alone [2, 4, 5]. Momoh and Dias [6] applied both FFT and wavelet transform to the extraction of features for fault detection and found that the wavelet transform scheme outperformed the FFT scheme.

Another method of fault detection is called Time Synchronous Average (TSA). TSA is a signal processing technique, which is used to extract repetitive signals from additive noise [7, 8]. Peng et al. [4] used a TSA technique in time and frequency domain. A TSA signal was obtained by applying the TSA technique to the vibration signal. Statistical features were then obtained from the TSA signal. Their results showed that the TSA in the frequency domain is more sensitive to fault detection; however, the spectral analysis may be incapable of detecting gear failures at an early stage [7]. Moreover, the TSA in frequency domain can be a successful technique if the frequency deterministic component is constant, but in reality a vibration signal contains small frequency variations [9, 10].

Do and Chong in [11] reported that the one-dimensional vibration signal could be converted to two-dimensional grayscale image. They extracted local features from the grayscale image and utilized scale invariant feature transform (SIFT). SIFT produced a 128-dimensional key point utilized for the classification of motor faults. The proposed method was efficient at diagnosing motor faults in the presence of background noise. However, there are some serious disadvantages of using SIFT. Firstly, there is an uncertainty in the number of key points for different images. Secondly, using SIFT has a high computational cost in processing 128-dimensional feature descriptors.

Shahriar et al. in [12] extracted an LBP feature from the images obtained from the vibration signal in order to create a fault diagnosis system for induction motors. These feature descriptors are then utilized by the classifier to diagnose faults on the motor. The method was effective in discriminating a normal and single fault in a time but was incapable of discriminating texture patterns for different fault categories. Moreover, the method required more complex computation such as the conversion of vibration signal into image followed by applying LBP.

In this paper, we use one-dimensional LBP inspired by the works in [13, 14], who were the first to adopt 1D LBP extraction from a one-dimensional speech signal. The advantage of 1D LBP is the possibility of choosing fewer than eight bits and consequently a smaller number of features. Additionally, there is no need to normalize the vibration signal value to be suitable to represent a proper image format. Our experimental results show comparable performance accuracy between our 1D LBP-based model that considers six neighbours and a 2D LBP scheme that exploits eight neighbours.

In order to investigate the effect of different conditions (speed and load), we adopt a special technique of cross-validation called Leave One Speed Out (LOSO) and Leave One Load Out (LOLO). This kind of cross-validation provides an experimental environment such that all the samples belonging to one condition will be used to test the model, while the model trained by samples belongs to different conditions.

Section 2 explains the processing of 1D LBP, Section 3 provides illustrations of data resulting from the experiments discussed in this paper, Section 4 explains the experiential

work, Section 5 discusses the results obtained, and Section 6 reaches a conclusion.

2. 1D Local Binary Pattern

The local binary pattern is a nonparametric operator. The LBP code can explain the data using the differences between a sample and its neighbours [15, 16]. LBPs have been widely used, particularly in face recognition systems [16–18]. At a fixed pixel position, the LBP operator is described as an ordered set of binary comparisons of pixel intensities between the centre pixel and its neighbouring pixels. However, LBPs used for images utilize the pixel neighbour in two dimensions, which is called 2D LBP.

Although it is not widely used, 1D LBP can provide similar characteristics to the 2D LBP. For example, the researchers in [13] showed a distinctive marker of certain features of the speech signal, where the 1D LBP features were able to distinguish the unvoiced and the voiced components of speech signals. Additionally, the authors of [14] adopted 1D LBP to segment and separate Voice Active Detection (VAD) of the speech signal.

The 1D LBP operator labels every single value of the vibration signal by considering its neighbourhoods and using the value of the centre position as a threshold for the neighbourhoods. If the neighbour value is less than the centre value, the value of the neighbour will turn to 0; otherwise it turns to 1. A local binary pattern code for a neighbourhood is then produced. The decimal value of the LBP binary code presents the local structural knowledge around the fixed value [15].

The histogram of the 1D LBP signal displays how often these various patterns appear in a given signal. The distribution of the patterns denotes the whole structure of the signal. The 1D LBP operation of a sample value can be defined as

$$\text{LBP}_P(x[i]) = \sum_{r=0}^{P/2-1} \left\{ f \left[x \left[i + r - \frac{P}{2} \right] - x[i] \right] 2^r + s \left[x[i + r + 1] - x[i] 2^{r+P/2} \right] \right\}, \quad (1)$$

where the Sign function is

$$f(x) = \begin{cases} 0, & x < 0 \\ 1, & x \geq 0, \end{cases} \quad (2)$$

where $x[i]$ is the signal and P is the number of considered neighbours. The Sign function $f[x]$ transforms the differences to a P -bit binary code.

In this paper only six neighbours are considered (three to the left of the centre and three to the right). Equation (1) illustrates how the 1D LBP is evaluated. Hence, the value range of the new signal is between 0 and 63. The obtained signal is discriminated into two parts, uniform and nonuniform number. The uniform number comprises the numbers with fewer than or equal to two transition bits from 1 to 0 or 0 to 1 in their circular bit patterns. The nonuniform

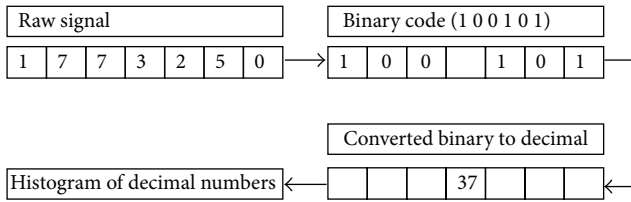


FIGURE 1: The whole processing of 1D LBP.

numbers have more than two transition bits. For instance, the patterns 11111 (0 transitions) and 100011 (2 transitions) are uniform, while the patterns 10101 (4 transitions) and 010101 (6 transitions) are nonuniform. There are 21 uniform numbers in the range 0–63 and the rest are nonuniform numbers. The histogram is computed such that an independent bin represents each uniform number, while all the nonuniform numbers are represented in one bin. Therefore, the set of features consists of 22 bins—21 bins for each uniform number and one bin for all nonuniform numbers. These bins are utilized as features to detect fault. The number of bins in the histogram depends on how many neighbours are considered.

Figure 1 demonstrates a 1D LBP operator for $P = 6$ with the centre sample as given. After processing 1D LBP, the 6-neighbour samples in the example above produce the 100101 codes. The code is then converted to a decimal number that is equal to 37 and substituted in the same index as the centre sample.

3. Vibration Data

Fault detection is an important problem in machinery diagnostics. There are many techniques that have been developed to detect fault in the rotation machinery throughout vibration signal analysis. Vibration analysis is a way of interpreting where the fault is occurring in a rotating machine (e.g., motor and gearbox). In this paper, the authors applied their investigation to vibration data designed by the Prognostics and Health Management Society, known as the Prognostic Health Monitoring (PHM) Data Challenge. The challenge is how to detect and isolate faults in an equipment industrial gearbox using vibration data that have been collected from two accelerometers. There are a total of 560 recorded samples for two typical gearboxes. One of the gearboxes contains spur gear and the other contains helical gear. The data were recorded at different shaft speeds 30, 35, 40, 45, and 50 Hz, each under high and low load (see Table 1). The data consist of three gear modes, which are No Fault (NF), Chipped Tooth (CT), and Broken Tooth (BT) [19]. In this paper, fault detection in helical gear is considered; hence the data comprise 120 recorded samples from the gearbox.

4. Experiential Work

The vibration data are used to detect fault in the gear. The data adopted in this paper consisted of three gear situations: NF, CT, and BT. One of the challenges of detecting fault in the gear is how to extract relevant features from the vibration signal.

TABLE 1: The adopted helical gear data distribution on speeds and loads.

Helical gear data	30 Hz	35 Hz	40 Hz	45 Hz	50 Hz	Sum
Low load	12	12	12	12	12	60
High load	12	12	12	12	12	60
Sum	24	24	24	24	24	120

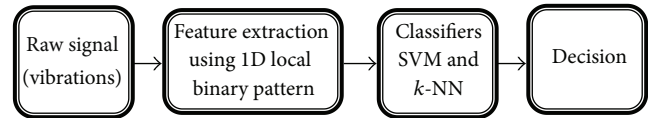


FIGURE 2: The procedure of the adopted algorithm for fault detection.

The 1D LBP is used as a technique to extract the features from the vibration signal. The procedure of 1D LBP is explained in Section 2. The features are then utilized as input to two classifiers (SVM and k -NN). In the case of the SVM scheme, a pairwise approach is adopted for our multiclass problem. The kernel function of the SVM is linear and the optimization method is sequential minimal optimization.

The second adopted classifier is the NN, which is a geometric classifier that considers only one neighbour. Three types of cross-validation are exploited, Leave One Out (LOO), Leave One Speed Out (LOSO), and Leave One Load Out (LOLO). In order to investigate the influence of different conditions it is necessary to train the classification model with samples belonging to one condition and evaluated with the samples of another condition. This investigation has been performed by adopting LOLO and LOSO cross-validation. Unlike LOLO and LOSO, LOO is considered for the experiments that do not consider the cross-condition (speed and load) in the training and testing data. Figure 2 illustrates the procedure of the adopted algorithm for fault detection.

We partition the experimental result into four different models. The first model can detect fault in the gear when the speed signal and load are fixed. We call this model Fixed Speed Fixed Load (FSFL). This model consists of 10 different cases because there are five speeds with two different loads. For example, one of the cases is when the speed of the vibration signal is 30 Hz with high load. The LOO cross-validation is used in each case.

The second model detects fault in the vibration signal when the speed is fixed and both loads are combined. We call this model Fixed Speed Various Load (FSVL). Five cases are considered in this model. An example is when the speed signal is 45 with both high and low loads. Two cross-validations are used in the second model, LOO and LOLO.

The third model is built for fault detection when the load is fixed and all the speeds are combined, for example, when the speed signal includes 30, 35, 40, 45, and 50 Hz with one load. We call this model Various Speed Fixed Load (VSFL). Here, two cases are considered and both LOO and LOSO are utilized as cross-validation.

TABLE 2: The performance of SVM in FSFL model when the 1D LBP scheme is used for feature extraction.

Speed	30	35	40	45	50
High	91.67	91.67	100	75	100
Low	66.67	75	100	100	100

TABLE 3: The performance of k -NN in FSFL model when the 1D LBP scheme is used for feature extraction.

Speed	30	35	40	45	50
High	100	100	100	100	100
Low	100	75	100	100	100

TABLE 4: The performance of SVM in FSFL model when the 2D LBP scheme is used for feature extraction.

SVM	30	35	40	45	50
High	100	100	100	100	100
Low	100	100	91.67	100	100

TABLE 5: The performance of k -NN in FSFL model when the 2D LBP scheme is used for feature extraction.

k -NN	30	35	40	45	50
High	83.33	100	100	100	91.67
Low	100	100	100	100	100

Finally, the fourth model is designed to detect fault when all the vibration data are combined, which means that all speeds and both loads are combined together. We call this model Various Speed Various Load (VSVL). In this model, three cross-validation methods are used, LOO, LOSO, and LOLO.

5. Result and Discussion

The fault detection is processed in all models mentioned in Section 4. The models are Fixed Speed Fixed Load (FSFL), Fixed Speed Various Load (FSVL), Various Speed Fixed Load (VSFL), and Various Speed Various Load (VSVL).

5.1. Model FSFL. It can be seen from Tables 2 and 3, which demonstrate the result of the FSFL model, that neither of the classifiers SVM and k -NN is significantly different in their performance based on a p value computed using a chi-square test for the cases of high load with speeds 30, 35, and 45 ($p = 0.3$, $p = 0.3$, and $p = 0.08$), while for the cases of low load with speeds 30 and 35 the p values are $p = 0.04$ and $p = 0.08$, respectively, which means that the only significant performance of k -NN over SVM happens with the speed of 30 Hz under the low load. The reason for this statistically unclear performance is the limited number of samples involved in this model.

In order to compare the results of the 1D LBP scheme with the 2D LBP scheme proposed in [12], Tables 4 and 5 demonstrate the result of the same condition using the 2D LBP scheme. However, there is no significant difference

TABLE 6: The performance of classifiers for the FSVL model when the 1D LBP scheme is used for feature extraction.

1D LBP	30 H&L	35 H&L	40 H&L	45 H&L	50 H&L
SVM	66.67	79.17	83.33	91.67	100
k -NN	91.67	87.5	100	100	100

TABLE 7: The performance of classifiers for the FSVL model when the 2D LBP scheme is used for feature extraction.

2D LBP	30 H&L	35 H&L	40 H&L	45 H&L	50 H&L
SVM	83.33	100	87.5	100	100
k -NN	91.67	100	100	100	95.83

TABLE 8: The performance of SVM in both schemes when LOLO cross-validation is used.

	LOLO at 30	LOLO at 35	LOLO at 40	LOLO at 45	LOLO at 50
1D LBP	66.67	41.67	66.67	66.67	66.67
2D LBP	45.83	33.33	41.67	41.67	50

between the two schemes in the case of using k -NN and 2D LBP scheme significantly outperforms the 1D LBP using SVM only in one case (speed 30 Hz with low load).

5.2. Model FSVL. The size of the data of this model (24 samples, eight for each class) is twice that of the data of the FSFL model because both loads are considered. From Table 6 it can be observed that the results of the FSVL model for both classifiers SVM and k -NN are not significantly different in their performance based on a p value calculated by a chi-square test for the cases of speeds 35, 45, and 50. However k -NN significantly outperform the SVM in both speeds 30 and 40 ($p = 0.03$ and $p = 0.04$, resp.).

In comparison with the 2D LBP approach, whose result is shown in Table 7, it can be observed that there is no significant improvement between 1D LBP and 2D LBP in the exception of the case of speed 35 when using SVM.

The result in Table 8 shows a comparison between 1D and 2D LBP by adopting LOLO cross-validation, which highlights the load effect on specific speed data. The results clearly show that 1D LBP outperforms 2D LBP (with the exception of 35 Hz speed) with p value of $p = 0.02$, $p = 0.15$, $p = 0.02$, $p = 0.02$, and $p = 0.04$ for 30, 35, 40, 45, and 50 Hz speeds, respectively.

5.3. Model VSFL. In this model we investigate the case of the availability of data of one load with various speeds, which means that 60 samples will participate in each experiment. In the case of SVM, there is no difference in the performance of both 1D and 2D LBP. Additionally, the 1D LBP with SVM has no significant difference with the k -NN. However, the 2D LBP outperforms the 1D LBP using k -NN in the case of low load ($p = 0.01$). The results are shown in Tables 9 and 10.

The effect of speed on fault detection is very clear in the low performance in the case of LOSO (see Table 11). However, neither LBP scheme shows significant improvement on the other. Removing samples at the same speed as the testing

TABLE 9: The performance of classifiers for VSFL model when the 1D LBP scheme is used for feature extraction.

1D LBP	All speeds and with high load	All speeds and with low load
SVM	93.33	78.33
k -NN	95	90

TABLE 10: The performance of classifiers for VSFL model when the 2D LBP scheme is used for feature extraction.

2D LBP	All speeds and with high load	All speeds and with low load
SVM	93.33	81.67
k -NN	93.33	100

TABLE 11: The performance of SVM in both schemes when LOSO cross-validation is used.

	LOSO at high load	LOSO at low load
1D LBP	41.67	46.67
2D LBP	40	46.67

TABLE 12: The performance of classifiers for VSVL model when the 1D LBP scheme is used for feature extraction.

1D LBP	SVM	k -NN
All data	81.67	90.83

TABLE 13: The performance of classifiers for VSVL model when the 2D LBP scheme is used for feature extraction.

2D LBP	SVM	k -NN
All data	86.67	96.67

sample from the training set led to a reduction in the performance accuracy of nearly 60%.

5.4. Model VSVL. The data for the model are collected from all speeds and both loads together. The size of the data of this model is 120 samples. The performance of both classifiers is high when the cross-validation is LOO. However, the performance of the k -NN significantly outperforms the SVM classifier with $p = 0.03$, as shown in Table 12. Furthermore, the performance of SVM in both 1D and 2D LBP is not significantly different ($p = 0.06$). But the 2D LBP outperforms the 1D LBP using k -NN with p value of 0.03. (see Tables 12 and 13).

A significant degradation in the performance occurs when LOLO and LOSO cross-validation are used. For example, when the cross-validation is LOSO, the performance of SVM is degraded by 56% and when the cross-validation is LOLO, the performance of SVM is degraded by 40%. The result of Table 14 also shows how 1D LBP is significantly more effective in fault detection in cross-condition; that is, the 1D LBP features can adapt the data of the different speeds and

TABLE 14: The performance of SVM in both schemes when the cross-validation is LOLO and LOSO.

	LOLO	LOSO
1D LBP	60.83	44.17
2D LBP	37.5	30.83

it is less sensitive than 2D LBP features with speed and load conditions.

6. Conclusion

In this paper, it has been shown that 1D LBP is an effective technique to extract features for detecting fault in gear when data with the same speed and/or load are available in training and testing the model. Moreover, the 1D LBP is cheaper in terms of computation than the 2D LBP scheme. The 1D LBP scheme is shown to be less sensitive to a specific load and speed; that is, 1D LBP features reduce the effect of different conditions such as speed and load. We have adopted the LOSO and LOLO cross-validation approaches to investigate the effect of speed and load in fault detection.

Conflict of Interests

The authors declare that there is no conflict of interests regarding the publication of this paper.

Acknowledgments

The authors would like to thank Charmo University, Koya University, and Halabja Institution for their support during the preparation of this work.

References

- [1] M.-C. Pan and P. Sas, "Transient analysis on machinery condition monitoring," in *Proceedings of the 3rd International Conference on Signal Processing*, IEEE, Beijing, China, October 1996.
- [2] S. Al-Arbi, *Condition Monitoring of Gear Systems Using Vibration Analysis*, University of Huddersfield, Huddersfield, UK, 2012.
- [3] H. Al-Atat, D. Siegel, and J. Lee, "A systematic methodology for gearbox health assessment and fault classification," *International Journal of Prognostics and Health Management*, vol. 2, no. 1, p. 16, 2011.
- [4] Z. Peng, F. Chu, and Y. He, "Vibration signal analysis and feature extraction based on reassigned wavelet scalogram," *Journal of Sound and Vibration*, vol. 253, no. 5, pp. 1087–1100, 2003.
- [5] W. J. Staszewski and G. R. Tomlinson, "Application of the wavelet transform to fault detection in a spur gear," *Mechanical Systems and Signal Processing*, vol. 8, no. 3, pp. 289–307, 1994.
- [6] J. A. Momoh and L. G. Dias, "Solar dynamic power system fault diagnosis," in *Proceedings of the HBCUs Research Conference Agenda and Abstracts*, (SEE N 96-35493 12-01), p. 30, Howard University, Washington, DC, USA, July 1996.
- [7] M. Lebold, K. McClintic, R. Campbell, C. Byington, and K. Maynard, "Review of vibration analysis methods for gearbox

- diagnostics and prognostics,” in *Proceedings of the 54th Meeting of the Society for Machinery Failure Prevention Technology*, pp. 623–634, Virginia Beach, Va, USA, May 2000.
- [8] E. Bechhoefer and M. Kingsley, “A review of time synchronous average algorithms,” in *Proceedings of the Annual Conference of the Prognostics and Health Management Society (PHM '09)*, San Diego, Calif, USA, October 2009.
- [9] P. D. McFadden, “Interpolation techniques for time domain averaging of gear vibration,” *Mechanical Systems and Signal Processing*, vol. 3, no. 1, pp. 87–97, 1989.
- [10] P. D. McFadden, “A revised model for the extraction of periodic waveforms by time domain averaging,” *Mechanical Systems and Signal Processing*, vol. 1, no. 1, pp. 83–95, 1987.
- [11] V. T. Do and U.-P. Chong, “Signal model-based fault detection and diagnosis for induction motors using features of vibration signal in two-dimension domain,” *Strojnicki Vestnik/Journal of Mechanical Engineering*, vol. 57, no. 9, pp. 655–666, 2011.
- [12] M. R. Shahriar, T. Ahsan, and U. Chong, “Fault diagnosis of induction motors utilizing local binary pattern-based texture analysis,” *EURASIP Journal on Image and Video Processing*, vol. 2013, no. 1, article 29, pp. 1–11, 2013.
- [13] N. Chatlani and J. J. Soraghan, “Local binary patterns for 1-D signal processing,” in *Proceedings of the 18th European Signal Processing Conference (EUSIPCO '10)*, pp. 95–99, IEEE, Aalborg, Denmark, August 2010.
- [14] Q. Zhu, N. Chatlani, and J. J. Soraghan, “1-D Local binary patterns based VAD used INHMM-based improved speech recognition,” in *Proceedings of the 20th European Signal Processing Conference (EUSIPCO '12)*, pp. 1633–1637, IEEE, Bucharest, Romania, August 2012.
- [15] T. Ojala, M. Pietikäinen, and T. Mäenpää, “Multiresolution gray-scale and rotation invariant texture classification with local binary patterns,” *IEEE Transactions on Pattern Analysis and Machine Intelligence*, vol. 24, no. 7, pp. 971–987, 2002.
- [16] T. Ahonen, A. Hadid, and M. Pietikäinen, “Face description with local binary patterns: application to face recognition,” *IEEE Transactions on Pattern Analysis and Machine Intelligence*, vol. 28, no. 12, pp. 2037–2041, 2006.
- [17] C. K. Tran, T. F. Lee, L. Chang, and P. J. Chao, “Face description with local binary patterns and local ternary patterns: improving face recognition performance using similarity feature-based selection and classification algorithm,” in *Proceedings of the 2nd International Symposium on Computer, Consumer and Control (IS3C '14)*, pp. 520–524, IEEE, Taichung, Taiwan, June 2014.
- [18] T. Ahonen, A. Hadid, and M. Pietikäinen, “Face recognition with local binary patterns,” in *Computer Vision—ECCV 2004*, pp. 469–481, Springer, Berlin, Germany, 2004.
- [19] PHM Challenge Competition Data Set, 2009, <https://www.phmsociety.org/references/datasets>.

Research Article

Fault Diagnosis of Rotating Machinery Based on Adaptive Stochastic Resonance and AMD-EEMD

Peiming Shi,¹ Cuijiao Su,¹ and Dongying Han²

¹*Institute of Electrical Engineering, Yanshan University, Qinhuangdao, Hebei 066004, China*

²*Institute of Vehicles and Energy, Yanshan University, Qinhuangdao, Hebei 066004, China*

Correspondence should be addressed to Peiming Shi; peiming.shi@163.com

Received 4 November 2015; Revised 15 December 2015; Accepted 5 January 2016

Academic Editor: Juan P. Amezcua-Sanchez

Copyright © 2016 Peiming Shi et al. This is an open access article distributed under the Creative Commons Attribution License, which permits unrestricted use, distribution, and reproduction in any medium, provided the original work is properly cited.

An adaptive stochastic resonance and analytical mode decomposition-ensemble empirical mode decomposition (AMD-EEMD) method is proposed for fault diagnosis of rotating machinery in this paper. Firstly, the stochastic resonance system is optimized by particle swarm optimization (PSO), and the best structure parameters are obtained. Then, the signal with noise is put into the stochastic resonance system and denoising and enhancing the signal. Secondly, the signal output from the stochastic resonance system is extracted by analytical mode decomposition (AMD) method. Finally, the signal is decomposed by ensemble empirical mode decomposition (EEMD) method. The simulation results show that the optimal stochastic resonance system can effectively improve the signal-to-noise ratio, and the number of effective components of EEMD decomposition is significantly reduced after using AMD, thus improving the decomposition results of EEMD and enhancing the amplitude of components frequency. Through the extraction of the rolling bearing fault signal feature proved that the method has a good effect.

1. Introduction

Rotating machinery plays a significant role in a wide range of industrial applications, such as aerospace, transportation vehicles, and power generators. The rotating machine faults can cause violent vibration on the machine and even endanger normal machine operation. Therefore, accurate health monitoring and diagnosis system is needed to identify incipient fault that may occur in a rotating machine [1–4]. However, the defect-induced fault signal of the rotating machine is often corrupted by the noise coming from other coupled machine components and working environment, which makes some incipient faults not easy to be recognized. The challenge of fault recognition requires enhancing the weak fault information from heavy background noise.

Stochastic resonance (SR) theory was proposed by Benzi et al. in 1981 to explain the periodicity of the Earth's ice ages [5]. It can make part of the noise energy transfer to the low frequency signal through a nonlinear system, so weak signal drowned in the noise has been greatly strengthened at the same time to reduce the noise, and greatly improve

the output signal-to-noise ratio (SNR) [6–11]. Therefore the stochastic resonance method has strong immunity to noise and can effectively extract weak signal under strong noise background. Stochastic resonance is actually the optimal matching relationship between signal, noise, and nonlinear system. However, the amplitude of the signal and the noise intensity may change over time in the actual engineering, so it is necessary to automatically adjust the nonlinear system parameters according to the different signal, in order to achieve stochastic resonance and improve the output SNR.

Ensemble empirical mode decomposition (EEMD) is a noise-assisted data analysis method which was proposed based on empirical mode decomposition (EMD) [12] by Huang et al. This method uses the Gauss white noise that has the statistical characteristics of frequency distribution; the signal after adding the Gauss white noise is continuous in different scales. It can effectively solve the mode mixing problem of EMD and successfully applied in some engineering practice [13–17].

Analytical modal decomposition (AMD) method was proposed by Chen and Wang [18]. This method can separate

different frequency components from the signal, but the premise is to know the frequency components in the signal and then determine the bisecting frequency. Therefore, if one wants to extract the known part of the signal, the signal can be processed by AMD method.

A method of rotating machinery fault diagnosis based on adaptive stochastic resonance and AMD-EEMD is proposed in this paper. Firstly, the bistable stochastic resonance system is optimized by particle swarm optimization (PSO) and putting the signal which containing noise into the stochastic resonance system and then denoising and enhancing the signal. Secondly, the signal output from the stochastic resonance system is extracted by AMD. Finally, the signal is decomposed by EEMD method. The simulation results show that the optimal stochastic resonance system can effectively improve the SNR, and the number of effective components of EEMD decomposition is significantly reduced after using AMD, thus improving the decomposition results of EEMD and enhancing the amplitude of components frequency.

The rest of the paper is organized as follows. The classical bistable SR theory, the PSO algorithm, and the theories of EEMD and AMD are given and the SR-AMD-EEMD method is proposed in Section 2. Section 3 describes the advantage of the proposed method by simulation experiment. The adaptive stochastic resonance and AMD-EEMD method is applied to the fault diagnosis of a rolling bearing in Section 4, and the application result proves the effectiveness of the proposed method. Finally, Section 5 provides the conclusion.

2. Adaptive Stochastic Resonance and AMD-EEMD Algorithm

2.1. Bistable Stochastic Resonance Model. Stochastic resonance is synergistic effect of the input signal and the noise signal on the nonlinear system with certain parameters, and then part of the energy of noise signal transfers to the input signal, which can improve the SNR to achieve the purpose of weak signal recognition.

The Langevin equation is to describe the typical model of nonlinear bistable system [19–21]. The Langevin equation of bistable system is considered as follows:

$$\begin{aligned} \frac{dx}{dt} &= -U'(x) + S(t) + N(t) \\ &= ax - bx^3 + S(t) + N(t), \end{aligned} \quad (1)$$

where a and b are the structural parameters of the bistable system, $S(t)$ is the input signal, and $N(t)$ is the noise signal. Let $\langle N(t) \rangle = 0$, $\langle N(t)N(t-\tau) \rangle = 2D\delta(t)$, and $N(t) = \sqrt{2D}\xi(t)$, where $\xi(t)$ is white noise with zero mean and unit variance and D is the noise intensity. The potential function for the above bistable system can be denoted as

$$U(x) = -\frac{1}{2}ax^2 + \frac{1}{4}bx^4. \quad (2)$$

The above equation has two minimum values in $x = \pm\sqrt{a/b}$ and has a maximum value in $x = 0$, corresponding to the system of two lowest points and a barrier point,

corresponding to the two potential hydrazine points and a barrier point of the system. And its barrier height is $\Delta U = a^2/(4b)$.

2.2. Particle Swarm Optimization Algorithm. Particle swarm optimization (PSO) algorithm is an evolutionary computing technology proposed by Eberhart and Kennedy. Assuming i particle position and velocity in d dimensional search space are $X^i = (x_{i1}, x_{i2}, \dots, x_{id})$ and $V^i = (v_{i1}, v_{i2}, \dots, v_{id})$, respectively, in each iteration, particles update their own by tracking two optimal solutions, one is the optimal solution $P^i = (p_{i1}, p_{i2}, \dots, p_{id})$ found by particle itself, and the other is the optimal solution of current population P_g . When finding the two best values, the particle updates its velocity and position according to the following formula:

$$\begin{aligned} v_{i,j}(t+1) &= \omega v_{i,j}(t) + c_1 r_1 [P_{i,j} - x_{i,j}(t)] \\ &\quad + c_2 r_2 [P_{g,j} - x_{i,j}(t)], \\ x_{i,j}(t+1) &= x_{i,j}(t) + v_{i,j}(t+1), \quad j = 1, 2, \dots, d, \end{aligned} \quad (3)$$

where ω is inertia weight, c_1 and c_2 are the learning factors, and r_1 and r_2 are random numbers between 0 and 1 uniform distribution [22, 23].

Because the larger weights are conducive to jumping out of the local minimum value, they are suitable for global search. And smaller weights are conducive for accurate local search in the current search area, which is helpful in the convergence of the algorithm.

Therefore, in order to prevent the phenomenon of premature convergence and oscillation occurred in the vicinity of the global optimal solution of PSO algorithm, you can use the linear decreasing weight as follows:

$$\omega = \omega_{\max} - \frac{t * (\omega_{\max} - \omega_{\min})}{t_{\max}}, \quad (4)$$

where ω_{\max} and ω_{\min} are maximum value and minimum value of ω , t is the current number of iterations, and t_{\max} is the maximum number of iterations. Usually, $\omega_{\max} = 0.9$ and $\omega_{\min} = 0.4$.

2.3. EEMD Based on AMD. A new signal decomposition method called AMD was proposed by Chen and Wang in 2012 [18]. This method can decompose signals with closely spaced frequency components, which means being able to extract the signal.

If a time series $x(t)$ is divided into two signals by bisecting frequency ω_b ,

$$x(t) = s_1(t) + \bar{s}_1(t). \quad (5)$$

We can get that

$$s_1(t) = \sin(\omega_b t) H[x(t) \cos(\omega_b t)] \quad (6)$$

$$- \cos(\omega_b t) H[x(t) \sin(\omega_b t)],$$

$$\bar{s}_1(t) = x(t) - s_1(t), \quad (7)$$

where $H[\cdot]$ is Hilbert transformation of the function in brackets.

So the original signal will get the two signals by using the AMD method.

The essence of EEMD method is repeated EMD decomposition added Gauss white noise. Finally, the original signal is decomposed into several intrinsic mode functions (IMFs) and a residue.

The specific steps of AMD-EEMD method are as follows:

- (1) The signal is extracted by AMD method firstly. Assuming there is a time series $x(t) = x_1(t) + x_2(t) + x_3(t)$, the frequencies are f_1, f_2, f_3 , respectively, and $f_1 < f_2 < f_3$. If one wants to extract f_1 frequency component of the signal, take between f_1 and f_2 as the bisecting frequency. If one wants to extract f_2 frequency component of the signal, decompose the first part of the signal which is taking frequency value between f_2 and f_3 as the bisecting frequency, and then subtract the first half part of the signal which is taking frequency value between f_1 and f_2 as the bisecting frequency.
- (2) Assuming that the signal after the extraction is $x_2(t)$, one uses EEMD method to decompose it.
- (3) Initialize the times of EMD decomposition M and white noise amplitude coefficient K , and let $m = 1$.
- (4) Perform the m time of EMD decomposition. Consider the following:
 - (a) Add a random sequence of Gauss white noise $n_i(t)$ on the input signal $x_2(t)$, and then get the signal with noise $x_2(t) = x_2(t) + k * n_i(t)$.
 - (b) Use EMD to decompose $x_2(t)$ and get I IMF $_{jm}$ ($j = 1, 2, \dots, I$), jm being the decomposition of the first j IMF in the m time of EMD test.
 - (c) If $m < M$, return to step (4), and let $m = m + 1$.
- (5) Calculate the mean value of each IMF in M times' test.
- (6) Take the output of IMF $_j$ as the first j IMF decomposed by EEMD.

Usually, M is 100, K takes 0.01~0.5 times the standard deviation of the original signal which is more appropriate.

2.4. Adaptive Stochastic Resonance and AMD-EEMD Algorithm. Stochastic resonance output SNR formula is defined as follows:

$$\text{SNR} = 10 \lg \frac{S}{N} = 10 \lg \frac{2 |X(k_0)|^2}{\sum_{k=0}^{L-1} |X(k)|^2 - 2 |X(k_0)|^2}, \quad (8)$$

where S is the signal power, N is the noise power, L is data length, and $X(k_0)$ is the unilateral amplitude of output signal frequency component.

When the system input is a small parameter signal, the output SNR approximately is as follows:

$$\text{SNR} = \frac{\sqrt{2}a^2 A^2 \exp(-a^2/4bD)}{4bD^2}. \quad (9)$$

Equation (8) shows that the output SNR is relevant to signal amplitude A , noise intensity D , and system parameters a and b . A signal amplitude as well as the noise intensity is known, so if one wants to get the maximum output SNR one needs to adjust the parameters of a and b .

A method of rotating machinery fault diagnosis based on adaptive stochastic resonance and AMD-EEMD is proposed in this paper. Firstly, the bistable stochastic resonance system is optimized by particle swarm optimization (PSO). Secondly, the signal output from the stochastic resonance system is intercepted and decomposed by AMD-EEMD method. The main steps are as follows:

- (1) Population initialization: Set up the PSO maximum generation t_{\max} , population quantity M , learning factors c_1 and c_2 , upper limit of inertia weight ω_{\max} , lower limit of inertia weight ω_{\min} , upper limit of flight speed V_{\max} , lower limit of flight speed V_{\min} , and the search range of the system parameters a and b . Initialize a group of particles' position and velocity randomly.
- (2) The fitness evaluation of each particle: Calculate every particle's fitness value $\text{fitness}(x)$ according to the SNR. Store the current position and fitness value of each particle in $pbest$ of each particle. Then, store the position and fitness value of the best individual of all $pbest$ in the $gbest$.
- (3) The velocity and position of particles being updated: The position and velocity of all particles are updated according to (3), and the weight value is updated according to (4). Recalculate every particle's fitness value. If local optimal fitness value $pbest$ or global optimal fitness value $gbest$ of the individual particle is better than the $pbest$ and $gbest$ of the generation particles, then update the corresponding individual particle's local optimal fitness value or global optimal fitness value.
- (4) To determine whether the end condition is met: When the evolution times reached the maximum number t_{\max} stop searching. Then output the optimal system parameters a and b and put the original signal into stochastic resonance system with the optimal parameters.
- (5) Using the AMD-EEMD method to intercept and decompose the signal which is output from the stochastic resonance system.

The specific process is shown as Figure 1.

3. Simulation Experiment

Assuming the input signal is

$$x(t) = A \sin(2\pi f_0 t) + N(t), \quad (10)$$

where $A = 0.3$, $f_0 = 0.01$ Hz, the strength D of Gauss white noise $N(t)$ is 0.31, the sampling frequency f_s is 5 Hz, the sampling points are 5000, the signal is decomposed by

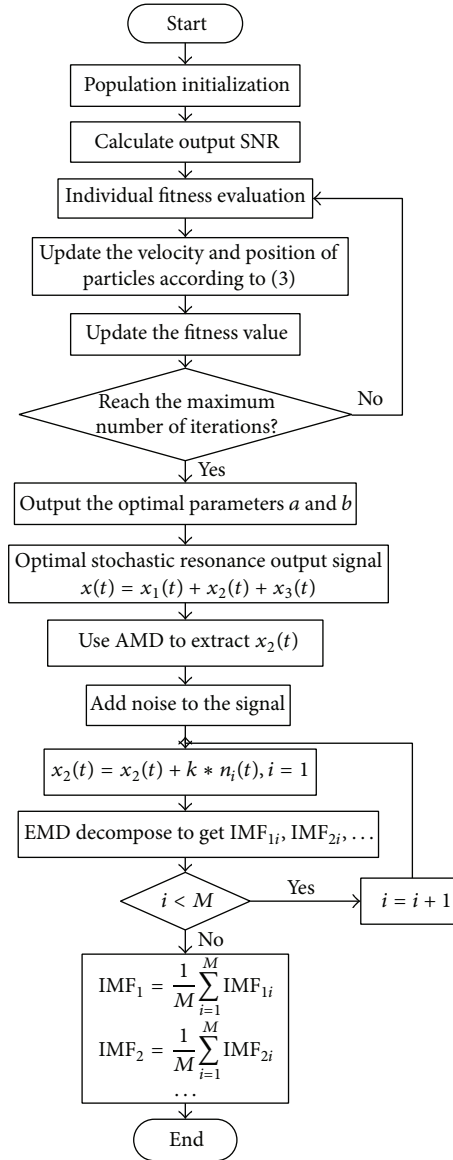


FIGURE 1: The flow chart of adaptive stochastic resonance and AMD-EEMD.

EEMD method directly and the first 8 components are taken, and the result is shown as Figure 2.

First of all, use particle swarm optimization algorithm to optimize parameters a and b of stochastic resonance system. Set the population number as 40, the search range of a and b as $[0, 2]$, the maximum value of flight speed as 0.01, and the maximum number of evolutions as 100. Because the signal amplitude as well as intensity of noise is known, (6) is regarded as the fitness function. From Figure 3 one can get that the maximum output SNR is 0.151 and the optimization result is $a = 0.7381$ and $b = 0.4393$. Use stochastic resonance system with the optimal parameters to process the original signal, and then get time-domain waveform and frequency spectrum which are shown as Figures 4(c) and 4(d). Figure 4

shows that the noise has been weakened and the 0.01 Hz frequency component has been greatly improved.

The 0~0.02 Hz band part of the original signal and the signal output from stochastic resonance system are extracted by the AMD method, respectively. Then they are decomposed by EEMD method and the frequency spectrum of each component is calculated; the decomposition results are shown as Figures 5 and 6. Comparing with Figure 2, the component is significantly reduced in Figure 5. Figure 5 shows that component C1 contains the signal whose frequency is 0.01 Hz and its frequency amplitude is 0.2716. Figure 6 shows that also component C1 contains the signal whose frequency is 0.01 Hz, but its frequency amplitude is 1.461. This shows that the original signal is processed by stochastic resonance and then

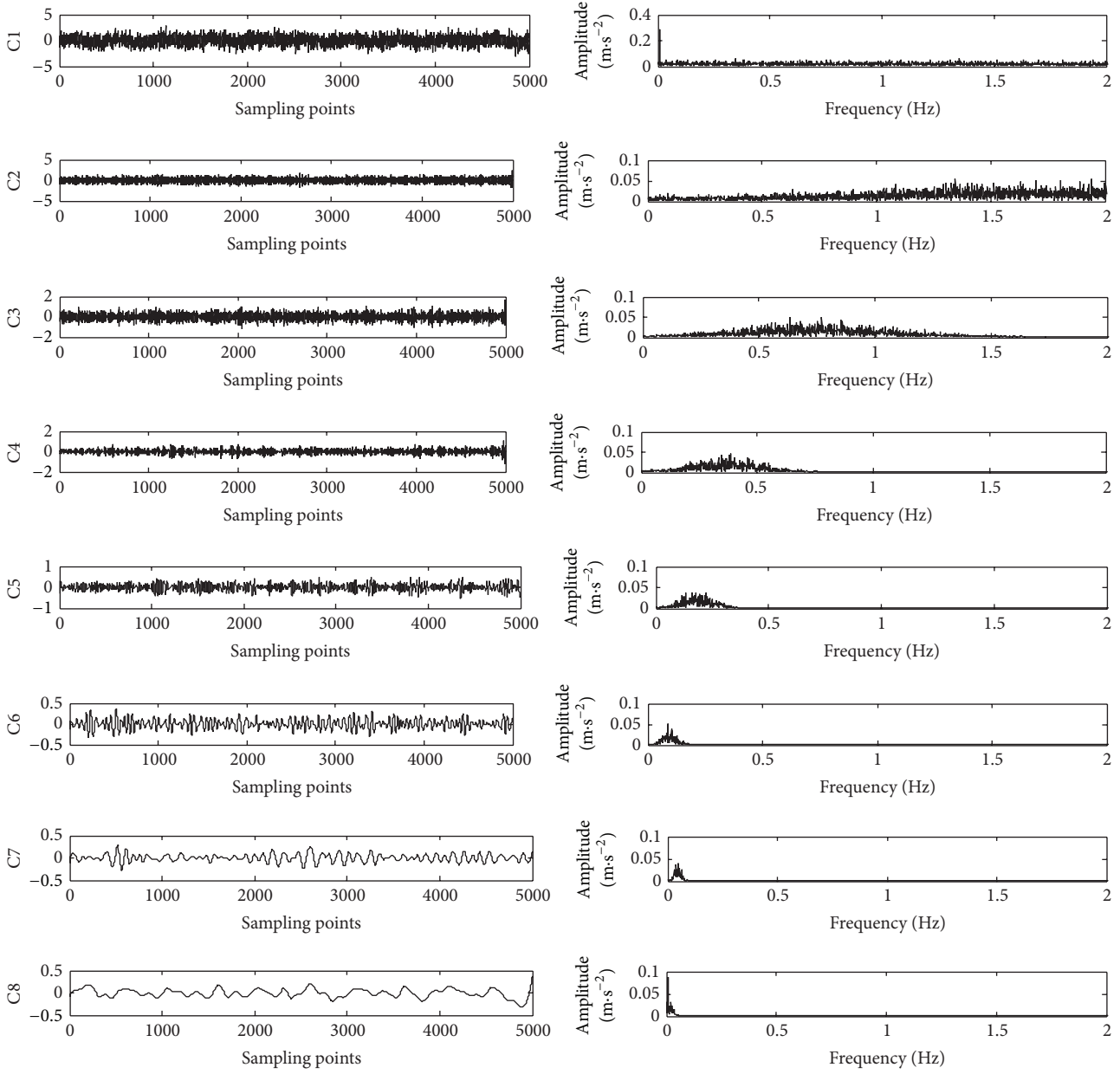


FIGURE 2: The EEMD components of original signal and its spectrum.

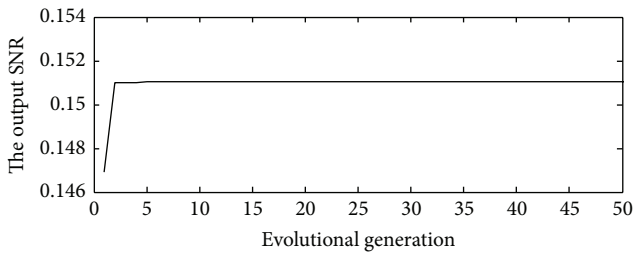


FIGURE 3: The optimal convergence curve of PSO algorithm.

EEMD decomposition, which can make the signal whose frequency is 0.01 Hz outstanding.

4. Application Example

For the Case Western Reserve University rolling bearing fault simulation test bench, the type of drive end bearing is SKF6205, the motor speed is 1797 r/min (29.95 Hz), and the sampling frequency is 12 kHz. The main parameters of the rolling bearing and the rolling bearing fault feature frequency of the different parts are shown as Tables 1 and 2, respectively.

Take the inner race fault of rolling bearing as an example; select a set of data for analysis and processing. By calculating the feature frequency is 162.18 Hz. The time-domain waveform of the bearing signal and its spectrum are shown as Figure 7. The original signal is decomposed by EEMD method and the first 8 components are taken; the result is shown as Figure 8.

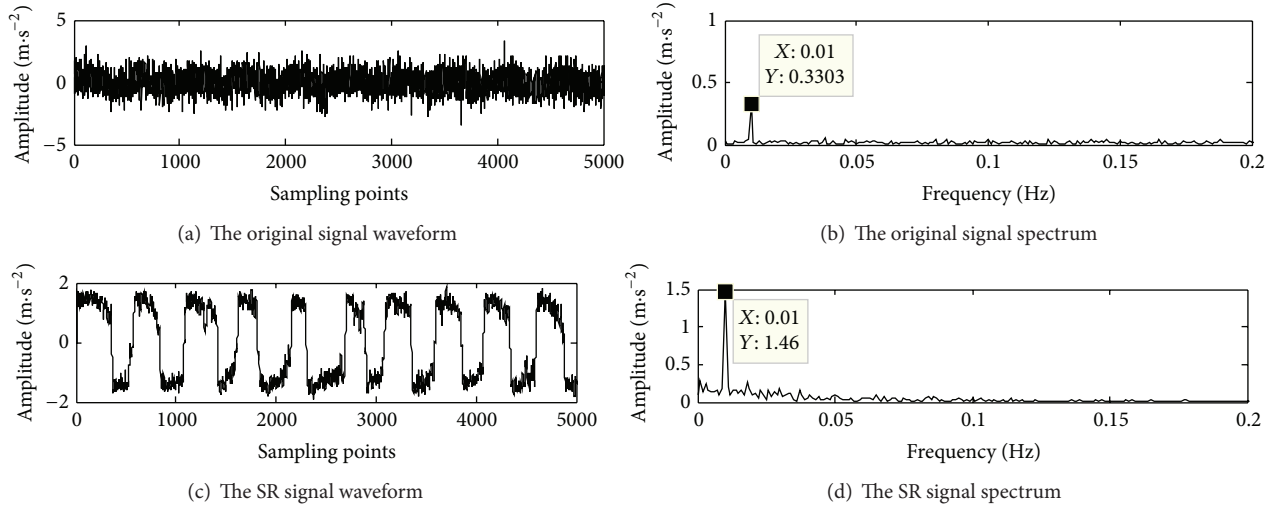


FIGURE 4: The time-domain waveform and frequency spectrum of original signal and stochastic resonance signal.

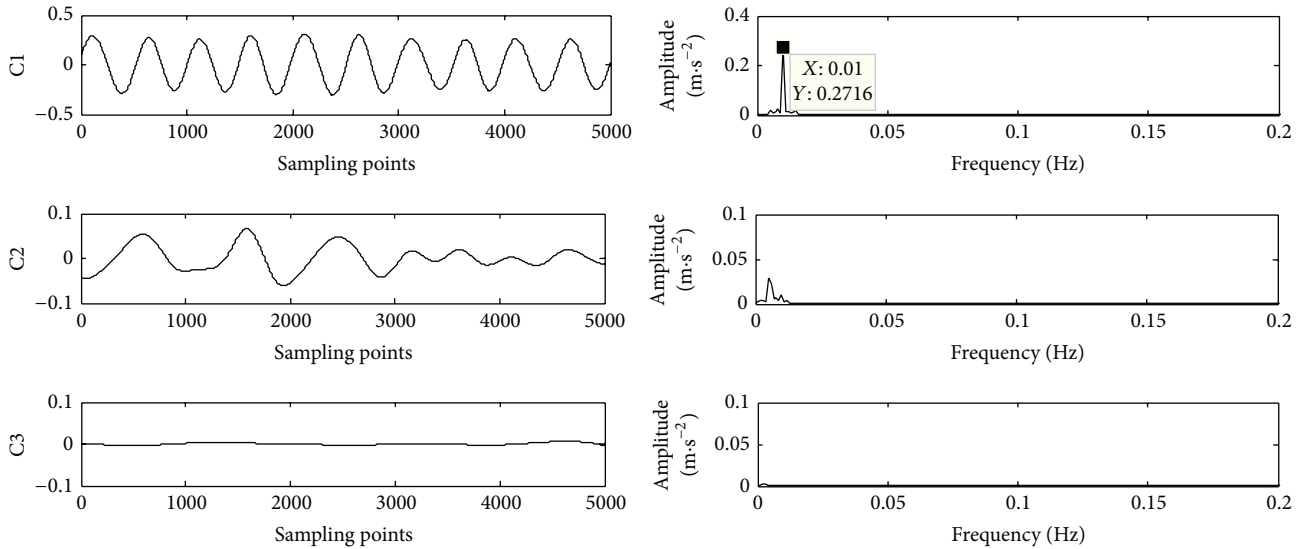


FIGURE 5: The AMD-EEMD components of original signal and its spectrum.

Because the bearing fault signal does not meet the requirements of the small parameter, the signal needs sampling second time. Set up the second sampling frequency $f_{sr} = f_s/R = 4$ Hz; that is to say the transformation scale R is 3000. Use particle swarm algorithm to optimize the parameters of stochastic resonance system. The noise strength of the bearing fault signal is unknown, so (5) is regarded as the fitness function. After optimizing by PSO algorithm the optimal parameters are $a = 0.15$ and $b = 2.14$. Then put the bearing signal into stochastic resonance system with the optimal parameters.

The 150~180 Hz band part of the original fault signal and the signal output from stochastic resonance system are extracted by the AMD method, respectively. Then they are decomposed by EEMD method and the frequency spectrum of each component is calculated. The decomposition results

are shown as Figures 9 and 10. Comparing with Figure 8, the component is significantly reduced in Figure 9.

Figure 9 shows that the main frequency component of C2 is 162 Hz, according to the inner race fault feature frequency, and its frequency amplitude is 0.01481. Figure 10 shows that the main frequency component of C2 is also 162 Hz, but its frequency amplitude is 0.02887, improving significantly compared with Figure 9.

The comparative analysis outlined above indicates that the adaptive stochastic resonance and AMD-EEMD method may not only increase the output SNR but also reduce the effective components of EEMD and improve the amplitude of components frequency. Therefore, the adaptive stochastic resonance and AMD-EEMD method and its application in fault diagnosis of rotating machinery have practical significance.

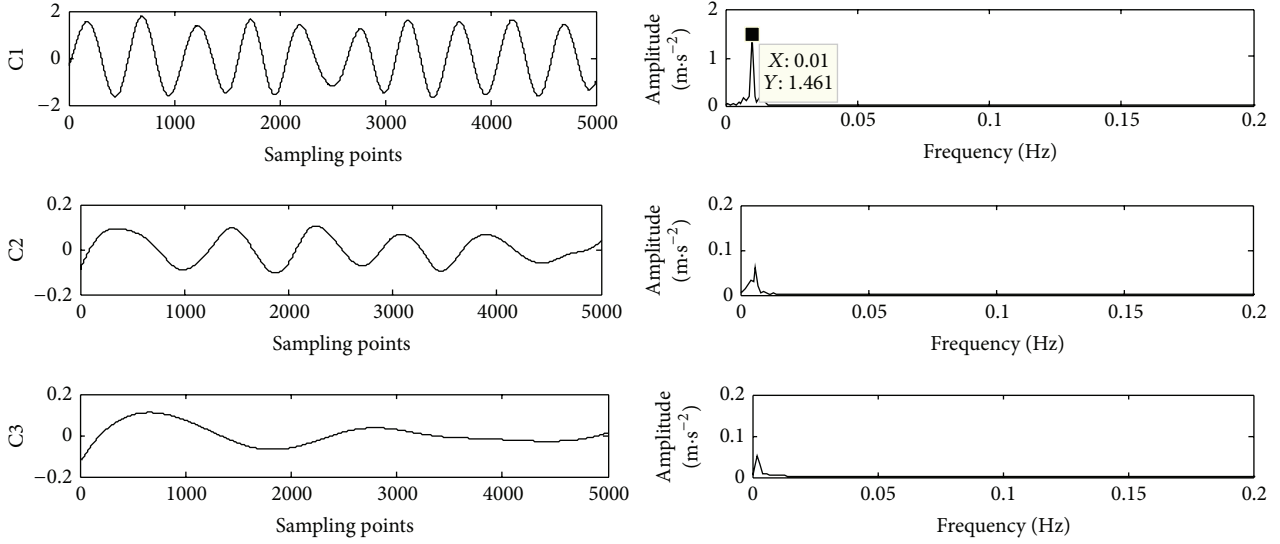


FIGURE 6: The AMD-EEMD components of stochastic resonance signal and its spectrum.

TABLE 1: The main parameters of the rolling bearing of SKF6205.

Out diameter R (mm)	Inner diameter r (mm)	Pitch diameter D (mm)	Ball diameter d (mm)	Ball number Z	Contact angle α
52.00	25.00	39.04	7.94	9	0°

TABLE 2: Rolling bearing fault feature frequency of SKF6205.

Bearing element	Inner ring	Outer ring	The retainer	Rolling body
Feature frequency	$5.4152f_r$	$3.5848f_r$	$0.39828f_r$	$4.7135f_r$

Note. $f_r = N/60$ and N is bearing speed.

For the Case Western Reserve University rolling bearing fault simulation test bench, the other type of fan end bearing is SKF6203 and the sampling frequency is 12 kHz. The main parameters of the rolling bearing and the rolling bearing fault feature frequency of the different parts are shown as Tables 3 and 4, respectively.

Forty-four groups of bearing inner fault data were analyzed by EMD, EEMD, SR-EMD, SR-EEMD, AMD-EMD, AMD-EEMD, and SR-AMD-EEMD method, respectively. Among them, forty-two groups of data can effectively increase the amplitude and reduce the number of components after SR-AMD-EEMD method; that is, the accuracy of this method is 95.45%.

Here take eight groups of bearing inner race fault of SKF6205 and SKF6203 that are analyzed under 1797 r/min, 1772 r/min, 1750 r/min, and 1730 r/min different speed, respectively. The frequency amplitude and component count are shown in Tables 5 and 6. From Tables 5 and 6, we can clearly see that the EMD and EEMD methods have similar amplitude and number of components, the SR-EMD and SR-EEMD methods increase the amplitude, but the number of the components is not changed, the AMD-EMD and AMD-EEMD methods reduce the number of components, but the amplitude is almost unchanged, and the SR-AMD-EEMD method has the largest amplitude, while the component is

the least. This shows the effectiveness of the proposed method in this paper.

Calculate the average value of the amplitude increment of eight groups which is compared with the EMD method. The percentage increase is shown in Figure 11. And the average number of components is shown in Figure 12. Figure 11 shows that the amplitude increased by about 10% after EEMD, AMD-EMD, and AMD-EEMD method compared with EMD method. And the amplitude increased by 96.74%, 116.10%, and 122.58% after SR-EMD, SR-EEMD, and SR-AMD-EEMD method, respectively. From Figure 12 we can see that the minimum average number of components is 3 processed by the SR-AMD-EEMD method. To sum up we know that the SR-AMD-EEMD method has the largest amplitude and the minimum number of components.

5. Conclusions

Consider the following:

- (1) This paper presents an adaptive stochastic resonance and AMD-EEMD method for fault diagnosis of rotating machinery. The process is as follows: firstly, the bistable stochastic resonance system is optimized by PSO, and the best structure parameters are obtained;

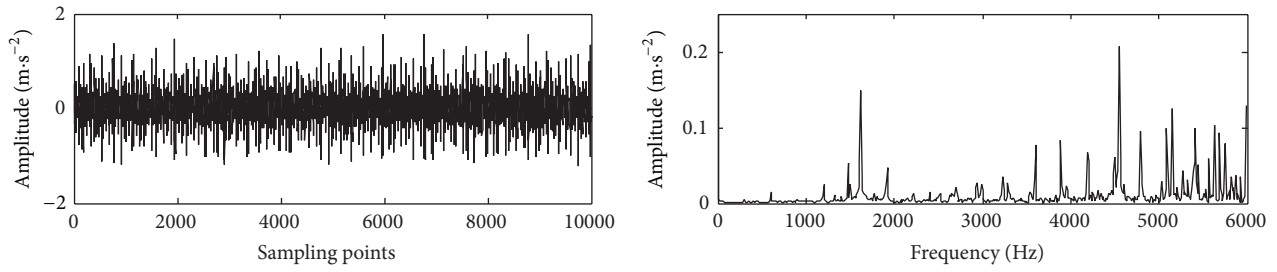


FIGURE 7: The bearing fault signal and its spectrum.

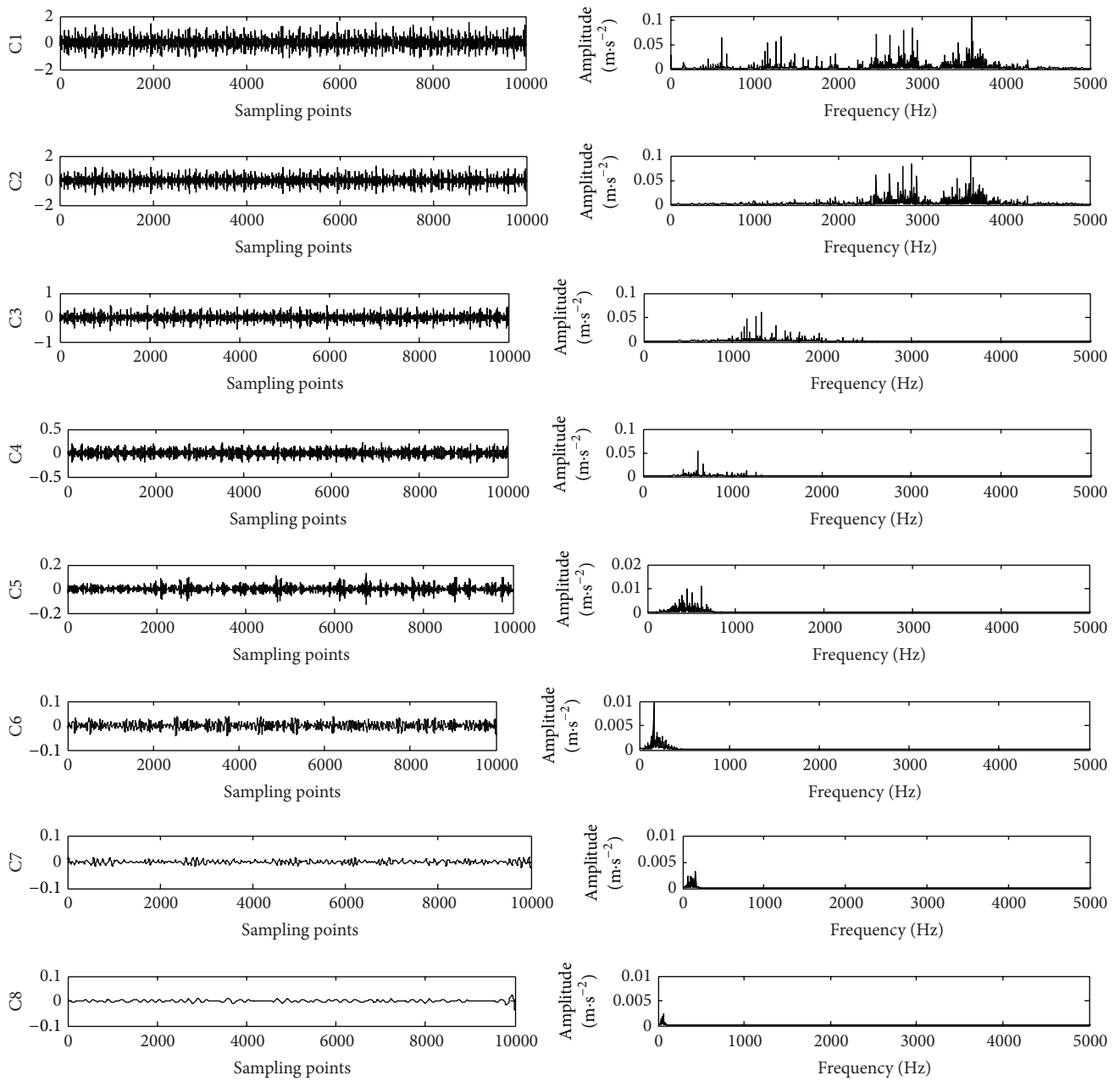


FIGURE 8: The EEMD components of original fault signal and its spectrum.

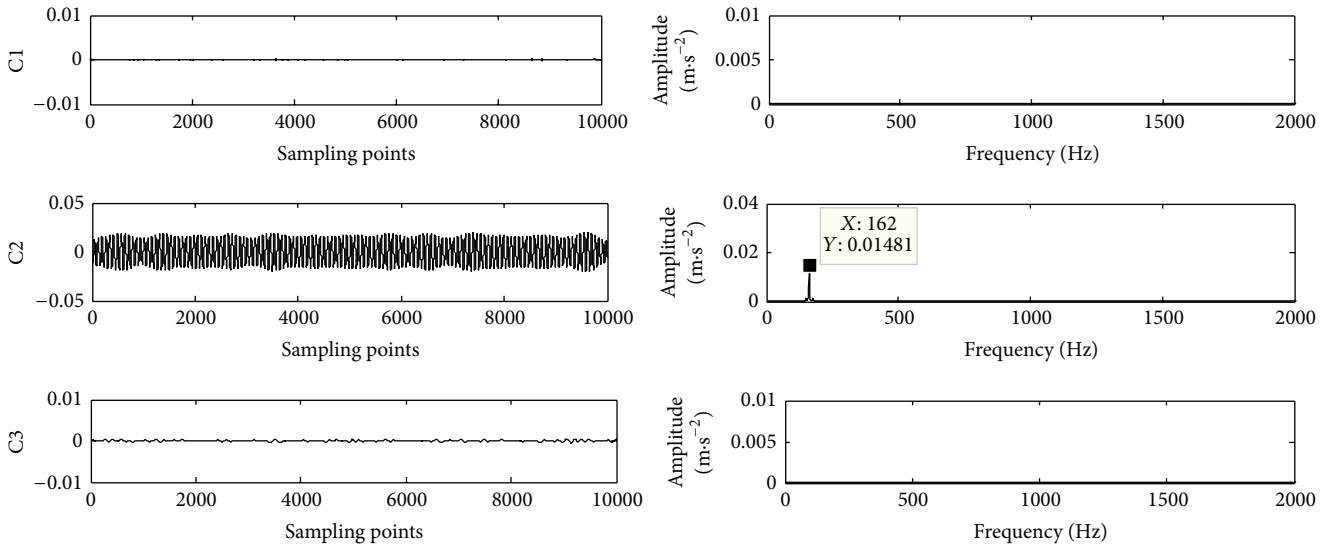


FIGURE 9: The AMD-EEMD components of original fault signal and its spectrum.

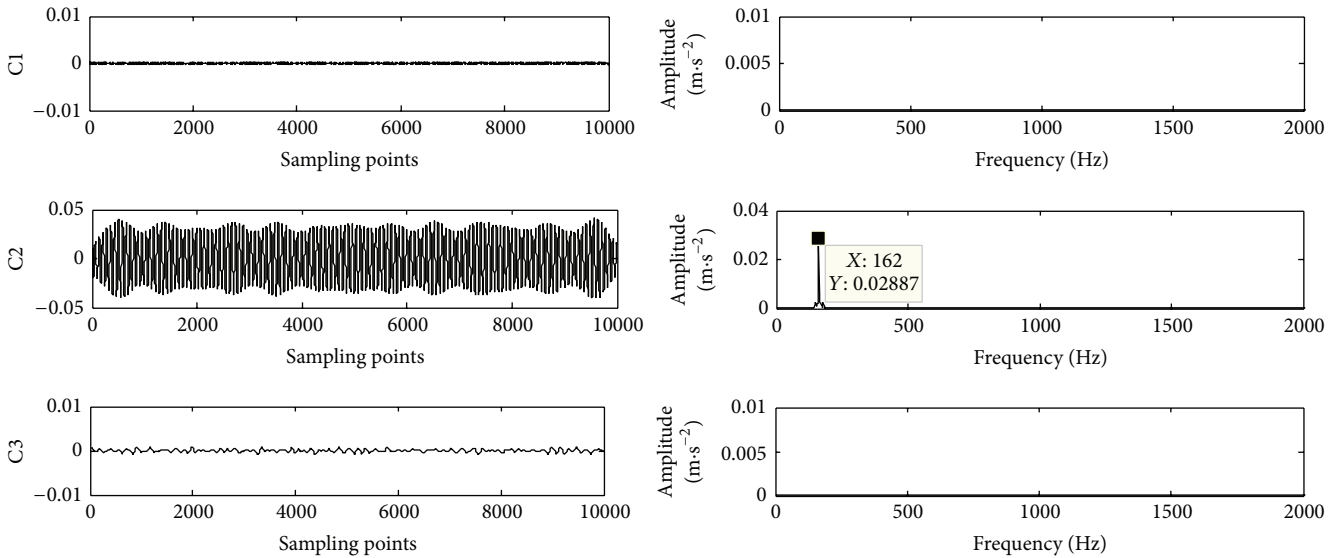


FIGURE 10: The AMD-EEMD components of stochastic resonance signal and its spectrum.

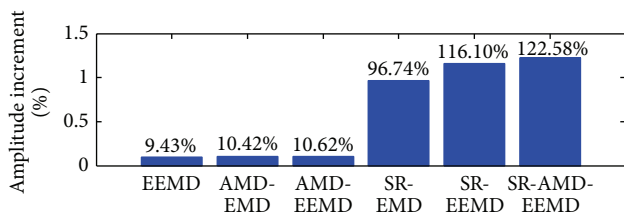


FIGURE 11: The column chart of percentage increase.

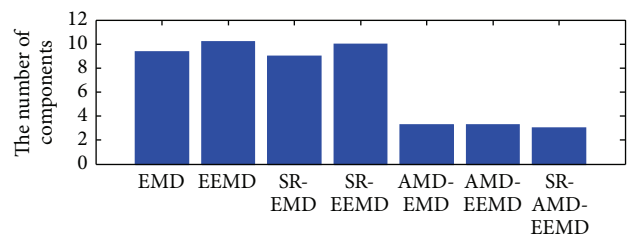


FIGURE 12: The average number of components.

then, the signal with noise is put into the stochastic resonance system in order to improve the SNR of the signal; secondly, the signal output from the stochastic resonance system is extracted by AMD method; finally, the signal is decomposed by EEMD method.

(2) By processing the simulation signal and application examples and comparing the SR-AMD-EEMD method and EMD, EEMD, SR-EEMD, SR-EEMD, AMD-EEMD, and AMD-EEMD method, respectively,

TABLE 3: The main parameters of the rolling bearing of SKF6203.

Out diameter R (mm)	Inner diameter r (mm)	Pitch diameter D (mm)	Ball diameter d (mm)	Ball number Z	Contact angle α
40.00	17.00	28.50	6.75	8	0°

TABLE 4: Rolling bearing fault feature frequency of SKF6203.

Bearing element	Inner ring	Outer ring	The retainer	Rolling body
Feature frequency	$4.9469f_r$	$3.0530f_r$	$0.3817f_r$	$3.9874f_r$

Note. $f_r = N/60$ and N is bearing speed.

TABLE 5: The amplitude and component count of fault feature frequency of SKF6205 under different rotational speed.

Bearing type	SKF6205							
Motor speed	1797 r/min		1772 r/min		1750 r/min		1730 r/min	
Frequency value	162 Hz		159.6 Hz		157.2 Hz		154.8 Hz	
	Amplitude	Component count						
SR-AMD-EEMD	0.02887	3	0.02164	2	0.02567	3	0.02608	2
AMD-EEMD	0.01481	3	0.01402	2	0.01518	3	0.00881	3
AMD-EMD	0.01536	3	0.01336	2	0.01528	4	0.00863	2
SR-EEMD	0.02880	11	0.02034	10	0.02555	10	0.02480	9
SR-EMD	0.02579	9	0.01738	9	0.02001	8	0.02729	10
EEMD	0.01324	10	0.01672	10	0.01314	10	0.00834	11
EMD	0.01163	10	0.01371	9	0.01224	9	0.00763	10

TABLE 6: The amplitude and component count of fault feature frequency of SKF6203 under different rotational speed.

Bearing type	SKF6203							
Motor speed	1797 r/min		1772 r/min		1750 r/min		1730 r/min	
Frequency value	147.6 Hz		146.4 Hz		144 Hz		142.8 Hz	
	Amplitude	Component count						
SR-AMD-EEMD	0.01287	4	0.00858	3	0.00754	3	0.00748	4
AMD-EEMD	0.00524	4	0.00342	3	0.00323	4	0.00375	4
AMD-EMD	0.00529	4	0.00345	3	0.00335	4	0.00382	4
SR-EEMD	0.01208	10	0.00854	10	—	—	—	—
SR-EMD	0.01228	9	0.00660	9	—	—	—	—
EEMD	0.00574	10	0.00364	10	—	—	—	—
EMD	0.00568	9	0.00469	9	—	—	—	—

Note. “—” expresses no result.

the result shows that the SR-AMD-EEMD method can effectively improve the SNR and also reduce the number of EEMD effective components, thus improving the quality and accuracy of EEMD decomposition and enhancing the amplitude of components frequency. Therefore, it is valuable in engineering applications.

Conflict of Interests

The authors declare that there is no conflict of interests regarding the publication of this paper.

Acknowledgments

This work was supported by the National Natural Science Foundation of China (Grant no. 51475407), Hebei Provincial Natural Science Foundation of China (no. E2015203190), and Key Project of Natural Science Research in Colleges and Universities of Hebei Province (Grant no. ZD2015050).

References

- [1] Y. Tian, J. Ma, C. Lu, and Z. Wang, “Rolling bearing fault diagnosis under variable conditions using LMD-SVD and

- extreme learning machine,” *Mechanism and Machine Theory*, vol. 90, pp. 175–186, 2015.
- [2] J. Zheng, J. Cheng, and Y. Yang, “A rolling bearing fault diagnosis approach based on LCD and fuzzy entropy,” *Mechanism & Machine Theory*, vol. 70, no. 6, pp. 441–453, 2013.
 - [3] H. Liu and M. Han, “A fault diagnosis method based on local mean decomposition and multi-scale entropy for roller bearings,” *Mechanism & Machine Theory*, vol. 75, pp. 67–78, 2014.
 - [4] J. Zheng, J. Cheng, Y. Yang, and S. Luo, “A rolling bearing fault diagnosis method based on multi-scale fuzzy entropy and variable predictive model-based class discrimination,” *Mechanism and Machine Theory*, vol. 78, pp. 187–200, 2014.
 - [5] R. Benzi, A. Sutera, and A. Vulpiani, “The mechanism of stochastic resonance,” *Journal of Physics A: Mathematical and General*, vol. 14, no. 11, pp. L453–L457, 1981.
 - [6] Y. Hang and H. Yan, “Research on weak signal detection based on cascaded stochastic bistable resonance,” *Computer Measurement & Control*, vol. 20, no. 7, pp. 1821–1836, 2012.
 - [7] P. Shi, X. Ding, and D. Han, “Study on multi-frequency weak signal detection method based on stochastic resonance tuning by multi-scale noise,” *Measurement*, vol. 47, no. 1, pp. 540–546, 2014.
 - [8] Y. G. Leng and T. Y. Wang, “Numerical research of twice sampling stochastic resonance for the detection of a weak signal submerged in a heavy noise,” *Acta Physica Sinica*, vol. 52, no. 10, pp. 2432–2437, 2003.
 - [9] S. Lu, Q. He, and F. Kong, “Effects of underdamped step-varying second-order stochastic resonance for weak signal detection,” *Digital Signal Processing*, vol. 36, pp. 93–103, 2015.
 - [10] Q. He and J. Wang, “Effects of multiscale noise tuning on stochastic resonance for weak signal detection,” *Digital Signal Processing*, vol. 22, no. 4, pp. 614–621, 2012.
 - [11] L. Zhang, F. Wang, and Z. Hui, “Detecting high frequency weak signal using parameter-adjusted frequency shifting based on stochastic resonance (SR),” *Physics Procedia*, vol. 24, pp. 382–389, 2012.
 - [12] N. E. Huang, Z. Shen, S. R. Long et al., “The empirical mode decomposition and the Hilbert spectrum for nonlinear and non-stationary time series analysis,” *Proceedings of the Royal Society of London, Series A: Mathematical, Physical and Engineering Sciences*, vol. 454, no. 1971, pp. 903–995, 1998.
 - [13] Z. Wu and N. E. Huang, “Ensemble empirical mode decomposition: a noise-assisted data analysis method,” *Advances in Adaptive Data Analysis*, vol. 1, no. 1, pp. 1–49, 2011.
 - [14] Y.-H. Wang, C.-H. Yeh, H.-W. V. Young, K. Hu, and M.-T. Lo, “On the computational complexity of the empirical mode decomposition algorithm,” *Physica A: Statistical Mechanics & Its Applications*, vol. 400, no. 2, pp. 159–167, 2014.
 - [15] W. Jin-Dun, C. Lue, and Q. Wei, *Research on Fault Weak Signal Feature Extraction Based on EEMD Method*, Electronic Design Engineering, Norco, Calif, USA, 2012.
 - [16] Y. Lei, N. Li, J. Lin, and S. Wang, “Fault diagnosis of rotating machinery based on an adaptive ensemble empirical mode decomposition,” *Sensors*, vol. 13, no. 12, pp. 16950–16964, 2013.
 - [17] F. Zhao, X. Mei, T. Tao, G. Jiang, and Y. Zhou, “Fault diagnosis of a machine tool rotary axis based on a motor current test and the ensemble empirical mode decomposition method,” *Proceedings of the Institution of Mechanical Engineers, Part C: Journal of Mechanical Engineering Science*, vol. 225, no. 5, pp. 1121–1129, 2011.
 - [18] G. Chen and Z. Wang, “A signal decomposition theorem with Hilbert transform and its application to narrowband time series with closely spaced frequency components,” *Mechanical Systems and Signal Processing*, vol. 28, pp. 258–279, 2012.
 - [19] S. Fauve and F. Heslot, “Stochastic resonance in a bistable system,” *Physics Letters A*, vol. 97, no. 1-2, pp. 5–7, 1983.
 - [20] Y.-G. Leng, T.-Y. Wang, Y. Guo, Y.-G. Xu, and S.-B. Fan, “Engineering signal processing based on bistable stochastic resonance,” *Mechanical Systems & Signal Processing*, vol. 21, no. 1, pp. 138–150, 2007.
 - [21] Y. Qin, Y. Tao, Y. He, and B. Tang, “Adaptive bistable stochastic resonance and its application in mechanical fault feature extraction,” *Journal of Sound and Vibration*, vol. 333, no. 26, pp. 7386–7400, 2014.
 - [22] J. Kennedy and R. Eberhart, “Particle swarm optimization,” in *Proceedings of the IEEE International Conference on Neural Networks*, vol. 4, pp. 129–132, Perth, Australia, December 1995.
 - [23] Y. Shi and R. C. Eberhart, “Parameter selection in particle swarm optimization,” in *Evolutionary Programming VII*, vol. 1447 of *Lecture Notes in Computer Science*, pp. 591–600, Springer, Berlin, Germany, 1998.

Research Article

Vibration Analysis of Partially Damaged Rotor Bar in Induction Motor under Different Load Condition Using DWT

Jose Rangel-Magdaleno,¹ Hayde Peregrina-Barreto,² Juan Ramirez-Cortes,¹
Roberto Morales-Caporal,³ and Israel Cruz-Vega⁴

¹Electronics Department, National Institute for Astrophysics, Optics and Electronics, Luis Enrique Erro No. 1, 72840 Tonantzintla, PUE, Mexico

²Computer Science Department, National Institute for Astrophysics, Optics and Electronics, Luis Enrique Erro No. 1, 72840 Tonantzintla, PUE, Mexico

³Technological Institute of Apizaco, 90300 Apizaco, TLAX, Mexico

⁴National Institute for Astrophysics, Optics and Electronics, Luis Enrique Erro No. 1, 72840 Tonantzintla, PUE, Mexico

Correspondence should be addressed to Jose Rangel-Magdaleno; jrangel@inaoep.mx

Received 23 October 2015; Revised 4 January 2016; Accepted 10 January 2016

Academic Editor: Daniel Morinigo-Sotelo

Copyright © 2016 Jose Rangel-Magdaleno et al. This is an open access article distributed under the Creative Commons Attribution License, which permits unrestricted use, distribution, and reproduction in any medium, provided the original work is properly cited.

The relevance of the development of monitoring systems for rotating machines is not only the ability to detect failures but also how early these failures can be detected. The purpose of this paper is to present an experimental study of partially damaged rotor bar in induction motor under different load conditions based on discrete wavelet transform analysis. The approach is based on the extraction of features from vibration signals at different level of damage and three mechanical load conditions. The proposed analysis is reliable for tracking the damage in rotor bar. The paper presents an analysis and extraction of vibration features for partially damaged rotor bar in induction motors. The experimental analysis shows the change in behavior of vibration due to load condition and progressive damage.

1. Introduction

The increasing need for production at low cost in a safe manner and high quality has accelerated a change in rotating machine maintenance from corrective to preventive [1]. The relevance of the development of monitoring systems for rotating machines is not only about the ability to detect failures but also about how early these failures can be detected [2]. As one of the major equipment items in modern industry, induction motor constitutes around 85% of the motors [3]. A common fault in induction motors is a broken rotor bar; this fault corresponds approximately to 10% of the failures [4]. In addition, this failure significantly increases power consumption and it is responsible for further damage to the machinery because of the undesired vibrations and shattering that are produced.

The most popular techniques for fault detection in induction motors are the motor current signature analysis (MCSA)

and the motor vibration signature analysis (MVSA). There are several current analysis techniques in literature about the identification of faults in induction motors such as broken bars [2, 5–11] and also vibration analysis techniques [12–25]. When it comes to vibration analysis techniques, there are several methodologies for the detection of broken bars. Su et al. analyzed the vibration signal using an Artificial Neural Network (ANN) for motor fault detection [12]. Gritli et al. investigated the impact of the control system related to fault diagnosis; they concluded that current signal is affected and vibration analysis showed better result for fault diagnosis [13]. Betta et al. proposed a vibration analyzer based on a digital signal processor (DSP) for fault diagnosis in rotating machine [16]. Sadoughi et al. proposed an intelligent diagnosis based on ANN and new features in vibration spectrum [19]. Climente-Alarcon et al. studied the effect of interbar currents attenuation and how they are greatly reduced if the bar is

severed at both ends. They used vibration spectrum analysis during stationary operation [25]. Several authors have used wavelet decomposition for broken bar detection. Antonio-Daviu et al. [20] developed an evaluation of different starting methods for motor fault detection; they showed how the advanced analysis based on startup technique relies on identifying the time-frequency evolutions of the rotor-fault-related components contained in the startup current signal. Miceli et al. [24] presented a time-frequency analysis from axial and radial core vibration signal for broken rotor bar detection. Ordaz-Moreno et al. [6] developed a methodology based on discrete wavelet transform (DWT) for broken bar detection during transient state using current signature analysis. Delgado-Arredondo et al. [15] presented a comparative study of time-frequency decomposition techniques for fault detection in induction motor using vibration analysis. A review of wavelet analysis applied to induction motor fault detection is presented in [26]. The works presented above are calibrated to one or two broken bar detections, in the better case a half broken bar can be detected, and the reason is due to the fact that amplitude of incipient broken bar is small and can be absorbed by the fundamental frequency in traditional MCSA methodology. Recently DWT has been used remarking the importance of wavelets analysis in induction motor fault detection, but the majority detects only one or half broken bar. Garcia-Perez et al. [27] proposed the use of MUSIC (Multiple Signal Classification) for analysis of incipient broken rotor bar in induction motor using current analysis. Their work represents a first study in partially broken bars and their detection using motor current signature analysis during the transient state. Nevertheless, their methodology was not tested with load variation, and then more investigation related to incipient broken bars is mandatory.

In this paper, the use of DWT and MVSA for the study of partially damaged rotor bar is presented. The contribution of the paper is the analysis of some features extracted from wavelets decomposition that allows detecting the change in vibration behavior due to progressive damage. The novelty of the paper is the detection of incipient broken bars (3 mm, 5 mm, 7 mm, and 10 mm) using vibration analysis during startup transient. The experimental analysis under different mechanical load levels shows the change in behavior and vibration due to progressive damage.

The remainder of this paper is organized as follows: Section 2 presents the theoretical background of motor vibration signature analysis, discrete wavelet transform, autocorrelation, and some estimation parameters; the experimental setup is presented in Section 3; Section 4 presents results from several cases of study. The conclusions are presented in Section 5.

2. Theoretical Background

The identification of incipient broken bars implies an appropriate feature extraction. The background of broken bar detection and the techniques used for it are presented in this section.

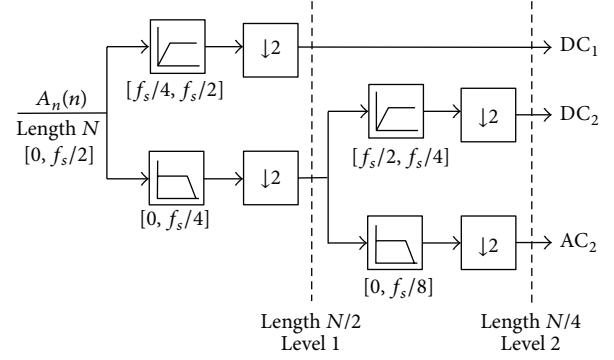


FIGURE 1: Mallat algorithm for DWT decomposition.

2.1. Motor Vibration Signature Analysis (MVSA). Several asymmetries on the rotor can be determined by the spectrum analysis of the motor vibration. A broken bar in an induction motor can be detected through MVSA. A broken bar induces a spurious component in the vibration spectrum given by [2]

$$f_{BB} = (1 \pm 2ks) f_{ss}, \quad (1)$$

where k is an integer, s is the per-unit slip, and f_{ss} is the supply frequency. Nevertheless, due to the small amplitude of frequencies of partially broken bar its detection is compromised. For this reason different methodologies have been proposed [2, 27].

2.2. Discrete Wavelet Transform (DWT). Discrete wavelet transform has widely been used for signal processing of nonstationary or transient signals. Mallat's algorithm is used to compute the DWT based on a set of discrete-time low- and high-pass filters. Figure 1 shows Mallat's algorithm for DWT decomposition [28]. The decomposition produced the approximation (low-frequency component) and the detail (high-frequency component) coefficients. According to the DWT filter bank properties, the frequency bands for approximation AC_L and detail DC_L at level L are given by

$$\begin{aligned} AC_L &= \left[0, \frac{f_s}{2^{L+1}} \right], \\ DC_L &= \left[\frac{f_s}{2^{L+1}}, \frac{f_s}{2^L} \right], \end{aligned} \quad (2)$$

where f_s is the sampling frequency. Table 1 shows an example of the frequency bands for detail and approximation levels.

Figure 2 shows an example of DWT decomposition of an induction motor vibration signal at healthy condition and full mechanical load. Seven levels were used for the decomposition. Figure 2(a) shows the approximation levels and Figure 2(b) shows the detail levels. Ordaz-Moreno et al. [6] and Antonino-Daviu et al. [20] proposed the analysis of current and vibrations signals during transient state, respectively. They analyzed the variability of the signal at different levels; nevertheless, for incipient broken bars the direct analysis of the signal is not enough. In this paper, an additional

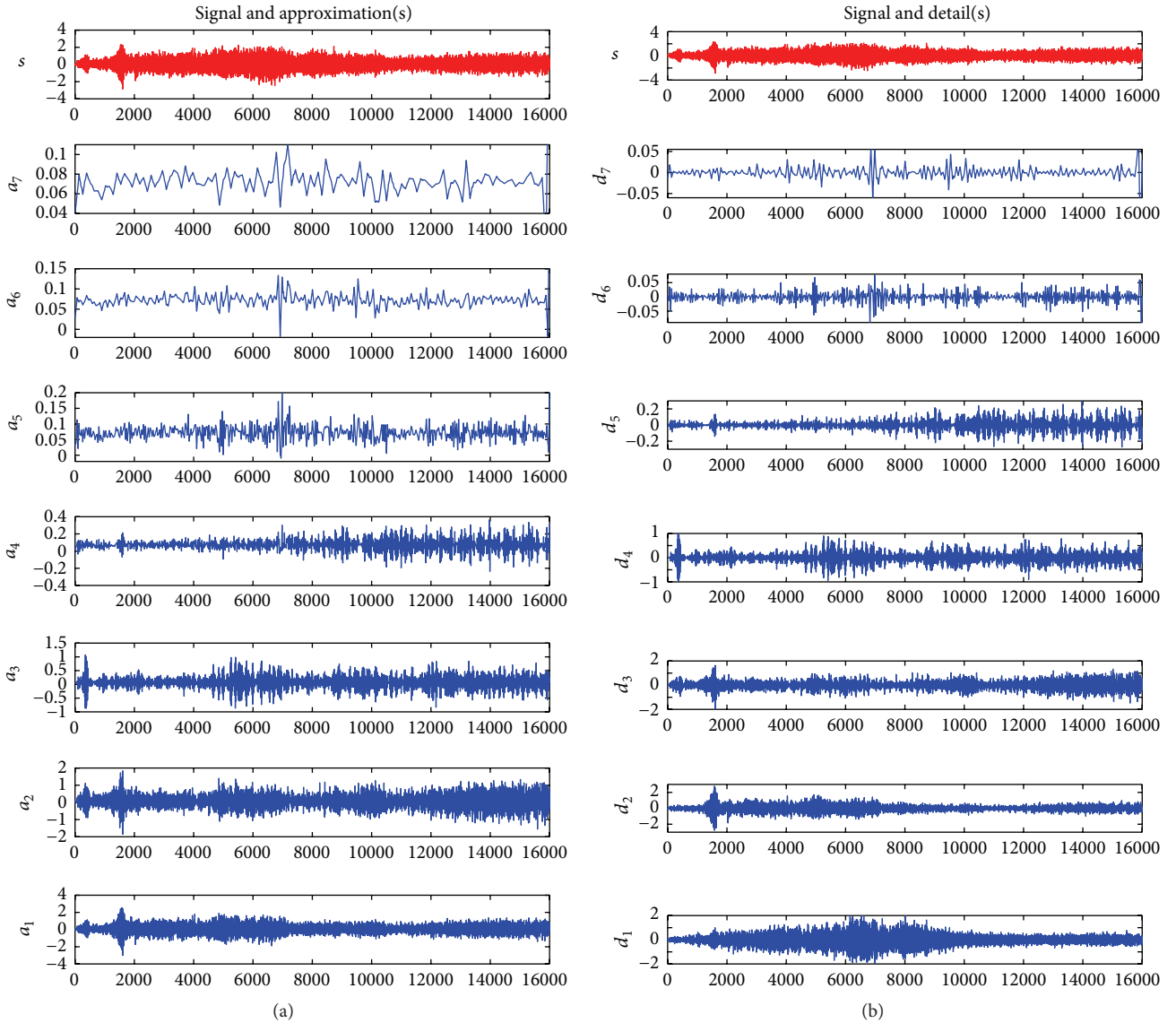


FIGURE 2: DWT decomposition, (a) approximation, and (b) detail.

TABLE 1: DWT decomposition level frequency bands for a sampling frequency $f_s = 3200$ Hz.

Level (L)	Approximation bandwidth (Hz)	Detail bandwidth (Hz)
1	AC_1 [0, 800]	DC_1 [800, 1600]
2	AC_2 [0, 400]	DC_2 [400, 800]
3	AC_3 [0, 200]	DC_3 [200, 400]
4	AC_4 [0, 100]	DC_4 [100, 200]
5	AC_5 [0, 50]	DC_5 [50, 100]
6	AC_6 [0, 25]	DC_6 [25, 50]
7	AC_7 [0, 12.5]	DC_7 [12.5, 25]

preprocessing step by means of autocorrelation of the signals is proposed; this helps to reduce the noise in acquired vibration signals.

2.3. Autocorrelation. The autocorrelation is defined as the cross-correlation of the signal with itself. The autocorrelation allows finding repeating patterns and measures the linear relationship between time series observations separated by a lag of n time units. The autocorrelation has shown good results in fault detection [29, 30]. The autocorrelation is given by

$$C_{xx} = E \{ X_{(n+m)} X_{(n)}^* \}, \quad (3)$$

where X is the vibration signal and E is the spectral estimation. Figure 3 shows an example of DWT decomposition of a healthy induction motor vibration signal at full mechanical load previously preprocessed by autocorrelation. Figure 3(a) shows the approximation levels and Figure 3(b) shows the detail levels.

An example of a DWT decomposition of a damage induction motor vibration signal is shown in Figure 4; it was

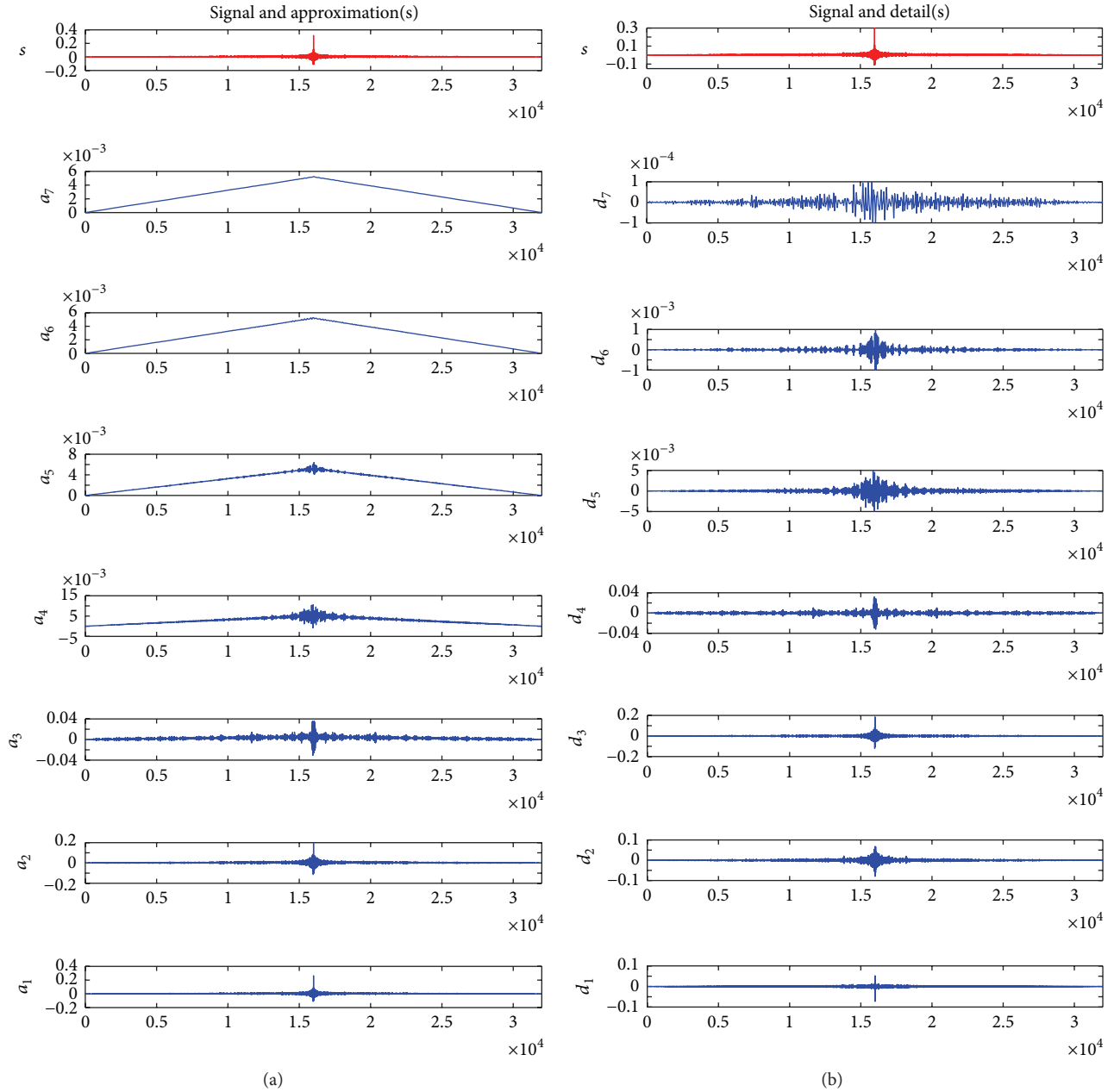


FIGURE 3: Autocorrelation and DWT decomposition for a healthy motor, (a) approximation, and (b) detail.

obtained at full mechanical load and previously preprocessed by means of autocorrelation. The motor has one broken rotor bar. The approximation and the detail levels are shown in Figures 4(a) and 4(b), respectively. Figure 3(a) at level 7 shows the expected triangle due to the autocorrelation process, whereas Figure 4(a) at level 7 shows a noisy triangle. The difference between a healthy and damaged motor signals is visually clear. The only difference in condition between the two motors is the broken rotor bar. Then, the signal contamination is due to the broken bar. In order to obtain a better interpretation the use of some basic statistic parameters like mean, zero-crossing, and standard deviation at level 3 of

decomposition is proposed. In this level the range of frequencies is from 0 to 200 Hz; then the fundamental and some harmonics are included.

2.4. Estimation Parameters. Three basic statistic parameters were used, the mean (\hat{x}) defined in (4), standard deviation (SD) defined by (5), and zero-crossing (ZC) that counts the number of times the signal crosses the zero value or presents a change in sign:

$$\hat{x} = \frac{1}{N} \sum_{i=0}^N x_i, \quad (4)$$

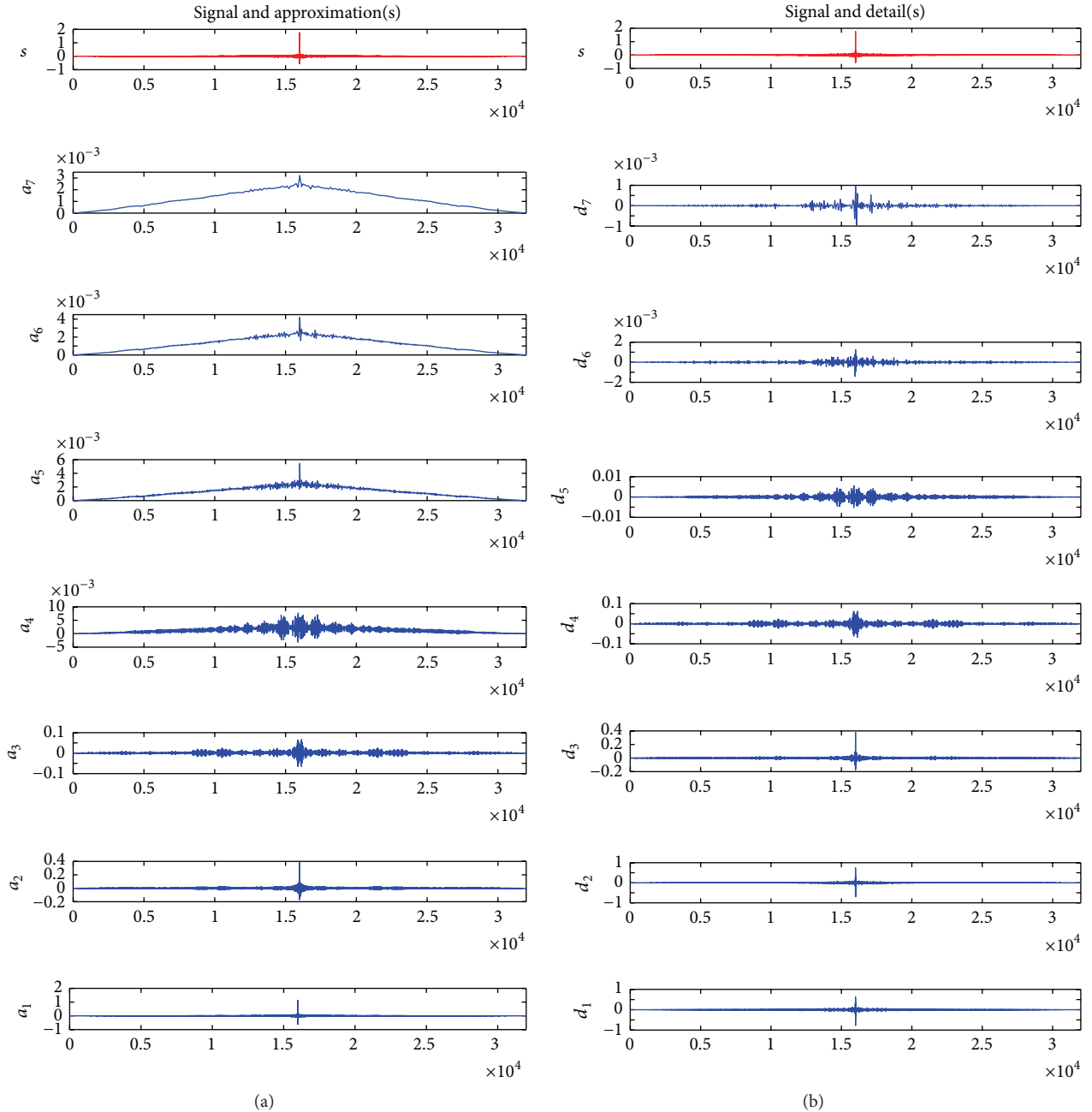


FIGURE 4: Autocorrelation and DWT decomposition for a motor with one broken bar, (a) approximation, and (b) detail.

$$SD = \left(\frac{1}{N} \sum_{i=0}^N (x_i - \hat{x})^2 \right)^{1/2}. \quad (5)$$

Also the variability, norm, kurtosis, skewness, and RMS value were computed; nevertheless, parameters like the mean, standard deviation, and zero-crossing provided better results of the information we expected to obtain.

2.5. Classification: *k*-Nearest-Neighbor Algorithm (*k*NN). A common reference among the classifiers due to the simplicity

of the learning rule is the *k*-nearest-neighbor classifier. This classifier is memory-based and requires no model to be fit. The basic idea is that, given a query point x_0 , it is found that k training points x_r , $r = 1, \dots, k$, are closest in distance to x_0 , and they are classified using the majority vote among the k neighbors [31]. Assuming that the features of the objects to be classified are real-value, a common distance measure in the feature space is the Euclidean, and all objects in the training set participate to determine *k*-nearest-neighbors to the query point. A common classifier is the 1-nearest-neighbor, which is used in this paper.

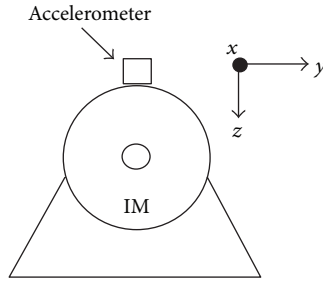


FIGURE 5: Accelerometer placed on induction motor.

3. Methodology

The methodology consists mainly in the following steps:

- (1) Vibration signals of the three axes are sensed online from the motor and saved in a PC.
- (2) Feature extraction stage is as follows:
 - (a) An autocorrelation function is applied to each axis.
 - (b) The decomposition at level three of each signal is obtained using DWT algorithm.
 - (c) Statistical parameters like mean, standard deviation, and zero-crossings are calculated for the decomposition coefficients.
- (3) Statistical analysis of the parameter is computed.
- (4) Classification stage is as follows: the motor condition is classified based on k NN algorithm.

3.1. Experimental Setup. The experimental test was performed on a 1-HP motor, the vibration signal was acquired using MEMS-based triaxial accelerometer with a user-selectable full scale ($\pm 2\text{ g}/\pm 6\text{ g}$); a resolution of 12 bits and an oversampling frequency of 3.2 KHz was used. The signals were acquired at the startup transient state of the motor during 5 s. Figure 5 shows the location and orientation of the accelerometer over the motor. The axis “ x ” is perpendicular to the rotor, where the best results to the analysis were obtained, axis “ y ” provided acceptable results, and axis “ z ” provided less satisfactory results.

The data were recorded in the following states: healthy, 3 mm, 5 mm, 7 mm, and 1 broken bar. For each state, 50 runs for unload, 50 runs for half load, and 50 runs for full load were recorded. In order to obtain the incipient conditions (3 mm, 5 mm, 7 mm, and 1 br) the rotor was externally drilled at different depths. A total of 750 runs were analyzed in this study.

4. Analysis Results

As it was described above, the three axes were previously pre-processed by autocorrelation and then the DWT was applied and level 3 of decomposition was obtained. At this level the mean, ZC, and SD were applied. Each database (without load, half load, and full load) are constituted by 250 runs. The results obtained for each condition are shown in Figures 6–17.

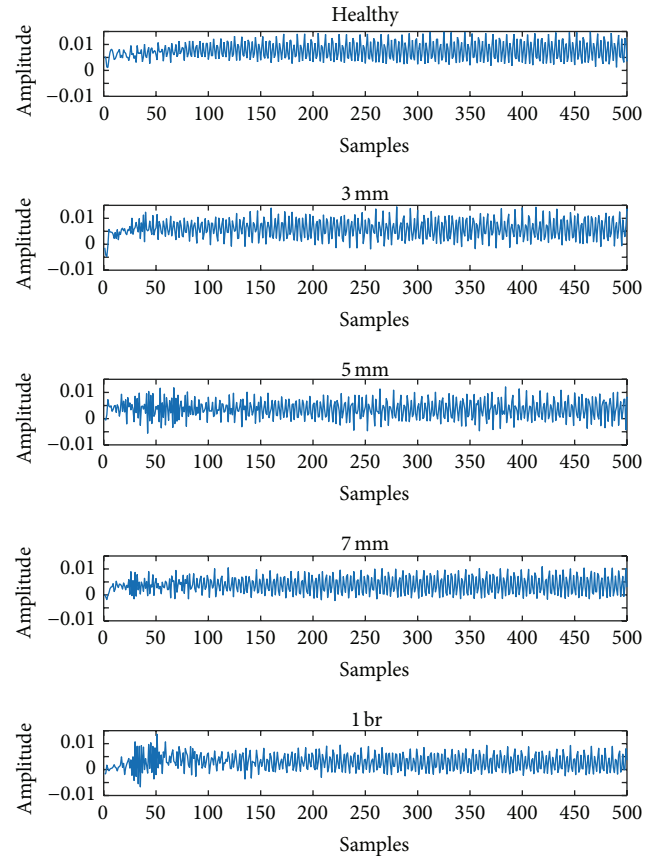


FIGURE 6: Approximation coefficients at no mechanical load, A_x -axis.

4.1. Without Mechanical Load. Figure 6 shows a section from the approximation coefficients at level 3 of decomposition. As can be seen, the coefficients show differences that can be evaluated by the proposed estimation parameters. Figure 6 shows the five conditions evaluated in this test. The three axes were analyzed to obtain better results.

In Figure 7, the analysis of the five conditions under test is shown for the A_z -axis. The analysis is performed by means of the SD and mean value parameters. One can see that the five regions present some degree of overlap; nevertheless, for the healthy, 7 mm, and one-broken bar conditions the separation between classes is more evident, allowing a better classification.

The A_y -axis analysis is depicted in Figure 8; the results are now obtained with the SD and ZC estimation parameters. As it can be seen, the conditions under test present a high dispersion degree and overlapping between them, which complicates the classification because none of the conditions are clearly separated.

Finally, Figure 9 shows the analysis of the A_x -axis, where the mean and ZC values were selected as estimation parameters. It is considerably clear that the A_x -axis shows the best results for classification; all the conditions are considerably grouped and separated. It is possible to detect not only the damage condition but also the level of such damage. The level

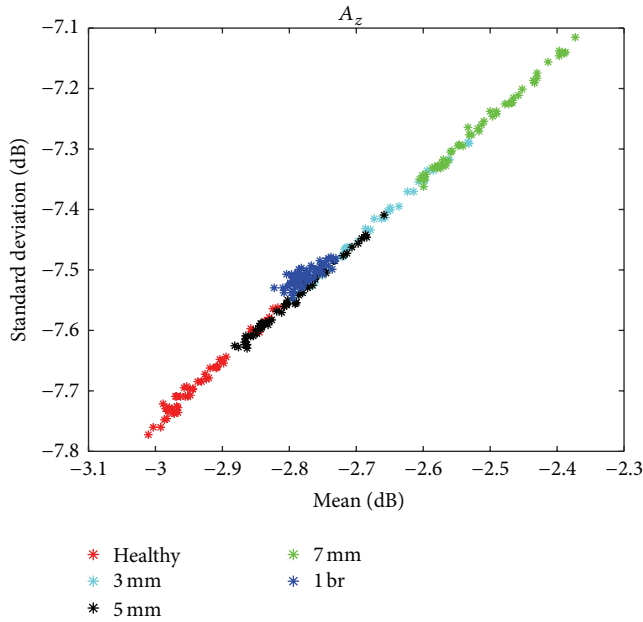


FIGURE 7: Unload condition analysis, A_z -axis.

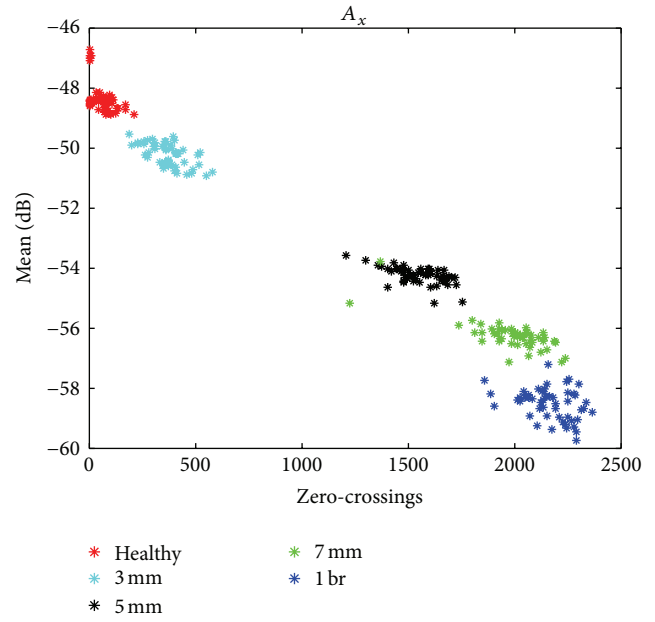


FIGURE 9: Unload condition analysis, A_x -axis.

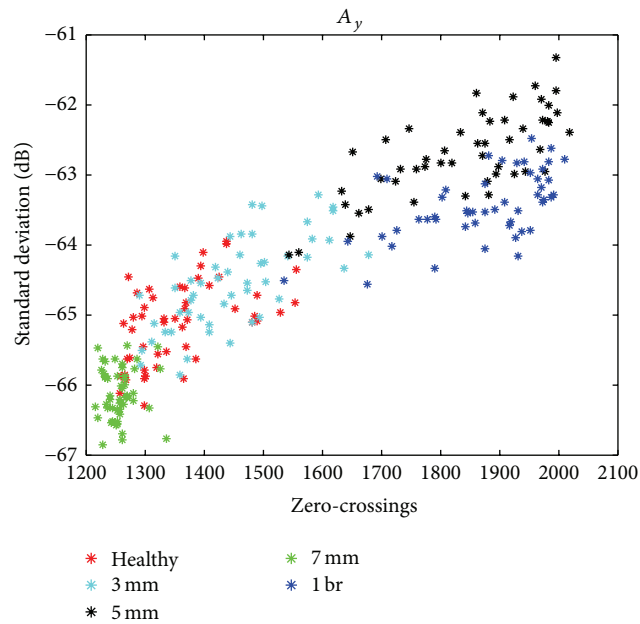


FIGURE 8: Unload condition analysis, A_y -axis.

of overlapping is too low showing that the analysis in the A_x -axis is the best option to obtain a clear classification of the damage level under a nonmechanical load condition.

4.2. Half-Mechanical Load. Figure 10 presents a section of the approximation coefficients at level 3 of decomposition for A_x -axis; all the conditions are shown. Differences among amplitudes of the signals can be seen. For better results the three axes were analyzed; mean and SD were selected for the analysis. Figure 11 shows the analysis for A_z -axis; in this case all the conditions are totally overlapped. This axis cannot

be used for condition classification; even healthy and one-broken bar conditions are not identifiable.

Figure 12 shows the analysis for A_y -axis; ZC and SD were selected for the analysis. Two main groups are presented; one for healthy and 3 mm conditions and the other one for 5 mm, 7 mm, and 1 br conditions. Under this condition of half-mechanical load and for this axis, the 3 mm depth drilled is considered as healthy whereas the damage condition is detected at a depth of 5 mm. In the second group, using an appropriate classification algorithm, the one-broken bar condition can be detected. The 5 mm and 7 mm have more overlapping degree.

Figure 13 presents the analysis for A_x -axis; ZC and SD were selected for the analysis. In this case, healthy condition has less overlap with 3 mm. For the rest conditions it is difficult to obtain a clear result due to the highly overlapping degree. Then, A_y and A_x axes can be used together for a better classification; using both, the healthy and damage conditions (3 mm, 5 mm, 7 mm, and 1 br) can be better classified. Depending on the classification technique other conditions can be estimated to obtain healthy, medium damage (3 mm, 5 mm and 7 mm), and one-broken bar conditions.

4.3. Full-Mechanical Load. Figure 14 shows a section of the approximation coefficients of A_x -axis for full-mechanical load. In the figure the differences among the five conditions are presented. In order to measure these differences the three axes were analyzed as is shown in Figures 15, 16, and 17.

Figure 15 shows the analysis of A_z -axis; mean and SD were selected for the analysis. The conditions are totally overlapped. It is clear that this axis does not help in the analysis of partially broken bars.

Figure 16 presents the analysis for A_y -axis; mean and SD were selected for the analysis. Four groups in the figure can be seen, for the 1-bar condition and 5 mm of a depth drilled

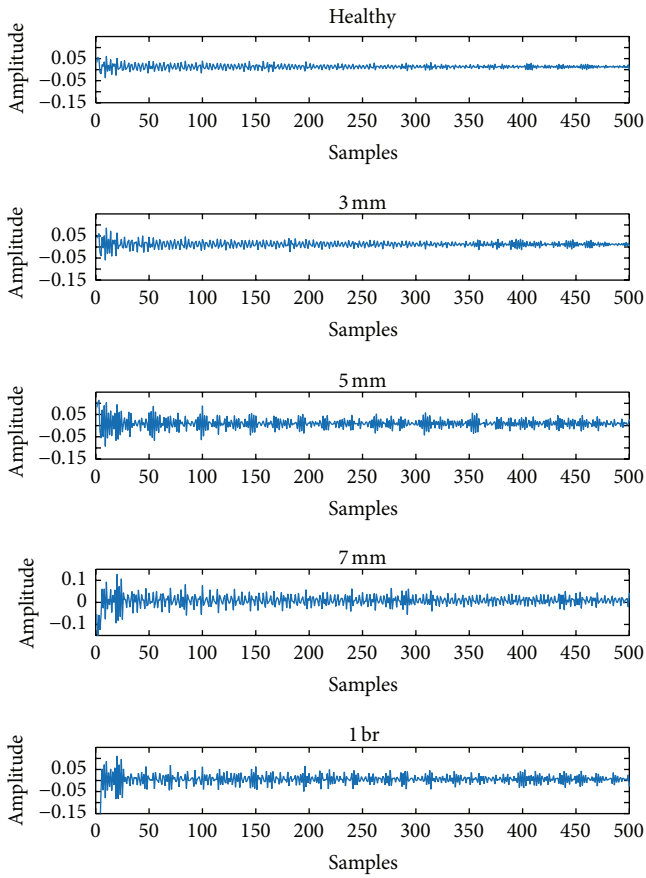
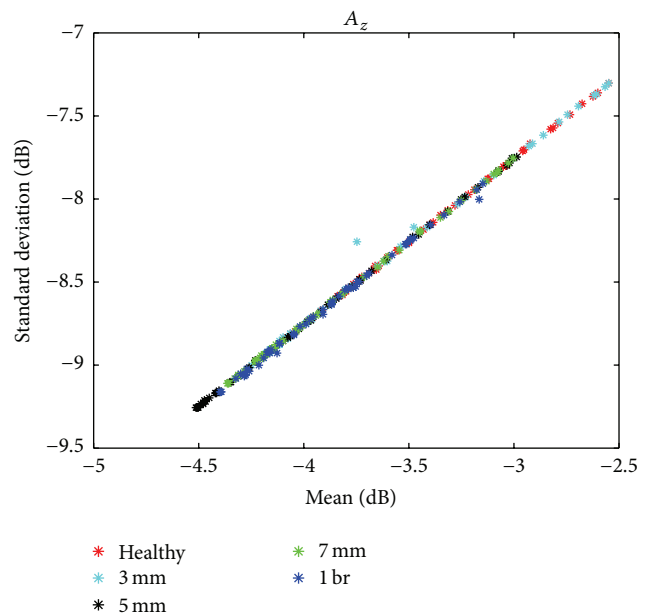


FIGURE 10: Approximation coefficients at half-mechanical load, A_x -axis.



- * Healthy
- * 3 mm
- * 5 mm
- * 7 mm
- * 1 br

FIGURE 11: Half-load condition analysis, A_z -axis.

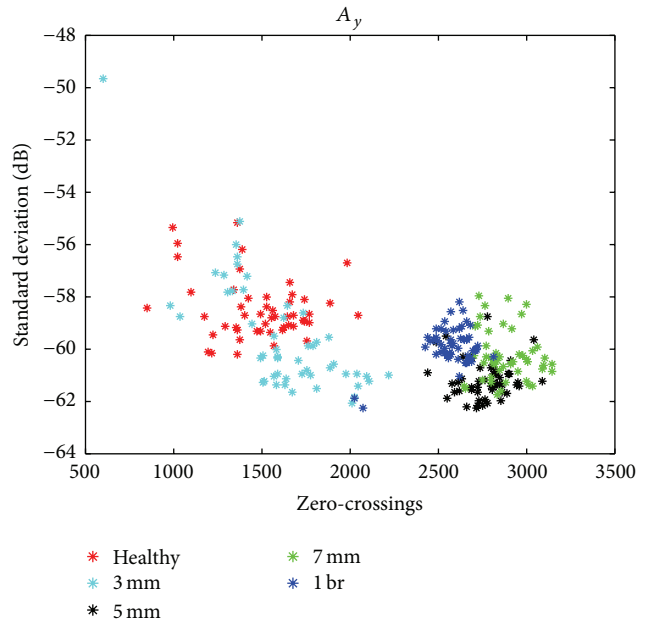


FIGURE 12: Half-load condition analysis, A_y -axis.

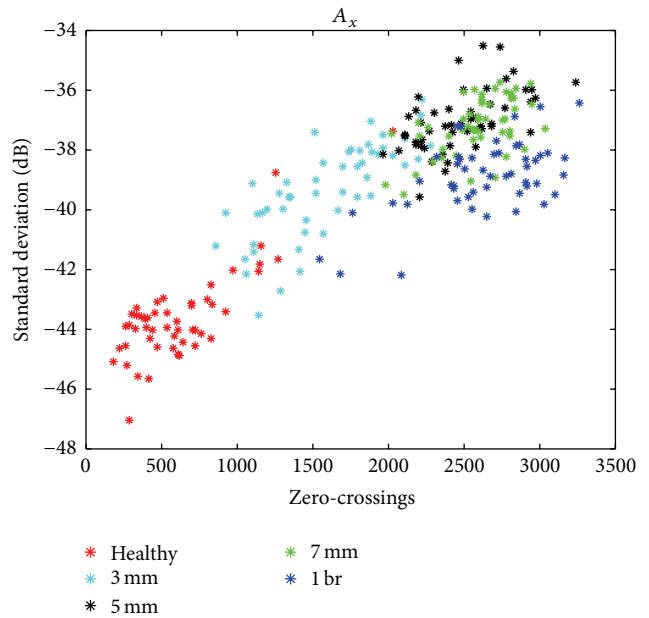


FIGURE 13: Half-load condition analysis, A_x -axis.

condition, a clearly division between classes is obtained, which does not happen with the 3 mm and healthy conditions and in certain degree of about 25% of the 7 mm condition; the A_x -axis is developed for this last group.

Figure 17 shows the analysis in A_x -axis; ZC and mean were the estimation parameters selected for the analysis. Three groups are showed in the figure, the first for healthy condition; the second for 3 mm; and the third is an overlap of 5 mm, 7 mm, and 1 br. Then the five conditions can be detected using a combination of A_y and A_x . A_y detects 1 br and 5 mm and 7 mm conditions with some overlap, and A_x

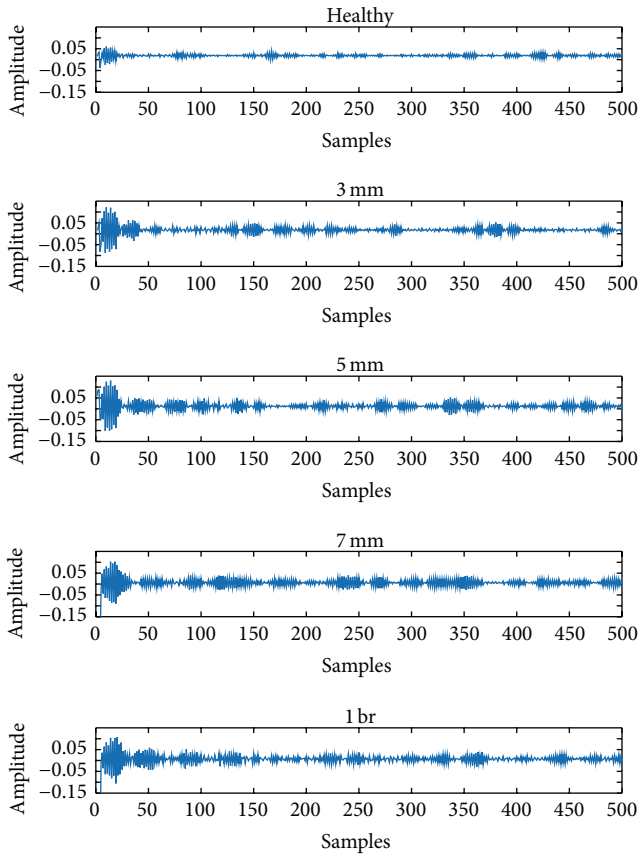


FIGURE 14: Approximation coefficients at full mechanical load, A_x -axis.

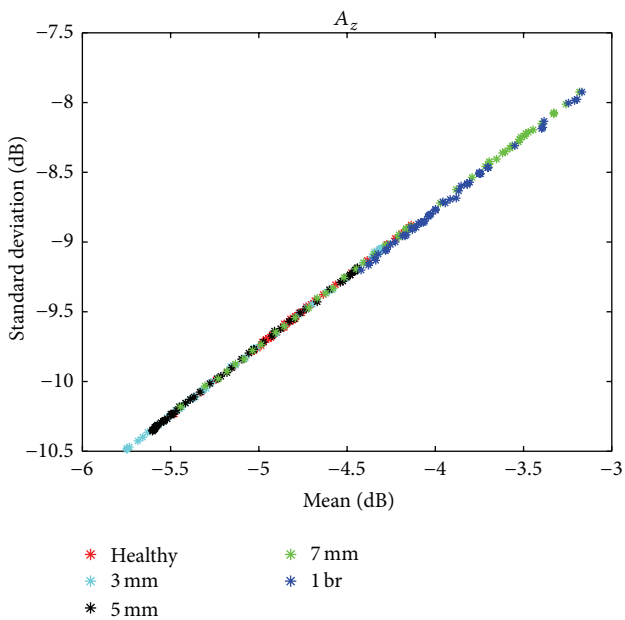


FIGURE 15: Full-load condition analysis, A_z -axis.

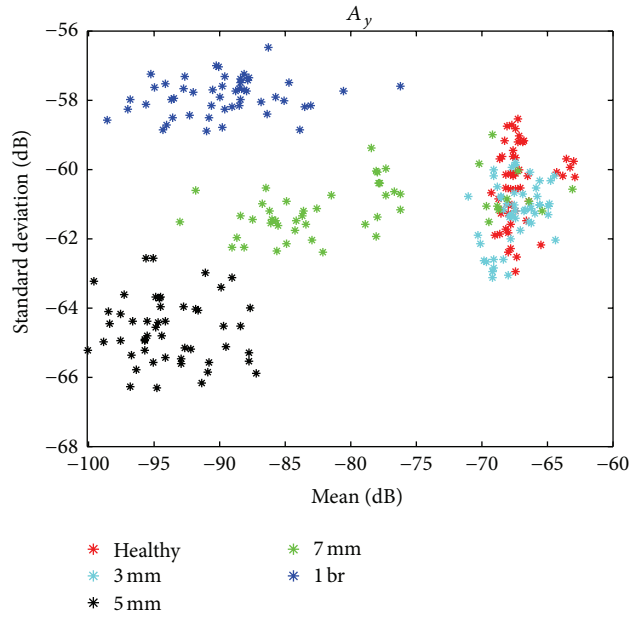


FIGURE 16: Full-load condition analysis, A_y -axis.

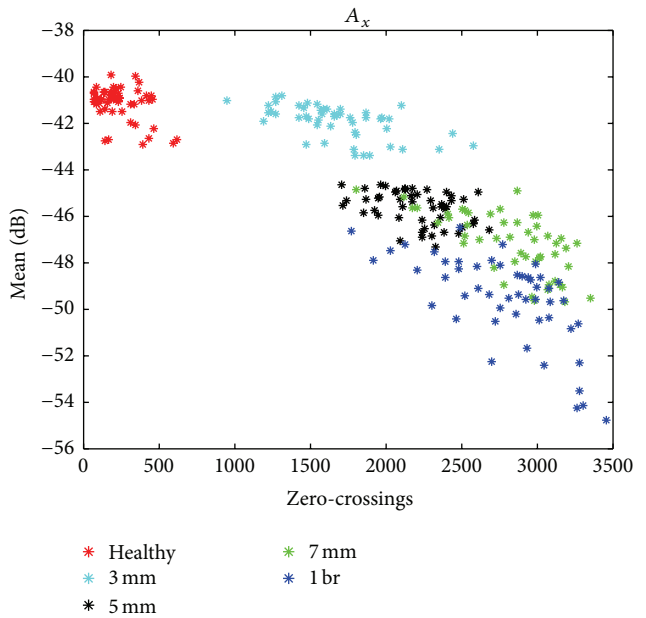


FIGURE 17: Full-load condition analysis, A_x -axis.

detects healthy and 3 mm conditions. In the case of the overlap in 7 mm in A_y -axis (group four) it is necessary to analyze the third group in A_x (5 mm, 7 mm, and 1 br), if the sample belongs to this group then it can be classified as 7 mm, and we know that it is not 5 mm or 1 br because these conditions are perfectly separable in A_y -axis.

4.4. *k*NN. A simple classification technique was used to prove the usefulness of the analysis. *k*-nearest-neighbors (*k*NN) algorithm was used. Also tests adding white noise were made; the level of noise was based on the signal-to-noise

TABLE 2: Classification percentage for each condition using k NN.

Condition/axis	A_x	SNR10	SNR5	SNR1
Unload	96.55%	96.70%	92.85%	89.8%
Half load	80.5%	81.5%	80.85%	80.55%
Full load	87.6%	85.85%	84.4%	85.15%

ratio (SNR). The values used were SNR = 10, 5, and 1. Table 2 shows the results of the classification for the A_x -axis with $k = 1$ and for the three cases of added noise. These results are obtained from a cross-validation process with 10-folds; the average loss for each cross-validation model is used to obtain the accuracy level in classification. We have to remark that the simple value of $k = 1$ was sufficient to obtain a desirable accuracy level in classification.

5. Conclusions and Future Work

In this paper a study of incipient broken bar detection based on vibration analysis is presented. The obtained results show that information regarding partial damage in broken rotor bar is reflected on vibration signals. An initial damage of 3 mm was detected using the autocorrelation and DWT. A simple k NN classification considering the healthy motor and the four levels of damage (3 mm, 5 mm, 7 mm, and 1 br) showed results of 96.55% for unload conditions and 80.5% for half-load and 87.6% for full-load condition.

Future work aims to employ different types of classifiers like the Multilayer Perceptron (MLP), Support Vector Machines (SVM), and Artificial Neural Networks (ANN), in order to improve the accuracy level in classification especially in the half- and full-load motor conditions.

Conflict of Interests

The authors declare that there is no conflict of interests regarding the publication of this paper.

References

- [1] R. Yan, R. X. Gao, and X. Chen, "Wavelets for fault diagnosis of rotary machines: a review with applications," *Signal Processing*, vol. 96, part A, pp. 1–15, 2014.
- [2] J. D. J. Rangel-Magdaleno, R. D. J. Romero-Troncoso, R. A. Osornio-Rios, E. Cabal-Yepez, and L. M. Contreras-Medina, "Novel methodology for online half-broken-bar detection on induction motors," *IEEE Transactions on Instrumentation and Measurement*, vol. 58, no. 5, pp. 1690–1698, 2009.
- [3] K. N. Gyftakis, D. V. Spyropoulos, J. C. Kappatou, and E. D. Mitronikas, "A novel approach for broken bar fault diagnosis in induction motors through torque monitoring," *IEEE Transactions on Energy Conversion*, vol. 28, no. 2, pp. 267–277, 2013.
- [4] P. Zhang, Y. Du, T. G. Habetler, and B. Lu, "A survey of condition monitoring and protection methods for medium-voltage induction motors," *IEEE Transactions on Industry Applications*, vol. 47, no. 1, pp. 34–46, 2011.
- [5] H. Razik, M. B. de Rossiter Corrêa, and E. R. C. da Silva, "A novel monitoring of load level and broken bar fault severity applied to squirrel-cage induction motors using a genetic algorithm," *IEEE Transactions on Industrial Electronics*, vol. 56, no. 11, pp. 4615–4626, 2009.
- [6] A. Ordaz-Moreno, R. D. J. Romero-Troncoso, J. A. Vite-Frias, J. R. Rivera-Gillen, and A. Garcia-Perez, "Automatic online diagnosis algorithm for broken-bar detection on induction motors based on discrete wavelet transform for FPGA implementation," *IEEE Transactions on Industrial Electronics*, vol. 55, no. 5, pp. 2193–2202, 2008.
- [7] M. Nemeč, K. Drobnič, D. Nedeljković, R. Fišer, and V. Ambrožič, "Detection of broken bars in induction motor through the analysis of supply voltage modulation," *IEEE Transactions on Industrial Electronics*, vol. 57, no. 8, pp. 2879–2888, 2010.
- [8] D. Z. Li, W. Wang, and F. Ismail, "A spectrum synch technique for induction motor health condition monitoring," *IEEE Transactions on Energy Conversion*, vol. 30, no. 4, pp. 1348–1355, 2015.
- [9] J. Faiz, V. Ghorbanian, and B. M. Ebrahimi, "EMD-based analysis of industrial induction motors with broken rotor bars for identification of operating point at different supply modes," *IEEE Transactions on Industrial Informatics*, vol. 10, no. 2, pp. 957–966, 2014.
- [10] A. Sapena-Baño, M. Pineda-Sanchez, R. Puche-Panadero, J. Martinez-Roman, and D. Matic, "Fault diagnosis of rotating electrical machines in transient regime using a single stator current's FFT," *IEEE Transactions on Instrumentation and Measurement*, vol. 64, no. 11, pp. 3137–3146, 2015.
- [11] A. Sadeghian, Z. Ye, and B. Wu, "Online detection of broken rotor bars in induction motors by wavelet packet decomposition and artificial neural networks," *IEEE Transactions on Instrumentation and Measurement*, vol. 58, no. 7, pp. 2253–2263, 2009.
- [12] H. Su, K. T. Chong, and R. Ravi Kumar, "Vibration signal analysis for electrical fault detection of induction machine using neural networks," *Neural Computing and Applications*, vol. 20, no. 2, pp. 183–194, 2011.
- [13] Y. Gritli, A. O. Di Tommaso, R. Miceli, F. Filippetti, and C. Rossi, "Closed-loop bandwidth impact on MVSA for rotor broken bar diagnosis in IRFOC double squirrel cage induction motor drives," in *Proceedings of the International Conference on Clean Electrical Power (ICCEP '13)*, pp. 529–534, IEEE, Alghero, Italy, June 2013.
- [14] L. Deng and R. Zhao, "A vibration analysis method based on hybrid techniques and its application to rotating machinery," *Measurement*, vol. 46, no. 9, pp. 3671–3682, 2013.
- [15] P. A. Delgado-Arredondo, A. Garcia-Perez, D. Morinigo-Sotelo et al., "Comparative study of time-frequency decomposition techniques for fault detection in induction motors using vibration analysis during startup transient," *Shock and Vibration*, vol. 2015, Article ID 708034, 14 pages, 2015.
- [16] G. Betta, C. Liguori, A. Paolillo, and A. Pietrosanto, "A DSP-based FFT-analyzer for the fault diagnosis of rotating machine based on vibration analysis," *IEEE Transactions on Instrumentation and Measurement*, vol. 51, no. 6, pp. 1316–1321, 2002.
- [17] A. Sadoughi, M. Ebrahimi, M. Moalem, and S. Sadri, "Intelligent diagnosis of broken bars in induction motors based on new features in vibration spectrum," in *Proceedings of the IEEE International Symposium on Diagnostics for Electric Machines, Power Electronics and Drives (SDEMPED '07)*, pp. 106–111, IEEE, Cracow, Poland, September 2007.
- [18] L. M. R. Baccarini, V. V. Rocha e Silva, B. R. de Menezes, and W. M. Caminhas, "SVM practical industrial application for mechanical faults diagnostic," *Expert Systems with Applications*, vol. 38, no. 6, pp. 6980–6984, 2011.

- [19] A. Sadoughi, M. Ebrahimi, and E. Rezaei, "A new approach for induction motor broken bar diagnosis by using vibration spectrum," in *Proceedings of the SICE-ICASE International Joint Conference*, pp. 4715–4720, Busan, Republic of Korea, October 2006.
- [20] J. A. Antonino-Daviu, J. Pons-Llinares, V. Climente-Alarcon, and H. Razik, "Evaluation of startup-based rotor fault severity indicators under different starting methods," in *Proceedings of the 40th Annual Conference of the IEEE Industrial Electronics Society (IECON '14)*, pp. 3361–3366, Dallas, Tex, USA, October–November 2014.
- [21] H. Su and K. T. Chong, "Induction machine condition monitoring using neural network modeling," *IEEE Transactions on Industrial Electronics*, vol. 54, no. 1, pp. 241–249, 2007.
- [22] P. J. Rodriguez, A. Belahcen, and A. Arkkio, "Signatures of electrical faults in the force distribution and vibration pattern of induction motors," *IEE Proceedings: Electric Power Applications*, vol. 153, no. 4, pp. 523–529, 2006.
- [23] P. C. M. L. Filho, J. N. Brito, V. A. D. Silva, and R. Pederiva, "Detection of electrical faults in induction motors using vibration analysis," *Journal of Quality in Maintenance Engineering*, vol. 19, no. 4, pp. 364–380, 2013.
- [24] R. Miceli, Y. Gritli, A. di Tommaso, F. Filippetti, and C. Rossi, "Vibration signature analysis for monitoring rotor broken bar in double squirrel cage induction motors based on wavelet analysis," *COMPEL*, vol. 33, no. 5, pp. 1625–1641, 2014.
- [25] V. Climente-Alarcon, J. A. Antonino-Daviu, F. Vedreño-Santos, and R. Puche-Panadero, "Vibration transient detection of broken rotor bars by PSH sidebands," *IEEE Transactions on Industry Applications*, vol. 49, no. 6, pp. 2576–2582, 2013.
- [26] R. Yan, R. X. Gao, and X. Chen, "Wavelets for fault diagnosis of rotary machines: a review with applications," *Signal Processing*, vol. 96, pp. 1–15, 2014.
- [27] A. Garcia-Perez, R. J. Romero-Troncoso, E. Cabal-Yepez, R. A. Osornio-Rios, J. D. J. Rangel-Magdaleno, and H. Miranda, "Startup current analysis of incipient broken rotor bar in induction motors using high-resolution spectral analysis," in *Proceedings of the IEEE International Symposium on Diagnostics for Electric Machines, Power Electronics & Drives (SDEMPED '11)*, pp. 657–663, IEEE, Bologna, Italy, September 2011.
- [28] S. G. Mallat, "Theory for multiresolution signal decomposition: the wavelet representation," *IEEE Transactions on Pattern Analysis and Machine Intelligence*, vol. 11, no. 7, pp. 674–693, 1989.
- [29] H. Samet, T. Ghanbari, and M. Ahmadi, "An auto-correlation function based technique for discrimination of internal fault and magnetizing inrush current in power transformers," *Electric Power Components and Systems*, vol. 43, no. 4, pp. 399–411, 2015.
- [30] T. Ghanbari, "Autocorrelation function-based technique for stator turn-fault detection of induction motor," *IET Science, Measurement & Technology*, 2015.
- [31] T. Hastie, J. Friedman, and R. Tibshirani, *The Elements of Statistical Learning*, Springer Series in Statistics, Springer, New York, NY, USA, 2001.

Research Article

Nonlinear Vibroimpact Characteristics of a Planetary Gear Transmission System

Jianxing Zhou,^{1,2} Wenlei Sun,¹ and Liang Yuan¹

¹School of Mechanical Engineering, Xinjiang University, Urumqi 830047, China

²Center for Post-Doctoral Studies of Mechanical Engineering, Urumqi 830047, China

Correspondence should be addressed to Jianxing Zhou; jianzhou82923@163.com

Received 31 July 2015; Revised 8 November 2015; Accepted 23 November 2015

Academic Editor: Juan P. Amezcua-Sanchez

Copyright © 2016 Jianxing Zhou et al. This is an open access article distributed under the Creative Commons Attribution License, which permits unrestricted use, distribution, and reproduction in any medium, provided the original work is properly cited.

In order to research the vibroimpact characteristics of a planetary gear transmission system under high speed and lightly loaded conditions, a new modeling method is proposed. In the modeling process, linear spring was used to simulate gear mesh elasticity under heavy load cases, and Hertz contact theory was used to calculate the contact force of gear pair under light load cases. Then, effects of the working conditions on the system vibroimpact characteristics are analyzed. The results show that, with input speed growing, the mesh force produced obvious fluctuations on the resonance frequencies of the sun gear and carrier torsion vibration, ring gear's transverse vibration under the heavy load. Under light load condition, the collision vibration occurs in the gear pair; the changing trend of the contact force shows strongly nonlinear characteristics. The time of mesh-apart in gears pair decreases gradually as the load is increased; until it reaches collision vibration threshold value, the gear pair is no longer mesh-apart. With increasing of the input speed, the time of mesh-apart is decreased gradually; the fluctuation amplitude of contact force shows a linearly increasing trend. The study provides useful theoretical guideline for planetary gear transmission low-noise design.

1. Introduction

Planetary gear transmission is characterized by large gear ratio, compact structure, and light weight and has been widely applied to various industries. Planetary gear transmission has become an indispensable key device in main power system in high speed and heavy load transmission device such as helicopter transmission and marine transmission; however, the wear in tooth profile and error in machining are likely to result in gear backlash in gear pair, which will bring repetitive collision phenomenon of contact [1], contact loss, and recontact between gears. At high speed, the gear transmission shows more obvious impact effect and leads to strong vibration, exerting an adverse influence on working performance and service life of equipment.

Impact process is a complex process associated with relative speed of objects in contact, geometrical shape of contact surface, duration of contact, and local plastic deformation [2]. High speed impact between gears in gear dynamics means gear's rapid rebound from the moment being mesh-apart in

contact each other, which is equivalent to low speed impact in structural dynamics, so the impact between gear teeth can be described by classical impact dynamics theory [3].

Typical analyses model of planetary gear transmission can be divided into two main groups: finite element model and lumped parameter model. The lumped parameter model is the most common model used to study dynamic behaviors of the planetary gear system. With the development of research, this kind of analytical model has developed from initial purely torsional model to torsion-transverse vibration coupling and torsion-transverse-axial coupling model [4]. Meanwhile, in order to make the analytical model closer to the physical prototype, a growing number of factors and application conditions are involved consecutively, such as external excitation [5], effect of oil film rigidity asymmetry of sliding bearing [6], and clearance of the bearing [7].

Some scholars use a clearance-type nonlinear restoring function in the model to describe the gear mesh and backlash. Walha et al. found that gear contact is characterized by a periodically changing stiffness and a backlash can lead to

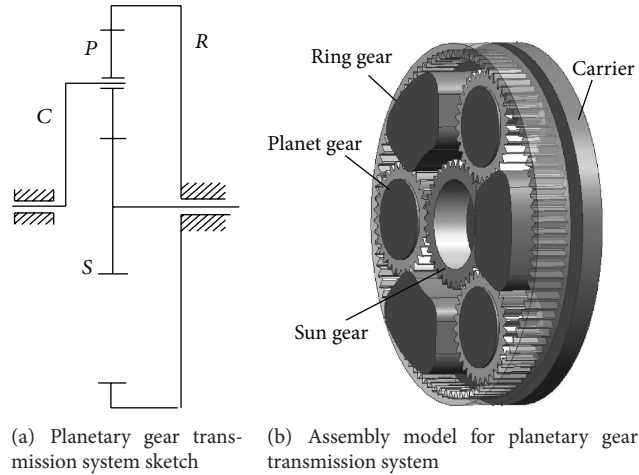


FIGURE 1: The planetary gear transmission system sketch and three-dimensional model.

loss of the contact [8]. Kahraman et al. analyzed steady state response period solution of time varying system with backlash [9]. Sun et al. made a study of influence of time varying mesh stiffness, error, and backlash on nonlinear dynamic behavior of system [10]. Eritenel and Parker examined nonlinearity due to partial contact loss, where segments of contact are lost between meshing teeth, using a rigid body dynamic model [11].

Through using this kind of model, the gear tooth flank backlash is considered, and the contact loss phenomenon and nonlinear dynamic characteristics are simulated. However, when the gear tooth recontact, the gear pairs impact will happened. The impact force and its influence on the system dynamics cannot be solved by this kind model. Barthod et al. indicate that the rattling noise is produced by gear system vibroimpact, and the rattling noise shall be enhanced evidently with the increase of excitation in frequency and amplitude [12]. Doğan et al. found that the influencing factors of rattling noise in reducer are divided into geometric parameter of gear (such as module, number of teeth, helix angle, and backlash) and parameter of operating condition (such as angular acceleration and excitation frequency) [13]. Kadmiri et al. consider that the impact load due to gear rattling is also associated with coefficient of impact recovery (such as structure material and contact shape and lubrication) [14]. Presently, there is almost no document about research on impact and vibration of planetary gear transmission system.

Finite element model has more geometry information of the tooth, so its result is more precise and intuitive. Generally, finite element model is used to analyze the gear loaded tooth contact analysis (LTCA) [15, 16], load sharing between the gears [17], and time varying meshing stiffness calculation [18]. The finite element models for dynamic response are rare because they require significant computational effort [19].

The paper presents vibroimpact analytical model building method of planetary gear transmission system using the lumped parameter method, in which the Hertz contact theory is induced to describe impact of the gear pairs, the influence of operating condition of system on dynamic engaging force

TABLE 1: The planetary gear transmission system parameters.

Parameter	Sun gear	Planet wheel	Ring gear
Number of teeth	34	31	96
Face width (mm)	42	42	42
Module (mm)	3	3	3
Pressure angle (°)	28	28	28
Modification coefficient	-0.02	0.02	0.02
Mass	2.7	2.5	5.3
Moment of inertia	0.008	0.007	0.178

is calculated, and the system vibroimpact characteristics are analyzed under the conditions of heavy load and light load.

2. Analytical Model

2.1. Analytical Model for Planetary Gear Transmission. The planetary gear transmission system given in the paper is as shown in Figure 1(a), the symbol R is ring gear, S is sun gear, P is planet wheel, and C is planet carrier. The system is composed of a sun gear, 3 planet wheels, a planet carrier, and a ring gear. Sun gear is input part, adopting slender elastic axis for connection to function as elastic floating action. Ring gear is fixed; planet carrier is output end.

The basic parameters for experimental prototype are as shown in Table 1; its moment of inertia and mass are obtained by UG NX through 3-dimension solid modeling. The 3-dimension assembly model for transmission system is as shown in Figure 1(b).

2.2. Planetary Gear Transmission System Dynamic Model. 2K-H planetary gear transmission system dynamic model is shown in Figure 2, the support stiffness, torsional stiffness, and gear mesh stiffness are replaced by spring, planet carrier taken as origin of coordinates, horizontal direction taken as X -direction, and vertical direction taken as Y -direction, and θ is direction of torsional angle. The symbol K is stiffness in

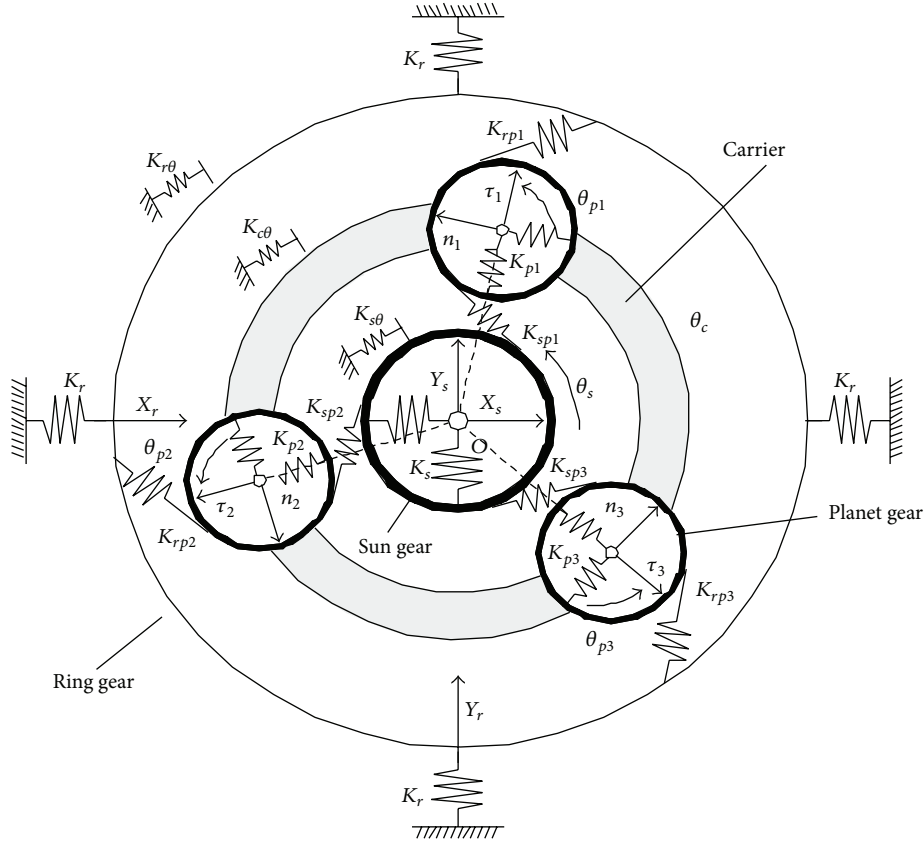


FIGURE 2: The planetary gear transmission system dynamic model.

the figure. K_s is support stiffness of sun gear, $K_{s\theta}$ is torsional stiffness of sun gear in model; planet gear adopts bearing for support; k_{pi} is support stiffness of number i ($i = 1, 2, 3$) planet wheel; K_r is support stiffness of ring gear, adopting four symmetric positions (on top, bottom, left, and right, resp.) to constrain annular gear structure. k_{spi} and k_{rpi} in model are gear mesh stiffness for sun gear and planet gear as well as planet gear and ring gear, respectively.

A number of simplifying assumptions were employed in establishing the gear transmission subsystem dynamic model through lumped parameter method:

- (1) The gear body and planet carrier are assumed to be rigid. The flexibilities of the gear teeth at each gear mesh interface are modeled by a spring having periodically time varying stiffness.
- (2) The engaging force between gears always exists along the gear line of action. Each support part's flexibility is included in the form of a linear spring, and the support stiffness is constant.
- (3) Planet gears are surrounding the central gear (including sun gear and planet carrier). Every planet gear has the same mass, moment of inertia, and support stiffness. Friction during gear engagement is neglected.
- (4) Each planet gear has the same meshing stiffness with the sun gear except for different phase positions. The

support stiffness of sun gear, ring gear, and planet carrier in all directions is the same.

- (5) The gear-shaft connections were assumed to be rigid, ignoring the stiffness of the connections and any consequent relative torsional motion between the shaft and gear hub.

Then in the system X and Y are transverse microdisplacement; θ is torsional microdisplacement. Supposing that all gears have degree of freedom along transverse and torsional directions, the generalized displacement vector of the system is as follows:

$$\{X\} = \{x_s, y_s, \theta_s, x_{p1}, y_{p1}, \theta_{p1}, \dots, x_r, y_r\}^T. \quad (1)$$

2.3. Engaging Force and Impact Force between Gear Pair. When load is large enough, the gear pair are always engaged and no contact loss happened, so engaging force generated on two tooth flanks and elastic deformation are in linear proportion. At this time, the gear pair stiffness is replaced by linear spring; the dynamic model for sun gear and planet gear is as shown in Figure 3. Both the torsion and transverse displacement of the gears have an effect on their engaging process, so all microdisplacements are translated to action

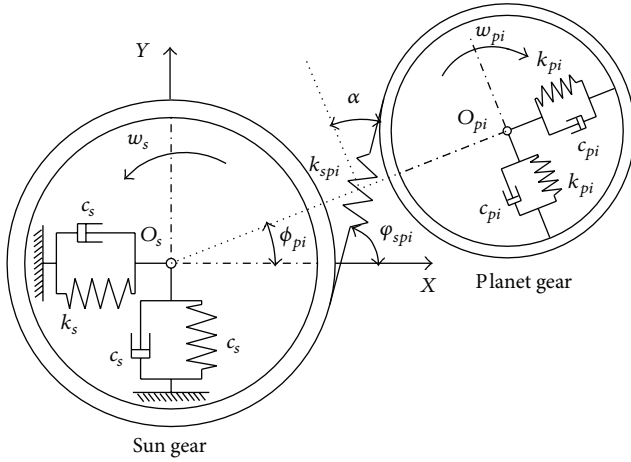


FIGURE 3: The dynamic model of sun gear and planet gear.

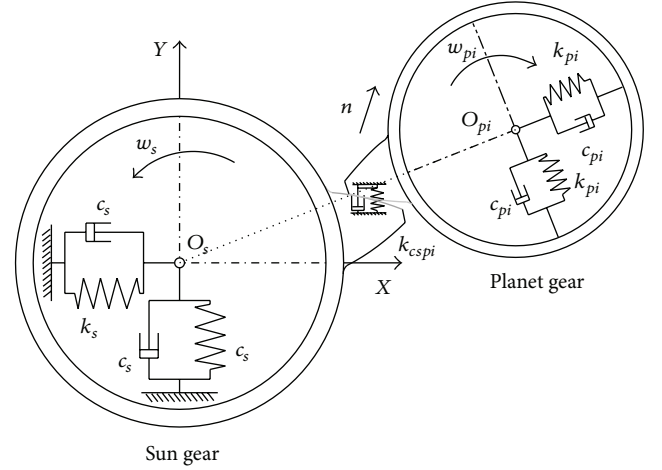


FIGURE 4: The vibroimpact model of sun gear and planet gear.

line of contact. When engaging spring compression is defined to be positive and its tension is defined to be negative, then

$$\begin{aligned} \delta_{spi} &= x_s \cos \varphi_{spi} + y_s \sin \varphi_{spi} + u_s - x_{pi} \sin \alpha \\ &\quad - y_{pi} \cos \alpha - u_{pi} - e_{spi}(t), \end{aligned} \quad (2)$$

where

$$\begin{aligned} \varphi_{spi} &= \phi_c - \alpha + \phi_{pi} + \frac{\pi}{2}, \\ u_s &= \theta_s r_s, \\ u_{pi} &= \theta_{pi} r_{pi}, \\ \phi_c &= \omega_c t, \end{aligned} \quad (3)$$

in which α is working pressure angle and ϕ_{pi} is phase angle ($\phi_i = 2\pi(i-1)/3$). r_s, r_{pi} are base circle radius of sun gear and planet gear; $e_{spi}(t)$ is engaging error.

Here, the engaging force is

$$F_{spi} = k_{spi} \delta_{spi} + c_{spi} \dot{\delta}_{spi}. \quad (4)$$

When transmission system load is light, the load is unable to make two tooth flanks maintain constant engaging, so the gear pair comes into instantaneous impact on two tooth flanks. Therefore, driven gear shall speed up in a second to separate from driving gear to reciprocate in such a way that the gear pair contact loss phenomenon appeared. In this process, the impact force is produced between the contacted gears. The paper describes elastic effect between gear teeth by Hertz contact mechanics. Under this condition, the dynamic model for sun gear and planet gear is as shown in Figure 4, in which the tooth flanks in contact between sun gear and planet gear are connected by contact spring and k_{cspi} is tooth flank contact stiffness.

In the gear engagement process, with the influence of errors and structure deformations, the direction of gear engaging force is not strictly along the theoretical action line. Since such errors and deformations are small enough,

here we suppose that the gear engaging force is still along theoretical action line, and the two gear teeth in contact shall be taken as two bodies in impact. Taking material damping into consideration, the generalized Hertz formula of the sun gear and planet gear is shown as the following forms:

$$F_{spi} = k_{cspi} \delta_{spi}^n + D_{cspi}(x) \dot{\delta}_{spi} \quad n = 1.5, \quad (5)$$

where δ is relative deformation of two bodies in contact and $\dot{\delta}$ is relative contact speed. Damping coefficient is $D(x) = \lambda x^n$, in which λ is hysteresis damping coefficient. k_{cspi} is Hertz stiffness in elasticity theory; it is dependent on material characteristic and radius of curvature, as shown in the following:

$$\begin{aligned} k_{cspi} &= \frac{4}{3\pi(h_1 + h_2)} \left[\frac{r_1 r_2}{r_1 + r_2} \right]^{1/2} \\ h_i &= \frac{1 - \nu_i^2}{\pi E_i}, \quad i = 1, 2, \end{aligned} \quad (6)$$

where r_1 and r_2 are sun gear and planet gear tooth profile radius of curvature, respectively, and E_i and ν_i are modulus of elasticity and Poisson's ratio.

The speed relation of hysteresis damping coefficient λ before and after impact according to energy relation and kinetic energy loss during impact is calculated based on Newton's coefficient of recovery e ,

$$\Delta T = \frac{1}{2} \bar{m} (v_{10} - v_{20})^2 (1 - e^2), \quad (7)$$

where $\bar{m} = m_1 m_2 / (m_1 + m_2)$.

In addition, impact is energy loss and indicated by

$$\Delta T = \oint D \dot{\delta} d\delta \approx 2 \int_0^{\delta_m} \lambda \delta^n \dot{\delta} d\delta = \frac{2}{3} \frac{\lambda}{k} \bar{m} (v_{10} - v_{20})^3. \quad (8)$$

Coefficient of recovery and hysteresis damping coefficient satisfy

$$\lambda = \frac{3}{4} \frac{k(1 - e^2)}{v_{10} - v_{20}}. \quad (9)$$

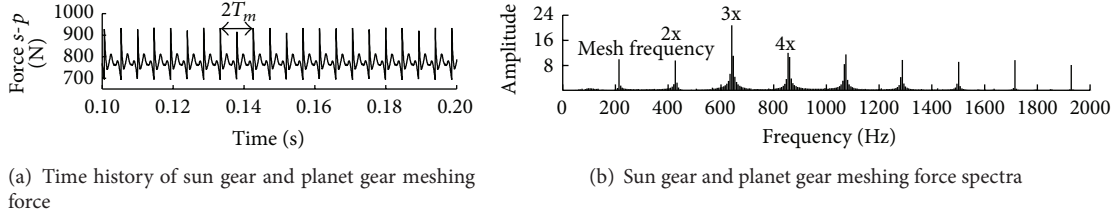


FIGURE 5: The dynamic force of sun gear and planet gear.

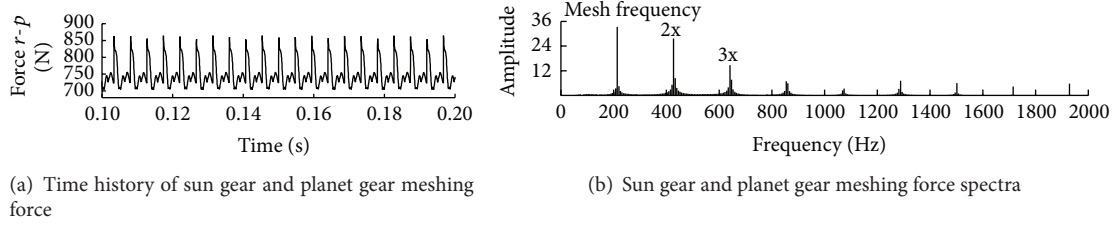


FIGURE 6: The dynamic force of ring gear and planet gear.

Contact force is equivalent to

$$f = k\delta^n \left(1 + \frac{3}{4} \frac{1 - e^2}{v_{10} - v_{20}} \delta \right). \quad (10)$$

The above-mentioned formula reveals the relation between contact force and coefficient of recovery and speed before and after impact.

2.4. Impact and Vibration Model for Planetary Gear Transmission System. Differential equation for system vibration is built based on stress condition of all parts

$$\begin{aligned} m_s \ddot{x}_s + c_s \dot{x}_s - \sum_{i=1}^3 F_{spi} \cos \varphi_{spi} + k_s x_s &= 0, \\ m_s \ddot{y}_s + c_s \dot{y}_s + \sum_{i=1}^3 F_{spi} \sin \varphi_{spi} + k_s y_s &= 0, \\ m_{spi} \ddot{u}_s + c_{\theta} \dot{u}_s + \sum_{i=1}^3 F_{spi} + k_{\theta} u_s &= \frac{T_{in}}{r_s}, \\ m_{pi} \ddot{x}_i - k_{pi} \delta_{pix} - F_{spi} \sin \alpha + F_{rpi} \sin \alpha &= 0, \\ m_{pi} \ddot{y}_i - k_{pi} \delta_{piy} - F_{spi} \cos \alpha - F_{rpi} \cos \alpha &= 0, \\ m_{eq,pi} \ddot{u}_i - F_{rpi} + F_{spi} &= 0, \\ m_{eqc} \ddot{u}_c + \sum_{i=1}^N c_{pi} \delta_{cpiy} + c_{cu} \dot{u}_c + \sum_{i=1}^N k_{pi} \delta_{cpiy} + k_{cu} u_c &= \frac{T_{out}}{r_c}, \end{aligned}$$

$$m_r \ddot{x}_r + c_r \dot{x}_r - \sum_{i=1}^3 F_{rpi} \cos \varphi_{rpi} + k_r x_r = 0,$$

$$m_r \ddot{y}_r + c_r \dot{y}_r + \sum_{i=1}^3 F_{rpi} \sin \varphi_{rpi} + k_r y_r = 0,$$

$$m_{rpi} \ddot{u}_r + c_{r\theta} \dot{u}_r + \sum_{i=1}^3 F_{rpi} + k_{r\theta} u_r = 0,$$

(11)

where m_{spi} is equivalent mass of sun gear and number i planet gear, $m_{spi} = \bar{m}_s \bar{m}_{pi} / (\bar{m}_s + \bar{m}_{pi})$, $\bar{m}_s = I_s / R_s^2$, $\bar{m}_g = I_{pi} / R_{pi}^2$, m_{pi} is mass of planet gear, m_s is mass of sun gear, and m_r is mass of ring gear.

3. Dynamic Characteristic of System under the Action of Large Load

3.1. Engaging Force of System. When the load act on the gear train is heavy, the tooth flanks of gear pair stay in contact all the time; the dynamic load of system is calculated at the speed of 500 r/min and under the load of 500 N·m.

The dynamic force of sun gear and planet gear is as shown in Figure 5(a), it is observed that dynamic load shows cyclical variation, its cycle is T_m (time of the mesh cycle), the average value of dynamic load is 774 N, and the amplitude in fluctuation is 168 N. As shown in Figure 5(b), the main frequency component in dynamic load of sun gear and planet gear is engaging frequency (212 Hz), 2-multiple-frequency, 3-multiple-frequency, and 4-multiple-frequency components, in which 3-multiple frequency component is the highest in energy.

The dynamic force of planet gear and ring gear is as shown in Figure 6(a); we can observe that the average value of dynamic load is 750 N; the amplitude in fluctuation is 118 N. As shown in Figure 6(b), the main frequency component in

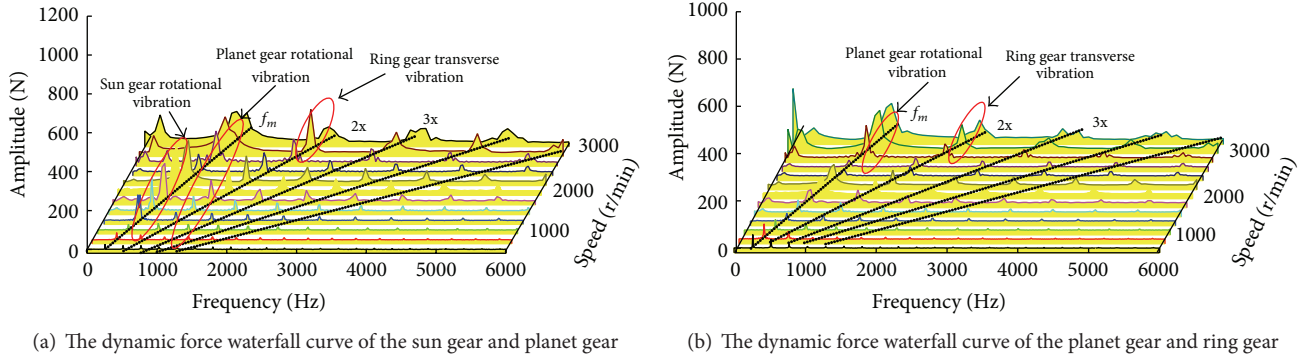


FIGURE 7: The dynamic force waterfall curve of the sun gear and planet gear.

dynamic load is engaging frequency, 2-multiple frequency, and 3-multiple frequency component, in which engaging frequency is the highest in energy.

3.2. Load Spectrum of System under Continuous Operating Condition. The vibration and excitation of planetary gear transmission system are composed of engaging frequency and multiple frequency; in addition, the relation between excitation component and natural frequency of transmission system also has direct effect on vibration amplitude. The dynamic response of gear box is as shown in Figure 7, in which f_m is engaging frequency. Since engaging frequency and multiple frequency components are linear proportion with the rotating speed, therefore, all harmonic components in excitation of gear are in radial distribution. The engaging frequency of dynamic load of sun gear and planet gear appears as obvious peak value around natural frequency (412 Hz, there are two orders of repetition frequency; the corresponding speed is 706 r/min) of sun gear rotational vibration. Given engaging frequency component from 2500 r/min to 3000 r/min and second harmonic component of 1500 r/min, under the action of third harmonic at 1000 r/min, there are the highest peak appearing around natural frequency of planet gear rotational vibration (889 Hz, there are three repetition frequencies, 919 Hz) and rotation vibration (1046 Hz) of planet carrier, in which 3000 r/min engaging frequency component is the highest in peak value. There is also peak value around natural frequency of ring gear transverse vibration (1791 Hz) under the action of 2800 r/min of second harmonic component.

Although vibration of parametric excitation of the gear system is linear matter, the dynamic load frequency components are complex due to coupled effect of the time varying mesh stiffness and the contact force of tooth profile. Meanwhile, different speed shall have a direct effect on excitation frequency component. In order to reveal the influence of rotating speed on fluctuation in dynamic load of bearing, the 1st harmonics variations of F_{spi} and F_{rpi} have been calculated within the range of the main operating speed (500 r/min~3000 r/min) as shown in Figure 8.

The first-order harmonic component variation of engaging force is divided into three sections, namely a, b, and c. The first section is from 500 r/min to 1050 r/min, F_{sp} and

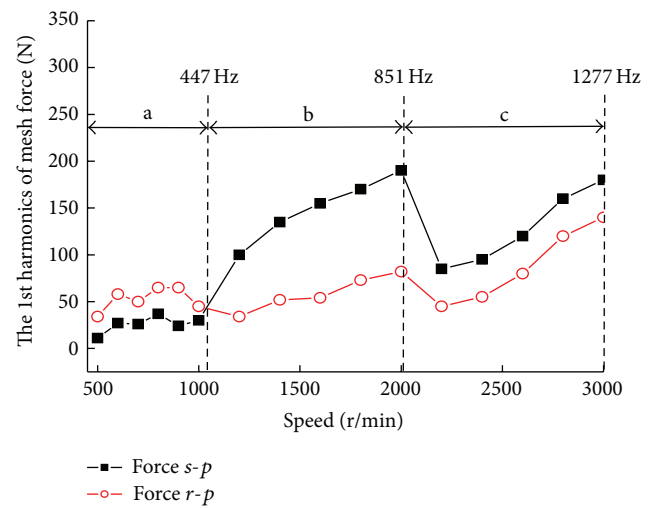


FIGURE 8: The dynamic force first-order harmonic component of ring gear and planet gear under different speed.

F_{rp} increased by degrees with the increase of speed, and this section only contains the first-order nature frequency of sun gear torsional vibration. However, accompanied by trend of fluctuation, F_{sp} is much higher than F_{rp} in speeding up in the section, since the torsional vibration of sun gear has a direct effect on engagement between sun gear and planet gear, and then the component of the dynamic load F_{sp} to approach F_{rp} , till they are identical at 1050 r/min; the second section is from 1050 r/min to 2000 r/min, in which the numbers of system natural frequency are added; there are planet gear transverse vibration (889 Hz, 919 Hz), planet carrier torsional vibration (1046 Hz). All the vibration modes have a direct effect on engagement of sun gear and planet gear, accordingly, so F_{sp} is increased to a great extent in the section. Since sun gear torsional vibration does not have a direct effect on engagement of ring gear and planet gear, F_{rp} experienced a process of gradual decrease at the beginning of the third section. Then insignificant increase happened to F_{rp} due to the number of system vibration modes being decreased, but only ring gear transverse vibration (1791 Hz).

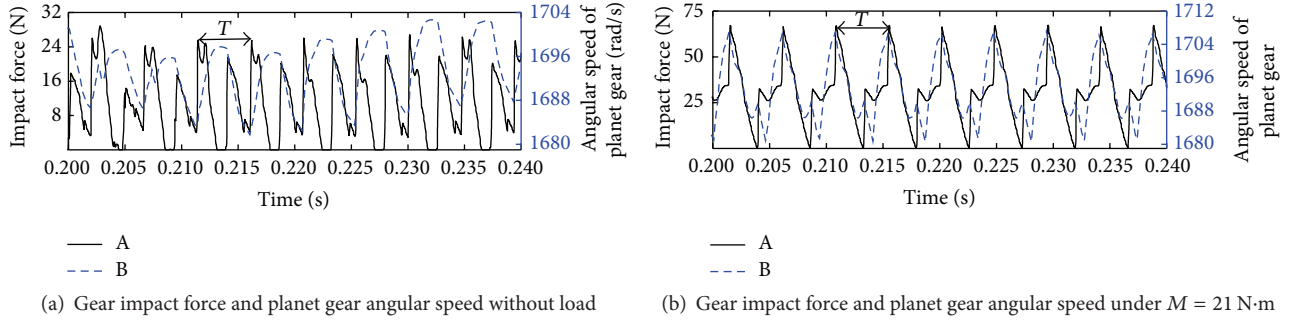


FIGURE 9: The dynamic impact force under different load.

4. Impact and Vibration Characteristic of System under Light Load

4.1. Influence of Load on Impact Force of Gears. The research of gear system vibroimpact does not take account of structural permanent deformation, but the process for gear from separated to contact is considered. With effect of relative velocity, the gear system is inevitably to bring impact between gear teeth of the driving and driven gear; then large impulsive load must be generated.

At the condition of the speed being 500 r/min and the load being light and gear contact force being as shown in Figure 9, in which curve A is time domain history of impact force and B is time domain history of angular speed of planet gear, it is observed that the impact force between planet gear and ring gear under the condition of load being 0 is still showing cyclical fluctuation. There is disengagement (the gears are in separate state) appearing in every cycle, when the gear recontact; the impact force is increased rapidly. During the time of gears disengagement, the impact force is 0 as a result of absence of external force, so the planet gear angular speed remains constant in a second.

In addition, we can see that there are two obvious peak values in every cycle, so the second harmonic component is main frequency component of impact force. With the increase of load, the time for disengagement shall gradually shorten. When load is 21 N·m, the gear pair is in critical state between normal engagement and disengagement, as shown in Figure 9(b). It is observed that the impact force and angular speed of planet gear also show cyclic variation, and only one point on impact forces is intersected with x -axis in every cycle (namely, it is equal to 0), and the angular speed of planet gear only shows inflection point in the position. It is also found that there is only one larger peak value in one cycle, so engaging frequency component is changed to be the main frequency component of contact force. The variation of impact force shows strong nonlinear feature; the load is not only to affect the average value of the force and amplitude in fluctuation, but also to have a direct effect on frequency components.

The influence of load on vibroimpact of planetary gear transmission system is shown in Figure 10. The gear engagement can be divided into two stages with change of the load;

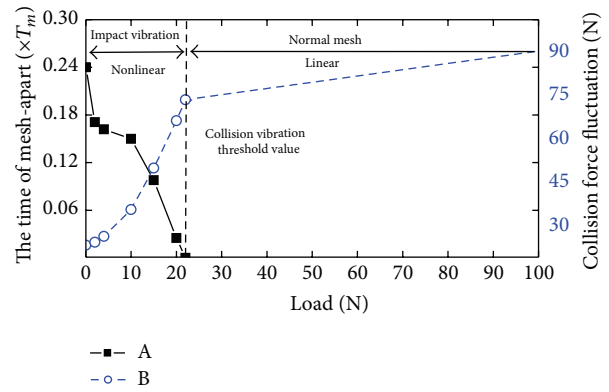


FIGURE 10: The effect of the load on gear vibroimpact characteristics.

the first stage is vibroimpact stage, in which the impact is larger than planet gear moment of retardation:

$$|m_{eq,pi}\ddot{u}_i| \geq T_{drag}, \quad (12)$$

where T_{drag} is moment of retardation dependent on driven gear damping force and load moment.

At this point, gear shall start vibroimpact of engagement, disengagement, and reengagement [20]. In general, time for gear to disengage shall gradually shorten with the increase of load. When load is smaller, since time for disengagement is longer, the time is $0.24T$ under the load which is 0. Then the load is effectively to reduce the speed of driven gear after impact. With the increase of load, the load shall increase relative impact speed of gear and impact force, so the disengagement time is shortened slowly. When load increases again, time for disengagement shall shorten rapidly again; gear contact force and amplitude in fluctuation show second function quadratic function curve change.

When load is up to threshold value (in the paper it is 21 N·m), gear engagement shall enter into normal engagement, in which gear shall not disengage again. With the increase of load, amplitude in fluctuation of engaging force shall show linear increase, but its increasing speed is reduced compared with that in vibroimpact stage.

4.2. Influence of Rotating Speed on Impact Force of Gear. The influence of rotating speed on engagement of planetary

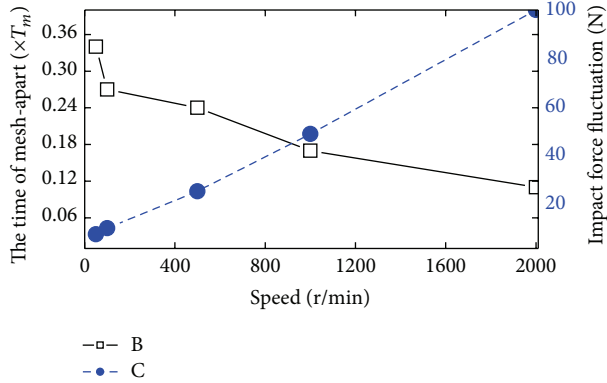


FIGURE 11: The effect of the input speed on gear vibroimpact characteristics.

gear transmission system is shown in Figure 11. When the load is 0, with the increase of input rotating speed, time for gear to disengage is decreased gradually. At lower rotating speed, the engaging period is longer and the relative rotating speed of gear is lower, so the impact force is smaller and gear shall have longer time to maintain disengagement after impact for one time. When rotating speed is 50 r/min, the time for disengagement is $0.34T$. As the increase of rotating speed, the relative rotating speed of gear is increased, and the impact force and collisional deformation will gradually increase; therefore, the contact time for two tooth flanks is longer, the time for disengagement shall be shorter, when rotating speed is 2000 r/min, and the time for disengagement is reduced to $0.11T$.

In the process of speed change, since torsional direction of planet gear is unconstrained, with torsional rigidity of sun gear being much smaller than contact rigidity, therefore, the influence of constraint elasticity of two tooth flanks on coefficient of recovery shall be very small; at this time, the impact of gear can be assumed as free body [21], with small influence of external elastic constraint on fluctuation of impact force; therefore, the inherent characteristic of system shall have direct effect on variation in impact force; the amplitude in fluctuation of impact force shall show linear increase with the increase of rotating speed; in addition, it is also observed that threshold value of impact and vibration of gear shall also show linear increase with the increase of speed.

4.3. Influence of Rotating Speed on Floating Trajectory of Center Gear. The floating trajectory of sun gear and ring gear at different input speed under the condition of the load is 0 as shown in Figure 12. We found that the floating range of sun gear increases as the speed increases; it is also subjected to the influence of the system inherent mode of vibration. The floating range at the 1000 r/min is the largest, because the third harmonic component at 1000 r/min shall meet the frequency of the planet carrier torsional vibration. There is no obvious resonance of ring gear within the range of rotating speed change, so the ring gear floating range shall monotonously increase with the increase of rotating speed.

When the gears tooth are contacted, the impact force which is produced by different speed between two faces of gear teeth is smaller, and the impact energy is also small and will be rapidly consumed; then the driven gear starts to speed down to give rise to second impact, so the system shows periodical vibration. Thus, when the rotating speed is 100 r/min, with effect of the gear impact, every impact between gears shall make floating trajectory generate larger deviation at instant. Therefore, the floating trajectory of center gear is regular and present Z_r (Z_r is the number of the ring gear teeth) leafy curves. When the speed increased, the difference in speed between gears also increases and the impact force shall gradually increase too; the system shall intensify vibroimpact. When rotating speed is 300 r/min, the leafy curve in floating trajectory of sun gear shall show heterogeneous distribution; the sun gear trajectory is showing change trend to quasi periodical curve and the floating trajectory of ring gear still being regular. When rotating speed is 1000 r/min, sun gear and planet gear show obviously vibroimpact; accordingly, the floating trajectory of sun gear is present noncyclic change and floating trajectory of ring gear showing regular radial curve. At this point, the sun gear generates beat vibration due to effect of the natural frequency of the sun gear torsion. At high speed, sun gear and planet gear show repeatedly impact of engagement and disengagement from time to time without regular pattern; the system vibration is changed to a typical chaos vibration. When rotating speed is 2000 r/min, the floating trajectory of sun gear is changed into noncyclic curve; the floating trajectory of ring gear is changed into radial curve.

When input rotating speed is 2000 r/min, the impact force between sun gear and planet gear shall increase; the system shows subharmonic resonance phenomenon, the time history of the sun gear microdisplacement along x -direction as shown in Figure 13(a). As frequency spectrum shown in Figure 13(b), the components around engaging frequency of the system are disorder in distribution, and the $1/2$ subharmonic component appeared. This phenomenon in gear system is also discussed in [9], in which it is verified existence by experiment.

5. Conclusions

This paper presents a novel modeling method of planetary gear system, in which the Hertz contact theory is induced to describe impact of the gear pairs under the condition of the high speed and light load. The vibroimpact characteristics of the system are analyzed; some interesting conclusions are obtained as follows:

- (1) As input speed continuously increased under large load condition, the harmonic components of dynamic mesh load show radial distribution. The dynamic load obvious fluctuation appeared when harmonic components are around natural frequency of system.
- (2) Under the light load condition, the vibroimpact phenomenon happened in planetary gear system. With increase of load, the main frequency component of impact force between the gears is changed

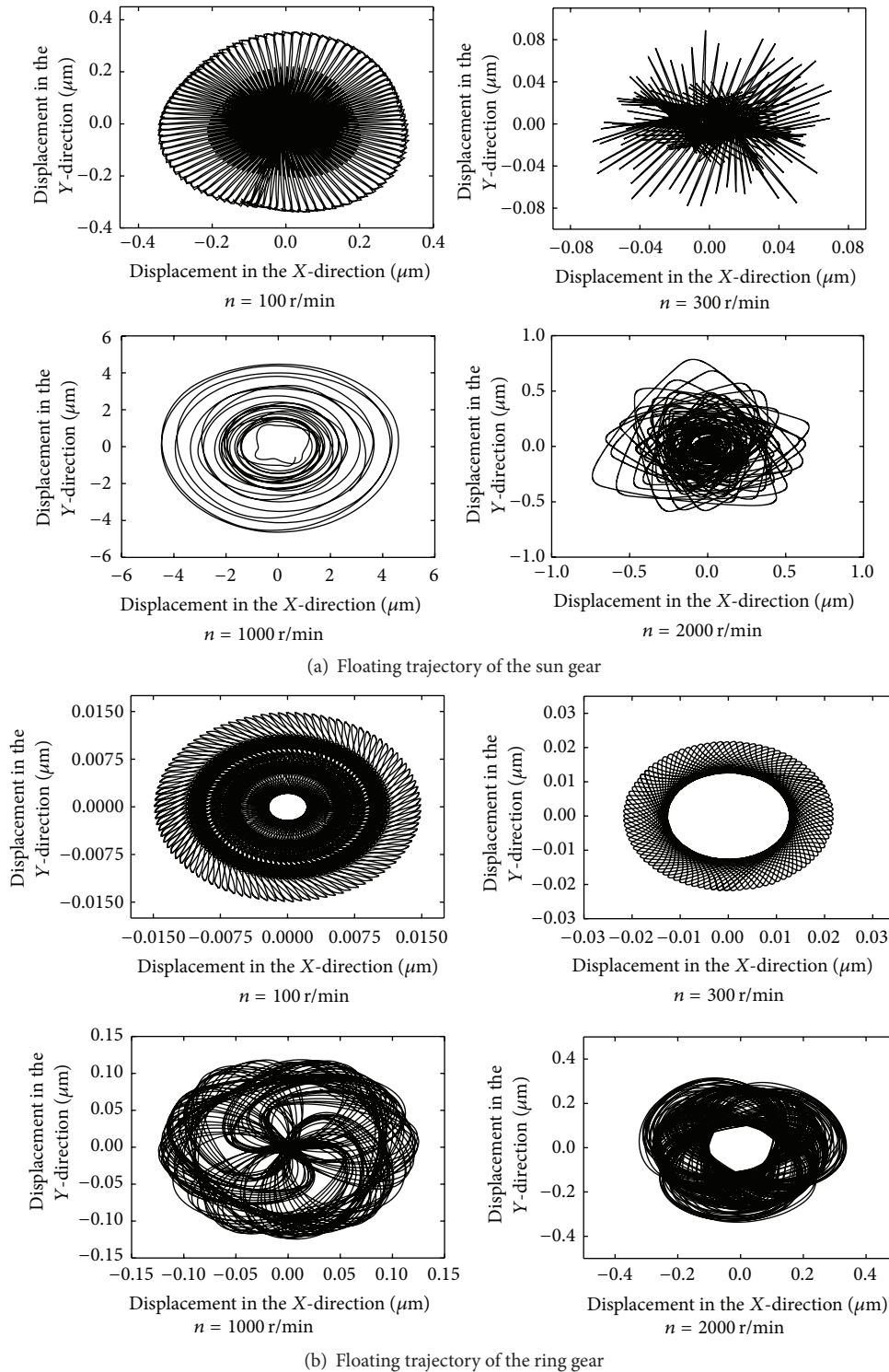


FIGURE 12: Floating trajectory of center gear at various speed.

from the second harmonic component into engaging frequency component. Meanwhile, the time of gear mesh-apart is decreased continuously, till load is big enough to make gear system engaged normally.

(3) With increasing of input speed under the light load condition, the gear mesh-apart time shortens gradually; the relative speed of the gear pairs is increased, so vibroimpact of the system increased in intensity, and

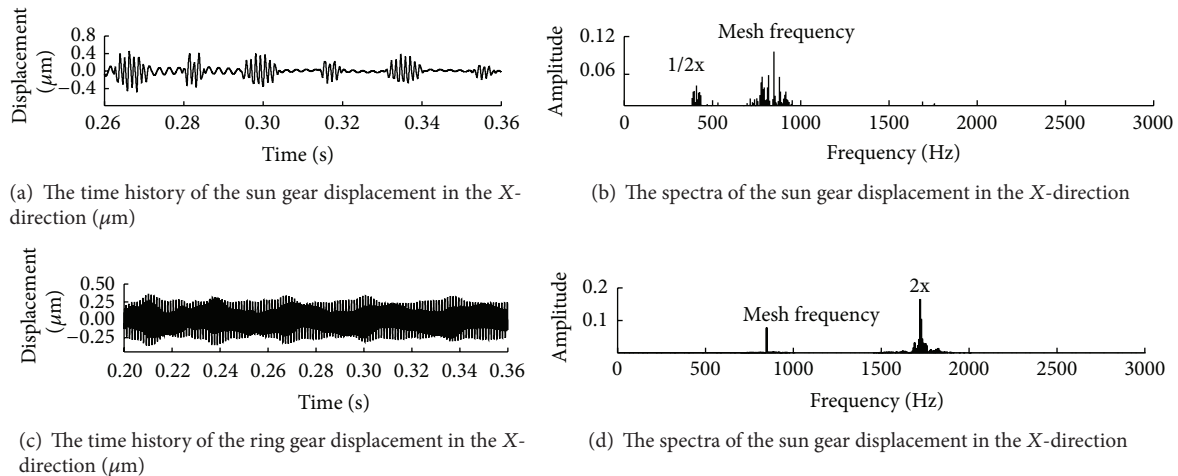


FIGURE 13: Time history and frequency spectrum for displacement of center gear along x direction at 2000 r/min.

amplitude of impact force between the gears increased linearly.

- (4) With increasing of input speed, the floating trajectory of the center gear is changed from regular leafy curves to the irregularly curves. Nonlinear feature of the center gear displacement can be observed at 2000 r/min.

Conflict of Interests

The authors declare that there is no conflict of interests regarding the publication of this paper.

Acknowledgments

Thanks must be given to Xinjiang University for giving the authors a good surrounding and Natural Science Foundation of Xinjiang Province (2014211B004, XJEDU2014S009, and BS130120) for giving the authors a good financial backing to finish the most important part of this research.

References

- [1] T. Sun and H.-Y. Hu, "Nonlinear dynamics of a planetary gear system with multiple clearances," *Mechanism and Machine Theory*, vol. 38, no. 12, pp. 1371–1390, 2003.
- [2] W.-C. Ding and J.-H. Xie, "Advances of research on bifurcations and chaos in vibro-impact system," *Advances in Mechanics*, vol. 32, no. 4, pp. 513–524, 2004.
- [3] H. J. Dong, Q. T. Chen, and Y. W. Shen, "On high speed impact and low speed contact in gear rattling," *China Mechanical Engineering*, vol. 17, no. 10, pp. 1068–1070, 2006.
- [4] A. Saada and P. Velex, "An extended model for the analysis of the dynamic behavior of planetary trains," *Journal of Mechanical Design*, vol. 117, no. 2, pp. 241–247, 1995.
- [5] D. Qin, M. Tian, and J. Yang, "Study on dynamic characteristics of gear transmission system of wind generator under varying wind load," *Acta Energetica Sinica*, vol. 33, no. 2, pp. 190–196, 2012.
- [6] Z. H. Bu, G. Liu, and L. Wu, "Natural characteristics analysis on herringbone planetary gear trains with slide bearing support," *Chinese Journal of Mechanical Engineering*, vol. 47, no. 1, pp. 80–88, 2011.
- [7] Y. Guo and R. G. Parker, "Dynamic analysis of planetary gears with bearing clearance," *Journal of Computational and Nonlinear Dynamics*, vol. 7, no. 4, Article ID 041002, 2012.
- [8] L. Walha, T. Fakhfakh, and M. Haddar, "Nonlinear dynamics of a two-stage gear system with mesh stiffness fluctuation, bearing flexibility and backlash," *Mechanism and Machine Theory*, vol. 44, no. 5, pp. 1058–1069, 2009.
- [9] A. Kahraman and G. W. Blankenship, "Interactions between commensurate parametric and forcing excitations in a system with clearance," *Journal of Sound and Vibration*, vol. 194, no. 3, pp. 317–336, 1996.
- [10] T. Sun, Y. W. Shen, and Z. M. Sun, "Study on nonlinear dynamic behavior of planetary gear train solution and dynamic behavior analysis," *Chinese Journal of Mechanical Engineering*, vol. 38, no. 3, pp. 11–15, 2002.
- [11] T. Eritenel and R. G. Parker, "Computational nonlinear vibration analysis of gear pairs using a three-dimensional model," in *Proceedings of the ASME International Design Engineering Technical Conferences and Computers and Information in Engineering Conference*, pp. 149–165, San Diego, Calif, USA, September 2009.
- [12] M. Barthod, B. Hayne, J.-L. Tébeca, and J.-C. Pinb, "Experimental study of dynamic and noise produced by a gearing excited by a multi-harmonic excitation," *Applied Acoustics*, vol. 68, no. 9, pp. 982–1002, 2007.
- [13] S. N. Doğan, J. Ryborz, and B. Bertsche, "Design of low-noise manual automotive transmissions," *Proceedings of the Institution of Mechanical Engineers Part K: Journal of Multi-body Dynamics*, vol. 220, no. 2, pp. 79–95, 2006.
- [14] Y. Kadmiri, E. Rigaud, J. Perret-Liaudet, and L. Vary, "Experimental and numerical analysis of automotive gearbox rattle noise," *Journal of Sound and Vibration*, vol. 331, no. 13, pp. 3144–3157, 2012.
- [15] S. Li, "Effects of machining errors, assembly errors and tooth modifications on loading capacity, load-sharing ratio and transmission error of a pair of spur gears," *Mechanism and Machine Theory*, vol. 42, no. 6, pp. 698–726, 2007.

- [16] S. Li, "Effects of misalignment error, tooth modifications and transmitted torque on tooth engagements of a pair of spur gears," *Mechanism and Machine Theory*, vol. 83, pp. 125–136, 2015.
- [17] A. Singh, "Application of a system level model to study the planetary load sharing behavior," *Journal of Mechanical Design*, vol. 127, no. 5, pp. 457–476, 2005.
- [18] X. Zhou, Y. Shao, Y. Lei, and M. Zuo, "Time-varying meshing stiffness calculation and vibration analysis for a 16DOF dynamic model with linear crack growth in a pinion," *Journal of Vibration and Acoustics*, vol. 134, no. 1, Article ID 011011, 2012.
- [19] C. G. Cooley, R. G. Parker, and S. M. Vijayakar, "A frequency domain finite element approach for three-dimensional gear dynamics," *Journal of Vibration and Acoustics*, vol. 133, no. 4, Article ID 041004, 9 pages, 2011.
- [20] R. F. Li and J. Wang, *System of the Gear Vibration Theory*, Science Press, 1997.
- [21] D. P. Jin and H. Y. Hu, *Vibro-Impact and Control*, Science Press, 2007.

Research Article

Structural Damage Detection by Using Single Natural Frequency and the Corresponding Mode Shape

Bo Zhao, Zili Xu, Xuanen Kan, Jize Zhong, and Tian Guo

State Key Laboratory for Strength and Vibration of Mechanical Structures, Xi'an Jiaotong University, Xi'an 710049, China

Correspondence should be addressed to Zili Xu; zlxu@mail.xjtu.edu.cn

Received 17 August 2015; Revised 29 October 2015; Accepted 16 November 2015

Academic Editor: Juan P. Amezcua-Sanchez

Copyright © 2016 Bo Zhao et al. This is an open access article distributed under the Creative Commons Attribution License, which permits unrestricted use, distribution, and reproduction in any medium, provided the original work is properly cited.

Damage can be identified using generalized flexibility matrix based methods, by using the first natural frequency and the corresponding mode shape. However, the first mode is not always appropriate to be used in damage detection. The contact interface of rod-fastened-rotor may be partially separated under bending moment which decreases the flexural stiffness of the rotor. The bending moment on the interface varies as rotating speed changes, so that the first- and second-modal parameters obtained are corresponding to different damage scenarios. In this paper, a structural damage detection method requiring single nonfirst mode is proposed. Firstly, the system is updated via restricting the first few mode shapes. The mass matrix, stiffness matrix, and modal parameters of the updated system are derived. Then, the generalized flexibility matrix of the updated system is obtained, and its changes and sensitivity to damage are derived. The changes and sensitivity are used to calculate the location and severity of damage. Finally, this method is tested through numerical means on a cantilever beam and a rod-fastened-rotor with different damage scenarios when only the second mode is available. The results indicate that the proposed method can effectively identify single, double, and multiple damage using single nonfirst mode.

1. Introduction

Damage in a structure produces variations in its geometric and physical properties, which can result in changes in its natural frequencies and mode shapes. In the last years, several researchers have developed many damage detection methods based on dynamic parameters. Fan and Qiao [1] and Jassim et al. [2] presented comprehensive reviews on modal parameters-based damaged identification methods. The most commonly used methods of damage detection use changes of natural frequencies and mode shape directly. Messina et al. [3] proposed a correlation coefficient termed the Multiple Damage Location Assurance Criterion (MDLAC) by introducing two methods for estimating the location and size of defects in a structure. Kim and Stubbs [4] proposed a single damage indicator (SDI) method to locate and quantify a single crack in slender structures by using changes in a few natural frequencies. Xu et al. [5] proposed an iterative algorithm to identify the locations and extent of damage in beams only using the changes in their first several natural frequencies. However, the natural frequency-based

methods are often ill-posed even without noise. Shi et al. [6] extended the Multiple Damage Location Assurance Criterion (MDLAC) by using incomplete mode shapes instead of natural frequencies. Pawar et al. [7] proposed a method of damage detection using Fourier analysis of mode shapes and neural networks, which is limited to detecting damage of beams with clamped-clamped boundary condition. Another important class of damage detection methods is based on flexibility matrix change between damaged and undamaged structures. Pandey and Biswas [8] first proposed the method based on change in flexibility matrix to detect structural damage. Yang and Liu [9] made use of the eigenparameter decomposition of structural flexibility matrix change and approached the location and severity of damage in a decoupled manner. Bernal and Gunes [10] use the flexibility proportional matrix method to quantify damage without the use of a model. Tomaszewska [11] investigated the effect of statistical errors on damage detection based on structural flexibility matrix and mode shape curvature. Li et al. [12] used the generalized flexibility instead of original flexibility matrix to detect structural damage, which can significantly reduce the effect

of truncating higher-order modal parameters. Masoumi et al. [13] proposed a new objective function formed by using generalized flexibility matrix. Then, imperialist competitive algorithm was used in damage identification. Yan and Ren [14] derived a closed form of the sensitivity of flexibility based on the algebraic eigensensitivity method. Montazer and Seyedpoor [15] introduced a new flexibility based damage index for damage detection of truss structures.

Although the generalized flexibility matrix based damage detection approach can precisely detect the location and severity of damage by using only the first natural frequency and the corresponding mode shape, there are still many limitations in these methods. One limitation lies in the damage detection of rod-fastened-rotor of heavy duty gas turbine. The flexural stiffness of the interface decreases when some zones of the contact interface are separated with bending moment on the rotor [16]. Flexural stiffness of interface in a rod-fastened-rotor induced by bending moment is different in first and second critical speed, because bending moment distribution varies as rotating speed changes. Therefore, only the second-modal parameters are available for the damage detection of rod-fastened-rotor in the second critical speed.

In this paper, a structural damage detection method based on changes in the flexibility matrix only using single natural frequency and the corresponding mode shape is presented. Firstly, restricted by the first several mode shapes, the system is updated. The flexibility matrix of updated system can be obtained by using non-first-modal parameters of original system. Then, sensitivity of flexibility of the updated system to damage is derived. Taking advantage of generalized flexibility matrix, which can considerably reduce the error caused by truncating higher-order modal parameters, the location and severity of the damage are calculated. Finally, two numerical examples for a cantilever beam and a rod-fastened-rotor are used to illustrate the effectiveness of the proposed method, when only the second natural frequency and the corresponding mode shape are available.

2. Structural Damage Detection Method

2.1. Structural System Updating Method. The differential equation governing the free vibration of a linear, undamped structural system can be expressed as

$$\mathbf{M}\ddot{\mathbf{x}} + \mathbf{K}\mathbf{x} = 0, \quad (1)$$

where \mathbf{M} is the global mass matrix, \mathbf{K} is the global stiffness matrix, and \mathbf{x} is the displacement vector. When the degree of freedom for the system is n , the eigenvalue problem can be written in the form

$$\mathbf{K}\Phi_i = \lambda_i \mathbf{M}\Phi_i, \quad i = 1, 2, \dots, n, \quad (2)$$

where λ_i and Φ_i are the i th eigenvalue and eigenvector, respectively. Restricting the system by the first r mode shapes,

$$\Phi_i^T \mathbf{M}\mathbf{x} = 0, \quad i = 1, 2, \dots, r. \quad (3)$$

Mode shape matrix, mass matrix, and displacement vector can be partitioned as

$$\begin{aligned} \Psi &= \begin{bmatrix} \Psi_{rr} & \Psi_{rs} \\ \Psi_{sr} & \Psi_{ss} \end{bmatrix}, \\ \mathbf{M} &= \begin{bmatrix} \mathbf{M}_{rr} & \mathbf{M}_{rs} \\ \mathbf{M}_{sr} & \mathbf{M}_{ss} \end{bmatrix}, \\ \mathbf{x} &= \begin{bmatrix} \mathbf{x}_r \\ \mathbf{x}_s \end{bmatrix}, \end{aligned} \quad (4)$$

where the i th column of Ψ is the i th eigenvector Φ_i . Substituting (4) into (3) yields

$$\begin{bmatrix} \Psi_{rr}^T & \Psi_{sr}^T \end{bmatrix} \begin{bmatrix} \mathbf{M}_{rr} & \mathbf{M}_{rs} \\ \mathbf{M}_{sr} & \mathbf{M}_{ss} \end{bmatrix} \begin{bmatrix} \mathbf{x}_r \\ \mathbf{x}_s \end{bmatrix} = 0. \quad (5)$$

Expanding (5) yields $\mathbf{x}_r = -(\Psi_{rr}\mathbf{M}_{rr} + \Psi_{rs}\mathbf{M}_{sr})^{-1}(\Psi_{rr}\mathbf{M}_{rs} + \Psi_{rs}\mathbf{M}_{ss})\mathbf{x}_s$; then the relationship between \mathbf{x}_s and \mathbf{x} is

$$\mathbf{x} = \mathbf{D}\mathbf{x}_s, \quad (6)$$

where $\mathbf{D} = \begin{bmatrix} \mathbf{TR} \\ \mathbf{I} \end{bmatrix}$, in which $\mathbf{TR} = -(\Psi_{rr}\mathbf{M}_{rr} + \Psi_{rs}\mathbf{M}_{sr})^{-1}(\Psi_{rr}\mathbf{M}_{rs} + \Psi_{rs}\mathbf{M}_{ss})$. Substituting (6) into original free vibration differential equation (1) yields

$$\mathbf{M}\mathbf{D}\ddot{\mathbf{x}}_s + \mathbf{K}\mathbf{D}\mathbf{x}_s = 0. \quad (7)$$

Left-multiplying (7) by \mathbf{D}^T yields the updated free vibration differential equation

$$\mathbf{M}^u \ddot{\mathbf{x}}_s + \mathbf{K}^u \mathbf{x}_s = 0. \quad (8)$$

The mass and stiffness matrix of the updated system can be obtained by

$$\begin{aligned} \mathbf{M}^u &= \mathbf{D}^T \mathbf{M} \mathbf{D}, \\ \mathbf{K}^u &= \mathbf{D}^T \mathbf{K} \mathbf{D}. \end{aligned} \quad (9)$$

The relationship between the updated and the original modal parameters can be described by

$$\begin{aligned} \lambda_i^u &= \lambda_{i+r}, \\ \Phi_i^u &= \mathbf{D}^{-1} \Phi_{i+r}, \\ i &= 1, 2, \dots, n-r, \end{aligned} \quad (10)$$

where λ_i^u and Φ_i^u are the i th eigenvalue and eigenvector of the updated system, respectively. \mathbf{D}^{-1} is a generalized inverse of \mathbf{D} , because \mathbf{D} is not a square matrix. Thus, a new $n-r$ dimension system based on the original n dimension system is established.

The complete mode shapes are difficult to obtain, particularly when a limited number of sensors are available. However, incomplete mode shape data can be expanded to

complete mode shapes by mode shape expansion technique. The expansion method in [17] is

$$\Phi_j = \begin{bmatrix} \mathbf{I} \\ -(\mathbf{K}_{ss} - \lambda_j \mathbf{M}_{ss})^{-1} (\mathbf{K}_{sm} - \lambda_j \mathbf{M}_{sm}) \end{bmatrix} \Phi_{mj}, \quad (11)$$

where Φ_{mj} is measured degrees of mode shape Φ_j and \mathbf{K}_{ss} , \mathbf{K}_{sm} and \mathbf{M}_{ss} , \mathbf{M}_{sm} are submatrix of global stiffness and mass matrix, respectively.

2.2. Structural Damage Detection Based on Generalized Flexibility Matrix Method. In this method, only the decrease in structure stiffness due to damage is considered. Changes in mass property are ignored. The damage parameters are denoted by d_i , which stands for damage extent of the i th element. The decrease of global stiffness matrix $\Delta \mathbf{K}$ can be expressed as a sum of each elemental stiffness matrix multiplied by damage parameters [9]; that is,

$$\Delta \mathbf{K} = \mathbf{K}_a - \mathbf{K}_d = \sum_{i=1}^e d_i \mathbf{K}_{ai}, \quad (12)$$

where \mathbf{K}_a is the global stiffness matrix of undamaged structure, \mathbf{K}_d is the global stiffness matrix of damaged structure, and \mathbf{K}_{ai} is the i th elemental stiffness matrix positioned within the global matrix for undamaged structure, and e is the number of elements. If the i th element is undamaged, the value of d_i is zero. The value of d_i is a nonnegative number less than one. Differentiating (12) with respect to d_i leads to

$$\frac{\partial \mathbf{K}_d}{\partial d_i} = -\mathbf{K}_{ai}. \quad (13)$$

According to the definition of flexibility and stiffness matrix, they satisfy the following relationship:

$$\mathbf{F}_d^u \mathbf{K}_d^u = \mathbf{I}, \quad (14)$$

where \mathbf{F}_d^u is the flexibility matrix of updated system for the damaged structure, \mathbf{K}_d^u is the stiffness matrix of updated system for the damaged structure, and \mathbf{I} is the identity matrix. Differentiating (14) with respect to d_i leads to

$$\frac{\partial \mathbf{F}_d^u}{\partial d_i} \mathbf{K}_d^u = -\mathbf{F}_d^u \frac{\partial \mathbf{K}_d^u}{\partial d_i}. \quad (15)$$

Postmultiplying (15) by \mathbf{F}_d^u yields

$$\frac{\partial \mathbf{F}_d^u}{\partial d_i} = -\mathbf{F}_d^u \frac{\partial \mathbf{K}_d^u}{\partial d_i} \mathbf{F}_d^u. \quad (16)$$

As the damage is a small amount, $\mathbf{F}_d^u \approx \mathbf{F}_a^u$ is satisfied. Substituting (9) and (13) into (16), the sensitivity of flexibility matrix to damage for the new system can be derived as

$$\begin{aligned} \frac{\partial \mathbf{F}^u}{\partial d_i} &\approx -\mathbf{F}^u \frac{\partial \mathbf{K}^u}{\partial d_i} \mathbf{F}^u \\ &= (\mathbf{D}^T \mathbf{K} \mathbf{D})^{-1} \mathbf{D}^T \mathbf{K}_{ai} \mathbf{D} (\mathbf{D}^T \mathbf{K} \mathbf{D})^{-1}. \end{aligned} \quad (17)$$

In order to reduce the error result from truncating higher-order modes, generalized flexibility matrix $\mathbf{f}^u = \mathbf{F}^u (\mathbf{M}^u \mathbf{F}^u)^l$ is used [12]. In this research, $l = 2$ is adopted. The generalized flexibility matrix for the updated system can be written as

$$\mathbf{f}^u = \mathbf{F}^u \mathbf{M}^u \mathbf{F}^u \mathbf{M}^u \mathbf{F}^u. \quad (18)$$

Differentiating (18) with respect to d_i leads to

$$\begin{aligned} \frac{\partial \mathbf{f}^u}{\partial d_i} &= \frac{\partial \mathbf{F}^u}{\partial d_i} \mathbf{M}^u \mathbf{F}^u \mathbf{M}^u \mathbf{F}^u + \mathbf{F}^u \mathbf{M}^u \frac{\partial \mathbf{F}^u}{\partial d_i} \mathbf{M}^u \mathbf{F}^u \\ &\quad + \mathbf{F}^u \mathbf{M}^u \mathbf{F}^u \mathbf{M}^u \frac{\partial \mathbf{F}^u}{\partial d_i}. \end{aligned} \quad (19)$$

Combining (17) and (19), the sensitivity of generalized flexibility matrix to damage can be obtained. Making use of Taylor's series expansion, change in generalized flexibility matrix can be described as

$$\Delta \mathbf{f}^u \approx \sum_{i=1}^e \frac{\partial \mathbf{f}^u}{\partial d_i} d_i. \quad (20)$$

The generalized flexibility matrix for the updated system can also be approximately determined by using its first frequency λ_1^u and the corresponding mode Φ_1^u , which can be acquired by the $r + 1$ th frequency λ_{r+1} and the corresponding mode Φ_{r+1} of original system, respectively. Then change in generalized flexibility matrix can be described as

$$\begin{aligned} \Delta \mathbf{f}^u &\approx \frac{1}{\lambda_{d,r+1}^3} (\mathbf{D}^{-1} \Phi_{d,r+1}) (\mathbf{D}^{-1} \Phi_{d,r+1})^T \\ &\quad - \frac{1}{\lambda_{u,r+1}^3} (\mathbf{D}^{-1} \Phi_{u,r+1}) (\mathbf{D}^{-1} \Phi_{u,r+1})^T, \end{aligned} \quad (21)$$

where $\lambda_{d,r+1}$ and $\Phi_{d,r+1}$ are the $r + 1$ th frequency and mode shape of the damaged structure and $\lambda_{u,r+1}$ and $\Phi_{u,r+1}$ are the $r + 1$ th frequency and mode shape of the undamaged structure, respectively. When first r modal parameters are unavailable, damage parameters can be acquired by manipulating (20) and (21) into a system of linear equations, which can be solved by using the least squares method.

3. Numerical Examples

In order to verify the effectiveness of the proposed method, two numerical examples are considered. The first numerical example is a cantilever beam, and the second one is a rod-fastened-rotor considering partial separation of interface.

3.1. Forty-Five-Element Cantilevered Beam. A two-dimensional cantilever beam with a rectangular section, as shown in Figure 1, is taken as a case study to verify the effectiveness of the proposed method. The basic parameters of material and geometrics are as follows: elastic modulus $E = 2.1$ GPa, density $\rho = 7800$ kg/m³, length $l = 0.45$ m, cross section area $A = 1.6129 \times 10^{-4}$ m², and the moment of inertia $I = 5.42 \times 10^{-8}$ m⁴. The total number of elements and degrees

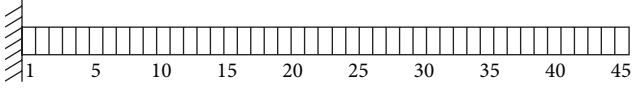


FIGURE 1: A cantilever beam.

of freedom are 45 and 90, respectively. The length of each element is 0.01 m. Two damage cases are presented here: case 1: element 28 is damaged with stiffness losses of 10%; case 2: elements 18 and 36 are damaged simultaneously with stiffness losses of 14% and 6%, respectively.

When the first mode is unavailable, location and severity of damage can be obtained by using the second natural frequency and the corresponding mode shape with the proposed method in this paper. Parameter r is the number of unavailable modes. Damage parameters can be acquired by solving (20) and (21) with $r = 1$.

The results are also compared with the results obtained by using the method in [6], which is an extension of the Multiple Damage Location Assurance Criterion (MDLAC). Making use of the mode shape directly, the damage sites can be approximately localized as those sites with the large MDLAC values. The MDLAC value in [6] is

$$\text{MDLAC}(\delta\mathbf{A}) = \frac{|\Delta\Phi^T \cdot \delta\Phi(\delta\mathbf{A})|^2}{(\Delta\Phi^T \cdot \Delta\Phi) \cdot (\delta\Phi(\delta\mathbf{A})^T \cdot \delta\Phi(\delta\mathbf{A}))}. \quad (22)$$

Figure 2 shows the results calculated by the methods proposed in this paper and [6] for damage case 1, which represents the case of single damage. The vertical axis of Figures 2(a) and 2(b) is absolute damage extent and normalized MDLAC value by using the methods proposed in this paper and [6], respectively. Results less than zero are ignored, because each a_i is assumed to be a nonnegative number. Damaged element can be located accurately by both methods, while damage extent can also be detected by the proposed method in this paper.

Similarly, Figure 3 displays the results calculated by the proposed methods in this paper and the method in [6] for damage case 2 (double damage). While the method in [6] that directly uses mode shape fails to detect the damage in element 36 only using the second mode shape, the method proposed in this paper predicts the location of the damage successfully. The damage extent detected is 0.163 and 0.064 for elements 18 and 36, respectively.

To consider effect of the measured noise of frequency and mode shape on accuracy of the proposed method, 1% and 5% random noise are added in the frequency and mode shape for damage detection, respectively [6, 18]. Figure 4 shows the results calculated by the proposed method in this paper for damage cases 1 and 2. The results show that accurate locations can also be estimated considering effect of measured noise.

To investigate effect of using incomplete mode shapes on accuracy of the proposed method, 80 and 60 nodal displacements of the complete second mode shape are used to detect the damage. The noise effect is also considered

TABLE 1: Location and extent of multiple damage of rod-fastened-rotor.

Element number	10	11	12	13
Damage extent	5.2%	16.2%	11.9%	2.2%

at the same time. Figure 5 shows the results calculated by the method proposed in this paper for damage cases 1 and 2 when 80 nodal displacements of the second mode shape are available. Figure 6 displays the results calculated by the method presented in this paper for damage cases 1 and 2 when only 60 nodal displacements of the second mode shape are available.

3.2. Simplified Rod-Fastened-Rotor. The rod-fastened-rotors are commonly used in heavy duty gas turbines and aero engines. As shown in Figure 7, the rod-fastened-rotor is comprised of a battery of discs clamped together by tie rods. There is contact interface between discs of the rod-fastened-rotor. Some zones of the contact interface are separated and the flexural stiffness of the rod-fastened-rotor decreases when bending moment exceeds critical value [16].

Detection of partial separation of contact interface for a rod-fastened-rotor in heavy duty gas turbine is investigated in this paper. The beam elements are used to model the rod-fastened-rotor. The total number of elements is 37, as shown in Figure 7. The unbalance response and distribution of flexural moment are calculated by using the common commercial finite element software ANSYS. Figure 8 shows the flexural moment on each element at the second critical speed. According to the relationship between bending moment and flexural stiffness in [19], damage ratio of each element is shown in Table 1.

The location and extent of damage are detected with the method proposed in this paper and the result is shown in Figure 9. The damage extent of damaged elements 10, 11, 12, and 13 detected by our method is 5.9%, 24%, 14%, and 0.7%, respectively. Although several undamaged elements are detected to be damaged with minor extent, the result can also help us to find the location of the damage.

From the results obtained above, the proposed method can effectively identify single, double, and multiple damage without the first frequency and the corresponding mode shape for numerical examples.

4. Conclusions

The first-modal parameter of system plays the most important role in its flexibility matrix; the original flexibility method cannot be used to detect damage when the first-modal parameter is unavailable. A damage detection method based on flexibility change by using single nonfirst mode is presented. The system is updated via restricting the first few mode shapes. The mass matrix, stiffness matrix, and modal parameters of the updated system are obtained. Then sensitivity of the new flexibility matrix to damage is derived. The damage extent of each element can be calculated by solving a linear equation. This method is tested through

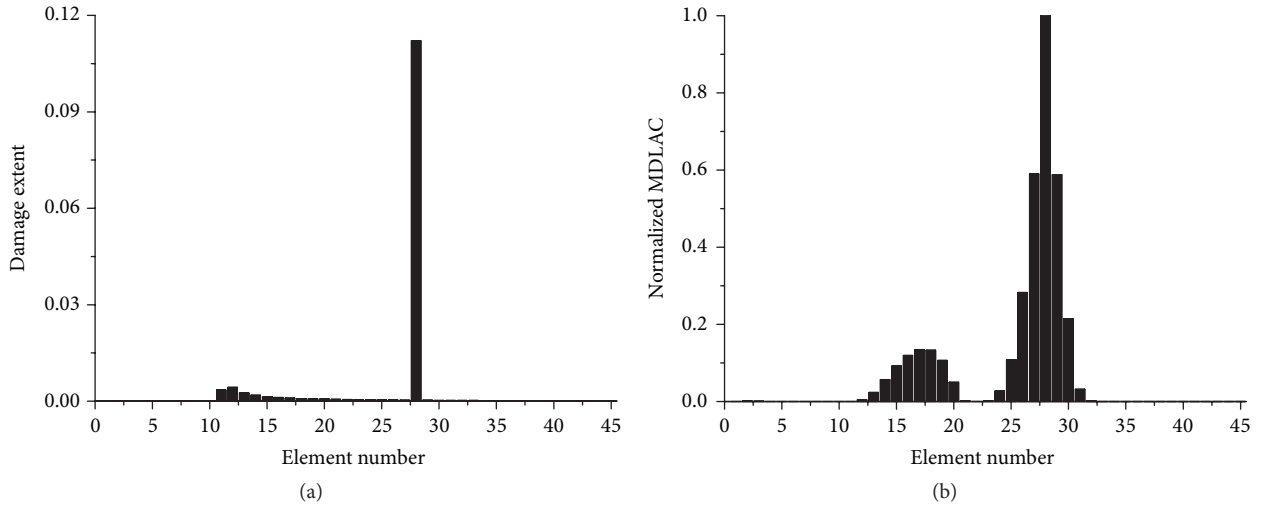


FIGURE 2: Damage detection by only using the second-modal parameters for damage case 1: (a) and (b) are the results by using the proposed method in this paper and the method in [6], respectively.

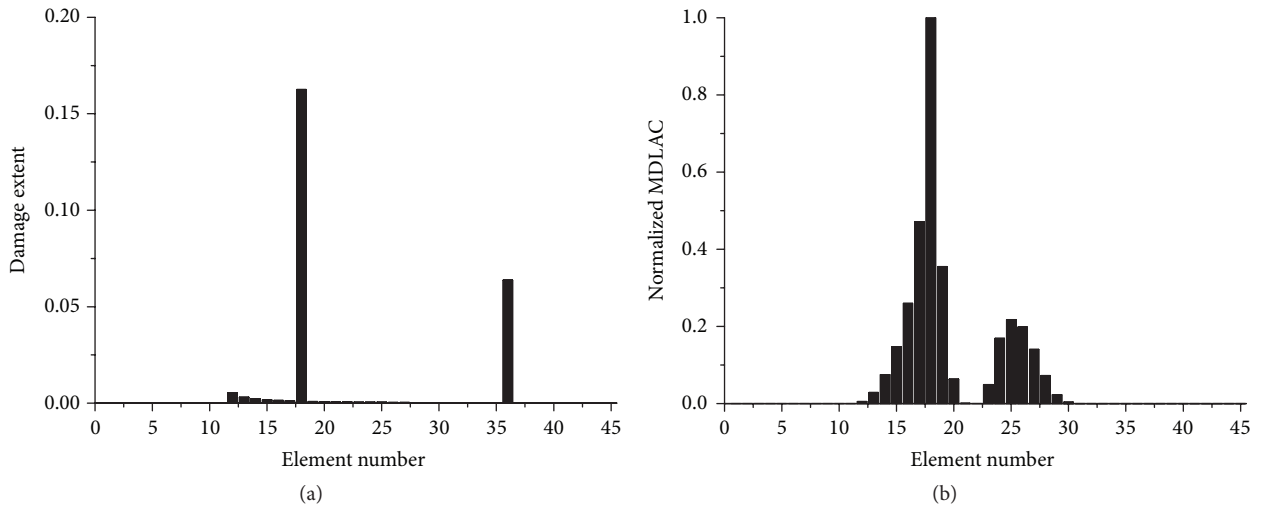


FIGURE 3: Damage detection by only using the second-modal parameters for damage case 2: (a) and (b) are the results by using the proposed method in this paper and the method in [6], respectively.

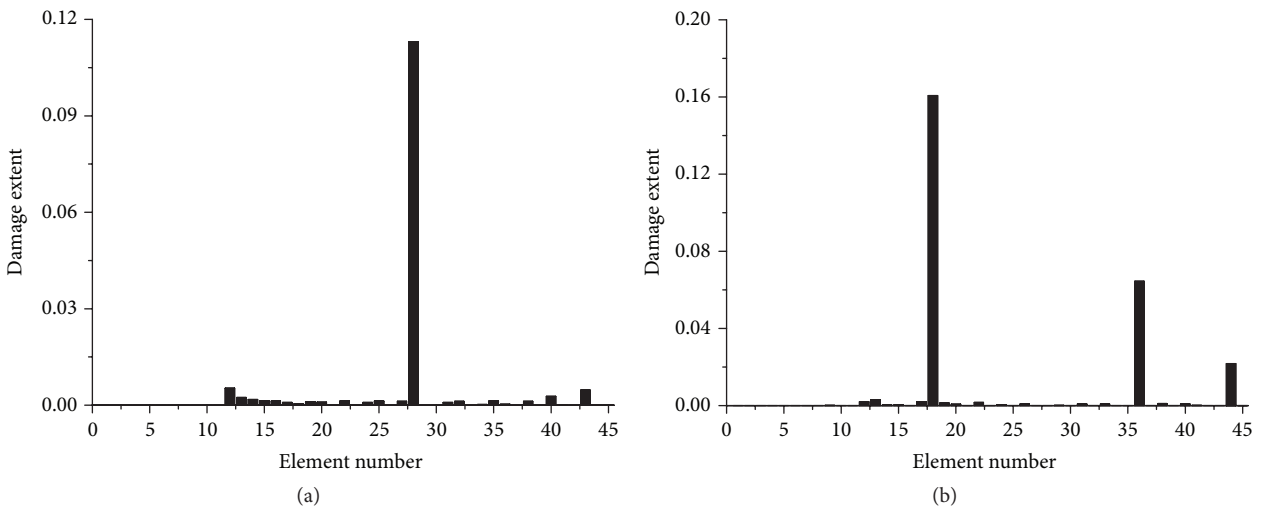


FIGURE 4: Damage detection by only using the second-modal parameters for damage (a) case 1 and (b) case 2, when 1% and 5% random noise are added in the frequencies and mode shapes, respectively.

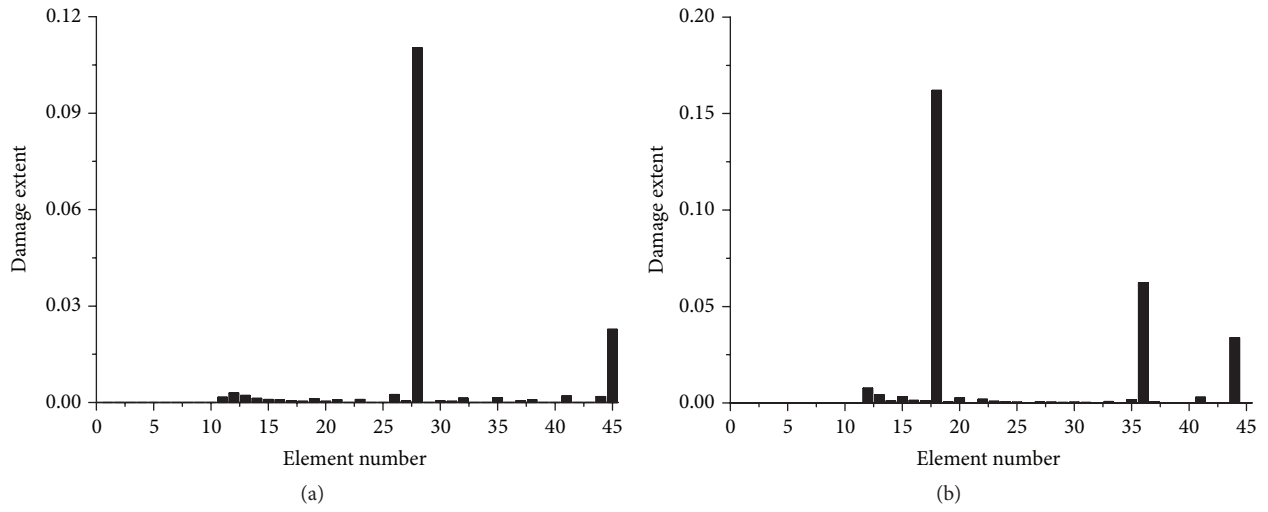


FIGURE 5: Damage detection by using the second natural frequency and 80 nodal displacements of the corresponding mode shape: (a) case 1; (b) case 2.

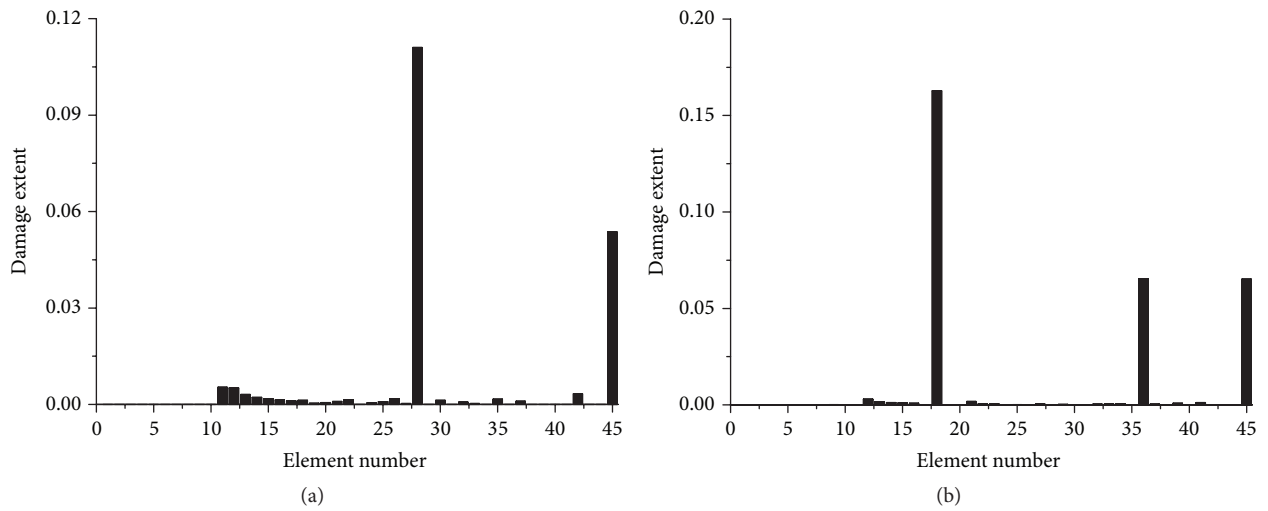


FIGURE 6: Damage detection by using the second natural frequency and 60 nodal displacements of the corresponding mode shape: (a) case 1; (b) case 2.

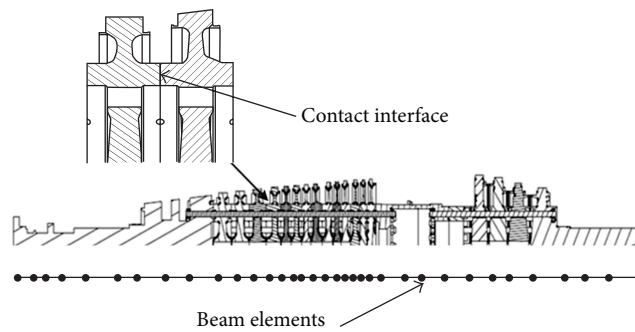


FIGURE 7: Schematic diagram of heavy duty gas turbine and node dividing.

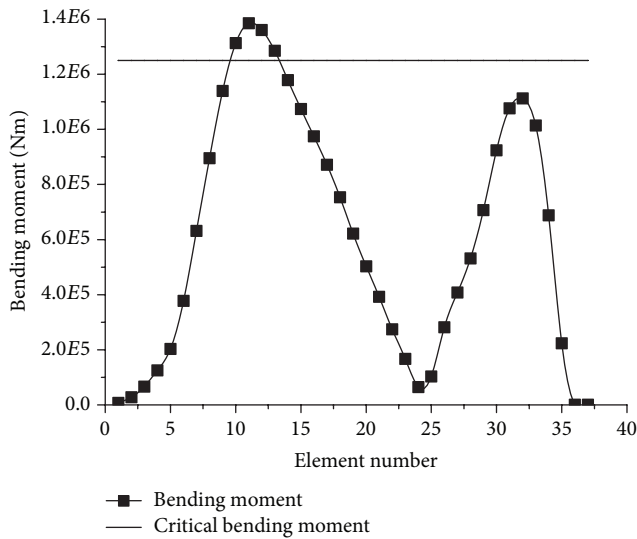


FIGURE 8: Bending moment on each interface of the rod-fastened-rotor at the second critical speed.

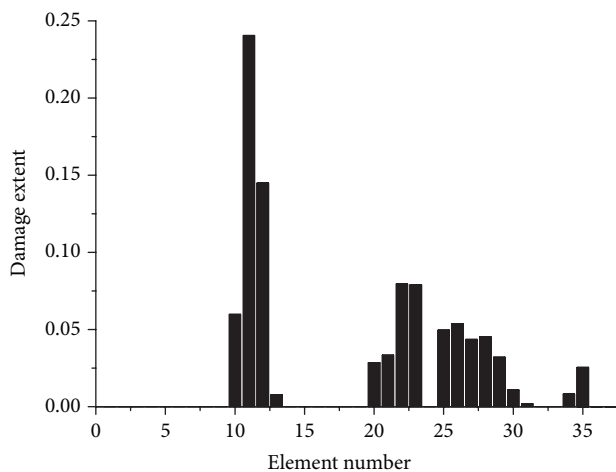


FIGURE 9: Damage detection by only using the second-modal parameter of the rod-fastened-rotor.

numerical means on a cantilever beam and a rod-fastened-rotor with different damage scenarios, when only the second natural frequency and mode shape are available. The results of the numerical examples indicate that the proposed method can effectively identify single, double, and multiple damage.

Conflict of Interests

The authors declare that there is no conflict of interests regarding the publication of this paper.

Acknowledgments

This work was supported by the Natural Science Foundation of China (no. 51275385) and Major State Basic Research Development Program of China (no. 2011CB706505).

References

- [1] W. Fan and P. Z. Qiao, "Vibration-based damage identification methods: a review and comparative study," *Structural Health Monitoring*, vol. 10, no. 1, pp. 83–111, 2011.
- [2] Z. A. Jassim, N. N. Ali, F. Mustapha, and N. A. Abdul Jalil, "A review on the vibration analysis for a damage occurrence of a cantilever beam," *Engineering Failure Analysis*, vol. 31, pp. 442–461, 2013.
- [3] A. Messina, E. J. Williams, and T. Contursi, "Structural damage detection by a sensitivity and statistical-based method," *Journal of Sound and Vibration*, vol. 216, no. 5, pp. 791–808, 1998.
- [4] J.-T. Kim and N. Stubbs, "Crack detection in beam-type structures using frequency data," *Journal of Sound and Vibration*, vol. 259, no. 1, pp. 145–160, 2003.
- [5] G. Y. Xu, W. D. Zhu, and B. H. Emory, "Experimental and numerical investigation of structural damage detection using changes in natural frequencies," *Journal of Vibration and Acoustics*, vol. 129, no. 6, pp. 686–700, 2007.
- [6] Z. Y. Shi, S. S. Law, and L. M. Zhang, "Damage localization by directly using incomplete mode shapes," *Journal of Engineering Mechanics*, vol. 126, no. 6, pp. 656–660, 2000.
- [7] P. M. Pawar, K. Venkatesulu Reddy, and R. Ganguli, "Damage detection in beams using spatial fourier analysis and neural networks," *Journal of Intelligent Material Systems and Structures*, vol. 18, no. 4, pp. 347–359, 2007.
- [8] A. K. Pandey and M. Biswas, "Damage detection in structures using changes in flexibility," *Journal of Sound and Vibration*, vol. 169, no. 1, pp. 3–17, 1994.
- [9] Q. W. Yang and J. K. Liu, "Damage identification by the eigenparameter decomposition of structural flexibility change," *International Journal for Numerical Methods in Engineering*, vol. 78, no. 4, pp. 444–459, 2009.
- [10] D. Bernal and B. Gunes, "Flexibility based approach for damage characterization: benchmark application," *Journal of Engineering Mechanics*, vol. 130, no. 1, pp. 61–70, 2004.
- [11] A. Tomaszewska, "Influence of statistical errors on damage detection based on structural flexibility and mode shape curvature," *Computers & Structures*, vol. 88, no. 3-4, pp. 154–164, 2010.
- [12] J. Li, B. Wu, Q. C. Zeng, and C. W. Lim, "A generalized flexibility matrix based approach for structural damage detection," *Journal of Sound and Vibration*, vol. 329, no. 22, pp. 4583–4587, 2010.
- [13] M. Masoumi, E. Jamshidi, and M. Bamdad, "Application of generalized flexibility matrix in damage identification using Imperialist Competitive Algorithm," *KSCE Journal of Civil Engineering*, vol. 19, no. 4, pp. 994–1001, 2015.
- [14] W.-J. Yan and W.-X. Ren, "Closed-form modal flexibility sensitivity and its application to structural damage detection without modal truncation error," *Journal of Vibration and Control*, vol. 20, no. 12, pp. 1816–1830, 2014.
- [15] M. Montazer and S. M. Seyedpoor, "A new flexibility based damage index for damage detection of truss structures," *Shock and Vibration*, vol. 2014, Article ID 460692, 12 pages, 2014.
- [16] J. Gao, Q. Yuan, P. Li, Z. Feng, H. Zhang, and Z. Lv, "Effects of bending moments and pretightening forces on the flexural stiffness of contact interfaces in rod-fastened rotors," *Journal of Engineering for Gas Turbines and Power*, vol. 134, no. 10, Article ID 102503, 2012.
- [17] J. Li, Z. Li, H. Zhong, and B. Wu, "Structural damage detection using generalized flexibility matrix and changes in natural frequencies," *AIAA Journal*, vol. 50, no. 5, pp. 1072–1078, 2012.

- [18] M. R. N. Shirazi, H. Mollamahmoudi, and S. Seyedpoor, "Structural damage identification using an adaptive multi-stage optimization method based on a modified particle swarm algorithm," *Journal of Optimization Theory and Applications*, vol. 160, no. 3, pp. 1009–1019, 2014.
- [19] Q. Yuan, J. Gao, and P. Li, "Nonlinear dynamics of the rod-fastened Jeffcott rotor," *Journal of Vibration and Acoustics*, vol. 136, no. 2, Article ID 021011, 2014.

Research Article

The Influence on Modal Parameters of Thin Cylindrical Shell under Bolt Looseness Boundary

Hui Li, Mingwei Zhu, Zhuo Xu, Zhuo Wang, and Bangchun Wen

School of Mechanical Engineering and Automation, Northeastern University, No. 3-11 Wenhua Road, Heping District, Shenyang 110819, China

Correspondence should be addressed to Hui Li; lh200300206@163.com

Received 20 July 2015; Revised 3 October 2015; Accepted 5 October 2015

Academic Editor: Daniel Morinigo-Sotelo

Copyright © 2016 Hui Li et al. This is an open access article distributed under the Creative Commons Attribution License, which permits unrestricted use, distribution, and reproduction in any medium, provided the original work is properly cited.

The influence on modal parameters of thin cylindrical shell (TCS) under bolt looseness boundary is investigated. Firstly, bolt looseness boundary of the shell is divided into two types, that is, different bolt looseness numbers and different bolt looseness levels, and natural frequencies and mode shapes are calculated by finite element method to roughly master vibration characteristics of TCS under these conditions. Then, the following measurements and identification techniques are used to get precise frequency, damping, and shape results; for example, noncontact laser Doppler vibrometer and vibration shaker with excitation level being precisely controlled are used in the test system; “preexperiment” is adopted to determine the required tightening torque and verify fixed constraint boundary; the small-segment FFT processing technique is employed to accurately measure nature frequency and laser rotating scanning technique is used to get shape results with high efficiency. Finally, based on the measured results obtained by the above techniques, the influence on modal parameters of TCS under two types of bolt looseness boundaries is analyzed and discussed. It can be found that bolt looseness boundary can significantly affect frequency and damping results which might be caused by changes of nonlinear stiffness and damping and in bolt looseness positions.

1. Introduction

Thin cylindrical shell (TCS) has long been an important structural component due to its high stiffness to weight and strength to weight ratios, which is widely used in the engineering fields, such as aircraft casings, pipes and ducts, rotary drums in granulator, and aircraft engine [1–5]. Modal parameters of TCS are mainly composed of natural frequencies, mode shapes, and damping ratio; these parameters are the basis of further study on vibration characteristics of TCS [6–8], which are of great importance to theoretical modeling, response prediction, vibration reduction optimization, vibration mechanism research, structural damage identification, and so forth. Generally, TCS is working at a very harsh environment, such as thermal expansion and contraction, strong vibration, and uneven exciting force generated by turbulent air flow, which may easily make TCS operate under elasticity or looseness boundary [9]. Besides, due to different installation forms, the connected or constraint end of TCS may not be well fixed [10]. For example, if TCS is connected

or constrained by many bolts, its constraint effectiveness will inevitably be weakened under complex external load [11, 12], especially when a bolt or some bolts come loose; the looseness condition will not only decrease constraint strength but also increase interface abrasion and the probability of fatigue failure, and, once the bolt fracture happens, it will severely affect the function of TCS and could even lead to serious accident [13].

At present great efforts have been made to study vibration character of TCS under complex and diverse boundary condition by scholars and researchers, for example, bolt looseness, elasticity, and other complex boundary conditions, and many encouraging research results have been obtained. For example, Forsberg [14] studied the influence of boundary conditions on the modal characteristics of thin cylindrical shells. Totally 16 possible sets of homogeneous boundary conditions were specified independently at each end of the shell, and these sets of conditions were discussed in detail. It has been found that even for long cylinders (length to radius ratio of 40 or more) the minimum natural frequency may

differ by more than 50% depending upon whether $u = 0$ or the longitudinal stress resultant $N_x = 0$ at both ends. Koga [15] studied the effects of boundary conditions on the free vibrations of TCS and a simple formula for the natural frequency was derived as an asymptotic solution for the eigenvalue problems of the breathing vibrations, whose accuracy was sequentially examined by a comparison with numerical solutions and experimental results. The results showed that the formula was accurate enough for engineering and it was applicable under any possible combinations of the boundary conditions for the simply supported, the clamped, and the free ends of the shell. Sofiyev et al. [16] proposed an analytical procedure to study the free vibration characteristics of laminated thin circular cylindrical shells resting on elastic foundation. They found that natural frequency was as a function of the shell displacement amplitude, and it was also close related to the effect of elastic foundation, nonlinearity, and number and ordering of layers of the shell. Liang and Zhang [17] studied stiffness optimization of TCS under elasticity boundary condition. The explicit formula of initial parameter solution of variable thickness shell was derived by transfer matrix method, and the optimization process was transformed into a constraint nonlinear solving process; thus the objective function can be successfully obtained by the stepped reduction method. Dong et al. [18] investigated the influences of bolt looseness in missile clamping support on vibration characteristics of the cylindrical shell structure by base excitation technique. Different steady response signals were obtained by varying bolt pretightening force of the attachment bolts in the structure, and power spectrum density diagrams of signals corresponding to different status of the structure were analyzed and an extraction method of the spectral moment looseness was proposed to distinguish fault characteristics of bolt looseness. Dong et al. [19] also experimentally studied how to monitor the attachment bolt looseness in a clamped cylindrical shell structure, and wavelet transform was used to analyze damage characteristic of bolt looseness based on the structural acceleration response data. Zhou et al. [20] used the wave propagation method to solve the equations of motion of TCS under elastic-support boundary condition, and the elastic-support boundary condition was specified in terms of 8 independent sets of distributed springs which have arbitrary stiffness values. Besides, the effects on nature frequencies of the restraining springs were also studied for a range of stiffness values and different geometrical characteristics of the shells, and it was found that the restraining stiffness can drastically affect frequency parameters of TCS. Sun [21] used transfer matrix method to study the free vibration of TCS under elasticity boundary condition, taking into account elastic connection stiffness, and the transfer matrix of global variables of TCS under elasticity boundary condition was obtained by multiplying transfer matrix of state variables in the connection boundary with the one of the shell itself.

However, most of researches done by the above scholars and researchers are mainly based on theory or simulation; experimental studies on the influence on modal parameters of TCS under bolt looseness boundary (BLB) are still scarce. And as a lack of the related test conclusion, theoretical

analysis results of the shell under more complex boundary condition can not be effectively verified, let alone validate some advanced shell theories.

This research combined theory with experiment to investigate the influence on modal parameters of TCS under BLB. Firstly, bolt looseness boundary of the shell is divided into two types, that is, different bolt looseness numbers and different bolt looseness levels, and natural frequencies and mode shapes of TCS under these conditions are calculated by finite element method (FEM) in Section 2; thus vibration characteristics of TCS under the above two types of bolt looseness boundaries can be roughly mastered. Then we go on to set up experiment system to accurately measure modal parameters of TCS, and the corresponding test procedures and identification techniques which are suitable for the thin walled shell are also proposed in Section 3. Finally in Section 4, based on the accurate measured data, the influence on natural frequencies, mode shapes, and damping ratios of TCS under two types of bolt looseness boundaries is analyzed and discussed in details. This research can provide dynamic modeling service for TCS under complex boundary condition, provide experimental data for effective selection of boundary parameters in the theoretical model, and also provide an important reference for analysis and diagnosis of bolt looseness fault of TCS.

2. Vibration Characteristic Analysis of TCS under Bolt Looseness Boundary

In this section, in order to deeply understand vibration characteristic of TCS, FEM is used to calculate vibration characteristic of TCS, such as natural frequencies and mode shapes, under two types of bolt looseness boundaries with different looseness numbers and different looseness levels, respectively. Although the resulting frequencies and shapes may inevitably contain some calculation errors, they are helpful for us to determine measured frequency range, build experimental model, understand geographic distributions of some nodes or nodal lines, and so forth.

2.1. Research Object. The TCS studied in this paper is shown in Figure 1 and dimension parameters are listed in Table 1. The material of TCS is structural steel with elastic modulus of 212 Gpa, Poisson's ratio of 0.3, and the density of 7850 kg/m³. Its length is 95 mm with 144 mm external radius and an average thickness of 2 mm. There is the extension edge with 150 mm external radius and 3 mm thickness on this shell which is machined to be clamped by a clamping-ring with eight M8 bolts, so that it can be certain that the shell is in cantilever boundary condition. Then, we can loosen some or all of bolts with certain tightening torque by torque wrench, so that we can analyze vibration characteristic of TCS under bolt looseness boundary.

2.2. Vibration Characteristic Analysis of TCS under BLB with Different Looseness Numbers. Finite element model of the TCS under BLB with different looseness numbers is established with ANSYS Parametric Design Language (APDL) in

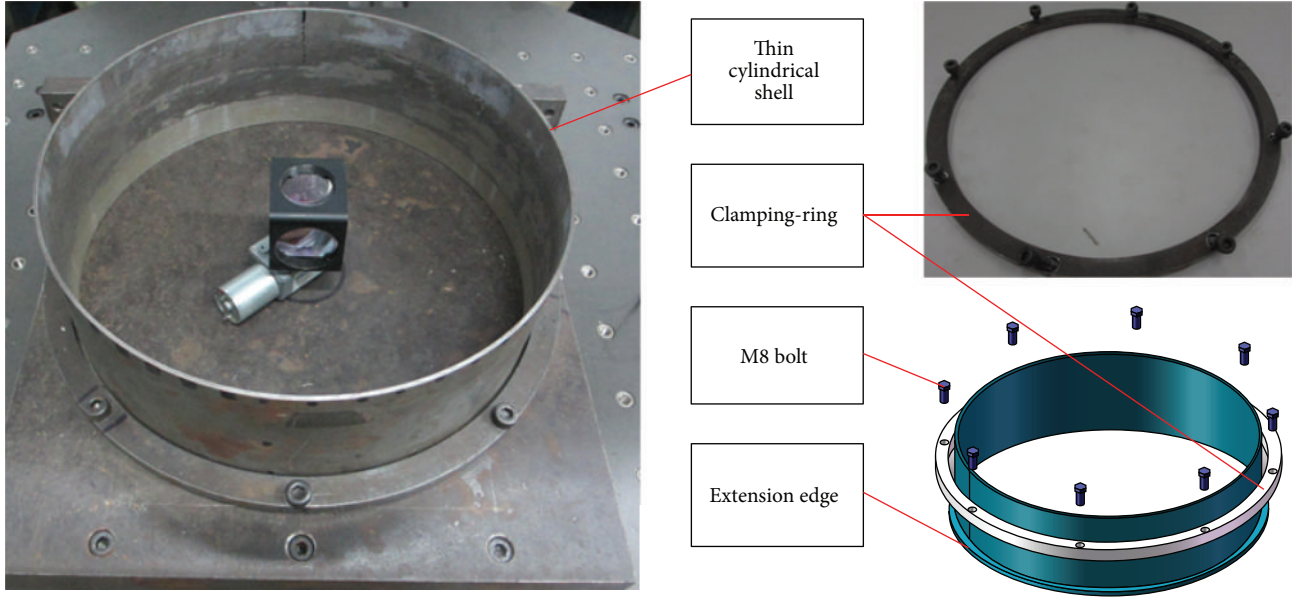


FIGURE 1: TCS and its clamped circular ring used in bolt looseness boundary.

TABLE 1: Dimension parameters of thin cylindrical shell.

Length (mm)	Thickness (mm)	Internal radius (mm)	External radius (mm)	Extension edge radius (mm)	Thickness of extension edge (mm)
95	2	142	144	150	3

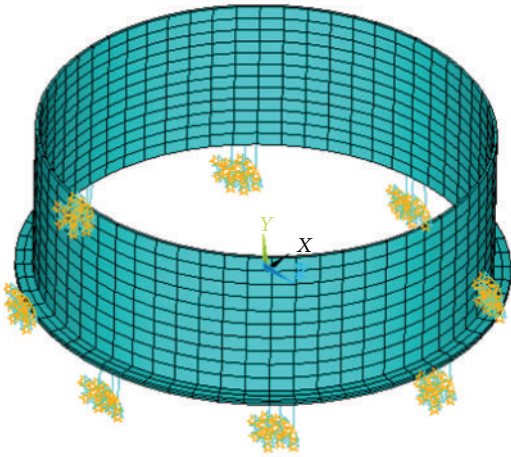


FIGURE 2: Finite element model of the TCS under BLB with different looseness numbers.

ANSYS software, as seen in Figure 2. SOLID186 element is used to create the model of the shell which consists of 6480 nodes and 960 elements, and MATRIX27 element is used as spring element to simulate bolt looseness boundary with different looseness numbers, whose stiffness can be adjusted in the x , y , and z direction. Firstly, use 8 spring elements with stiffness value of 1×10^8 in the above three directions to simulate the free-clamped boundary condition,

and the resulting natural frequencies and mode shapes are obtained by Block Lanczos method, as listed in Tables 2 and 3, respectively. Then, use different numbers of spring elements to simulate different bolt looseness numbers and calculate the corresponding frequencies and shape results, according to the sequence of loosening 1 bolt, 2 bolts, 3 bolts, and 4 bolts, from sequence I to sequence IV as shown in Figure 3, and the calculated results are given in Table 2 and Table 3. Additionally, the frequencies differences under the constraint boundary (or no loose boundary) and bolt looseness boundary with different looseness numbers are also compared in Table 2, and Figure 4 gives the relations between natural frequency and mode shape under BLB with different looseness numbers. It should be noted that, due to the specificity of the first mode shape, it is difficult to use traditional number of axial half-waves, m , and circumferential waves, n , to describe its vibration shape; thus the first special frequency and shape result are not compared under BLB in Table 2 (the calculated results are only for roughly understanding vibration characteristic of TCS when the constraint bolts are loose; they inevitably contain some calculation errors because constraint stiffness and damp parameters in bolt looseness positions are hard to simulate without experimental test, and they are not the focus of this paper).

It can be found from the above analysis results in Tables 2 and 3 and Figure 4 that (I) bolt looseness will result in the decrease of natural frequencies of TCS, and with the increasing of bolt looseness numbers the frequency results will further decrease; (II) high order natural frequencies of

TABLE 2: Natural frequencies of TCS under BLB with different looseness numbers.

Modal order	No looseness A (Hz)	Loosen 1 bolt B (Hz)	Difference I (B - A)/A (%)	Loosen 2 bolts C (Hz)	Difference II (C - A)/A (%)	Loosen 3 bolts D (Hz)	Difference III (D - A)/A (%)	Loosen 4 bolts E (Hz)	Difference IV (E - A)/A (%)
1	—	786.2	—	678.0	—	591.9	—	554.4	—
2	976.5	974.2	-0.2	935.0	-4.3	831.6	-14.8	758.9	-22.3
3	1068.7	1065.0	-0.3	1043.2	-2.4	1035.4	-3.1	1013.0	-5.2
4	1313.8	1298.5	-1.2	1248.4	-5.0	1193.3	-9.2	1146.8	-12.7
5	1535.9	1461.0	-4.9	1310.0	-14.7	1275.1	-17.0	1269.0	-17.4
6	1603.2	1597.6	-0.3	1629.0	1.6	1591.1	-0.8	1403.4	-12.5
7	1841.9	1743.4	-5.3	1681.1	-8.7	1655.8	-10.1	1588.3	-13.8
8	2000.8	1995.6	-0.3	1991.7	-0.5	1988.0	-0.6	1984.9	-0.8

TABLE 3: Mode shapes of TCS under BLB with different looseness numbers.

Modal order	No looseness A (m, n)	Loosen 1 bolt B (m, n)	Loosen 2 bolts C (m, n)	Loosen 3 bolts D (m, n)	Loosen 4 bolts E (m, n)
1	—	(Special)	(Special)	(Special)	(Special)
2	(1, 5)	(1, 5)	(1, 5)	(1, 5)	(1, 5)
3	(1, 6)	(1, 6)	(1, 6)	(1, 6)	(1, 6)
4	(1, 7)	(1, 7)	(1, 4)	(1, 4)	(1, 4)
5	(1, 4)	(1, 4)	(1, 7)	(1, 7)	(1, 7)
6	(1, 8)	(1, 8)	(1, 8)	(1, 8)	(1, 3)
7	(1, 3)	(1, 3)	(1, 3)	(1, 3)	(1, 8)
8	(1, 9)	(1, 9)	(1, 9)	(1, 9)	(1, 9)

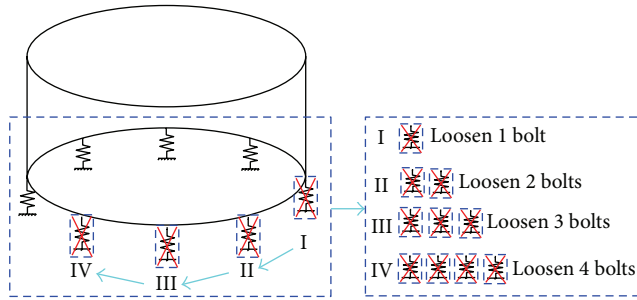


FIGURE 3: Schematic of bolt loosening sequence under BLB with different looseness numbers.

the shell, for example, the 8th natural frequency, basically will not be affected by BLB with different looseness numbers, and the frequency difference related to the BLB and no loose condition is less than 0.8%; (III) with the increase of bolt looseness number, low order mode shapes of TCS will be changed, but high order mode shapes will still be unchanged; (IV) although frequencies and shapes of TCS will be changed under BLB, the changing trend of natural frequencies with mode shapes is constant when the number of axial half-waves $m = 1$, which shows that frequency values are up after the decline with the increase of the number of circumferential waves n , and usually frequency values related to $n > 8$ are higher than $n = 2 \sim 7$.

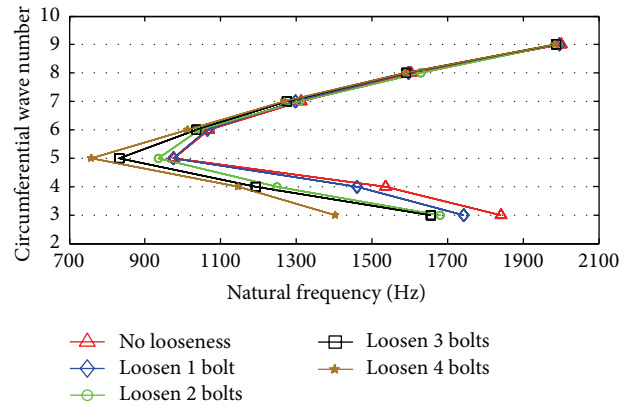


FIGURE 4: The relation between natural frequency and mode shape under BLB with different looseness numbers.

2.3. *Vibration Characteristic Analysis of TCS under BLB with Different Looseness Levels.* Similarly, SOLID186 element is used to create the model of the shell which consists of 6480 nodes and 960 elements, and MATRIX27 element is used as spring element to simulate bolt looseness boundary with different looseness levels; for example, set the stiffness value of Matrix27 element in x , y , and z direction to 0.75×10^8 , 0.25×10^8 , and 0.25×10^7 , respectively (namely, 25% looseness, 75% looseness, and 97.5% looseness), as seen in Figure 5.

TABLE 4: Natural frequencies of TCS under BLB with different looseness levels.

Modal order	No looseness A (Hz)	25% looseness B (Hz)	Difference I $(B - A)/A$ (%)	75% looseness C (Hz)	Difference II $(C - A)/A$ (%)	97.5% looseness D (Hz)	Difference III $(D - A)/A$ (%)
1	—	965.2	—	940.8	—	858.1	—
2	976.5	973.2	-0.3	956.0	-2.1	898.6	-8.0
3	1068.7	1067.4	-0.1	1056.0	-1.2	1035.4	-3.1
4	1313.8	1312.9	-0.1	1308.9	-0.4	1293.1	-1.6
5	1535.9	1530.7	-0.3	1504.3	-2.1	1382.8	-10.0
6	1603.2	1602.8	0	1601.5	-0.1	1594.9	-0.5
7	1841.9	1835.4	-0.4	1802.5	-2.1	1650.2	-10.4
8	2000.8	2000.5	0	1999.3	-0.1	1993.5	-0.4

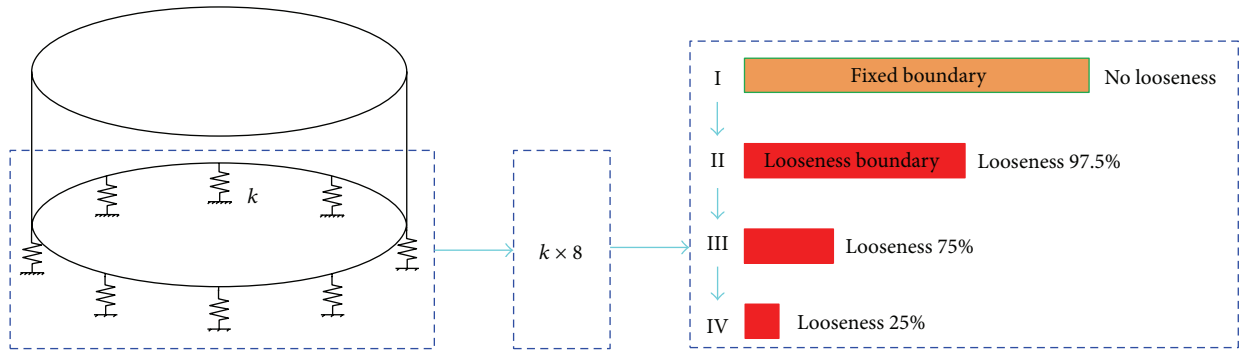


FIGURE 5: Schematic of different bolt looseness level adopted by FEM.

TABLE 5: Mode shapes of TCS under BLB with different looseness levels.

Modal Order	No looseness A (m, n)	25% looseness B (m, n)	75% looseness C (m, n)	97.5% looseness D (m, n)
1	—	(Special)	(Special)	(Special)
2	(1, 5)	(1, 5)	(1, 5)	(1, 5)
3	(1, 6)	(1, 6)	(1, 6)	(1, 6)
4	(1, 7)	(1, 7)	(1, 7)	(1, 4)
5	(1, 4)	(1, 4)	(1, 4)	(1, 3)
6	(1, 8)	(1, 8)	(1, 8)	(1, 7)
7	(1, 3)	(1, 3)	(1, 3)	(1, 8)
8	(1, 9)	(1, 9)	(1, 9)	(1, 9)

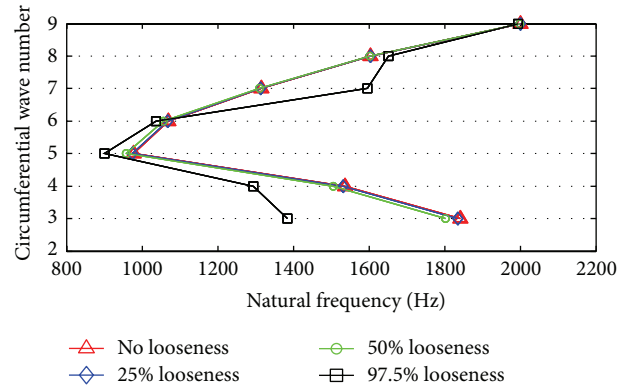


FIGURE 6: The relation between natural frequency and mode shape under BLB with different looseness levels.

Firstly, use 8 spring elements with stiffness value of 1×10^8 in above three directions to simulate the free-clamped boundary condition, and the resulting natural frequencies and mode shapes are obtained by Block Lanczos method, as listed in Tables 4 and 5. Then, use 0.75×10^8 , 0.25×10^8 , and 0.25×10^7 of 8 spring elements to simulate different bolt looseness levels, according to the sequence of 25% looseness, 75% looseness, and 97.5% looseness to calculate the corresponding frequencies and shape results, from sequence I to sequence III as shown in Figure 5, which are also given in Tables 4 and 5. Additionally, the frequencies differences

under the constraint boundary (or no loose boundary) and bolt looseness boundary with different looseness levels are also compared in Table 4, and Figure 6 gives the relations between natural frequency and mode shape under BLB with different looseness levels.

It can be found from the above analysis results in Tables 4 and 5 and Figure 6 that (I) bolt looseness will result in the decrease of natural frequencies of TCS, and with the increasing of bolt looseness levels the frequency results will further decrease; (II) high order natural frequencies of the

TABLE 6: The disadvantages of different vibration excitation devices for modal test of TCS under under bolt looseness boundary.

Excitation device	Modal parameters of TCS			Disadvantage
	Natural frequency	Mode shape	Damping ratio	
Hammer	√	√	×	Pulse excitation level can not be precisely controlled and the excitation force varies for each measurement, and double hit can often lead to test errors.
Electromagnetic exciter	×	×	×	The related force sensor will bring added mass and stiffness to TCS, which will severely affect test results of damping and natural frequency.
Piezoelectric ceramic exciter	√	√	×	The excitation energy of piezoelectric ceramic exciter is often insufficient for TCS, which will result in poor response signal with low level of signal noise ratio.
Vibration shaker	√	√	√	Excitation frequencies are not that high, which are often limited to 1 Hz~3000 Hz, and the test procedures are often complicated.

shell, for example, the 8th natural frequency, basically will not be affected by BLB with different looseness levels, and the frequency difference related to the BLB and no loose condition is less than 0.4%; (III) with the increase of bolt looseness levels, low order mode shapes of TCS will be changed, but high order mode shapes will still be unchanged; (IV) although frequencies and shapes of TCS will be changed under BLB, the changing trend of natural frequencies with mode shapes is constant when the number of axial half-waves $m = 1$, which shows that frequency values are up after the decline with the increase of the number of circumferential waves n , and usually frequency values related to $n > 8$ are higher than $n = 2\sim 7$.

3. Test System and Method of Modal Parameters of TCS under Bolt Looseness Boundary

In Section 2, vibration characteristic of TCS under BLB and its influence is analyzed. But due to the complexity of bolt looseness boundary, the real influence of such boundary on modal parameters, especially the damping characteristics of the shell can not be accurately analyzed by simulation method. Therefore, it is necessary to employ experimental test to investigate on the influence on modal parameters of bolt constrained shell under different looseness boundaries. In this section, experiment system is firstly established to accurately measure modal parameters of the shell, and the corresponding test procedures and identification techniques which are suitable for the thin walled shell are also proposed.

3.1. Test System of Modal Parameters of TCS under Bolt Looseness Boundary. On the one hand, due to light weight, closed modes, low level, and complicated local vibration of TCS, traditional accelerometer will bring added mass and stiffness to the tested shell [22], which will severely affect the tested frequency and damping results, so laser Doppler vibrometer is used as noncontact response sensor to measure the vibration and frequency information of the shell. On the other hand, different excitation techniques also will result in test error, so the disadvantages of four common vibration excitation devices are compared in Table 6; combining the proposed test method in [23], vibration shaker is finally chosen as excitation source with excitation level being precisely controlled, and test system of modal parameters of TCS under bolt looseness boundary is given in Figure 7. The instruments used in the test are as follow: (I) Polytec PDV-100 laser Doppler vibrometer; (II) king-design EM-1000F vibration shaker systems; (III) LongWei PS-305DM DC power supply; (IV) Aslong JGA25 DC geared motor; (V) 45° rotation mirror and 45° fixed mirror; (VI) LMS SCADAS Mobile Front-End and Dell notebook computer.

In these devices, LMS SCADAS Mobile Front-End and Dell notebook computer are responsible for recording and saving response signal from laser Doppler vibrometer. Dell notebook computer with Intel Core i7 2.93 GHz processor and 4 G RAM is used to operate LMS Test.Lab 10 B software and store measured data. For the frequency and damping test, sine sweep excitation is conducted with a closed loop control via accelerometer on the countertop of the vibration shaker, and point 1, point 2, and point 3 (being 180° with each other) are used to get response signal by adjusting laser point and average is used as the final results. In this test,

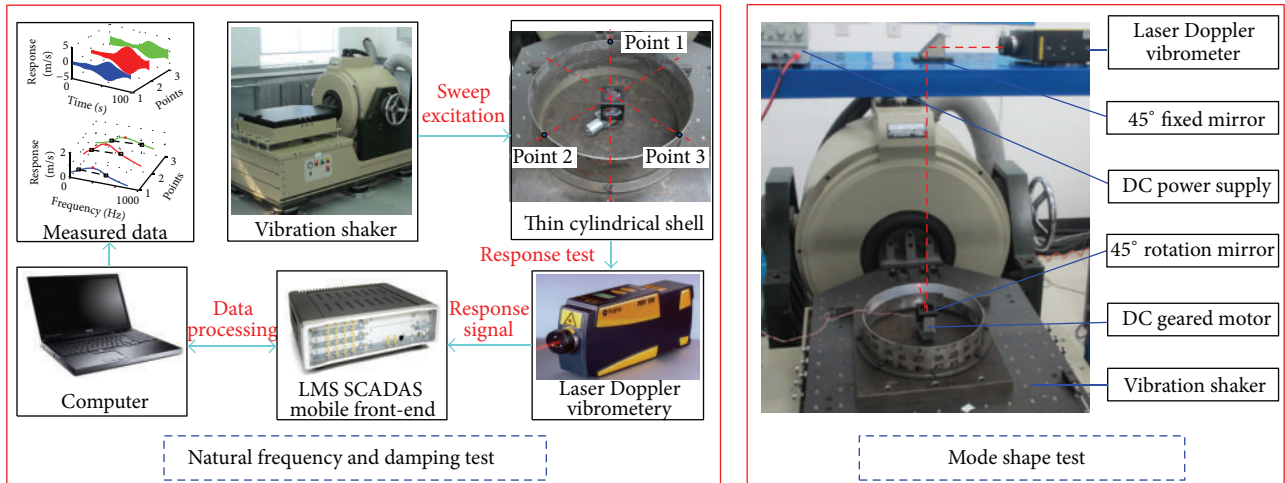


FIGURE 7: Schematic of test system of modal parameters of TCS under bolt looseness boundary.

natural frequency can be precisely determined through each resonant peak in frequency domain, and damping ratio can also be identified by the half-power bandwidth method which is calculated by measuring the bandwidth of the frequency curve (or approximately 3 dB) down from the resonant peak. For mode shape test, laser rotating scanning technique is used to get shape results of TCS. Firstly, employ one of natural frequencies of TCS to drive the tested shell under the resonance state by vibration shaker, and then DC power supply is used to provide stable voltage and current for DC geared motor, and the motor is to drive the 45° rotation mirror to complete a set of cross-sectional scan with 360° circumferential coverage for the tested shell, and in this way mode shapes data at certain mode can be obtained in a shorter amount of time than traditional test methods.

3.2. Test Method of Modal Parameters of TCS under Bolt Looseness Boundary. In this section, the test procedures of modal parameters and the related identification techniques which are suitable for TCS under bolt looseness boundary are proposed, as seen in the following four key steps.

3.2.1. Accurately Determine Tightening Torque under Fixed Constraint Boundary. Because modal parameters of TCS are closely related to constraint boundary, in actual test, we must ensure that one end of the tested shell is effectively clamped; to this end, a torque wrench is used to determine the level of tightening torque on the M8 bolts of clamping-ring, as seen in Figure 1, and the “preexperiment” is adopted to determine the required tightening torque as well as verify whether or not the tested shell is under fixed constraint boundary. For instance, it should be done at least three times to test natural frequencies, and every time the same level of torque value should be applied on M8 bolts. If test results of the first 3 natural frequencies under three preexperiments are close to each other (e.g., 1~3 Hz), we will regard this torque value as the determined tightening torque under fixed constraint boundary. If the differences between each natural frequency

are big, more than 5~20 Hz, we need to increase torque value and to repeat preexperiments several times.

3.2.2. Measure Modal Parameters of TCS under Fixed Constraint Boundary. This step involves three different measurements and identification techniques. Firstly, using sine sweep excitation by vibration shaker to test natural frequencies of TCS and in order to get precise frequency results, the small-segment FFT processing technique is employed to deal with the measured sweep signal. The time domain signal involving the 3rd natural frequency of the tested shell is shown in Figure 8(a). If FFT processing technique is directly applied on this sweep signal, we can obtain its frequency spectrum, as seen in Figure 8(b), and the frequency of the response peak is 1024.8 Hz. However, if the whole time of sweep signal can be divided into small segments, and we conduct FFT on each segment of them (in this example, it is 1 s with respect to the whole time of 68 s), the resulting frequency spectrum, as seen in Figure 8(c), is plotted through the combination of the response peak of each segment (also treated with interpolation and smoothing); the frequency value related to the peak is 1025.7 Hz, which is truly accurate result of the 3rd natural frequency. Therefore, for time-dependent sweep signal of TCS, it is necessary to use the small-segment FFT processing technique to accurately get frequency results.

Then, use the half-power bandwidth technique to identify each damping ratio of TCS from the frequency spectrum obtained by small-segment FFT processing technique. Because the resonant peak in the spectrum is already known, we can identify two half-power bandwidth points by measuring the bandwidth of the frequency curve (or approximately 3 dB) down from the resonant peak, consequently according to the damping formula to calculate the corresponding damping results based on the MATLAB program. Figure 9 gives time waveform and frequency spectrum for the third natural frequency and damping ratio of TCS at 3 measuring points, and, in order to improve accuracy of frequency and damping results, the final results are obtained by averaging the test results at these points.

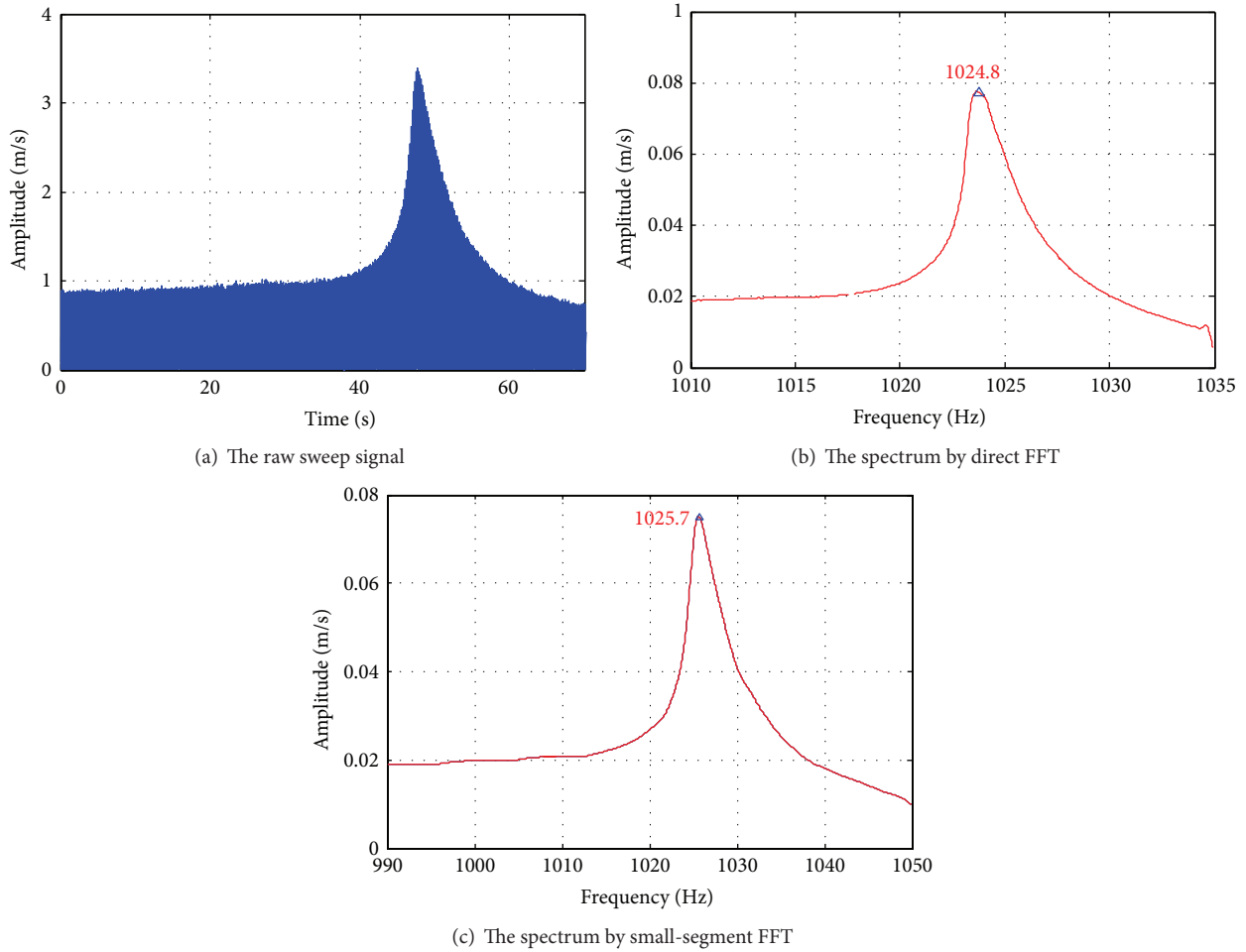


FIGURE 8: The 3rd natural frequency of CTCS obtained by different FFT processing techniques.

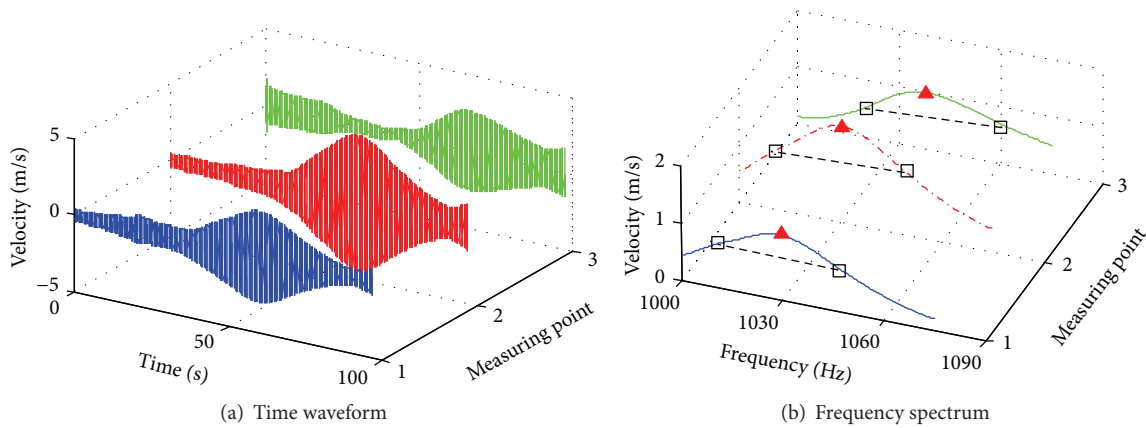


FIGURE 9: Time waveform and frequency spectrum for the third natural frequency and damping ratio of TCS at 3 measuring points.

Finally, use each of natural frequency to excite TCS at resonance state, and gradually obtain each mode shape with obvious reduction in time costs by laser rotating scan method.

3.2.3. Measure Modal Parameters of TCS under BLB with Different Looseness Numbers. After finishing the measurement work under fixed constraint boundary, use torque wrench to

loosen bolts on the clamping-ring, according to the sequence of loosening 1 bolt, 2 bolts, 3 bolts, and 4 bolts to conduct modal parameter test, as seen in Figure 10. It should be noted that the excitation level and the position of the three measuring points must be the same as the ones under fixed constraint boundary, and the same test methods, such as the small-segment FFT processing technique, the half-power

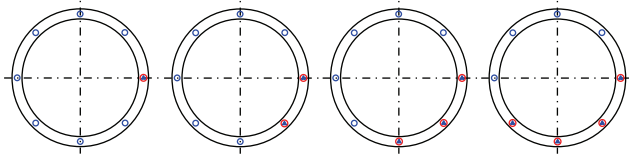


FIGURE 10: Schematic of bolt loosening sequence.

bandwidth technique, and the laser rotating scan technique, are employed to get natural frequencies, mode shapes, and damping ratios of TCS under BLB with different looseness numbers.

3.2.4. Measure Modal Parameters of TCS under BLB with Different Looseness Levels. In this step, firstly it is needed to restore boundary condition to the fixed state, so the same level of tightening torque which is determined by the preexperiment in the first step is again used to tighten eight M8 bolts on the clamping-ring. Then, set the torque value to 75%, 50%, and 25% of this tightening torque, according to the sequence of 25% looseness, 50% looseness, and 75% looseness to carry out experimental test. Applying the same excitation level and using the same test method, we can get the corresponding frequency, damping, and shape results of TCS under BLB with different looseness levels.

4. The Influence Analysis of Modal Parameters of TCS under Bolt Looseness Boundary

In this section, on the basis of both theoretical and experimental results, that is, the simulation results calculated by FEM in Section 2 and the accurate measured data obtained by the test system and test method in Section 3, the influence on natural frequencies, mode shapes, and damping ratios of TCS under two types of bolt looseness boundaries is analyzed and discussed in detail.

4.1. Test Results of Modal Parameters of TCS under BLB with Different Looseness Numbers. According to the proposed test method and procedures in Section 3, point 1, point 2, and point 3 are used as the response points, which are 180° with each other and in the same cross section of the shell the axial distance from this section to free end of TCS is about 5 mm, as seen in Figure 7. For the natural frequency and damping test, the following setups and parameters are chosen: (I) excitation level of 1g; (II) sweep rate of 1 Hz/s; (III) frequency resolution of 0.125 Hz; (IV) Hanning window for sweep response signal with upward sweep direction; (V) frequency range of 0–2048 Hz. For the mode shape test, the following setups and parameters are chosen: (I) excitation level of 1g; (II) frequency resolution of 0.125 Hz; (III) rectangular window for stable response signal; (IV) sampling frequency of 12800 Hz; (V) rotated scan speed of 2 r/min. Besides, the first 8 mode shapes of TCS are obtained in the test, and each mode shape is assembled from two sets of cross-sectional scans; one is in the section which includes point 1, point 2, and point 3 and the other is about 25 mm to

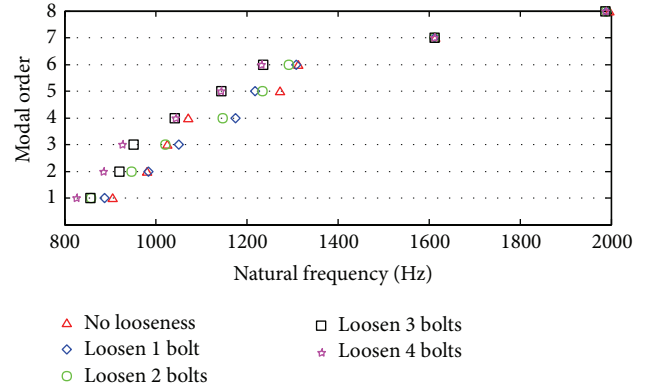


FIGURE 11: Scattergram of natural frequencies of TCS under BLB with different looseness numbers.

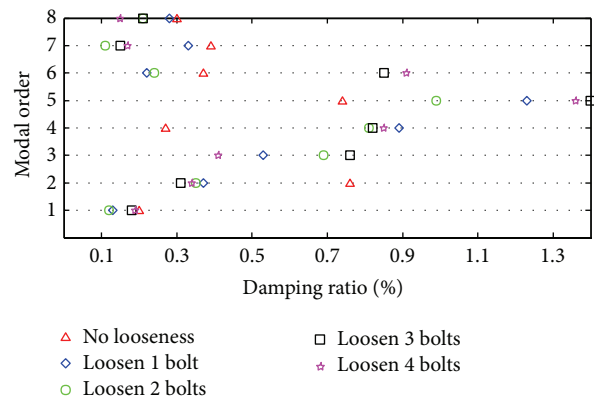


FIGURE 12: Scattergram of damping ratios of TCS under BLB with different looseness numbers.

the clamped end of the shell (restricted by the height of DC geared motor itself but do not affect the test results when the number of axial half-waves $m = 1$).

The measured frequency, damping, and shape results under BLB with different looseness numbers are listed in Tables 7, 8, and 9, respectively. Besides, in order to clearly describe the effect degree and trend of the shell under different bolt looseness boundaries, the scattergrams of natural frequencies and damping ratios of TCS related to different bolt looseness number are also given, as shown in Figures 11 and 12, and Figure 13 gives the relations between natural frequency and mode shape under BLB with different looseness numbers.

4.2. The Influence Analysis of Modal Parameters under BLB with Different Looseness Numbers

4.2.1. The Influence on Natural Frequencies of TCS. From Table 7 and Figure 11, the following can be found. (I) For the most modes of TCS, the increase of bolt looseness number would reduce the natural frequencies of TCS, but if only 1 bolt is loosened, the decreased degree of natural frequencies of TCS is not obvious. With the increase of bolt looseness number, the decreased degree of frequency values

TABLE 7: Natural frequencies of TCS under BLB with different looseness numbers.

Modal order	No looseness A (Hz)	Loosen 1 bolt B (Hz)	Effect degree (B - A)/A (%)	Loosen 2 bolts C (Hz)	Effect degree (C - A)/A (%)	Loosen 3 bolts D (Hz)	Effect degree (D - A)/A (%)	Loosen 4 bolts E (Hz)	Effect degree (E - A)/A (%)
1	906.3	888.7	-1.9	857.9	-5.3	857.5	-5.4	827.9	-8.6
2	980.8	980.0	0	947.1	-3.4	920.6	-6.1	886.5	-9.6
3	1025.7	1051.2	2.5	1021.0	-0.5	951.8	-7.2	927.9	-9.5
4	1072.3	1175.3	9.6	1147.0	7.0	1042.2	-2.8	1045.6	-2.5
5	1274.0	1218.6	-4.3	1235.0	-3.1	1145.1	-10.1	1143.8	-10.2
6	1312.8	1309.1	-0.3	1292.6	-1.5	1236.2	-5.8	1233.3	-6.1
7	1613.8	1612.2	-0.1	1613.0	0	1613.2	0	1612.3	-0.1
8	1996.3	1990.2	-0.3	1989.1	-0.4	1988.0	-0.4	1989.6	-0.3

TABLE 8: Damping ratios of TCS under BLB with different looseness numbers.

Modal order	No looseness A (%)	Loosen 1 bolt B (%)	Effect degree (B - A)/A (%)	Loosen 2 bolts C (%)	Effect degree (C - A)/A (%)	Loosen 3 bolts D (%)	Effect degree (D - A)/A (%)	Loosen 4 bolts E (%)	Effect degree (E - A)/A (%)
1	0.20	0.13	-35.0	0.12	-40.0	0.18	-10.0	0.19	-5.0
2	0.76	0.37	-51.3	0.35	-53.9	0.31	-59.2	0.34	-55.3
3	1.14	0.53	-53.5	0.69	-39.5	0.76	-33.3	0.41	-64.0
4	0.27	0.89	229.6	0.81	200.0	0.82	203.7	0.85	214.8
5	0.74	1.23	66.2	0.99	33.8	1.40	89.2	1.36	83.8
6	0.37	0.22	-40.5	0.24	-35.1	0.85	129.7	0.91	145.9
7	0.39	0.33	-15.4	0.11	-71.8	0.15	-61.5	0.17	-56.4
8	0.30	0.28	-6.7	0.21	-30.0	0.21	-30.0	0.15	-50.0

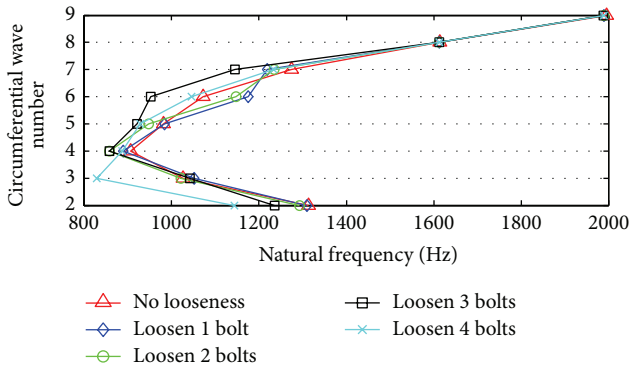


FIGURE 13: The relation between natural frequency and mode shape under BLB with different looseness numbers.

is becoming more obvious than the ones under the fixed state. For example, the 1st and 2nd natural frequencies are decreased nearly to 10%. (II) The increase of bolt looseness number would also result in the decrease of high order of natural frequencies, but the decreased degree is very small. Taking the 7th and 8th natural frequencies for example, they only decrease to 0.4% compared with the ones under the fixed state. Therefore, it can be concluded that high order natural

frequencies are basically not affected by BLB with different looseness numbers. (III) For some modes, their natural frequencies will go up when the lower looseness numbers are reached (loosening 1~2 bolts); for example, the maximum increased degree of the 3rd and the 4th natural frequencies of TCS can increase to 9.6%. Because the corresponding shape results are not changed, the increased frequency values might be caused by the changes of nonlinear stiffness in bolt looseness positions.

4.2.2. *The Influence on Damping Ratios of TCS.* From Table 8 and Figure 12, the following can be found. (I) For most modes of TCS, bolt looseness would reduce the damping of TCS. For example, for different bolt looseness number, the decreased range of damping results is about 5% ~70%, but the decreased degree of damping is not proportional to the bolt looseness number. (II) For a small part of modes of TCS, the damping results will rise with the increase of bolt looseness number, especially when the looseness number goes up to some extent, for example, loosening 3~4 bolts; the resulting damping values related to the 4th and the 6th mode are nearly 1~2 times larger than the ones under no loose condition, which may be largely caused by the changes of mode shape or increased interface friction in bolt looseness positions.

TABLE 9: Mode shapes of TCS under BLB with different looseness numbers.

Modal order	No looseness $A(m, n)$	Loosen 1 bolt $B(m, n)$	Loosen 2 bolts $C(m, n)$	Loosen 3 bolts $D(m, n)$	Loosen 4 bolts $E(m, n)$
1	 (1, 4)	 (1, 4)	 (1, 4)	 (1, 4)	 (1, 3)
2	 (1, 5)	 (1, 5)	 (1, 5)	 (1, 5)	 (1, 4)
3	 (1, 3)	 (1, 3)	 (1, 3)	 (1, 6)	 (1, 5)
4	 (1, 6)	 (1, 6)	 (1, 6)	 (1, 3)	 (1, 6)
5	 (1, 7)	 (1, 7)	 (1, 7)	 (1, 7)	 (1, 2)
6	 (1, 2)	 (1, 2)	 (1, 2)	 (1, 2)	 (1, 7)
7	 (1, 8)	 (1, 8)	 (1, 8)	 (1, 8)	 (1, 8)
8	 (1, 9)	 (1, 9)	 (1, 9)	 (1, 9)	 (1, 9)

4.2.3. *The Influence on Mode Shapes of TCS.* From Table 9 and Figure 13, the following can be found. (I) When bolt looseness number is little, such as loosening 1 or 2 bolts, the resulting shapes of TCS can hardly be changed. (II) With the increase of bolt looseness number, low order mode shapes of TCS are varied at different levels, but for high order mode shapes, such as the 7th and the 8th shape results, they are unchanged and still the same as the ones under no loose condition. (III) The changing trend of natural frequencies with mode shapes is constant when the number of axial half-waves $m = 1$, which shows that frequency values firstly decline and then rise with the increase of the number of circumferential waves n , and usually frequency values related to $n > 8$ are higher than $n = 2 \sim 7$, and this frequency-shape relation agrees well with the result calculated by FEM.

4.3. *Test Results of Modal Parameters of TCS under BLB with Different Looseness Levels.* Similarly, based on the same test system and test method, modal parameters of TCS under different bolt looseness levels can be obtained. The measured

frequency, damping, and shape results under BLB with different looseness levels are listed in Tables 10, 11, and 12, respectively. Besides, in order to clearly describe the effect degree and trend of the shell under different bolt looseness boundaries, the scattergrams of natural frequencies and damping ratios of TCS related to different bolt looseness number are also given, as shown in Figures 14 and 15, and Figure 16 gives the relations between natural frequency and mode shape under BLB with different looseness levels.

4.4. *The Influence Analysis of Modal Parameters under BLB with Different Looseness Levels*

4.4.1. *The Influence on Natural Frequencies of TCS.* From Table 10 and Figure 14, it can be found that: (I) For the most modes of TCS, the increase of bolt looseness level would reduce the natural frequencies of TCS, but if looseness level is small, the decreased degree of natural frequencies of TCS is not obvious. For example, the resulting natural frequencies

TABLE 10: Natural frequencies of TCS under BLB with different looseness levels.

Modal order	No looseness A (Hz)	25% looseness B (Hz)	Effect degree (B - A)/A (%)	50% looseness C (Hz)	Effect degree (C - A)/A (%)	75% looseness D (Hz)	Effect degree (D - A)/A (%)
1	906.3	904.6	-0.2	887.8	-2.0	806.7	-11.0
2	980.8	978.2	-0.3	915.4	-6.7	848.8	-13.5
3	1025.7	1011.1	-1.4	980.1	-4.4	951.5	-7.2
4	1072.3	1062.3	-0.9	1072.0	0	1010.7	-5.7
5	1274.0	1267.0	-0.5	1268.3	-0.4	1279.1	0.4
6	1312.8	1309.3	-0.3	1310.6	-0.2	1319.6	0.5
7	1613.8	1613.3	0	1612.4	-0.1	1608.8	-0.3
8	1996.3	1992.4	-0.2	1990.8	-0.3	1987.9	-0.4

TABLE 11: Damping ratios of TCS under BLB with different looseness levels.

Modal order	No looseness A (Hz)	25% looseness B (Hz)	Effect degree (B - A)/A (%)	50% looseness C (Hz)	Effect degree (C - A)/A (%)	75% looseness D (Hz)	Effect degree (D - A)/A (%)
1	0.20	0.12	-40.0	0.16	-20.0	0.18	-10.0
2	0.76	0.37	-51.3	0.17	-77.6	0.53	-30.3
3	1.14	1.02	-10.5	0.51	-55.3	1.03	-9.6
4	0.27	0.36	33.3	0.33	22.2	0.72	166.7
5	0.74	0.85	14.9	0.84	13.5	0.88	18.9
6	0.37	0.24	-35.1	0.25	-32.4	0.95	156.8
7	0.39	0.3	-23.1	0.19	-51.3	0.17	-56.4
8	0.30	0.13	-56.7	0.15	-50.0	0.17	-43.3

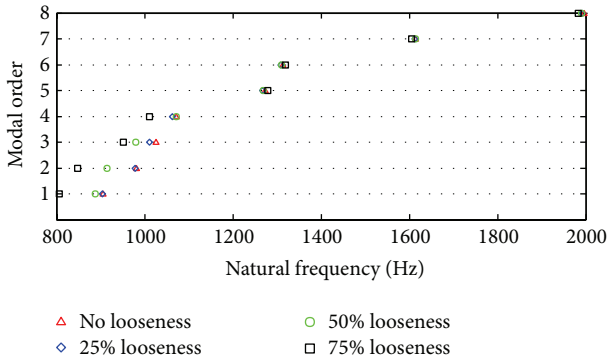


FIGURE 14: Scattergram of natural frequencies of TCS under BLB with different looseness levels.

are decreased from 0.2% to 1.4% under looseness level of 25% compared with the ones under the fixed state. (II) With the increase of bolt looseness level, the decreased degree of low order frequency values becomes more obvious, and taking the 1st and 2nd natural frequencies for example, they basically decrease from 11% to 13.5% compared with the ones under the fixed state. (III) The increase of bolt looseness level would also result in the decrease of high order of natural frequencies, but the decreased degree is very small. Taking the 7th and 8th natural frequencies for an example, the maximum of the decreased frequency results is about 0.4% compared with the ones under the fixed state. Therefore, it can be concluded that

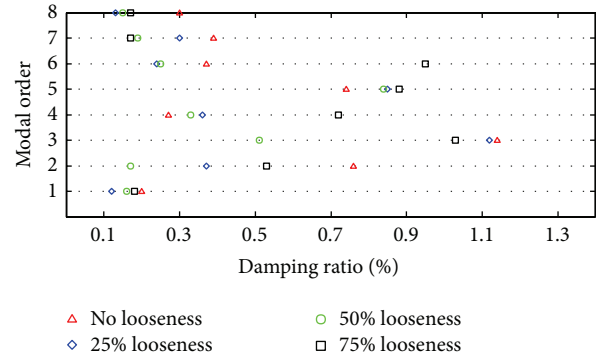


FIGURE 15: Scattergram of damping ratios of TCS under BLB with different looseness levels.

high order natural frequencies are basically not affected by BLB with different looseness levels. (IV) For some modes, their natural frequencies will go up slightly when the higher looseness level is reached (75% looseness). However, the maximum increased degree of the 5th and the 6th natural frequencies of TCS increases less than 0.5%, so basically we can ignore the effect of increased frequency values, which might be caused by the changes of nonlinear stiffness in bolt looseness positions.

4.4.2. *The Influence on Damping Ratios of TCS.* From Table 11 and Figure 15, it can be found that: (I) For most modes

TABLE 12: Mode shapes of TCS under BLB with different looseness levels.

Modal order	No looseness $A(m, n)$	25% looseness $B(m, n)$	50% looseness $C(m, n)$	75% Looseness $D(m, n)$
1阶	 (1, 4)	 (1, 4)	 (1, 4)	 (1, 4)
2阶	 (1, 5)	 (1, 5)	 (1, 3)	 (1, 5)
3阶	 (1, 3)	 (1, 3)	 (1, 5)	 (1, 6)
4阶	 (1, 6)	 (1, 6)	 (1, 6)	 (1, 3)
5阶	 (1, 7)	 (1, 7)	 (1, 7)	 (1, 7)
6阶	 (1, 2)	 (1, 2)	 (1, 2)	 (1, 2)
7阶	 (1, 8)	 (1, 8)	 (1, 8)	 (1, 8)
8阶	 (1, 9)	 (1, 9)	 (1, 9)	 (1, 9)

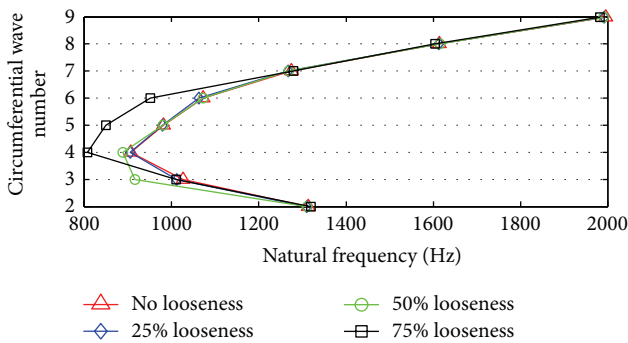


FIGURE 16: The relation between natural frequency and mode shape under BLB with different looseness levels.

of TCS, bolt looseness would reduce the damping of TCS. For example, for different bolt looseness level, the decreased range of damping results is obvious and is within 10% ~78%, but the decreased degree of damping is not proportional to the bolt looseness level. (II) For a small part of modes of TCS, the damping results will rise with the increase of bolt

looseness level, especially when the looseness level goes up to some extent; for example, when looseness level of 75% is reached, the resulting damping values related to the 4th and the 6th mode are nearly 1.5 times larger than the ones under no loose condition, which may be caused by the changes of mode shape or increased interface friction in bolt looseness positions.

4.4.3. *The Influence on Mode Shapes of TCS.* From Table 12 and Figure 16, it can be found that: (I) When bolt looseness level is relatively low, for example, when it is less than 25%, the resulting shapes of TCS can hardly be changed. (II) With the increase of bolt looseness level, low order mode shapes of TCS are varied, but for the intermediate and high order mode shapes, such as the 5th, the 6th, the 7th, and the 8th shape results, they are unchanged and are still the same as the ones under no loose condition. (III) Both natural frequencies and mode shapes of TCS would be changed under different bolt looseness levels, but the changing trend of natural frequencies with mode shapes is constant when the number of axial

half-waves $m = 1$, which shows that frequency values firstly decline and then rise with the increase of the number of circumferential waves n , and usually frequency values related to $n > 8$ are higher than $n = 2\sim 7$, and this frequency-shape relation agrees well with the result calculated by FEM.

5. Conclusions

This research combines theory with experiment to investigate the influence on modal parameters of TCS under bolt looseness boundary. Based on the analysis and experimental results, the following conclusions can be drawn as follows.

(1) Finite element method is adopted to roughly master vibration characteristics of shell structure, and theoretical analysis results of natural frequency and mode shape provide an important reference for experimental investigation on the influence on modal parameters of bolt constrained shell under different looseness boundaries.

(2) Test system and method under bolt looseness boundary is proposed to accurately measure modal parameters of TCS, and the following measurements and identification techniques are used to get precise frequency, damping, and shape results: (I) noncontact laser Doppler vibrometer and vibration shaker with excitation level being precisely controlled are used in the test system; (II) "preexperiment" is adopted to determine the required tightening torque and verify fixed constraint boundary; (III) the small-segment FFT processing technique is employed to accurately measure nature frequency; (IV) laser rotating scanning technique is used to get shape results with high efficiency.

(3) The influence on modal parameters of TCS under different bolt looseness numbers and different bolt looseness levels is analyzed in detail. It can be found that bolt looseness boundary can significantly affect frequency and damping results which might be caused by changes of nonlinear stiffness and damping and in bolt looseness positions. However, high order natural frequencies and mode shapes are still the same as the ones under no loose condition, and the changing trend of natural frequencies with mode shapes is constant when the number of axial half-waves $m = 1$, which agrees well with the result calculated by finite element method. Besides, bolt looseness would reduce the damping for most modes of TCS, but the decreased degree of damping is not proportional to the bolt looseness number or the bolt looseness level.

Conflict of Interests

The authors declare that there is no conflict of interests regarding the publication of this paper.

Acknowledgments

This study was supported by the National Natural Science Foundation of China Grant no. 51505070, the National Natural Science Foundation of China Grant no. 51375079, and the National Key Scientific Instrument and Equipment Development Project of China Grant no. 2013YQ470765.

References

- [1] A. W. Leissa, *Vibrations of Shells*, Acoustical Society of America, Columbus, Ohio, USA, 1973.
- [2] K. H. Ip, W. K. Chan, P. C. Tse, and T. C. Lai, "Vibration analysis of orthotropic thin cylindrical shells with free ends by the rayleigh-ritz method," *Journal of Sound and Vibration*, vol. 195, no. 1, pp. 117–135, 1996.
- [3] M. Amabili, "Free vibration of a fluid-filled circular cylindrical shell with lumped masses attached, using the receptance method," *Shock and Vibration*, vol. 3, no. 3, pp. 159–167, 1996.
- [4] C. T. Loy, K. Y. Lam, and C. Shu, "Analysis of cylindrical shells using generalized differential quadrature," *Shock and Vibration*, vol. 4, no. 3, pp. 193–198, 1997.
- [5] A. Farshidianfar, M. H. Farshidianfar, M. J. Crocker, and W. O. Smith, "Vibration analysis of long cylindrical shells using acoustical excitation," *Journal of Sound and Vibration*, vol. 330, no. 14, pp. 3381–3399, 2011.
- [6] R. L. Goldman, "Mode shapes and frequencies of clamped-clamped cylindrical shells," *AIAA Journal*, vol. 12, no. 12, pp. 1755–1756, 1974.
- [7] D. J. Ewins, *Modal Testing: Theory and Practice*, Research Studies Press, Latchworth, UK, 1984.
- [8] B. Peeters, H. D. V. Auweraer, P. Guillaume, and J. Leuridan, "The PolyMAX frequency-domain method: a new standard for modal parameter estimation?" *Shock and Vibration*, vol. 11, no. 3-4, pp. 395–409, 2004.
- [9] L. H. Sobel, "Effects of boundary conditions on the stability of cylinders subject to lateral and axial pressures," *The AIAA Journal*, vol. 2, no. 8, pp. 1437–1440, 1964.
- [10] S. Sun, S. Chu, and D. Cao, "Vibration characteristics of thin rotating cylindrical shells with various boundary conditions," *Journal of Sound and Vibration*, vol. 331, no. 18, pp. 4170–4186, 2012.
- [11] H. T. Wang, "Casing stiffness analysis of pretightening force bolt joint," *Aeroengine*, vol. 36, no. 3, pp. 32–35, 2010.
- [12] Y.-D. Kwon, H.-W. Kwon, J.-H. Hwangbo, and S.-H. Jang, "Finite element modeling for static and dynamic analysis of structures with bolted joint," *Key Engineering Materials*, vol. 306–308, pp. 547–552, 2006.
- [13] L. Liu, Z. Sun, M. Miao, and P. Li, "Fracture analysis of connection bolts of aero-engine," *Failure Analysis and Prevention*, vol. 7, no. 4, pp. 244–247, 2012.
- [14] K. Forsberg, "Influence of boundary conditions on the modal characteristics of thin cylindrical shells," *AIAA Journal*, vol. 2, no. 12, pp. 2150–2157, 1964.
- [15] T. Koga, "Effect of boundary conditions on the free vibrations of circular cylindrical shells," *AIAA journal*, vol. 26, no. 11, pp. 1387–1394, 1988.
- [16] A. H. Sofiyev, S. N. Keskin, and A. H. Sofiyev, "Effects of elastic foundation on the vibration of laminated non-homogeneous orthotropic circular cylindrical shells," *Shock and Vibration*, vol. 11, no. 2, pp. 89–101, 2004.
- [17] B. Liang and W. Zhang, "Two types of optimization of cylindrical shell on deformation," *Journal of Ship Mechanics*, vol. 9, no. 4, pp. 98–102, 2005.
- [18] G. M. Dong, J. Chen, X. Y. Lei et al., "Study on diagnosing attachment bolt looseness in missile clamping support," *Journal of Vibration Measurement & Diagnosis*, vol. 25, no. 3, pp. 98–102, 2005.

- [19] G. M. Dong, J. Chen, and N. Zhang, "Experimental study on monitoring the attachment bolt looseness in a clamping support structure model," in *Engineering Asset Management: Proceedings of the 1st World Congress on Engineering Asset Management (WCEAM) 11–14 July 2006*, pp. 964–970, Springer, London, UK, 2006.
- [20] H. Zhou, W. Li, B. Lv, and W. L. Li, "Free vibrations of cylindrical shells with elastic-support boundary conditions," *Applied Acoustics*, vol. 73, no. 8, pp. 751–756, 2012.
- [21] S. P. Sun, *Study on dynamic characteristics of rotating thin-walled cylindrical shells [Ph.D. thesis]*, Harbin Institute of Technology, 2013.
- [22] M. Amabili, R. Garziera, and A. Negri, "Experimental study on large-amplitude vibrations of water-filled circular cylindrical shells," *Journal of Fluids and Structures*, vol. 16, no. 2, pp. 213–227, 2002.
- [23] H. Li, W. Sun, Z. Xu, and Q. K. Han, "An experimental method of laser rotating canting to measure mode shape of constrained thin cylindrical shell," *Journal of Vibration and Shock*, vol. 33, no. 16, pp. 155–159, 2014.

Research Article

Rolling Bearing Diagnosing Method Based on Time Domain Analysis and Adaptive Fuzzy C-Means Clustering

Sheng Fu, Kun Liu, Yonggang Xu, and Yi Liu

College of Mechanical Engineering and Applied Electronics Technology, Beijing University of Technology, Beijing 100124, China

Correspondence should be addressed to Kun Liu; qk14335992@163.com

Received 22 July 2015; Revised 19 September 2015; Accepted 27 September 2015

Academic Editor: Arturo Garcia-Perez

Copyright © 2016 Sheng Fu et al. This is an open access article distributed under the Creative Commons Attribution License, which permits unrestricted use, distribution, and reproduction in any medium, provided the original work is properly cited.

Vibration signal analysis is one of the most effective methods for mechanical fault diagnosis. Available part of the information is always concealed in component noise, which makes it much more difficult to detect the deflection, especially at early stage of the development. This paper presents a new approach for mechanical fault diagnosis based on time domain analysis and adaptive fuzzy C-means clustering. By analyzing vibration signal collected, nine common time domain parameters are calculated. This lot of data constitutes data matrix as characteristic vectors to be detected. And using adaptive fuzzy C-means clustering, the optimal clustering number can be gotten then to recognize different fault types. Moreover, five parameters, including variance, RMS, kurtosis, skewness, and crest factor, of the nine are selected as the new eigenvector matrix to be clustered for more optimal clustering performance. The test results demonstrate that the proposed approach has a sensitive reflection towards fault identifications, including slight fault.

1. Introduction

Rolling bearing element is a key component in engineering machinery and any slight damage may lead to unexpected suspension of production, even industrial accidents. Common bearing faults develop for variety of reasons, such as unpredictable heavy loads and insufficient lubrication. It is of vital importance to know its defect before it is too late. As a rule, faults, which often occur in rolling elements, such as the ball and inner and outer race, generate and grow during bearing operation. It is very necessary to diagnose faults at early stage of their development. So far, for lack of cyclostationarity [1] of the vibration signal, a number of diagnosis methods have been proposed, which are variedly classified as vibration analysis [2], wear debris detection [3], current and temperature monitoring [4], and so on. Acoustic emission (AE) [5] is considered as one of the most effective acoustic-based bearing health monitoring techniques. It is a high frequency, transient impulse emitted by the rapid local stress redistributions in solid material under working load conditions. Examples of AE applications are crack growth, corrosion, and wear [6]. Compared to other methods,

it has special advantages, but the situation that no acoustic emission signal will be detected for a stable deflection limits its application.

Vibration analysis, another one of the most effective rolling bearing fault diagnosis techniques, hops off the limitation of AE. A periodic shock impulse appears every time one component contacts another if there is a local fault. It is vibration analysis that makes the detection of the fault quantitatively. Time domain analysis, frequency domain analysis, and time-frequency domain analysis are the three main branches. Time domain analysis has the disadvantages of low sensitivity and low accuracy, but its simple calculations and direct signal processing contribute to shortening of the processing time. Simple time domain method is not suitable for effective fault diagnosis, but it is much better when combined with other approaches, for example, neural network [7], pattern recognition, and artificial intelligence. Muralidharan et al. [8] finished fault diagnosis of self-aligning carrying idler in different conditions, by using statistical measures to get useful features and then to classify them with decision tree algorithm.

Frequency domain analysis, also called spectral analysis, is used to transform the signals acquired from time domain into frequency domain through fast Fourier transform (FFT). Each component of bearing has a fault characteristic frequency calculated according to a series of empirical formulas. Monitoring these fault characteristic frequencies and their low-frequency harmonics is a classic method for bearing fault diagnosis [9]. However, the background noise makes it difficult to identify valid frequency component. To weaken the noise level and strengthen the signal to noise ratio, researchers have adopted some new approaches, like amplitude spectrum, power spectrum, cepstrum, and Hilbert demodulation [10–13], for bearing detection. However, the accuracy of these methods highly depends on the bearing dimensions and rotational speed [6].

Time-frequency analysis provides the joint distribution information of time and frequency domain, which clearly illustrates frequency of the signal varying as a function of time. To characterize the energy intensity of one signal at different time and frequency, a variety of approaches have been proposed, such as short time Fourier transform [14], Wigner-Ville distribution [15], and continuous wavelet transform [16]. However, the computation of these methods takes too much time so that the classification process becomes more complicated. Though a lot of researches have been carried out in the field of fault diagnosis, it is evident that very few literatures reported the enhancement of the algorithms to effectively recognize faults of micro size.

In order to analyze the vibration signal, new unpitched sound would be unexpectedly added by complex approaches to weaken the original noise, either frequency domain analysis or time-frequency analysis, which makes it difficult to detect micro fault. Hence, relatively original time domain analysis method becomes a potential one for micro size fault. Moreover, more reliable and robust diagnoses will be acquired if multiple methods associated with vibration analysis like fuzzy *C*-means (FCM) clustering and singular entropy. Fuzzy *C*-means clustering is a clustering algorithm based on division, ensuring the maximal similarity among the data points divided into one cluster and minimum similarity among different clusters. Furthermore, feature weighted FCM cluster analysis [17] is applied to recognize different fault categories and fault severities but no exposition about the corresponding relationship between fault category and clustering center. X. He and Q. He [18] proposed a fault diagnosis approach based upon principal component analysis (PCA) method and fuzzy *C*-means (FCM) clustering. However, it is stretched thin by the case of unpredictable operating conditions.

The present paper proposes a new method based on time domain analysis and adaptive fuzzy *C*-means clustering. Nine feature parameters of the vibration signals are extracted as the eigenvectors to be clustered. Then these data points will be separated into different piles using the adaptive algorithm. To further bear fault related feature extraction from the signal, five parameters of the nine are selected as the new eigenvector matrix to be clustered. And the experiment results showed the validity and robustness of the method in the application of fault detection of micro size, which

would be potential for diagnosing faults at early stage of their development.

2. Theoretical Basis of the Analysis

2.1. Time Domain Feature Parameters. As we know, acquired vibration signal is amplitude as a function of time. Its mean equals the average value of the absolute value of amplitude, which is calculated as

$$\bar{X} = \frac{1}{n} \sum_{i=1}^n |x_i|. \quad (1)$$

Variance, a physical quantity which reflected stability level of data, is the average of quadratic summation, which sums the square value of difference value of each data and the mean:

$$X_{\text{var}} = \frac{1}{n} \sum_{i=1}^n (x_i - \bar{X})^2. \quad (2)$$

Standard deviation shows dispersion of a group of data with respect to the mean, and its magnitude equals arithmetic mean value of the variance.

Root mean square (RMS) indicates the energy of the signal and has a positive effect on wear fault and a weak sensitivity to early fault. Consider

$$X_{\text{RMS}} = \sqrt{\frac{1}{n} \sum_{i=1}^n x_i^2}. \quad (3)$$

Kurtosis reflects the characteristic of random variable distribution, and the kurtosis value of bearing vibration signal generally varies between 3 and 45. It indicates that there is a certain degree of damage when the value is up to 4. Compared with RMS, kurtosis is sensitive to early fault; expect its poor stability. Consider

$$X_{\text{kur}} = \frac{1}{n} \frac{\sum_{i=1}^n x_i^4}{X_{\text{RMS}}^4}. \quad (4)$$

Peak, maximum amplitude at some time, is always used to detect breakdown accompanied by instantaneous impact. Consider

$$X_p = \frac{1}{n} \sum_{i=1}^n X_{pi}. \quad (5)$$

Crest factor is defined as the ratio of peak value and RMS. The threshold value to judge physical condition of bearing is approximately 1.5. Generally speaking, there is local defect if the crest factor value exceeds 1.5 [19]. Consider

$$X_{\text{cf}} = \frac{X_p}{X_{\text{RMS}}}. \quad (6)$$

Skewness is the characteristic parameter to attribute asymmetry degree of probability density curve relative to the

mean. Skewness is, by definition, the order three standard moments of the sample. Consider

$$X_{\text{skew}} = E \left[\left(\frac{x - \mu}{\sigma} \right)^3 \right]. \quad (7)$$

Kurtosis [19, 20] is a measure of the heaviness of the tails in the distribution of the signal. It is the non-Gaussianity of the signal that makes the tails of the distribution heavier and destroys the symmetry of the distribution, resulting in high values of the kurtosis parameter, which is suitable for flaking failures. Crest factor [19] is usually used for faults like local spalling, scratching, and nick. The two above have a good sensitivity for discrete faults and are unacted on bearing rotating speed, dimension, and load. Skewness [21] is a measure of the asymmetry of the data around the mean. Variance [21] and RMS [19] have well reliability on continuous faults like wearing. In general, kurtosis and crest factor are used for discrete faults, while variance and RMS are used for continuous faults. Hence, the five time domain parameters were picked out for the consideration of the complement among different types of parameters and also the gains of the same type. According to their complementarity and consistency, the optimal combination contained with five parameters (variance, RMS, kurtosis, skewness, and crest factor) was selected as the eigenvector matrix to be clustered.

2.2. Adaptive Fuzzy C-Means Clustering. The aim to cluster is to get as large between-class distance and as small in-class distance as possible when classifying data. To avoid the validation problem of giving the number of clusters in advance, adaptive fuzzy C-means clustering is applied, and its basic idea is as follows.

The central vector of population sample is calculated as

$$\bar{x} = \frac{\sum_{i=1}^c \sum_{j=1}^n u_{ij}^m x_j}{n}. \quad (8)$$

Membership matrix $U^{(k)}$ is calculated as

$$u_{ij}^{(k)} = \frac{1}{\sum_{r=1}^c (d_{ij}^{(k)} / d_{rj}^{(k)})^{2/(m-1)}}. \quad (9)$$

Clustering center matrix $V^{(k+1)}$ is calculated as

$$v_i^{(k+1)} = \frac{\sum_{j=1}^n (u_{ij}^{(k)})^m x_j}{\sum_{j=1}^n (u_{ij}^{(k)})^m}. \quad (10)$$

Adaptive function of clustering-C is as follows:

$$L(c) = \frac{\sum_{i=1}^c \left(\sum_{j=1}^n u_{ij}^m \right) \|v_i - \bar{x}\|^2 / (c-1)}{\sum_{i=1}^c \left(\sum_{j=1}^n u_{ij}^m \right) \|x_j - v_i\|^2 / (n-c)}. \quad (11)$$

In function (11), the numerator shows between-class distance, while the denominator shows in-class distance. It is obvious that the larger $L(c)$ would get, the more reasonable clustering would be. Figure 1 shows the adaptive process of clustering number-C.

3. Experimental Analysis and Verification

3.1. Data Sources. The data is from the Case Western Reserve University Bearing Data Center Website, which provides access to ball bearing test data for normal and faulty bearings. As shown in Figure 2, the test stand consists of a 2 hp motor, a dynamometer, and control electronics (not shown). Testing bearing, located in the driving end, is deep groove ball bearing of SKF6205. Single point faults are introduced to the test bearings using electrical discharge machining, and accelerometers are attached to the housing with magnetic bases to collect vibration data.

3.2. Diagnosis in Condition of Nine Time Domain Parameters. Analysis based upon four cases of bearing conditions (health, inner race, ball, and outer race) is conducted. There are 28 groups of signals for four bearing conditions and two fault diameters of 0.007 inches and 0.014 inches. The sample frequency is 12 kHz. Nine statistic parameters at time domain of the 28 groups of vibration signals are shown in Table 1.

In allusion to four types of bearing signals, a 9×16 data matrix (9 means nine time domain feature parameters and 16 represents the fact that there are four groups of signal data for each bearing condition and the total is sixteen) is constituted to be the eigenvector matrix for clustering analysis after taking 16 groups of signals as a data sample. In the course of clustering analysis, $\varepsilon = 0.001$, the center of clustering is being constantly revised through iterative algorithm until convergence. As shown in Figure 3, 16 groups of signals are clustered into four sorts, which represents four conditions of bearing, and accordingly adaptive function of clustering-C in Table 2 values the maximum only when the number clustering is four, which means consistent results. Sixteen groups of sample data distribute around four clustering centers, each of which denotes one kind of bearing condition. It evolves that the diagnosing method proposed in the paper has good effects on the recognition of mechanical fault. In fact, there are many alternative array modes for a 9×16 data matrix from the 28 groups of data, and the rate of accurate diagnosing is not as satisfying as we have expected after dozens of experiments.

3.3. Diagnosis in Condition of Five Optimal Time Domain Parameters. In the previous section, because of the data redundancy of different parameters, nonideal bunching result was gotten in Figure 3, where sample data of the same bearing condition is not in such concentrating distribution. Meanwhile, adaptive function of clustering-C in Table 2 did not occupy obvious advantages with respect to the situation of 5 clusters, which probably implied poor robustness.

Effective feature parameters should be chosen to constitute the new eigenvector matrix. For further study, two 5×16 data matrices (5 means five time domain feature parameters and 16 represents the fact that there are four groups of signal data for each bearing condition and the total is sixteen) are constituted to be the eigenvector matrix for clustering analysis after taking 16 groups of signals as a data sample. One is for the fault size of 0.014 inches, and

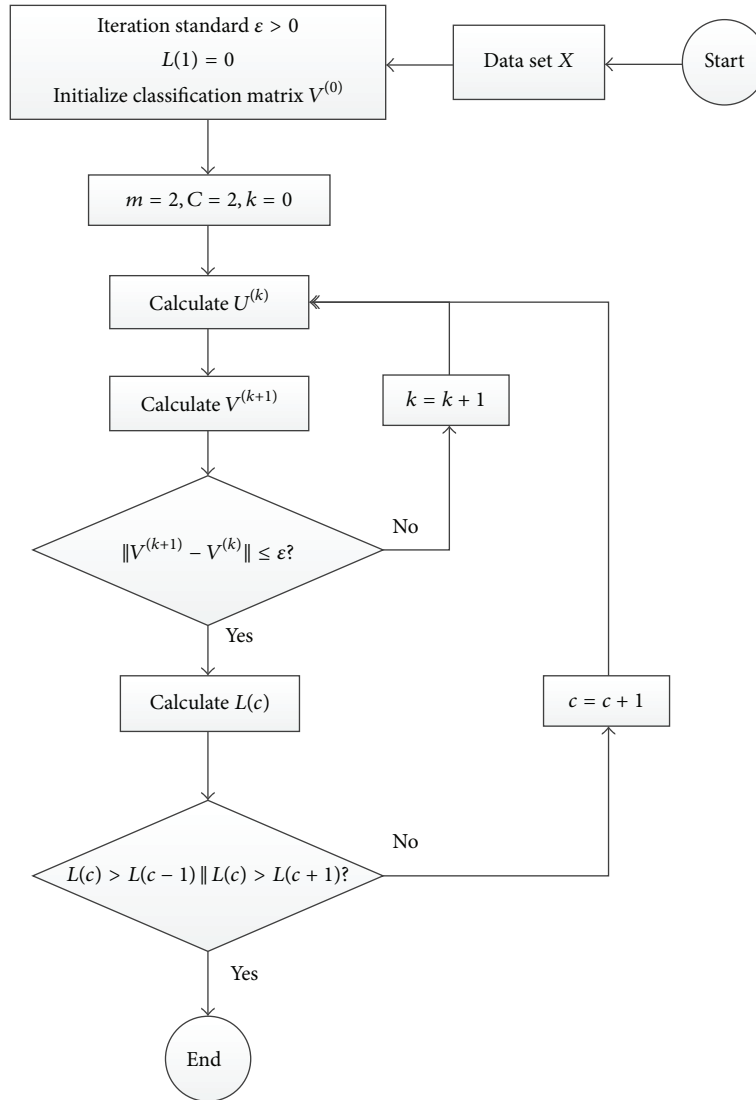


FIGURE 1: Adaptive fuzzy C-means clustering flow chart.

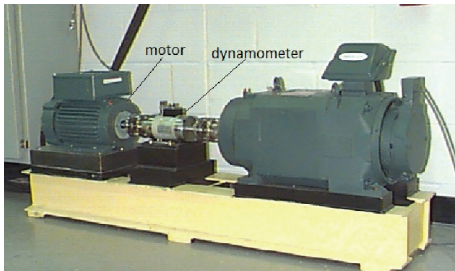


FIGURE 2: The test stand (bearing data center of CWRU).

the other is for the fault size of 0.007 inches. As shown in Figure 4(a), 16 data sets (0.014 inches), which contained four bearing conditions of health, inner race, ball, and outer race, were divided into four groups, one of which means one bearing condition, and the clustering functions in Table 3

verify the availability of the clustering. The other 16 data sets (0.007 inches) in Figure 4(b) were clearly clustered into four piles.

There is no obvious aliasing phenomenon among different distributed data in Figure 4, which shows the two different cases when the deflection is of, respectively, micro size of 0.007 inches and 0.014 inches. Obviously, four types of bearing conditions could be easily identified from Figure 4 and corresponding data points gathered together around the four clustering centers. Moreover, the fact that adaptive clustering- C function $L(c)$ gets the value at $c = 4$ much larger than others in Tables 3 and 4 declared the validity and rationality of the new eigenvector matrix of the five parameters.

Then, the method with five-parameter feature matrix was applied to the situation of single fault. Thereinto, the diagnosis of inner and outer race single fault of 0.007 inches was shown in Figure 5. The result shown in Figure 5 and

TABLE 1: Statistic parameters in time domain of the vibration signals.

Fault diameter (inch)	Name	Mean	Var.	RMS	Median	Kur.	Skew.	Std.	Peak	Crest
0	H-P0	0.0126	0.0053	0.0738	0.0125	2.7642	-0.0354	0.0727	0.0765	1.0372
0	H-P1	0.0126	0.0042	0.0664	0.0150	2.9306	-0.1730	0.0652	0.0578	0.8708
0	H-P2	0.0123	0.0040	0.0643	0.0146	2.9251	-0.1671	0.0631	0.0592	0.9196
0	H-P3	0.0125	0.0042	0.0659	0.0144	2.9572	-0.1275	0.0647	0.0613	0.9297
0.007	I7-P0	0.0134	0.0848	0.2915	0.0071	5.3959	0.1640	0.2912	0.2750	0.9432
0.007	I7-P1	0.0058	0.0858	0.2929	-0.0003	5.5423	0.1304	0.2928	0.2687	0.9173
0.007	I7-P2	0.0046	0.0897	0.2995	0.0013	5.5638	0.0904	0.2995	0.2728	0.9107
0.007	I7-P3	0.0047	0.0983	0.3136	0.0023	5.2911	-0.0132	0.3136	0.2892	0.9222
0.007	B7-P0	0.0126	0.0192	0.1392	0.0128	2.9847	-0.0089	0.1387	0.1597	1.1473
0.007	B7-P1	0.0039	0.0193	0.1391	0.0037	2.9638	0.0075	0.1390	0.1529	1.0994
0.007	B7-P2	0.0046	0.0217	0.1473	0.0039	2.8314	0.0271	0.1472	0.1628	1.1054
0.007	B7-P3	0.0042	0.0236	0.1536	0.0037	2.8897	0.0204	0.1536	0.1669	1.0861
0.007	O7-P0	0.0232	0.4477	0.6695	0.0219	7.6494	0.0569	0.6691	0.5767	0.8614
0.007	O7-P1	0.0041	0.3504	0.5919	0.0004	7.5950	0.0334	0.5919	0.5128	0.8663
0.007	O7-P2	0.0039	0.3251	0.5702	0.0032	7.8522	0.0195	0.5702	0.4780	0.8383
0.007	O7-P3	0.0045	0.3368	0.5804	0.0037	7.9637	-0.0021	0.5804	0.4857	0.8369
0.014	I14-P0	0.0344	0.0380	0.1978	0.0339	21.957	-0.0588	0.1948	0.1746	0.8824
0.014	I14-P1	0.0036	0.0274	0.1655	0.0031	22.084	0.0030	0.1655	0.1299	0.7849
0.014	I14-P2	0.0037	0.0266	0.1631	0.0026	21.686	0.0235	0.1630	0.1301	0.7976
0.014	I14-P3	0.0030	0.0327	0.1808	0.0034	18.164	0.0334	0.1808	0.1483	0.8203
0.014	B14-P0	0.0047	0.0233	0.1527	0.0045	17.769	0.2251	0.1526	0.1293	0.8469
0.014	B14-P1	0.0045	0.0198	0.1409	0.0041	8.8371	0.0157	0.1408	0.1255	0.8909
0.014	B14-P2	0.0046	0.0206	0.1435	0.0044	9.7522	0.1433	0.1434	0.1298	0.9049
0.014	B14-P3	0.0045	0.0179	0.1337	0.0065	14.859	0.1638	0.1336	0.1157	0.8652
0.014	O14-P0	0.0144	0.0099	0.1007	0.0142	3.0560	0.0006	0.0996	0.1121	1.1130
0.014	O14-P1	0.0031	0.0087	0.0936	0.0028	2.9403	0.0089	0.0935	0.0967	1.0339
0.014	O14-P2	0.0032	0.0094	0.0968	0.0035	3.0241	0.0002	0.0968	0.0992	1.0249
0.014	O14-P3	0.0025	0.0090	0.0947	0.0027	3.7970	0.0042	0.0947	0.0918	0.9691

TABLE 2: Adaptive clustering-C function for Figure 3.

c	1	2	3	4	5	6
$L(c)$	0	123.96	163.15	328.48	314.45	0

Tables 5 and 6 indicates that the method is able to recognize bearing fault of micro size, namely, at early stage of defection.

4. Result and Discussion

From the experiments above, we could know that the method proposed in this paper can be applied to diagnosis of bearing faults of micro size, no matter single or multiple faults.

Next, in order to verify the correction and superiority of the method, diagnosing method based on Hilbert transformation and wavelet denoising was applied to the same vibration signals of Figure 5. After preliminary calculation of empirical equation, the fault character frequencies of the inner race and outer race are 162.18 Hz and 107.37 Hz.

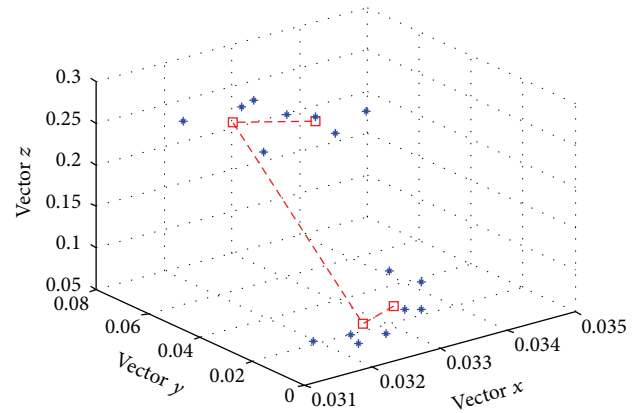


FIGURE 3: The 3D diagram of four types of bearing conditions (9×16 matrix).

The spectrogram after Hilbert envelope demodulation and wavelet denoising is displayed in Figure 6. As shown in

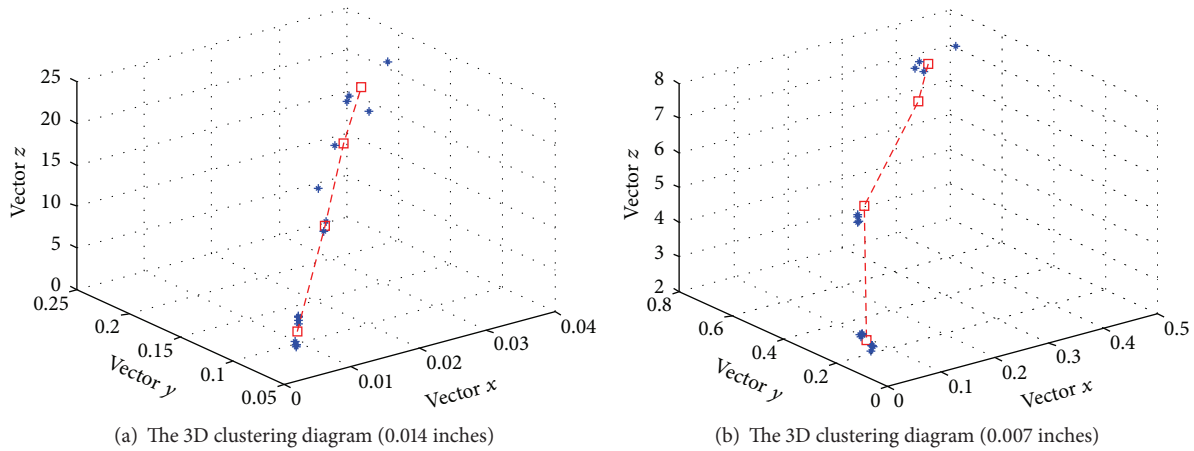


FIGURE 4: The 3D diagram of four types of bearing conditions with five parameters.

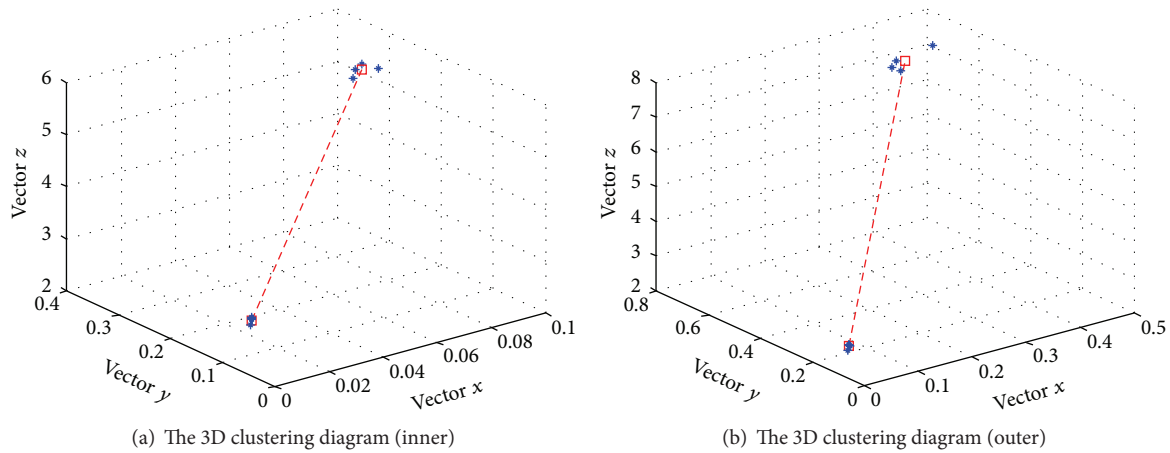


FIGURE 5: The 3D diagram of two types of bearing conditions.

TABLE 3: Adaptive clustering-C function for Figure 4(a).

c	1	2	3	4	5	6
$L(c)$	0	129.7	180.17	566.53	437.1	0

TABLE 4: Adaptive clustering-C function for Figure 4(b).

c	1	2	3	4	5	6
$L(c)$	0	13.30	38.06	531.49	165.06	0

TABLE 5: Adaptive clustering-C function for Figure 5(a).

c	1	2	3	4
$L(c)$	0	671.69	498.06	0

TABLE 6: Adaptive clustering-C function for Figure 5(b).

c	1	2	3	4
$L(c)$	0	1840.54	1074.56	0

Figure 6(a), the frequency domain diagnostic approach is able to detect the inner race point faults of 0.007 inches, except for several unfathomed frequency components. There is no evident frequency value and homologous frequency multiplication in the other diagram of Figure 6(b). The fact that no resultful information was extracted from the signal with noisy environment implies the shortage of the approach.

By contrast, the method present in this paper is an efficient and robust way to detect the micro size fault.

Time domain analysis is a direct signal processing method with simple calculations, and each of the nine time domain parameters can reflect the different characteristics of the signal to be extracted as significant basis for initial diagnosis to some extent.

In this paper, a method based on time domain analysis and adaptive fuzzy C -means clustering was proposed. Judging by the complementarity and consistency of the nine time domain parameters, five of them, namely, variance,

5. Conclusion

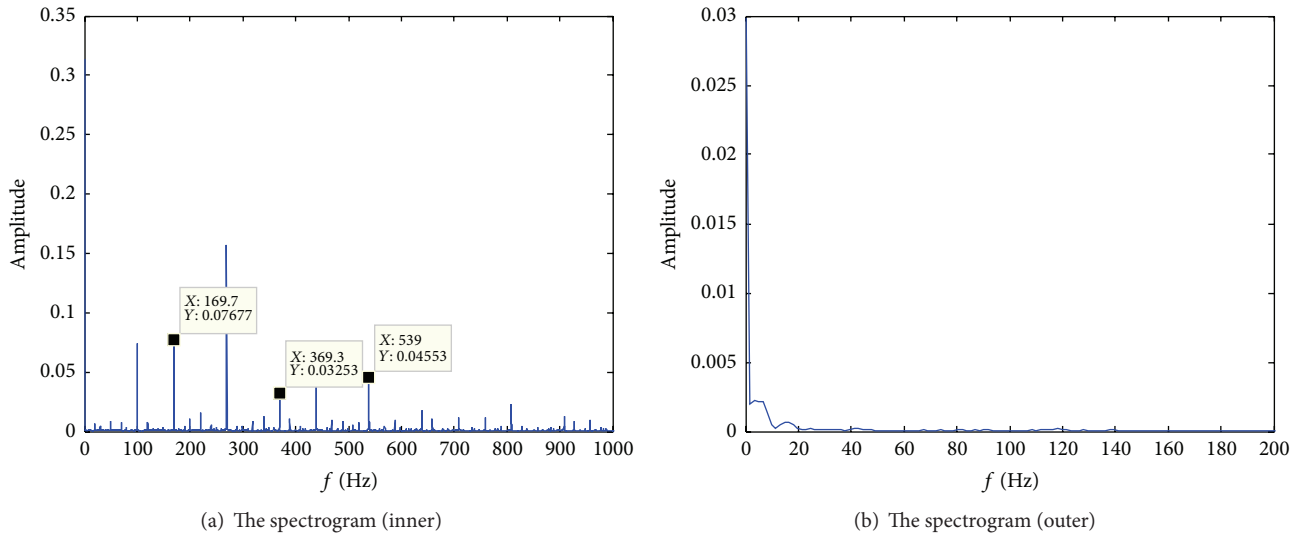


FIGURE 6: The spectrogram of the fault signals (0.007 inches).

RMS, kurtosis, skewness, and crest factor, were selected as the feature matrix for clustering algorithm. Benefiting from the adaptivity of the clustering algorithm, unknown operating conditions of the bearing could be detected fast and accurately, to estimate whether the rolling bearing is healthy or not, even single fault or multiple faults. The experiments proved the validity and robustness of the method in the application of fault detection of micro size, which would be potential for diagnosing faults at early stage of their development.

Conflict of Interests

The authors declare that there is no conflict of interests regarding the publication of this paper.

Acknowledgments

This work is supported by the National Science and Technology Major Project of China (Grant no. 2010ZX04007-051), Beijing Research Institute of Automation for Machinery Industry, Machinery Industry Key Laboratory of Precision Measurement & Control Technology and Instruments, and Bearing Data Center of Case Western Reserve University.

References

- [1] J. Urbanek, T. Barszcz, and J. Antoni, "Time-frequency approach to extraction of selected second-order cyclostationary vibration components for varying operational conditions," *Measurement*, vol. 46, no. 4, pp. 1454–1463, 2013.
- [2] J. Dybała and R. Zimroz, "Rolling bearing diagnosing method based on empirical mode decomposition of machine vibration signal," *Applied Acoustics*, vol. 77, pp. 195–203, 2014.
- [3] A. Zmitrowicz, "Wear debris: a review of properties and constitutive models," *Journal of Theoretical and Applied Mechanics*, vol. 43, no. 1, pp. 3–35, 2005.
- [4] J. Seo, H. Yoon, H. Ha, D. Hong, and W. Kim, "Infrared thermographic diagnosis mechanism for fault detection of ball bearing under dynamic loading conditions," *Advanced Materials Research*, vol. 295–297, pp. 1544–1547, 2011.
- [5] R. Hill and R. W. B. Stephens, "Simple theory of acoustic-emission-consideration of measurement parameters," *Acustica*, vol. 31, no. 4, pp. 224–230, 1974.
- [6] M. S. Safizadeh and S. K. Latifi, "Using multi-sensor data fusion for vibration fault diagnosis of rolling element bearings by accelerometer and load cell," *Information Fusion*, vol. 18, no. 1, pp. 1–8, 2014.
- [7] S. Zhang, T. Asakura, X. Xu, and B. Xu, "Fault diagnosis system for rotary machine based on fuzzy neural networks," *JSME International Journal Series C: Mechanical Systems, Machine Elements and Manufacturing*, vol. 46, no. 3, pp. 1035–1041, 2003.
- [8] V. Muralidharan, S. Ravikumar, and H. Kangasabapathy, "Condition monitoring of Self aligning carrying idler (SAI) in belt-conveyor system using statistical features and decision tree algorithm," *Measurement*, vol. 58, pp. 274–279, 2014.
- [9] J. I. Taylor, "Identification of bearing defects by spectral analysis," *Journal of Mechanical Design*, vol. 102, no. 2, pp. 199–204, 1980.
- [10] A. Sadoughi, M. Ebrahimi, M. Moallem, and S. Sadri, "Intelligent diagnosis of broken bars in induction motors based on new features in vibration spectrum," *Journal of Power Electronics*, vol. 8, no. 3, pp. 228–238, 2008.
- [11] B. Liang, S. D. Iwnicki, and Y. Zhao, "Application of power spectrum, cepstrum, higher order spectrum and neural network analyses for induction motor fault diagnosis," *Mechanical Systems and Signal Processing*, vol. 39, no. 1-2, pp. 342–360, 2013.
- [12] R. Jiang, S. Liu, Y. Tang, and Y. Liu, "A novel method of fault diagnosis for rolling element bearings based on the accumulated envelope spectrum of the wavelet packet," *Journal of Vibration and Control*, vol. 21, no. 8, pp. 1580–1593, 2015.
- [13] S. Agrawal, S. R. Mohanty, and V. Agarwal, "Bearing fault detection using Hilbert and high frequency resolution techniques," *IETE Journal of Research*, vol. 61, no. 2, pp. 99–108, 2015.
- [14] O. R. Seryasat, M. A. Shoorehdeli, M. Ghane, J. Haddadnia, and M. Zeinali, "Intelligent fault detection of ball bearing using FFT,

- STFT energy entropy and RMS,” *Life Science Journal*, vol. 9, pp. 1781–1786, 2012.
- [15] H. Wang, K. Li, and H. Sun, “Feature extraction method based on pseudo-Wigner-Ville distribution for rotational machinery in variable operating conditions,” *Chinese Journal of Mechanical Engineering*, vol. 24, no. 4, pp. 661–668, 2011.
- [16] P. K. Kankar, S. C. Sharma, and S. P. Harsha, “Fault diagnosis of ball bearings using continuous wavelet transform,” *Applied Soft Computing Journal*, vol. 11, no. 2, pp. 2300–2312, 2011.
- [17] W. Sui, C. Lu, and D. Zhang, “Bearing fault diagnosis based on feature weighted FCM cluster analysis,” in *Proceedings of the International Conference on Computer Science and Software Engineering*, vol. 5, pp. 518–521, IEEE, Wuhan, China, December 2008.
- [18] X. He and Q. He, “Application of PCA method and FCM clustering to the fault diagnosis of excavator’s hydraulic system,” in *Proceedings of the International Conference on Automation and Logistics (ICAL ’07)*, pp. 1635–1639, Jinan, China, August 2007.
- [19] Q. Shen and S. Zheng, *Machinery Fault Diagnosis*, Chemical Industry Press, 2009.
- [20] L. Yuan, Y. He, J. Huang, and Y. Sun, “A new neural-network-based fault diagnosis approach for analog circuits by using kurtosis and entropy as a preprocessor,” *IEEE Transactions on Instrumentation and Measurement*, vol. 59, no. 3, pp. 586–595, 2010.
- [21] A. Tafazzoli, N. M. Steiger, and J. R. Wilson, “N-Skart: a nonsequential skewness- and autoregression-adjusted batch-means procedure for simulation analysis,” *IEEE Transactions on Automatic Control*, vol. 56, no. 2, pp. 254–264, 2011.